

ABSTRACT

An accurate depth-velocity model is the key for obtaining good quality and reliable depth images in areas of complex geology. In such areas, velocity-model definition should use methods that describe the complexity of wavefield propagation, such as focusing and defocusing, multiple arrivals, and frequency-dependent velocity sensitivity. Wave-equation tomography in the image space has the ability to handle these issues because it uses wavefields as carriers of information. However, its high cost and low flexibility for parametrizing the model space has prevented its routine industrial use.

This thesis aims at overcoming those limitations by using new wavefields as carriers of information: the image-space generalized wavefields. These wavefields are synthesized by using a pre-stack generalization of the exploding-reflector model. Cost of wave-equation tomography in the image space is decreased because only a small number of image-space generalized wavefields are necessary to accurately describe the kinematics of velocity errors and because these wavefields can be easily used in a target-oriented way. Flexibility is naturally incorporated into wave-equation tomography in the image space by using these wavefields because their modeling have as the initial conditions some key selected reflectors, allowing a layer-based parametrization of the model space.

To use the image-space generalized wavefields in wave-equation tomography in the image space, the method is extended from the shot-profile domain to the image-space generalized-sources domain. In this new domain, the velocity updates are very fast. Migration with the optimized velocity model provides good quality and reliable depth images, as can be seen in a 3D-field data example. Introduction The last decade has seen the development of migration-velocity analysis (MVA) by wavefield extrapolation (Biondi and Sava, 1999; Shen et al., 2003; Sava, 2004; Shen, 2004). Provided the finite frequency nature of wavefield extrapolation, this MVA technique does not suffer from the limitations caused by the high-frequency approximation, which are present in the ray-based methods, namely the need of smooth velocity contrasts. However, despite its theoretical superiority, MVA by wavefield extrapolation has rarely been used in 3D projects (?). This is because of its higher cost and because it is less flexible than its ray-based counterpart in parameterizing the velocity model. Therefore, decreasing its cost and improving its flexibility is crucial to implement MVA by wavefield extrapolation as a routine process.

Because of the linearity of wavefield propagation

We start by describing the prestack exploding-reflector model and how using this new concept can drastically decrease data size especially for 3D applications. Then, using phase-encoding techniques, we introduce the image-space phase-encoded wavefields, further decreasing data size. After introducing the theory of MVA by wavefield extrapolation using image-space generalized wavefields, we illustrate their use to optimize the migration velocity for the Marmousi model. Finally, we show the application on a 3D field data from the North Sea, which presents different challenges to migration-velocity definition.

Applying the properties of linear, time-invariant systems enables us to consider source functions other than punctual. This characterizes generalized source functions defined in the generalized source domain. For instance, according to the superposition principle, a hypothetical experiment in which all the point sources are initiated in unison generates a horizontal plane wave. Another thought experiment would be to initiate all the sources of the seismic survey at random times, using the superposition and the time-shift properties. This concept is used in simultaneous Vibroseis acquisition, where different arrays of vibrators are initiated independently and with no synchronization between them, allowing great improvement in productivity (Howe et al., 2009).

Those experiments can be easily synthesized in the seismic processing environment, by combining the recorded wavefields with the same scheme as that used for point sources. In this way, the migrated image computed using the combined source functions and the combined recorded wavefields is similar to the one we would obtain by migrating the original data, provided that certain conditions particular to each combination method are fulfilled. However, the imaging cost can be smaller by orders of magnitude with generalized wavefields than with conventional wavefields.

The idea of synthesizing generalized sources during processing is not new in seismic exploration. Plane-wave synthesis (Whitmore, 1995), controlled illumination (Rietveld et al., 1992), and random-phase encoding (Romero et al., 2000) are methods that synthesize generalized sources. In the plane-wave synthesis method, linear time shifts are applied to the shot records to simulate slanted plane waves. In the controlled illumination method, a wavefield with a pre-defined shape is upward propagated and collected at the surface, defining a synthesis operator to be convolved with the original data. The generalized wavefields synthesized by the controlled illumination method tend to assume the shape of the pre-defined wavefield during the downward propagation. In the random-phase encoding method, source functions and the corresponding receiver gathers are encoded with the same random-code function, so that during migration cross-correlation of unrelated wavefields is attenuated, whereas the cross-correlation of related wavefields is minimally affected.

The methods described above for generating generalized sources are illustrated in Figures 2-4. In these figures, on the top left is the generalized source function, on the top right is the generalized receiver gather, and on the bottom is the areal-shot migrated image. In Figure 2 the plane-wave synthesis method creates horizontal plane waves at the surface. In Figure 3 a horizontal plane wave at depth 2300 m is synthesized by the method of controlled illumination. In Figure 4, the random-phase encoding method is used to combine every 20 shots into one generalized receiver gather. Migrating

data from only one generalized source is not sufficient to recover a similar image quality as the migration of the original 375 shot-profiles (Figure 1). Therefore, it is usual to synthesize more generalized sources to achieve a reasonable quality. Even so, the cost of migrating generalized sources is much smaller than that of migrating the original shot-profiles.

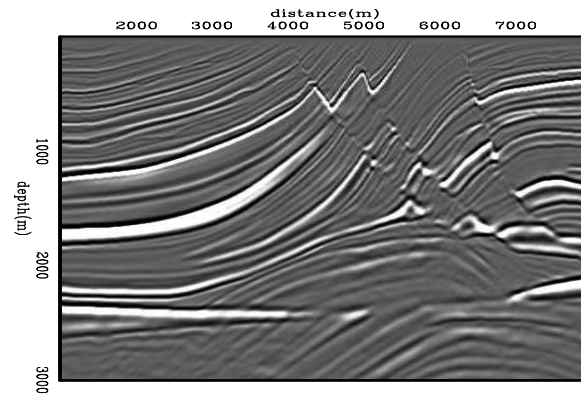


Figure 1: Migration of the original 375 shot-profiles.

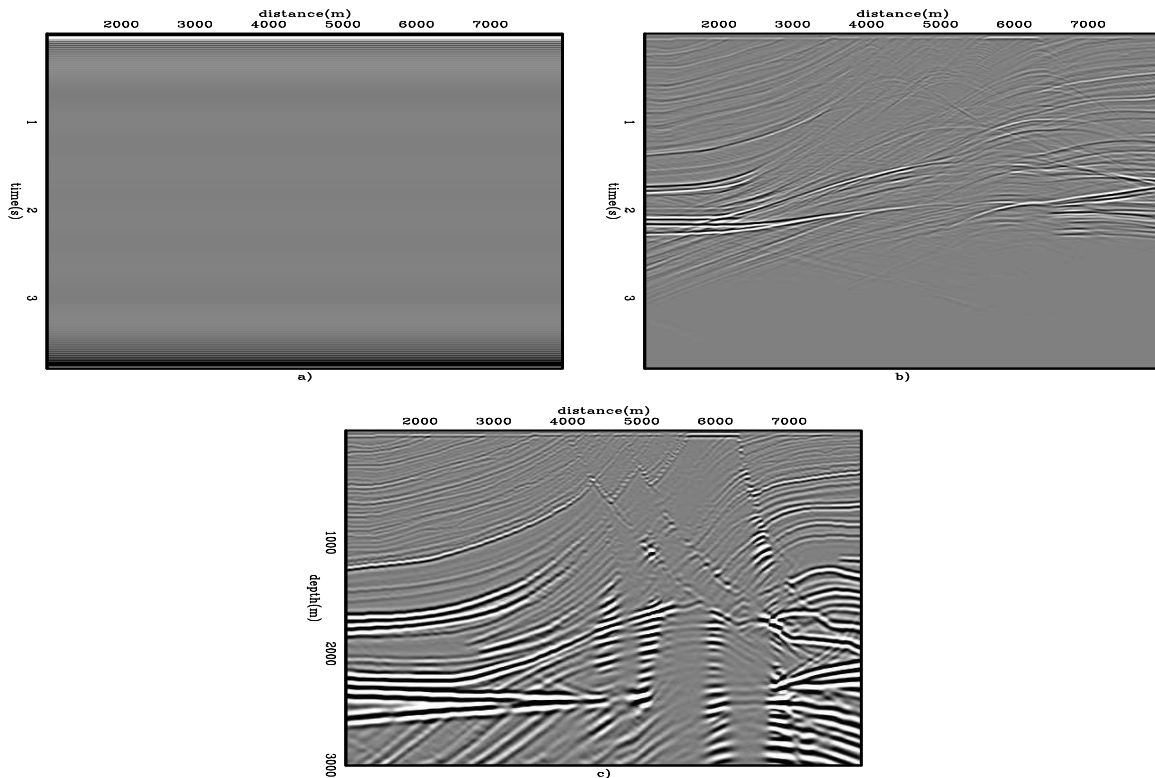


Figure 2: Horizontal plane-wave synthesis. a) generalized source function, b) generalized receiver gather, and c) areal-shot migration.

The methods for computing generalized sources discussed above operate in the data space, characterizing the data-space generalized sources. This thesis introduces a new category of generalized sources that are initiated from selected reflectors, using the pre-stack exploding-reflector model (PERM) (Biondi, 2006).

PERM is an extension of the exploding-reflector model (Loewenthal et al., 1976). Because PERM wavefields are initiated in the image space, they are called the image-space generalized sources. The image-space generalized sources are suitable for migration-velocity analysis. After optimizing for the velocity model, any migration scheme can be used to generate the final image using the original data. Figure 5a shows the Marmousi image computed with shot-profile migration using an initial velocity model, which is inaccurate below the top of the anticline at a depth of 1700 m. The inaccuracy of the velocity model is indicated by reflectors being pulled up in the center of the image below 2000 m. Figure 5b shows the Marmousi image computed with shot-profile migration using a velocity model optimized with

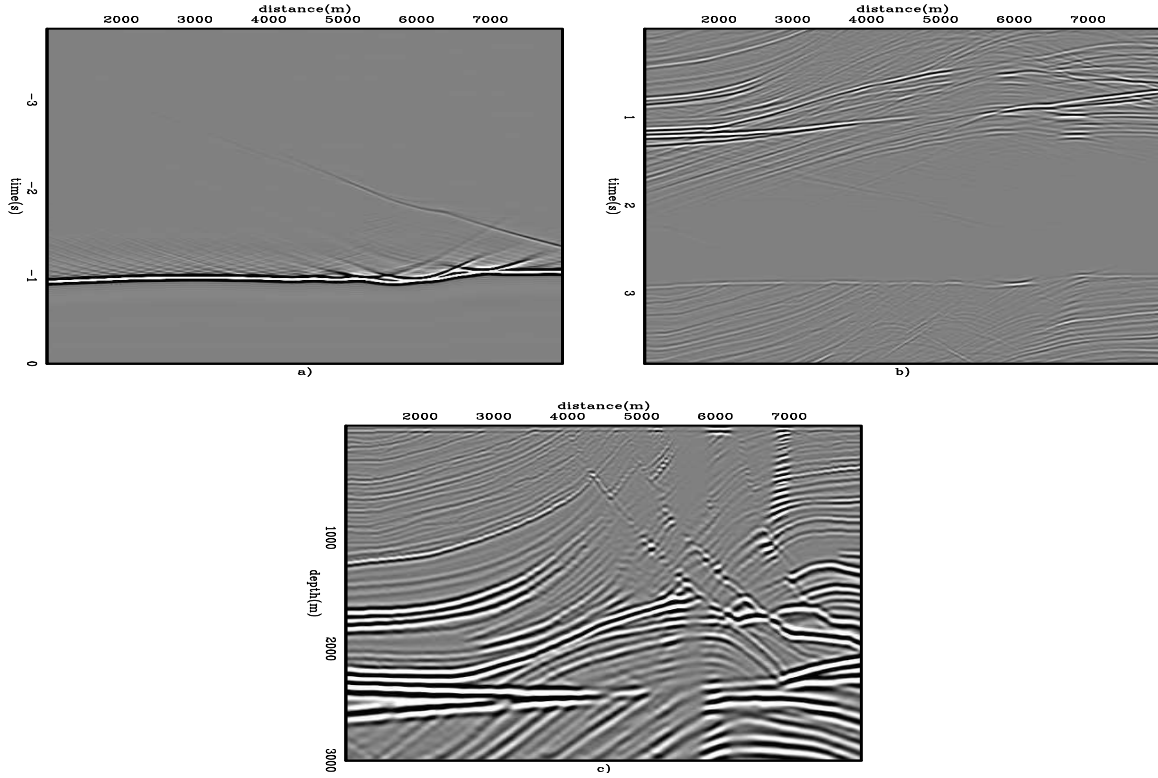


Figure 3: Horizontal plane-wave at depth 2300 m by the controlled illumination method. a) generalized source function, b) generalized receiver gather, and c) areal-shot migration.

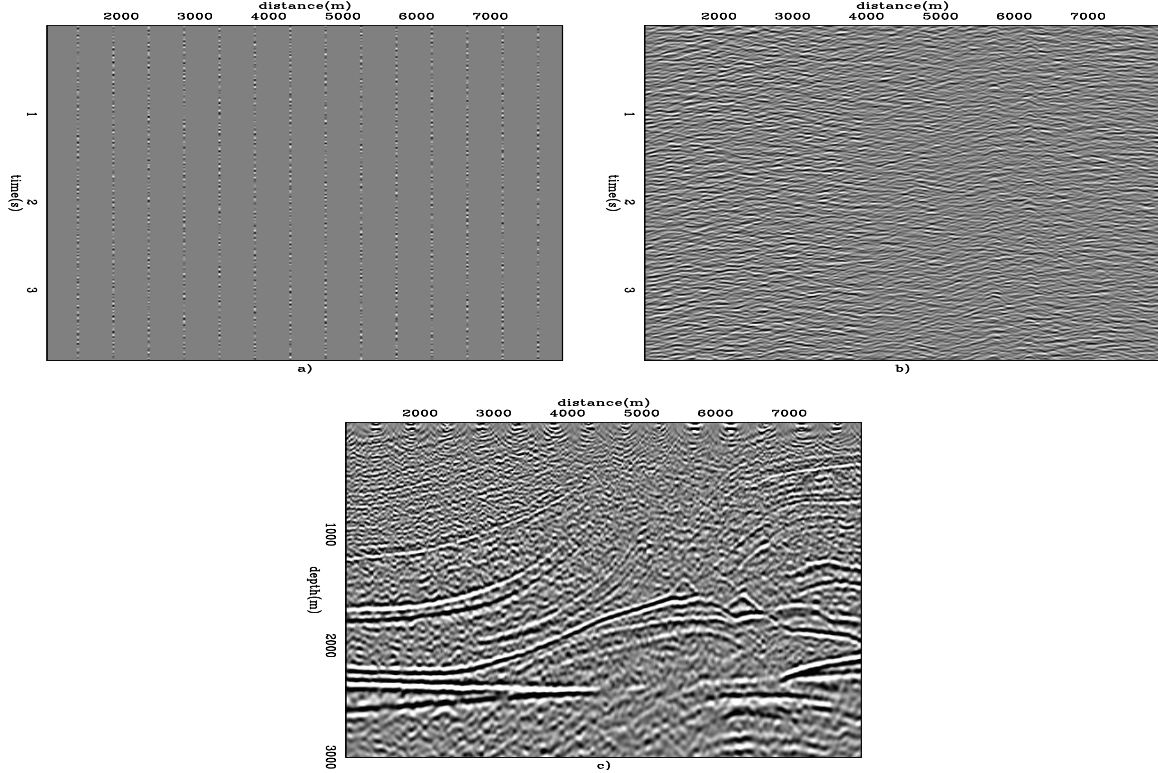


Figure 4: Random-phase encoding combining every 20 shots. a) generalized source function, b) generalized receiver gather, and c) areal-shot migration.

ISWET. ISWET was performed with 11 pairs of image-space generalized sources synthesized from 12 selected reflectors and collected at a depth of 1500 m. The pull up effect has been corrected, and the reflectors are better focused. Compare Figure 5b with Figure 1, which was computed with the true velocity model. For this example, each iteration of ISWET using the image-space generalized wavefields is approximately 60 times faster than that with the conventional 375 shot-profiles.

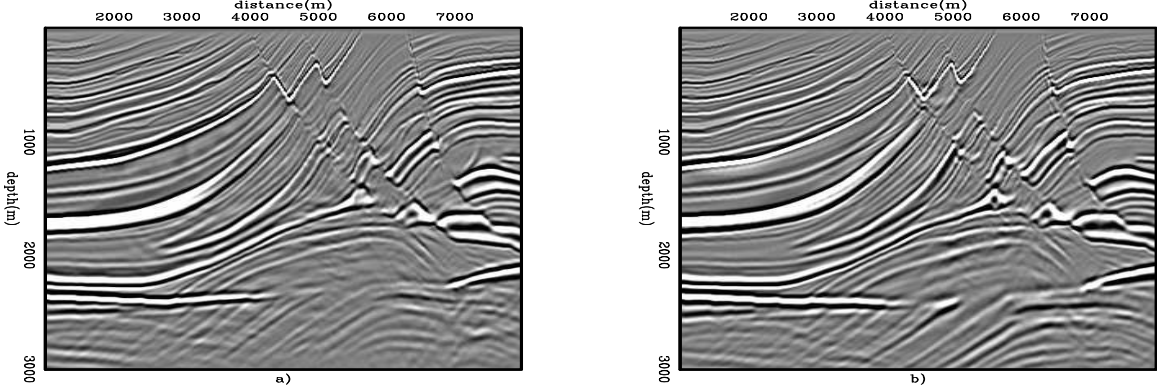


Figure 5: Shot-profile migrated images of Marmousi obtained with: a) An initial velocity model, which is inaccurate below the top of the anticline at depth 1700 m, b) a velocity model optimized with ISWET, using 11 pairs of image-space generalized sources synthesized from 12 selected reflectors and collected at depth 1500 m.

As will be shown, in 3D a dramatic data reduction is possible with these generalized sources. Since they are initiated at selected reflectors, a horizon-based strategy to parameterize the velocity model can be naturally incorporated into ISWET. Moreover, image-space generalized sources can be collected at any depth during the upward propagation, making a target-oriented approach also easily integrated. This thesis is one step forward in making 3D-ISWET a standard for depth-imaging projects in the presence of complex geology.

PRE-STACK-EXPLODING-REFLECTOR MODEL

The fundamental idea of PERM is to model data that describes the correct kinematics of an isolated SODCIG computed by a wavefield-extrapolation method. In conventional Born modeling, as we do not know beforehand which shot records contribute to forming the image at a point in the subsurface, we would have to perform several modeling experiments to synthesize these shot records. Ideally, instead of several modeling experiments, we would like to synthesize a small amount of data with the condition that migration produces the same kinematics as the initial SODCIG. This can be achieved by using the prestack exploding-reflector model (PERM). A prestack image is used as the initial conditions for the modeling of upward and downward PERM wavefields. The modeling is performed in a way similar to the exploding-reflector model (ERM). Since migration of PERM data can produce a prestack image, PERM can be considered a generalization of ERM.

The modeling of PERM wavefields can be carried out by any wavefield-continuation scheme. Here, we use the following one-way wave equations:

$$\begin{cases} \left(\frac{\partial}{\partial z} \pm i\sqrt{\omega^2 s_0^2(\mathbf{x}) - |\mathbf{k}|^2} \right) P_{u,d}(\mathbf{x}, \omega; \mathbf{x}_m) = I_{u,d}(\mathbf{x}_m, \mathbf{h}) \\ P_{u,d}(x, y, z = z_{\max}, \omega; \mathbf{x}_m) = 0 \end{cases}, \quad (1)$$

where $P_{u,d}$ represent upward and downward PERM wavefields, $I_{u,d}(\mathbf{x}_m, \mathbf{h})$ are subsets of the prestack image centered around the SODCIG under study at \mathbf{x}_m for a single reflector, suitable for the initial conditions for the upward and downward PERM wavefields, respectively. The sign in front of the square root is positive for the upward PERM wavefield and negative for the downward PERM wavefield. The subsurface-offset \mathbf{h} is parameterized as $\mathbf{h} = (h_x, h_y)$, where h_x and h_y are the inline- and the crossline-subsurface offsets, respectively. If the prestack image has energy focused at zero subsurface offset, the initial conditions can be parameterized only by its spatial coordinates, and PERM is equivalent to ERM.

The initial conditions are obtained by rotating the original unfocused SODCIGs according to the apparent geological dip of the reflector. This corrects for the image-point dispersal due to velocity inaccuracy, causing events with different reflection angles from the same reflection point in the subsurface to be imaged at different locations. The geometry of the rotation is shown in Figures 6a and 6b for velocities which are slower and faster than the correct velocity, respectively. In 3D, the cross-line offsets also must be rotated according to the apparent geological dip in the cross-line direction in

addition to the in-line rotation. By assuming that source and receiver rays are coplanar such that they cross, the 3D transformation to the reflection-angle domain (Biondi and Tisserant, 2004) is given by

$$k_{h_x} = -k_z \sec \alpha_{y'} \tan \gamma, \quad (2)$$

and

$$k_{h_y} = -k_{y'} \tan \gamma \tan \alpha_{x'}, \quad (3)$$

where $\alpha_{x'}$ and $\alpha_{y'}$ are the apparent geological dips in the in-line and cross-line directions, respectively. Notice that the 3D transformation is dependent on the apparent geological dip in contrast with the 2D case. In the spatial domain, equations 15 and 16 define slant-stack transformations along the paths

$$z = z_{h_x} + \frac{h_x}{\cos \alpha_{y'}} \tan \gamma, \quad (4)$$

and

$$z = z_{h_y} + h_y \tan \alpha_{x'} \tan \alpha_{y'} \tan \gamma, \quad (5)$$

respectively. The term $\cos \alpha_{y'}$ in equation 17 stretches the in-line-subsurface-offset axis, while the combination of terms $\tan \alpha_{x'}$ and $\tan \alpha_{y'}$ in equation 18 can stretch or shrink the cross-line-subsurface-offset axis.

Under the common-azimuth approximation, the 3D rotation is similar to the 2D rotation (equation 10) except for the subsurface-offset stretching factor (equation 17). Later in this chapter, we will see areal-shot migration results of 3D-PERM wavefields modeled from the initial conditions computed with and without considering the stretching term. Appendix 1 shows the complete derivation of equations *** and ***.

$$\tan(\gamma - \alpha) = \frac{dz}{dh_{x_u}}, \quad (6)$$

$$\tan(\gamma + \alpha) = -\frac{dz}{dh_{x_d}}. \quad (7)$$

align the initial conditions with the geological dip, we need to change the dip along the subsurface-offset axis according to the apparent geological dip, yielding the new subsurface offset $\widetilde{h_{x_s}}$ and $\widetilde{h_{x_r}}$ for the initial conditions of the modeling of source and receiver wavefield, respectively. This is accomplished by solving the following differential equations:

It is represented the situation of a single subsurface offset Notice that when the migration velocity is slower, the image point .

Shot-profile and areal-shot migrations by wavefield extrapolation compute pre-stack images by means of the multi-offset imaging condition (Rickett and Sava, 2002), in which source and receiver wavefields are laterally shifted prior to time correlation. However, the shift between wavefields might not be restricted to the horizontal direction. For instance, vertical shifts of the wavefields produce the vertical-subsurface-offset gathers, which provide reliable velocity information in the presence of steep dips (Biondi and Shan, 2002).

Ideally, wavefields should be shifted along the geological dip direction. According to Biondi and Symes (2004), SOD-CIGs computed this way do not suffer from image-point dispersal in the presence of dip and inaccuracies in the migration velocity. The image-point dispersal causes events with different reflection angles from the same reflection point in the subsurface to be imaged at different locations.

The image-point dispersal in 2D is illustrated in Figure 6 for the case of migrating with a velocity slower (Figure 6a) and faster (Figure 6b) than the true velocity. For simplicity, let us consider constant velocity in the vicinity of the image point, so source and receiver rays are straight.

When the migration velocity is too low, the reflector is imaged at a shallower depth. The image point computed with horizontal shifts of the wavefields l_{hx} is shifted down-dip with respect to the image point computed with shifts along the apparent geological dip l_{hg} . The geological dip is called apparent because of the migration velocity error. The point l is where source and receiver rays cross at an angle that is twice the apparent reflection angle γ . Source and receiver rays cross deeper than the image points, causing events to curve downward in the SODCIG.

When the migration velocity is too high, the reflector is imaged at a greater depth. The image point l_{hx} is shifted up-dip with respect to l_{hg} . Source and receiver rays cross shallower than the image points, causing events to curve upward in the SODCIG.

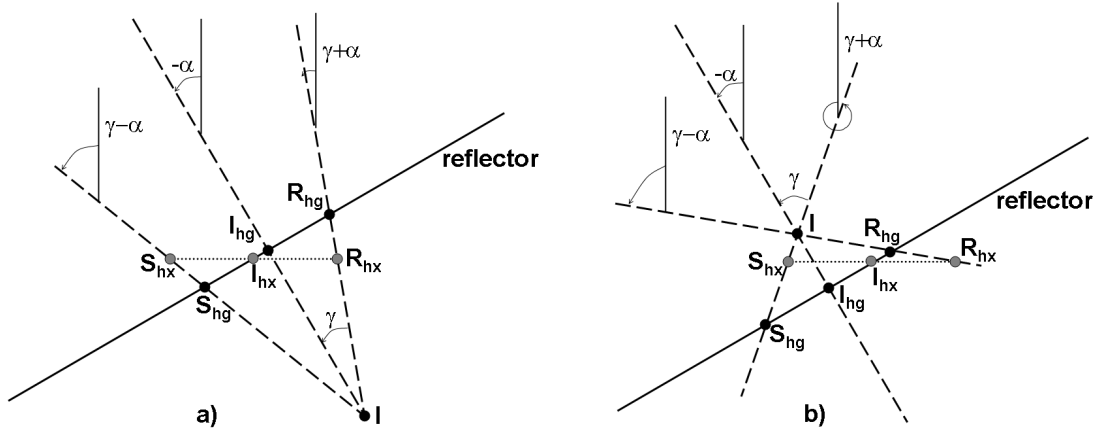


Figure 6: Geometry for the computation of SODCIGs. Source, receiver and image points are labeled with S, R and I, respectively. The subscript hx corresponds to subsurface offsets computed with horizontal shift. The subscript hg corresponds to subsurface offsets computed by shifting along the apparent geological dip α . a) Underestimated velocity, and b) overestimated velocity. Modified from Biondi and Symes (2004).

Generating SODCIGs along the geological-dip direction overcomes the problem of the image-point dispersal. However, it is computationally demanding since, wavefields must be stored at various depths. Furthermore, accurate dip information is difficult to obtain, especially when events cross because of velocity inaccuracy.

Biondi and Symes (2004) point out that, at least to the first order, the reflection-angle domain is immune to image-point dispersal. This is because the SODCIG to ADCIG transformation shifts events to the line connecting I and I_{hg} in Figure 6 at the same image point shared by all the reflection angles.

In the presence of dip, to accurately model PERM data it is crucial that the initial conditions are free of image-point dispersal, so that all the energy of a point in the subsurface is contained by the corresponding SODCIG injected into the modeling. Since SODCIGs along the geological dip are not easily computed, can we pre-process the SODCIGs computed with horizontal shifts of the wavefields such that they are transformed into a good approximation of the SODCIGs along the geological dip?

To answer this question, let us first examine the angle relationships in Figure 6. The angles $\gamma + \alpha$ and $\gamma - \alpha$ are the source and receiver ray angles, respectively. They are the propagation directions of the wavefields locally at the image point. In 2D, α and γ are related to slopes in the pre-stack image according to

$$\tan \alpha = -\frac{dz_m}{dx_m} \quad (8)$$

and

$$\tan \gamma = -\frac{dz}{dh_x}, \quad (9)$$

where the subscript m in equation 8 refers to the local nature of the relationship. The solutions of the differential equations 8 and 9 define slant-stack paths, which allow us to transform the 2D pre-stack image $I(x, z, h_x)$ into $I(x, z, \alpha, \gamma)$ by angle decomposition according to the following integrals:

$$I(x, z, \alpha, \gamma) = \int_{x_{m_i}}^{x_{m_f}} \int_{-h_x}^{h_x} W(x_m - x) \frac{dI(x, z, h_x)}{dz} dx_m dh_x \Bigg|_{\substack{z=z_h+h_x \tan \gamma \\ z=z_m+x_m \tan \alpha}} \quad (10)$$

where the derivative with respect to z is performed to recover the correct phase. The local window $W(x_m - x)$ is used in the local slant-stack integral on x_m , being defined as

$$\begin{cases} 1, & x_{m_i} \leq x \leq x_{m_f}, \\ 0, & \text{elsewhere} \end{cases}$$

where $x_{m_i} = x_m - \frac{x_w}{2}$ and $x_{m_f} = x_m + \frac{x_w}{2}$, with x_w being the width of the local window.

Again, using simple trigonometry, we have

$$\tan(\gamma + \alpha) = \frac{\tan \gamma + \tan \alpha}{1 - \tan \gamma \tan \alpha}, \quad (11)$$

$$\tan(\gamma - \alpha) = \frac{\tan \gamma - \tan \alpha}{1 + \tan \gamma \tan \alpha}. \quad (12)$$

To align the initial conditions with the geological dip, we need to change the dip along the subsurface-offset axis according to the apparent geological dip, yielding the new subsurface offset \widetilde{h}_{x_s} and \widetilde{h}_{x_r} for the initial conditions of the modeling of source and receiver wavefield, respectively. This is accomplished by solving the following differential equations:

$$\tan(\gamma + \alpha) = -\frac{dz}{d\widetilde{h}_{x_s}}, \quad (13)$$

$$\tan(\gamma - \alpha) = \frac{dz}{d\widetilde{h}_{x_r}}. \quad (14)$$

The solutions of equations 13 and 14 define new slant-stack operations which, in combination with equations 11 and 12, reduce the dimensionality of the decomposed pre-stack image (equation 10) by transforming $I(x, z, \alpha, \gamma)$ into $I_D(x, z, \widetilde{h}_{x_s})$ and $I_U(x, z, \widetilde{h}_{x_r})$.

In 3D, the cross-line offsets also must be rotated according to the apparent geological dip in the cross-line direction in addition to the in-line rotation. By assuming that source and receiver rays are coplanar such that they cross, the 3D transformation to the reflection-angle domain (Biondi and Tisserant, 2004) is given by

$$k_{h_x} = -k_z \sec \alpha_{y'} \tan \gamma, \quad (15)$$

and

$$k_{h_y} = -k_{y'} \tan \gamma \tan \alpha_{x'}, \quad (16)$$

where $\alpha_{x'}$ and $\alpha_{y'}$ are the apparent geological dips in the in-line and cross-line directions, respectively. Notice that the 3D transformation is dependent on the apparent geological dip in contrast with the 2D case. In the spatial domain, equations 15 and 16 define slant-stack transformations along the paths

$$z = z_{h_x} + \frac{h_x}{\cos \alpha_{y'}} \tan \gamma, \quad (17)$$

and

$$z = z_{h_y} + h_y \tan \alpha_{x'} \tan \alpha_{y'} \tan \gamma, \quad (18)$$

respectively. The term $\cos \alpha_{y'}$ in equation 17 stretches the in-line-subsurface-offset axis, while the combination of terms $\tan \alpha_{x'}$ and $\tan \alpha_{y'}$ in equation 18 can stretch or shrink the cross-line-subsurface-offset axis.

Under the common-azimuth approximation, the 3D rotation is similar to the 2D rotation (equation 10) except for the subsurface-offset stretching factor (equation 17). Later in this chapter, we will see areal-shot migration results of 3D-PERM wavefields modeled from the initial conditions computed with and without considering the stretching term.

To illustrate the generation of dip-independent initial conditions, 801 split-spread shots 10 m apart with maximum offset of 3250 m were modeled with a velocity of 1000 m/s and migrated with velocity underestimated by 10% (Figure 7). The model has a 20° dipping reflector and a horizontal reflector at a depth of 2500 m. The SODCIG located at 0 m was used as the initial condition for the modeling of PERM data without applying the pre-processing described above. Since PERM models one event of one isolated SODCIG, the dipping reflector and the horizontal reflector originate two different pairs of PERM wavefields. This means that reflectors used in the modeling need to be interpreted in the pre-stack volume. The pair of source and receiver wavefields for the dipping reflector are shown in Figure 8.

Since the modeling of a single non-rotated SODCIG carries no dip information, migration of the corresponding PERM data using the correct velocity does not shift events laterally, as can be seen in Figure 9. As expected, the horizontal reflector focuses at zero-subsurface offset. However, notice how the dipping reflector still presents a residual curvature. Migration of PERM data from SODCIGs within a neighborhood around $x_m = 0$ m is shown in Figure 10. Again, the residual curvature is present and any migration velocity analysis using this result will lead to incorrect velocity updates. This residual curvature is a result of not having corrected the image-point dispersal. Unless stated, SODCIGs in the figures are selected at $x = 0$ m.

The rotation was applied to the image in Figure 7, and the new PERM data was modeled using the initial conditions shown in Figure 11. Notice that the initial condition for modeling the source wavefield (Figure 11a) and the initial condition for modeling the receiver wavefield (Figure 11b) have the dipping event oriented in opposite directions in the

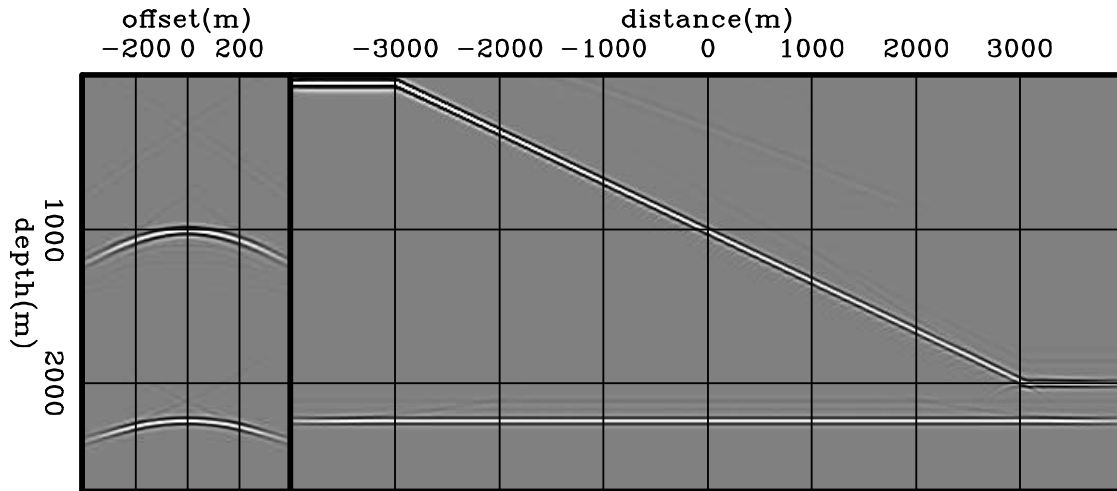


Figure 7: Shot-profile migration of 801 split-spread shots 10 m apart with velocity 10% slower than the true velocity. The model is represented by a 20° dipping reflector and a horizontal reflector at a depth of 2500 m embedded in a medium with a constant velocity of 1000 m/s.

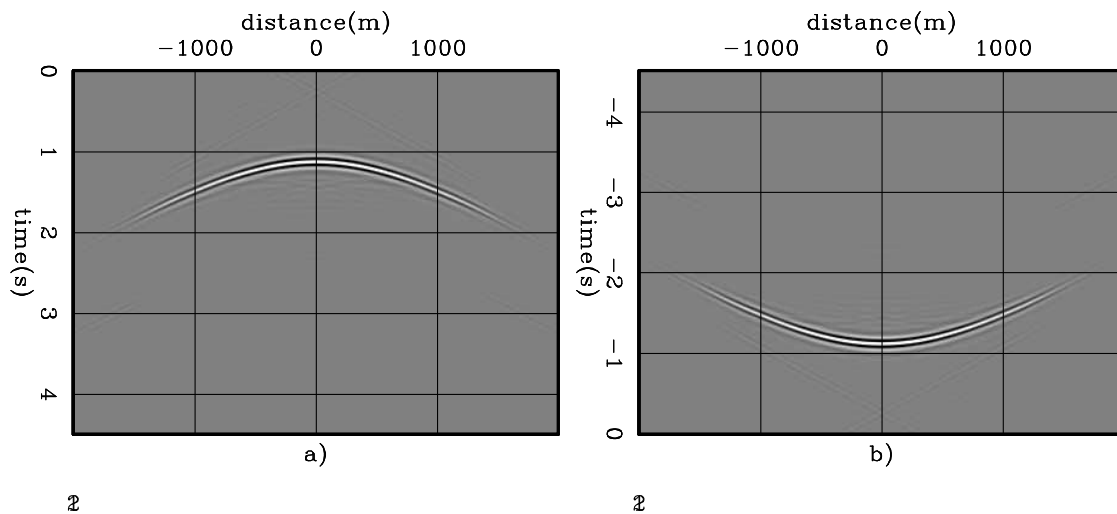


Figure 8: Data synthesized by PERM having as the initial condition the dipping reflector in the SODCIG at $x_m = 0$ m. a) The receiver wavefield. b) The source wavefield.

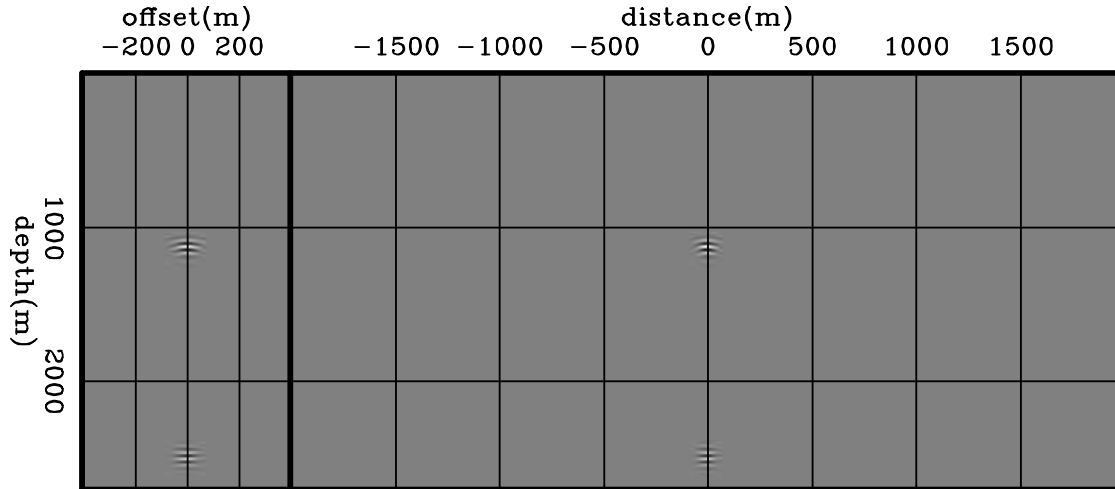


Figure 9: Areal-shot migration of PERM data shown in Figure 8 using the correct velocity. The horizontal reflector is focused at zero-subsurface offset, but the dipping reflector shows residual curvature.

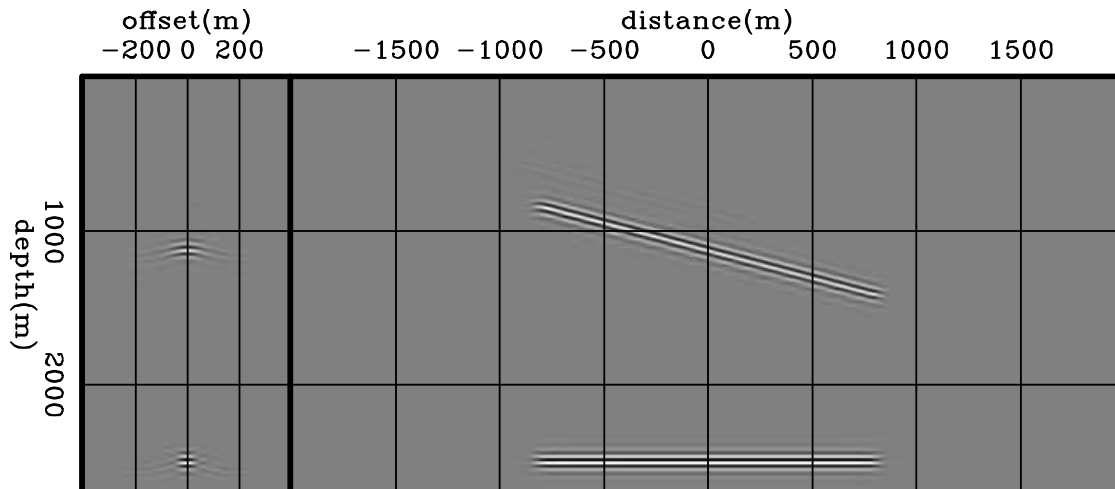


Figure 10: Areal-shot migration with correct velocity of PERM data having a set of isolated SODCIGs around $x_m = 0$ m as the initial conditions. As in Figure 9, the horizontal reflector is focused at zero-subsurface offset, but the dipping reflector shows residual curvature.

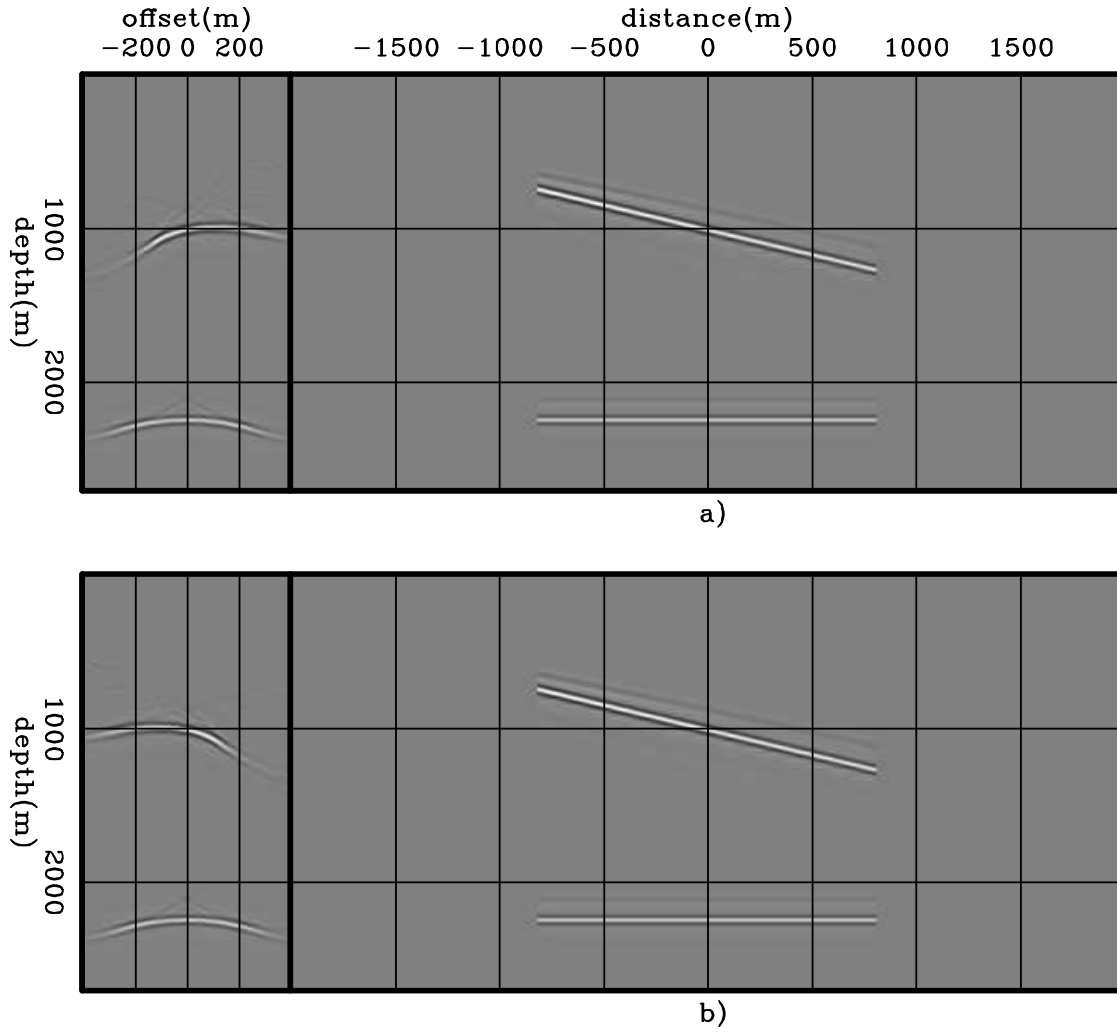


Figure 11: Initial conditions for modeling a) source and b) receiver wavefields. The dipping reflector is oriented in opposite directions in the SODCIG. Rotation affects neither the horizontal reflector nor the-zero subsurface offset, as can be seen in the right panels.

SODCIG. The rotation changes neither the horizontal reflector nor the-zero subsurface offset, as can be seen in the right panels.

The source and receiver wavefields for the dipping reflector after rotation are shown in Figure 12. The events in Figures 12a and 12b are shown in the same areal shot for illustration only. Actually, they pertain to different areal shots since each reflector was injected separately into the modeling.

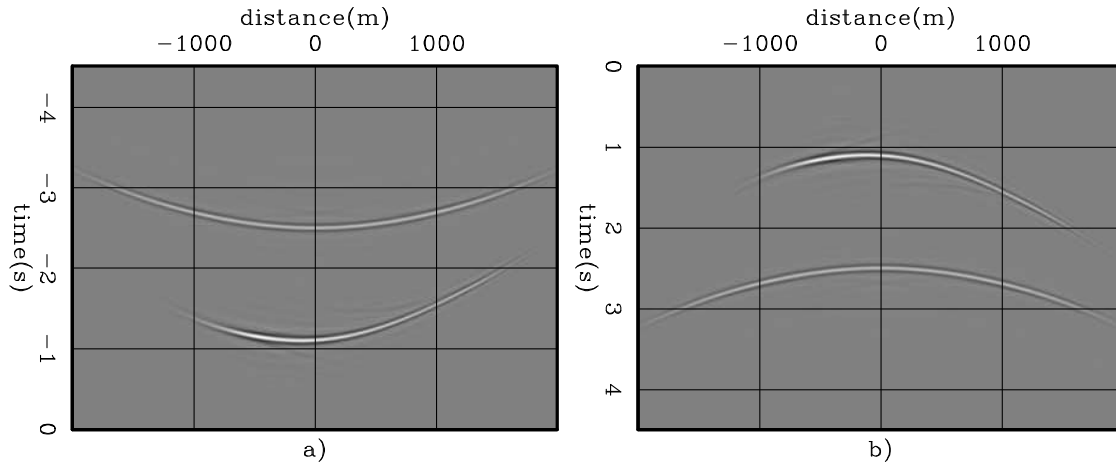


Figure 12: Dip-independent PERM data for the dipping reflector from the rotated SODCIG at $x_m = 0$ m. a) The receiver wavefield. b) The source wavefield.

Areal-shot migration of dip-independent PERM data is shown in Figure 13. Notice that the segment of the dipping reflector is shifted laterally with respect to that of the horizontal reflector. Since the dip-independent wavefields carry information about the dip of the reflector, the observed reflector movement is now consistent with migration with a higher velocity.

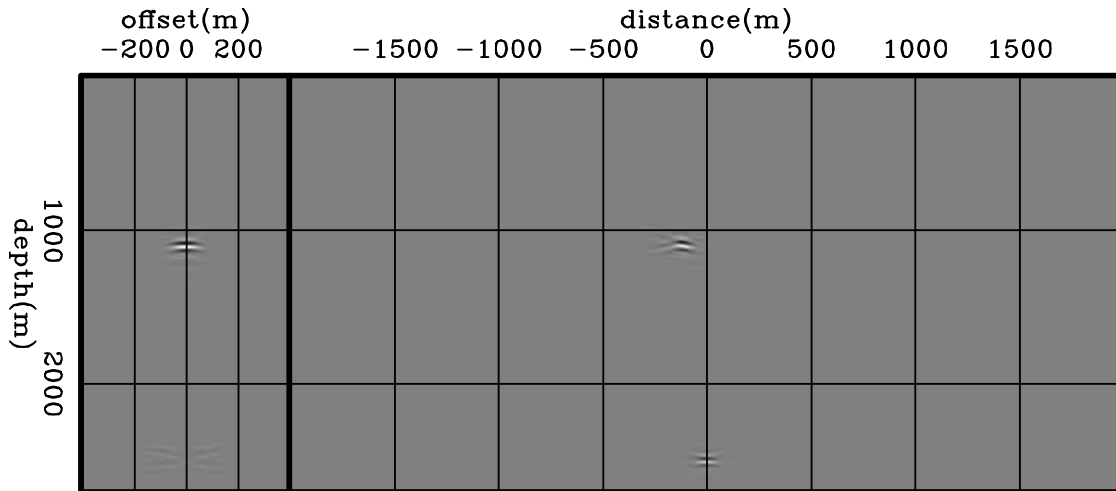


Figure 13: Areal-shot migration with the correct velocity of dip-independent PERM data having the rotated the SODCIGs at $x_m = 0$ m as the initial condition. The SODCIG on the left is selected at the horizontal position where the dipping reflector was laterally shifted to. Compare with Figure 9. The dipping reflector is now focused in contrast to the image in Figure 9, where it shows residual curvature.

Migration with the correct velocity of dip-independent PERM data modeled from a set of SODCIGs in a neighborhood around $x_m = 0$ m confirms the correctness of the rotation (Figure 14). The focusing of the dipping reflector around zero subsurface offset is greatly improved when compared with Figure 10. The corresponding ADCIGs confirm the more consistent move-out after rotation (Figure 15). Note the residual move-out in the angle gather corresponding to the image computed with wavefields with non-rotated initial conditions (Figure 15a), and the image from wavefields computed with the proposed rotation is much flatter (Figure 15b).

Let us now illustrate the generation of PERM data synthesized from a single SODCIG. We start with a pre-stack

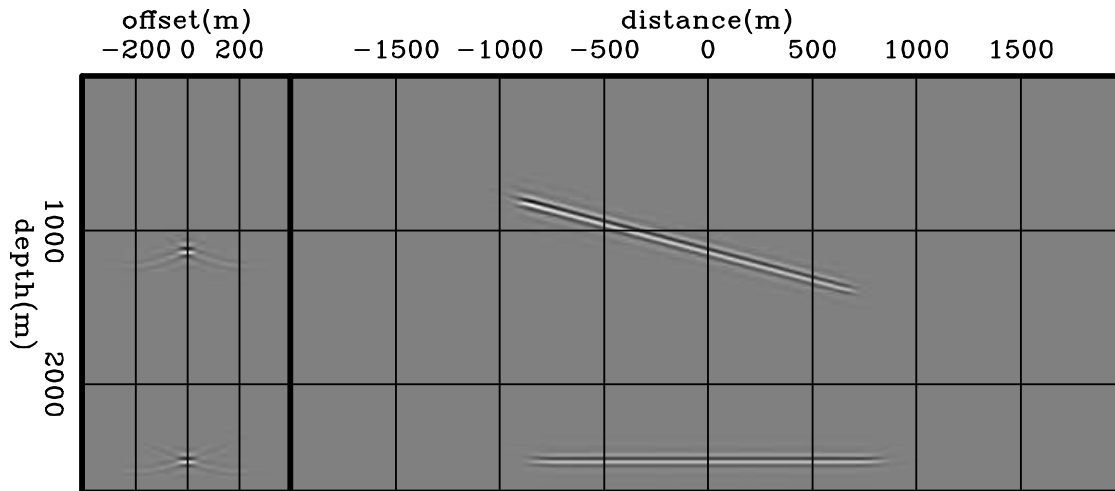


Figure 14: Areal-shot migration with correct velocity of dip-independent PERM data having a set of rotated SODCIGs around $x_m = 0$ m as the initial conditions. Compare with Figure 10. The focusing of the dipping reflector is greatly improved when using the rotated initial conditions.

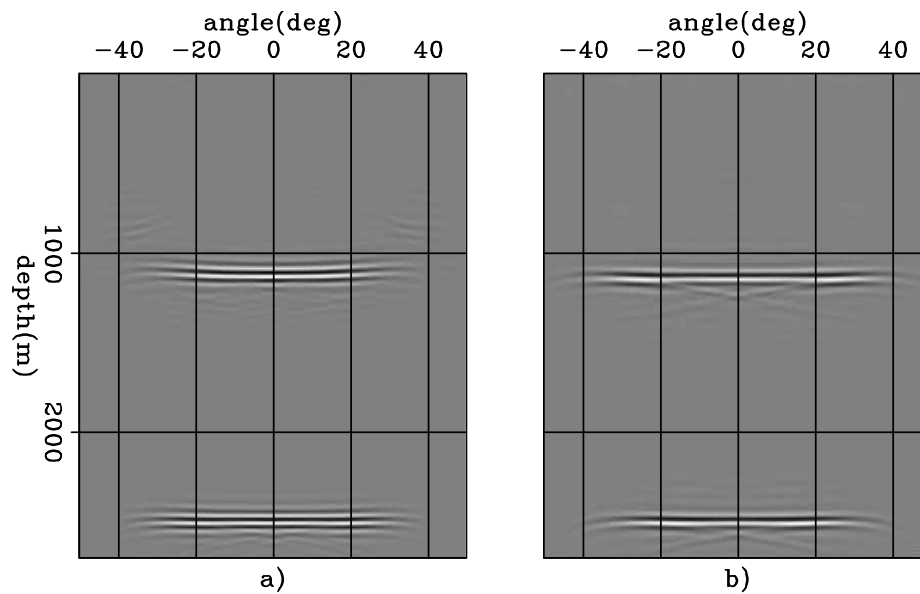


Figure 15: ADCIGs of images computed with the correct migration velocity using PERM data having: a) non-rotated initial conditions, and b) rotated initial conditions. Note the residual move-out in a) and the flatter response in b).

image computed with shot-profile migration of 401 split-spread shots at every 10 m and maximum offset of 2250 m, using a 10% lower velocity (Figure 16). The model consists of one reflector at 750 m depth embedded in a medium with a constant velocity of 1000 m/s. The pre-stack image has 81 subsurface offsets ranging from -400 m to 400 m. Notice the poor focusing of energy around the zero-subsurface offset due to inaccurate velocity.

The SODCIG at $x_m = 0$ m was used as the initial condition for modeling the corresponding pair of PERM source and receiver wavefields using the same inaccurate velocity. The wavefields are upward propagated according to equations ?? and ??. The PERM data is shown in Figure 17. Notice that the receiver wavefield (Figure 17a) occurs at positive times, while the source wavefield (Figure 17b) occurs at negative times. According to the imaging principle (Claerbout, 1971), reflectors explode at time zero. This is the time at which the source wavefield impinges on the reflector. Because the receiver wavefield exists after the source wavefield has reached the reflector, the areal receiver data $U_P(x, y, z = 0, \omega; \mathbf{x}_m)$ is upward propagated forward in time. For the same reason, the areal source data $D_P(x, y, z = 0, \omega; \mathbf{x}_m)$ is upward propagated backward in time.

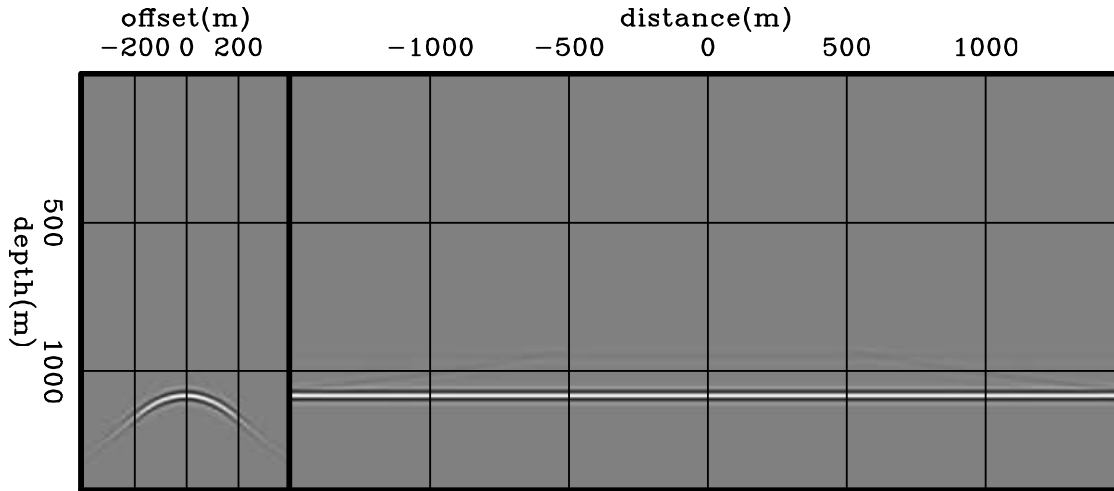


Figure 16: Shot-profile migration of 401 split-spread shots 10 m apart with a 10% slower velocity. The model consists of a horizontal reflector embedded in constant velocity of 1000 m/s.

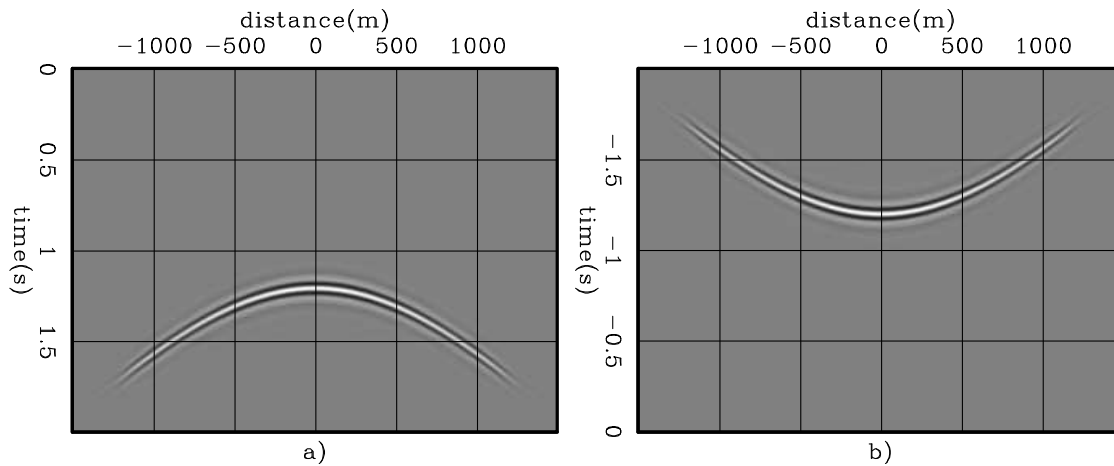


Figure 17: Data synthesized by PERM having as the initial condition the SODCIG at $x_m = 0$ m. a) The receiver wavefield. b) The source wavefield.

Areal-shot migration of data from Figure 17 with the same inaccurate velocity shows kinematics at near subsurface offsets similar to those of the original shot-profile migration (compare Figures 18 and 16). However, for farther subsurface offsets energy is not adequately imaged. This can be easily explained by analyzing how the image $I_P(\mathbf{x}, \mathbf{h}; \mathbf{x}_m)$ is formed when applying the multi-offset imaging condition to the downward propagated PERM wavefields modeled from a SODCIG located at \mathbf{x}_m . For one particular frequency, it reads

$$I_P(\mathbf{x}, \mathbf{h}; \mathbf{x}_m) = D_P^*(\mathbf{x} - \mathbf{h}; \mathbf{x}_m)U_P(\mathbf{x} + \mathbf{h}; \mathbf{x}_m), \quad (19)$$

where ‘*’ stands for the complex conjugate. Notice that the maximum absolute distance at which wavefields still correlate is $|2h_{max}|$ for symmetric SODCIGs with respect to subsurface offset or, more generally, twice the subsurface offset range. Therefore, to ensure that the areal-shot migrated image has kinematics at all subsurface offsets similar to those in the original isolated SODCIG, we need to model PERM data from a set of SODCIGs within that neighborhood around the central SODCIG.

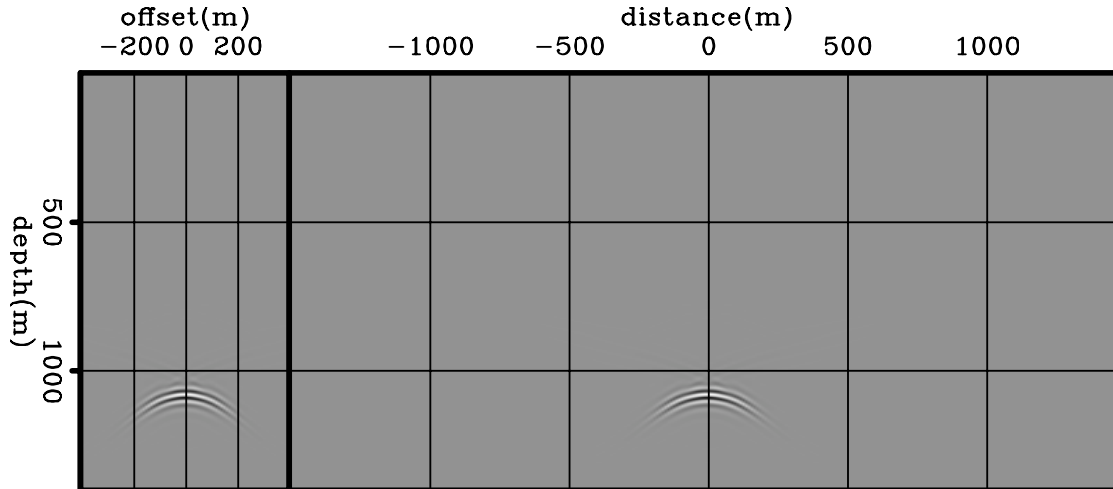


Figure 18: Areal-shot migration of PERM data shown in Figure 17 with a 10% slower velocity. By comparing with Figure 16 we see that far subsurface-offsets are not properly imaged.

The areal-shot migration of PERM data synthesized by isolated SODCIGs within the interval $(-2max|h_x|, 2max|h_x|)$ is shown in Figure 19. By using more data, energy is adequately imaged at far subsurface offsets (compare with Figures 16 and 18). To further understand the behavior of the areal-shot migrated image, let us examine the reflection angle-domain common-image gathers (ADCIGs) (Sava and Fomel, 2003). ADCIGs computed from the SODCIGs of Figures 16, 18 and 19 attest to the more accurate imaging when migrating data modeled from the set of SODCIGs around x_m (Figure 20). Although the ADCIG from the the image computed with a single pair of PERM data (Figure 20b) shows reasonable kinematics, the amplitude of wide-aperture angles is weaker than that of the original ADCIG (Figure 20a). Notice that the amplitude behavior of the ADCIG computed with several areal shots from SODCIGs within the neighborhood of x_m (Figure 20c) better matches that of the original isolated SODCIG.

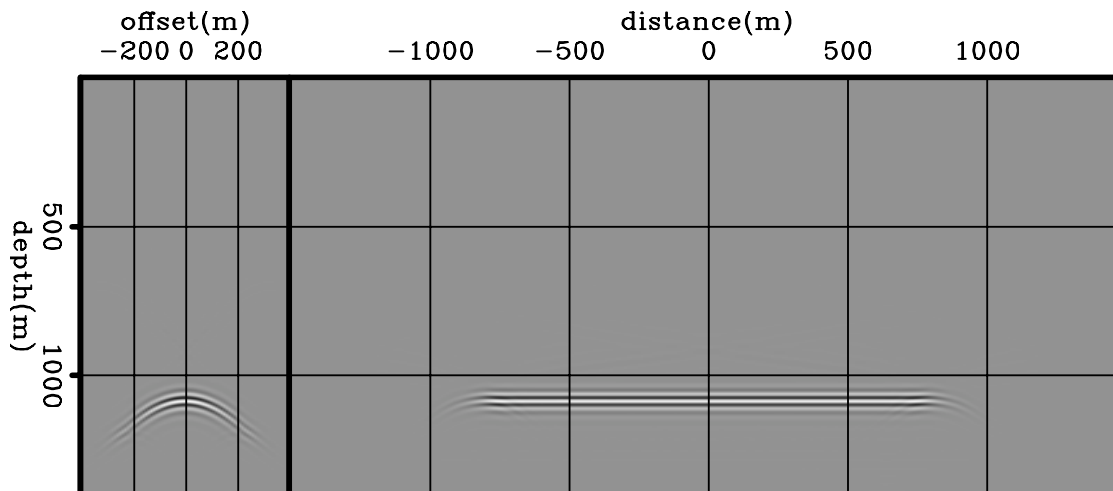


Figure 19: Areal-shot migration of PERM data having a set of isolated SODCIGs around $x_m = 0$ m as the initial condition with a 10% slower velocity. By comparing with Figure 16 we see that the kinematics of far subsurface-offsets is properly recovered.

If, instead of using the incorrect migration velocity, we input the correct migration velocity to the areal-shot migration, energy nicely focuses at zero subsurface offset (Figure 21). This property will be used to perform migration velocity updates in Chapter 3.

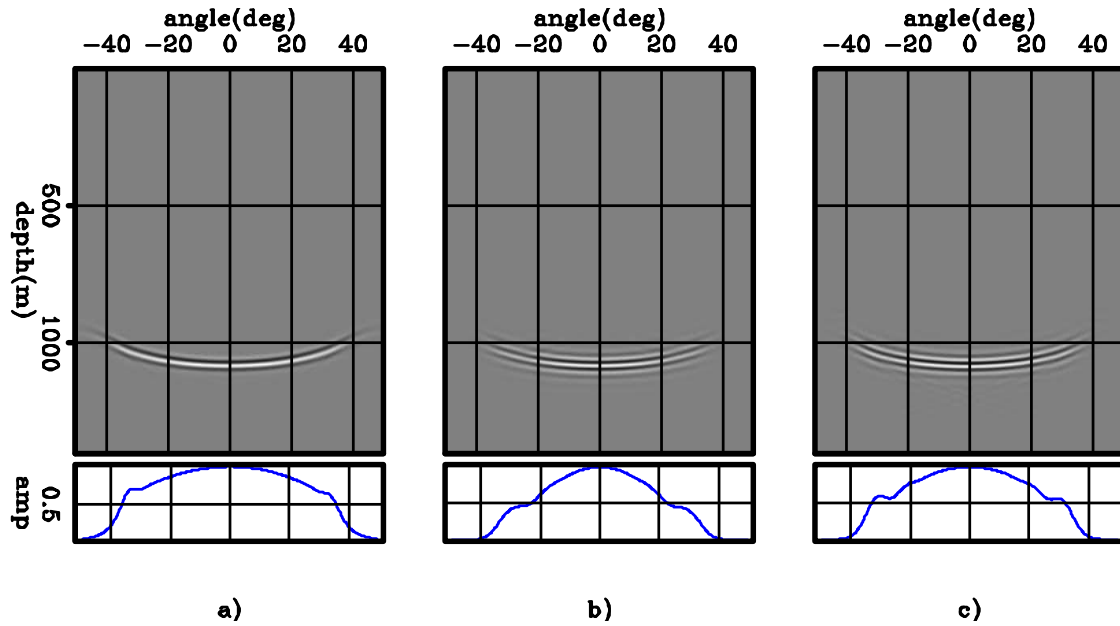


Figure 20: ADCIGs selected at $x_m = 0$ m. a) Computed from the shot-profile migration; b) computed from the areal-shot migration of one pair of PERM data modeled from the SODCIG at $x_m = 0$ m; and c) computed from the areal-shot migration of pairs of PERM data modeled from a set of SODCIGs around $x_m = 0$ m. Notice that although the kinematics are similar, the amplitudes in c) better match those of a).

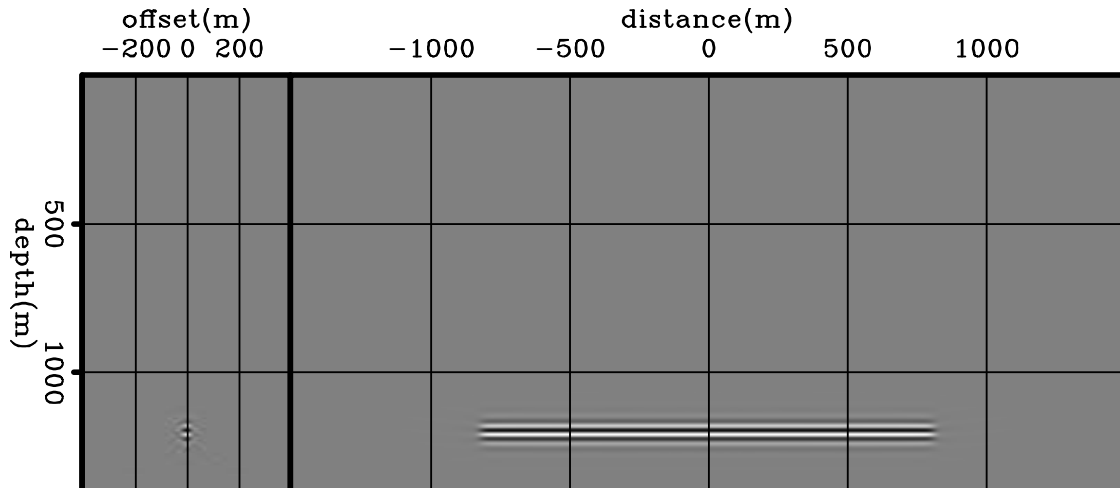


Figure 21: Areal-shot migration of PERM data having a set of isolated SODCIGs around $x_m = 0$ m as the initial condition with the correct velocity. Energy nicely focuses at zero-subsurface offset.

In the previous examples we saw that PERM data contains all the kinematic information needed to perform migration velocity analysis and the image computed with PERM wavefields resembles the original shot-profile migrated image. However, by carefully examining these images we can see that the former has stronger side lobes due to the squaring of the wavelet, which is mathematically explained by the modeling and migration of PERM wavefields initiated at a single SODCIG selected at \mathbf{x}_m . For one particular frequency, and considering, for simplicity, a plane reflector so that the initial conditions are the same for modeling source D_P and receiver U_P wavefields, PERM modeling can be described by

$$D_P(\boldsymbol{\xi}; \mathbf{x}_m) = \sum_{\mathbf{x}} \sum_{\mathbf{h}} G_0(\boldsymbol{\xi}, \mathbf{x} - \mathbf{h}) I(\mathbf{x}_m, \mathbf{h}), \quad (20)$$

and

$$U_P(\boldsymbol{\xi}; \mathbf{x}_m) = \sum_{\mathbf{x}} \sum_{\mathbf{h}} G_0(\boldsymbol{\xi}, \mathbf{x} + \mathbf{h}) I(\mathbf{x}_m, \mathbf{h}). \quad (21)$$

The pre-stack image is injected to the modeling by projecting the subsurface offsets \mathbf{h} on the spatial axis \mathbf{x} . The Green's function G_0 upward propagates the wavefields from the subsurface (represented by the coordinates \mathbf{x}) up to the depth level where the wavefields are collected (represented by the coordinates $\boldsymbol{\xi}$). Its subscript denotes that the wavefield propagation is performed with the background slowness $s_0(\mathbf{x})$ used to migrate the original shot-profiles.

The wavefields are recursively downward propagated in depth according to

$$D_P(\mathbf{x}; \mathbf{x}_m) = \sum_{\boldsymbol{\xi}} G_1^*(\boldsymbol{\xi}, \mathbf{x}) D_P(\boldsymbol{\xi}; \mathbf{x}_m), \quad (22)$$

and

$$U_P(\mathbf{x}; \mathbf{x}_m) = \sum_{\boldsymbol{\xi}} G_1^*(\boldsymbol{\xi}, \mathbf{x}) U_P(\boldsymbol{\xi}; \mathbf{x}_m). \quad (23)$$

Note that in equations 22 and 23 the subscript of the Green's function indicates the use of a different migration velocity.

The lateral shifts of the wavefields for the multi-offset imaging condition are represented by

$$D_P(\mathbf{x} - \mathbf{h}; \mathbf{x}_m) = \sum_{\boldsymbol{\xi}} G_1^*(\boldsymbol{\xi}, \mathbf{x} - \mathbf{h}) \sum_{\mathbf{x}'} \sum_{\mathbf{h}'} G_0(\boldsymbol{\xi}, \mathbf{x}' - \mathbf{h}') I(\mathbf{x}_m, \mathbf{h}'), \quad (24)$$

and

$$U_P(\mathbf{x} + \mathbf{h}; \mathbf{x}_m) = \sum_{\boldsymbol{\xi}} G_1^*(\boldsymbol{\xi}, \mathbf{x} + \mathbf{h}) \sum_{\mathbf{x}'} \sum_{\mathbf{h}'} G_0(\boldsymbol{\xi}, \mathbf{x}' + \mathbf{h}') I(\mathbf{x}_m, \mathbf{h}'). \quad (25)$$

The PERM image is obtained by inserting equations 24 and 25 into equation 19

$$\begin{aligned} I_P(\mathbf{x}, \mathbf{h}; \mathbf{x}_m) &= \sum_{\boldsymbol{\xi}} \sum_{\mathbf{x}'} \sum_{\mathbf{h}'} G_0(\boldsymbol{\xi}, \mathbf{x}' - \mathbf{h}') G_1^*(\boldsymbol{\xi}, \mathbf{x} - \mathbf{h}) I(\mathbf{x}_m, \mathbf{h}') \\ &\times \sum_{\boldsymbol{\xi}} \sum_{\mathbf{x}'} \sum_{\mathbf{h}'} G_1^*(\boldsymbol{\xi}, \mathbf{x} + \mathbf{h}) G_0(\boldsymbol{\xi}, \mathbf{x}' + \mathbf{h}') I(\mathbf{x}_m, \mathbf{h}'), \end{aligned} \quad (26)$$

which finally gives

$$\begin{aligned} I_P(\mathbf{x}, \mathbf{h}; \mathbf{x}_m) &= \sum_{\boldsymbol{\xi}'} \sum_{\mathbf{x}'} \sum_{\mathbf{h}'} \sum_{\boldsymbol{\xi}''} \sum_{\mathbf{x}''} \sum_{\mathbf{h}''} G_0(\boldsymbol{\xi}', \mathbf{x}' - \mathbf{h}') G_1^*(\boldsymbol{\xi}', \mathbf{x} - \mathbf{h}) \\ &\times G_1^*(\boldsymbol{\xi}'', \mathbf{x} + \mathbf{h}) G_0(\boldsymbol{\xi}'', \mathbf{x}'' + \mathbf{h}'') I(\mathbf{x}_m, \mathbf{h}') I(\mathbf{x}_m, \mathbf{h}''), \end{aligned} \quad (27)$$

From equation 27, we can see that, if the velocity used in the downward propagation is the same as that in the upward propagation, the pre-stack image I_P at x_m is approximately a squared version of the original image. This means that in addition to the stronger side lobes, reflectors in the PERM image will always have positive polarity and the amplitude variation in the PERM image will be more pronounced than that in the original image. The last amplitude effect can be mitigated by taking the square root of the absolute value of initial conditions while keeping its polarity.

Migration of PERM wavefields generated at all SODCIGs is obtained by summing over all \mathbf{x}_m

$$\begin{aligned} I_P(\mathbf{x}, \mathbf{h}) &= \sum_{\mathbf{x}_m} \sum_{\boldsymbol{\xi}'} \sum_{\mathbf{x}'} \sum_{\mathbf{h}'} \sum_{\boldsymbol{\xi}''} \sum_{\mathbf{x}''} \sum_{\mathbf{h}''} G_0(\boldsymbol{\xi}', \mathbf{x}' - \mathbf{h}') G_1^*(\boldsymbol{\xi}', \mathbf{x} - \mathbf{h}) \\ &\times G_1^*(\boldsymbol{\xi}'', \mathbf{x} + \mathbf{h}) G_0(\boldsymbol{\xi}'', \mathbf{x}'' + \mathbf{h}'') I(\mathbf{x}_m, \mathbf{h}') I(\mathbf{x}_m, \mathbf{h}''). \end{aligned} \quad (28)$$

For the simple case of a horizontal reflector in a constant velocity medium, we have shown that migration of PERM data produces images with the same kinematics as the shot profile migration. Now, we introduce a dipping reflector in the same constant background velocity medium. In the presence of a non-zero geological dip, a pre-processing of the initial conditions is necessary to obtain correct kinematics. This pre-processing step is represented by a rotation of the pre-stack image according to the apparent geological dip. In the example with two reflectors, we initiated each modeling experiment from one isolated SODCIG of one single reflector to compute a pre-stack image restricted to a certain region in the output space. However, depending on the number of reflectors and the size of the prestack image, this procedure can generate a dataset even larger than the original shot-profiles, defeating the original purpose of PERM, which is to synthesize a smaller dataset to be used in migration velocity analysis. We see next that using a combination of modeling experiments can decrease the size of PERM data.

Combination of modeling experiments

In the previous examples, if we were to fully image the reflectors, there might be twice as many areal shots as in the original shot-profiles. In equation 28, there is a summation over \mathbf{x}_m since the initial conditions are isolated SODCIGs. To decrease the number of modeling experiments, we can apply the concept of generalized sources and use the linearity of wavefield propagation to combine isolated SODCIGs and inject them simultaneously into one single model experiment as

$$\begin{cases} \left(\frac{\partial}{\partial z} - i\sqrt{\omega^2 s_0^2(\mathbf{x}) - |\mathbf{k}|^2} \right) \widehat{D}_P(\mathbf{x}, \omega) = \widehat{I}_D(\mathbf{x} - \mathbf{h}) \\ \widehat{D}_P(x, y, z = z_{\max}, \omega) = 0 \end{cases}, \quad (29)$$

and

$$\begin{cases} \left(\frac{\partial}{\partial z} + i\sqrt{\omega^2 s_0^2(\mathbf{x}) - |\mathbf{k}|^2} \right) \widehat{U}_P(\mathbf{x}, \omega) = \widehat{I}_U(\mathbf{x} + \mathbf{h}) \\ \widehat{U}_P(x, y, z = z_{\max}, \omega) = 0 \end{cases}, \quad (30)$$

where $\widehat{I}_D(\mathbf{x} - \mathbf{h})$ and $\widehat{I}_U(\mathbf{x} + \mathbf{h})$ are the combination of SODCIGs for a single reflector to be used as the initial conditions for the modeling of combined wavefields, $\widehat{D}_P(\mathbf{x}, \omega)$ and $\widehat{U}_P(\mathbf{x}, \omega)$, the source and receiver wavefields, respectively. The selection of SODCIGs can be thought of as the multiplication of the pre-stack image by a 2D-comb function, which is shifted laterally to select new set of SODCIGs to initiate the modeling of another pair of combined wavefields. After shifting along one period of the sampling function in the x and y directions, all the points on the reflector are used in the modeling. Consequently, the number of modeling experiments equals the number of lateral shifts of the sampling function.

Since the wavefields are initiated on the reflectors using combinations of SODCIGs, the idea of generalized sources applies, characterizing the image-space generalized source domain.

Again, for one particular frequency and a plane reflector so that the initial conditions are the same for modeling source \widehat{D}_P and receiver \widehat{U}_P wavefields, the modeling of a pair of PERM wavefields starting from combined SODCIGs can be described by

$$\widehat{D}_P(\boldsymbol{\xi}; \Delta \mathbf{x}) = \sum_{\mathbf{x}} \sum_{\mathbf{h}} \sum_m G_0(\boldsymbol{\xi}, \mathbf{x} - \mathbf{h}) \delta(\widehat{\mathbf{x}} - m\Delta \mathbf{x}) I(\widehat{\mathbf{x}}, \mathbf{h}), \quad (31)$$

and

$$\widehat{U}_P(\boldsymbol{\xi}; \Delta \mathbf{x}) = \sum_{\mathbf{x}} \sum_{\mathbf{h}} \sum_m G_0(\boldsymbol{\xi}, \mathbf{x} + \mathbf{h}) \delta(\widehat{\mathbf{x}} - m\Delta \mathbf{x}) I(\widehat{\mathbf{x}}, \mathbf{h}), \quad (32)$$

where $\sum_m \delta(\widehat{\mathbf{x}} - m\Delta \mathbf{x})$ is the 2D-sampling function.

The wavefields are recursively downward propagated in depth according to

$$\widehat{D}_P(\mathbf{x}; \Delta \mathbf{x}) = \sum_{\boldsymbol{\xi}} G_1^*(\boldsymbol{\xi}, \mathbf{x}) \widehat{D}_P(\boldsymbol{\xi}), \quad (33)$$

and

$$\widehat{U}_P(\mathbf{x}; \Delta \mathbf{x}) = \sum_{\boldsymbol{\xi}} G_1^*(\boldsymbol{\xi}, \mathbf{x}) \widehat{U}_P(\boldsymbol{\xi}). \quad (34)$$

The lateral shifts of the wavefields for the multi-offset imaging condition are represented by

$$\begin{aligned}\widehat{D}_P(\mathbf{x} - \mathbf{h}; \Delta \mathbf{x}) &= \sum_{\xi} G_1^*(\xi, \mathbf{x} - \mathbf{h}) \\ &\times \sum_{\mathbf{x}'} \sum_{\mathbf{h}'} \sum_m G_0(\xi, \mathbf{x}' - \mathbf{h}') \delta(\widehat{\mathbf{x}} - m\Delta \mathbf{x}) I(\widehat{\mathbf{x}}, \mathbf{h}'),\end{aligned}\quad (35)$$

and

$$\begin{aligned}\widehat{U}_P(\mathbf{x} + \mathbf{h}; \Delta \mathbf{x}) &= \sum_{\xi} G_1^*(\xi, \mathbf{x} + \mathbf{h}) \\ &\times \sum_{\mathbf{x}'} \sum_{\mathbf{h}'} \sum_m G_0(\xi, \mathbf{x}' + \mathbf{h}') \delta(\widehat{\mathbf{x}} - m\Delta \mathbf{x}) I(\widehat{\mathbf{x}}, \mathbf{h}').\end{aligned}\quad (36)$$

Applying the cross-correlation imaging condition to the wavefields of equations 35 and 36 gives

$$\begin{aligned}\widehat{I}_P(\mathbf{x}, \mathbf{h}; \Delta \mathbf{x}) &= \sum_{\xi'} \sum_{\mathbf{x}'} \sum_{\mathbf{h}'} \sum_m \sum_{\xi''} \sum_{\mathbf{x}''} \sum_{\mathbf{h}''} \sum_n G_0(\xi', \mathbf{x}' - \mathbf{h}') G_1^*(\xi', \mathbf{x} - \mathbf{h}) \\ &\times G_1^*(\xi'', \mathbf{x} + \mathbf{h}) G_0(\xi'', \mathbf{x}'' + \mathbf{h}'') \delta(\widehat{\mathbf{x}} - m\Delta \mathbf{x}) \delta(\widehat{\mathbf{x}} - n\Delta \mathbf{x}) \\ &\times I(\widehat{\mathbf{x}}, \mathbf{h}') I(\widehat{\mathbf{x}}, \mathbf{h}''),\end{aligned}\quad (37)$$

which can be recast as

$$\begin{aligned}\widehat{I}_P(\mathbf{x}, \mathbf{h}; \Delta \mathbf{x}) &= I_P(\mathbf{x}, \mathbf{h}; \Delta \mathbf{x}) \\ &+ \sum_{\xi'} \sum_{\mathbf{x}'} \sum_{\mathbf{h}'} \sum_{\xi''} \sum_{\mathbf{x}''} \sum_{\mathbf{h}''} \sum_{n \neq m} G_0(\xi', \mathbf{x}' - \mathbf{h}') G_1^*(\xi', \mathbf{x} - \mathbf{h}) \\ &\times G_1^*(\xi'', \mathbf{x} + \mathbf{h}) G_0(\xi'', \mathbf{x}'' + \mathbf{h}'') \delta(\widehat{\mathbf{x}} - m\Delta \mathbf{x}) \delta(\widehat{\mathbf{x}} - n\Delta \mathbf{x}) \\ &\times I(\widehat{\mathbf{x}}, \mathbf{h}') I(\widehat{\mathbf{x}}, \mathbf{h}'').\end{aligned}\quad (38)$$

The first term in the right-hand side of equation 38 is the desired image we would obtain by independently modeling and migrating PERM wavefields. The second term represents crosstalk. To obtain a crosstalk-free image, the sampling period must be large enough that wavefields initiated at different SODCIGs do not correlate. As previously shown when discussing how to compute PERM images with kinematics similar to those of the original shot-profile migration, PERM wavefields generated from SODCIGs within an interval equals to twice the subsurface-offset range η still contribute to the image at the central SODCIG. Crosstalk will occur if the sampling period is shorter than that interval. This is easily seen by realizing that the terms $\delta(\widehat{\mathbf{x}} - m\Delta \mathbf{x}) I(\widehat{\mathbf{x}}, \mathbf{h}')$ and $\delta(\widehat{\mathbf{x}} - n\Delta \mathbf{x}) I(\widehat{\mathbf{x}}, \mathbf{h}'')$ are 2D-periodic-rectangular functions with period $\Delta \mathbf{x}$ and width η . We want the spatial 2D-correlation of these functions to be a 2D-periodic triangular function, without interference between the individual 2D-triangles. This is achieved by setting $\Delta \mathbf{x} > \eta$.

The combination of modeling experiments is illustrated in Figure 22. We model PERM data starting with the rotated images from the previous section and combine SODCIGs into sets using the sampling period of 163 SODCIGs. Recalling that the number of subsurface-offsets is 81, it is expected that no crosstalk will occur when migrating the set with sampling period of 163 SODCIGs. In this case, since each reflector is used separately in the modeling, the total number of areal shots is 326, which is less than half of the original shot profiles.

We saw that carefully combining the modeling experiments decreases the data size while maintaining the correct kinematics, which is important for migration velocity analysis. However, combining the modeling experiments using a decorrelation distance between events does not achieve a significant data reduction, at least in 2D. In this case, data reduction depends on the number of subsurface-offsets which are necessary to capture all the relevant velocity information. In the example, the number of independent experiments is only less than one half as many as in the original dataset. Data reduction techniques like plane-wave decomposition, for instance, could lower data size by a factor of ten. As we will see in Chapter , further data reduction can be achieved by using the phase-encoding technique (Romero et al., 2000) to linearly combine the modeling experiments. This will enable us to use a shorter sampling period of SODCIGs, and also to inject more than one reflector in the modeling.

Although PERM theory was developed in 3D, all the examples I have shown so far have been 2D. Next, I discuss a 3D example under the common-azimuth approximation (Biondi and Palacharla, 1996) and show that in this case the SODCIGs in the y direction can be continuously sampled, and the number of modeling experiments will depend only on the sampling period in the x direction, drastically decreasing data size.

3D-PERM from common-azimuth migrated images

In the way PERM is formulated there is no restriction on the dimensionality of the pre-stack image used as the initial condition for the modeling, which means that if the original data have sufficient cross-line offsets as in the acquisition

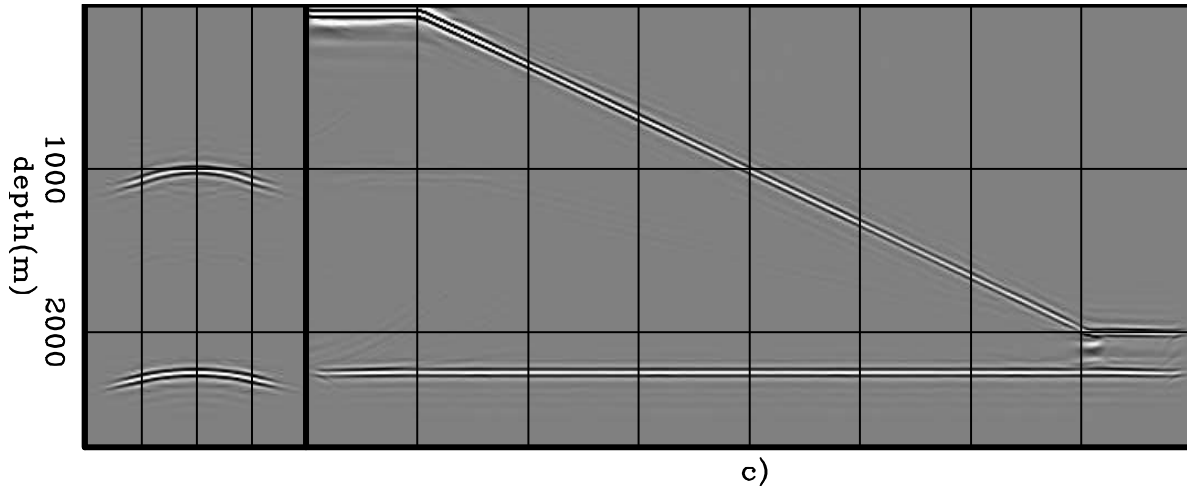


Figure 22: Areal-shot migration of PERM data synthesized from sets of SODCIGs selected with sampling period of 163 SODCIGs. Notice that no crosstalk is generated when the sampling period is larger than twice the subsurface-offset range.

geometries with wide range of azimuths (Regone, 2007; Kapoor et al., 2007; Moldoveanu et al., 2008), the initial conditions are a five-dimensional hypercube on \mathbf{x} , h_x and h_y .

To synthesize PERM data starting with the five-dimensional initial conditions such that no crosstalk is generated during migration, the minimum number of modeling experiments is $4n_{h_x}n_{h_y}$, where n_{h_x} and n_{h_y} are the number of subsurface offsets in the x and y directions. Considering the usual parameters, the number of modeling experiments may be as low as several hundreds. This data reduction is very substantial if we compare, for instance, with data reduction achieved by 3D-plane-wave migration. Using plane waves, to obtain artifact-free SODCIGs due to the lack of illumination from some propagation directions we need to migrate roughly 2000 plane waves. This means that 3D-PERM data size can be one order of magnitude smaller than 3D-plane wave data.

Despite the recent good migration results obtained in geologically complex areas using wide-azimuth data, narrow-azimuth acquisition is still the industry standard. Narrow-azimuth data can be efficiently imaged by common-azimuth wave-equation migration (CAM) (Biondi and Palacharla, 1996). CAM reduce the dimensionality of the pre-stack wavefields, and therefore the cost of migration, by assuming zero cross-line offset. That does not mean that the cross-line offset wavenumber is zero. Rather, its asymptotic approximation is a function of the the in-line midpoint and in-line offset wavenumbers. Therefore, instead of a five-dimensional hypercube, CAM images are four-dimensional hypercubes in \mathbf{x} and h_x .

Because of the zero-cross-line offset assumption, when using CAM images as the initial conditions to synthesize PERM data, the SODCIGs in the cross-line direction can be sampled continuously, as depicted in Figure 23b. Recall that PERM is equivalent to ERM if energy is focused at the zero subsurface offset, as well as if this is the only available subsurface offset. Contrast this case with the five-dimensional initial conditions for the full azimuth case of Figure 23a.

The continuous sampling of SODCIGs in the cross-line direction yields one more order of magnitude of data reduction. Therefore, under the common-azimuth approximation, 3D-PERM data size can be two orders of magnitude smaller than 3D-plane wave data.

To illustrate the validity of the above assumptions, a split-spread data with maximum offset of 1587.5 m was computed using 3D-Born modeling (Rickett et al., 1996) on a 30° dipping reflector with 45° azimuth with respect to the acquisition direction, which is aligned with the in-line direction. There are 96 in-lines and cross-lines spaced 25 m apart. The offset interval is 25 m. The velocity used in the modeling is the 1D function $v(z) = (1500 + 0.5z)$ m/s.

The Born data was input to CAM with a 5% slower velocity. Migration results can be seen in Figures 24a and 24b for SODCIGs positioned at $(x = 750 \text{ m}, y = 600 \text{ m})$ and $(x = 750 \text{ m}, y = 1000 \text{ m})$, respectively. The panel on the left is the SODCIG, which contains 21 subsurface offsets ranging from -250 m to 250 m . The panel in the middle is the in-line at zero subsurface offset, with $y = 600 \text{ m}$ (Figure 24a) and $y = 1000 \text{ m}$ (Figure 24b). The panel on the right is the cross-line at zero subsurface offset, with $x = 750 \text{ m}$.

In the common-azimuth regime, the computation of the dip-independent initial conditions is performed by simply stretching the in-line-subsurface-offset axis by $\sec \alpha_{y'}$ and rotating the SODCIGs in the in-line direction, since no cross-line offset is computed in migration.

To illustrate the effect of not stretching the in-line-subsurface-offset axis, source and receiver wavefields were modeled

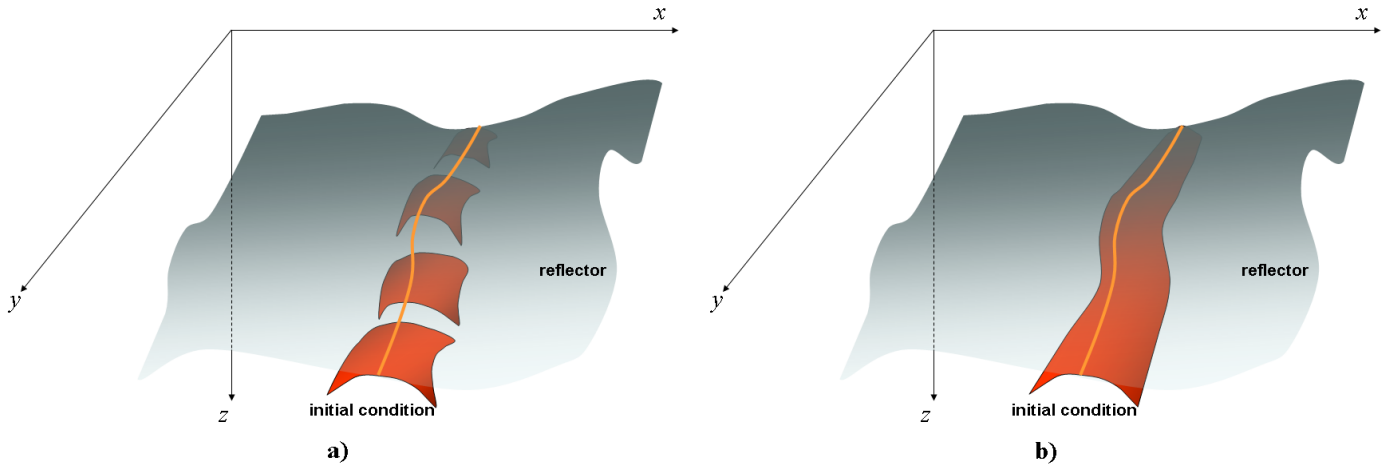


Figure 23: The initial conditions for synthesizing PERM data from CAM images can be specified as in b) because no pre-stack information exists in the cross-line direction, in contrast with the full azimuth situation in a).

from two different initial conditions: one after simple rotation, and the other after stretching and rotation. Both used continuous sampling along the cross-line direction and sampling period of 48 in the in-line direction. This period is sufficient to avoid crosstalk during the areal-shot migration, given that the number of subsurface-offsets of the pre-stack image is 21. Only the synthesized 3D receiver wavefield for the non stretched case is shown in Figure 25. The left panel is the in-line at $y = 1200$ m, the right panel is the cross-line at $x = 1400$ m, and the top panel is the time-slice at $t = 0.5$ s. The 3D migrations of the 48 areal shots with the velocity underestimated by 5% are shown in Figures 26a-b for the non stretched case and Figures 27a-b for the stretched case. SODCIGs are positioned at $(x = 750$ m, $y = 600$ m) in Figures 26a and 27a, and at $(x = 750$ m, $y = 1000$ m) in Figures 26a and 27a. To facilitate the comparison with the CAM images of Figures 24a-b, the polarity of the areal-shot migrated image is inverted due to the squaring of the wavelet. The kinematics of the SODCIGs computed with PERM wavefields overall matches those of the SODCIGs computed with CAM. However, notice how the images computed with PERM wavefields from the subsurface-offset stretched SODCIGs show slightly better amplitudes at farther subsurface offsets.

The correct kinematics shown in Figures 26 and 27 enables the use of 3D PERM wavefields computed from CAM images in the optimization of migration velocity. As the initial conditions for the modeling are continuously sampled in the cross-line direction, data size is drastically reduced.

CONCLUSIONS

In this chapter image-space generalized sources were obtained by combining PERM wavefields. We saw that wavefields synthesized by PERM provide migrated images with correct kinematics while decreasing data size. Data reduction is achieved by combining the modeling experiments and is controlled by the number of subsurface offsets that will be computed during areal-shot migration of PERM data. Recall that SODCIGs in the initial conditions must be separated by at least twice the maximum absolute subsurface-offset value to prevent crosstalk. Implicit to PERM is the requirement that reflectors must be identified in order to avoid reflector crosstalk during migration. 3D Pre-stack interpretation can be cumbersome, but it allows avoiding the use of reflectors with low signal-to-noise ratios in migration-velocity estimation. Moreover, in commercial software for migration velocity estimation reflector picking is a standard and almost entirely automated procedure.

Whereas in 2D PERM data size is comparable to that of the plane-wave decomposition, in 3D it is one order of magnitude smaller when computing cross-line subsurface-offsets. Further data size reduction by another order of magnitude is achieved if the initial conditions are computed with common-azimuth migration.

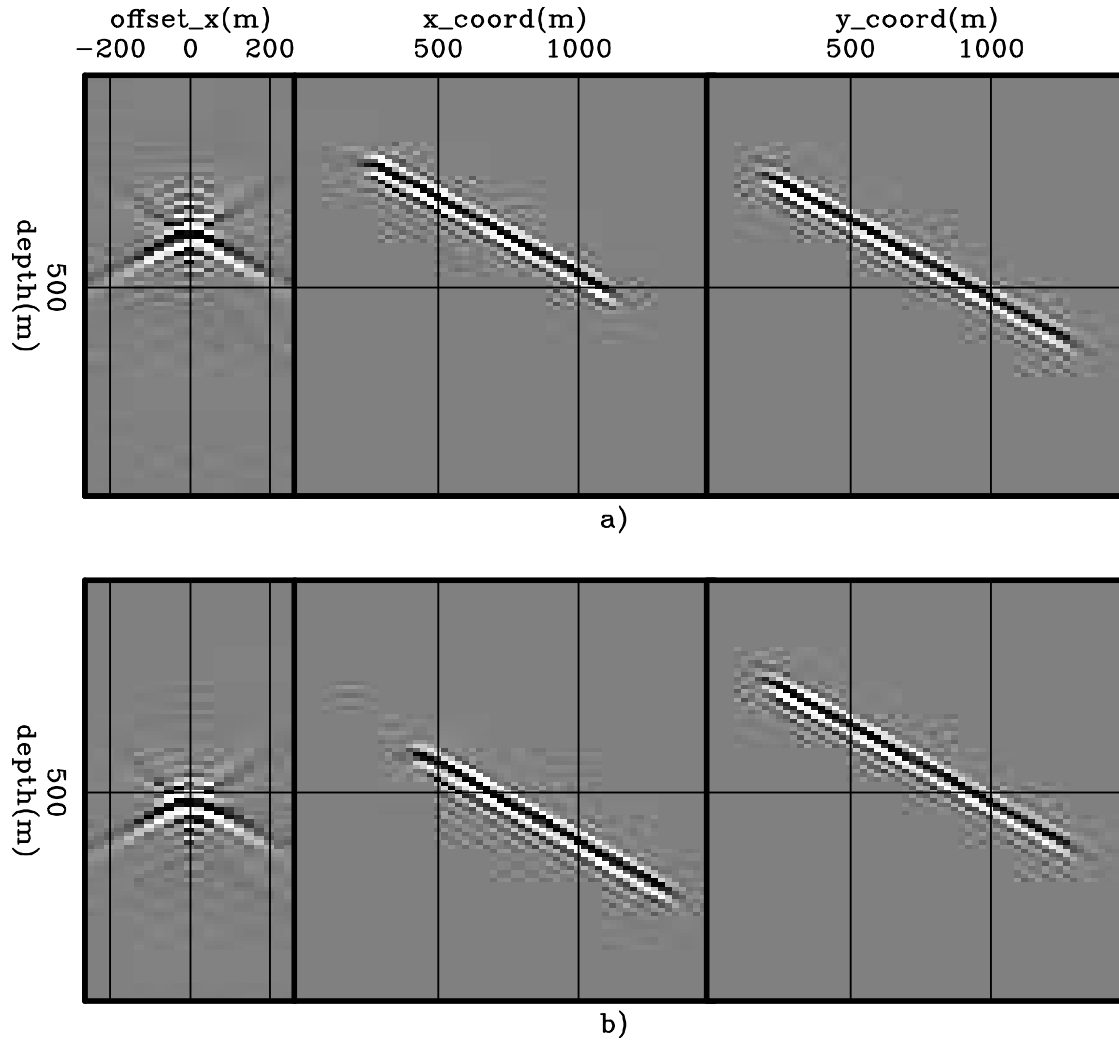


Figure 24: Common-azimuth migration of 3D-Born data modeled from a 30° dipping reflector with 45° azimuth with respect to the acquisition direction. The panel in the middle is the in-line at the zero-subsurface offset, and $y = 600$ m (Figure 24a) and $y = 1000$ m (Figure 24b). The panel on the right is the cross-line at the zero-subsurface offset, and $x = 750$ m.

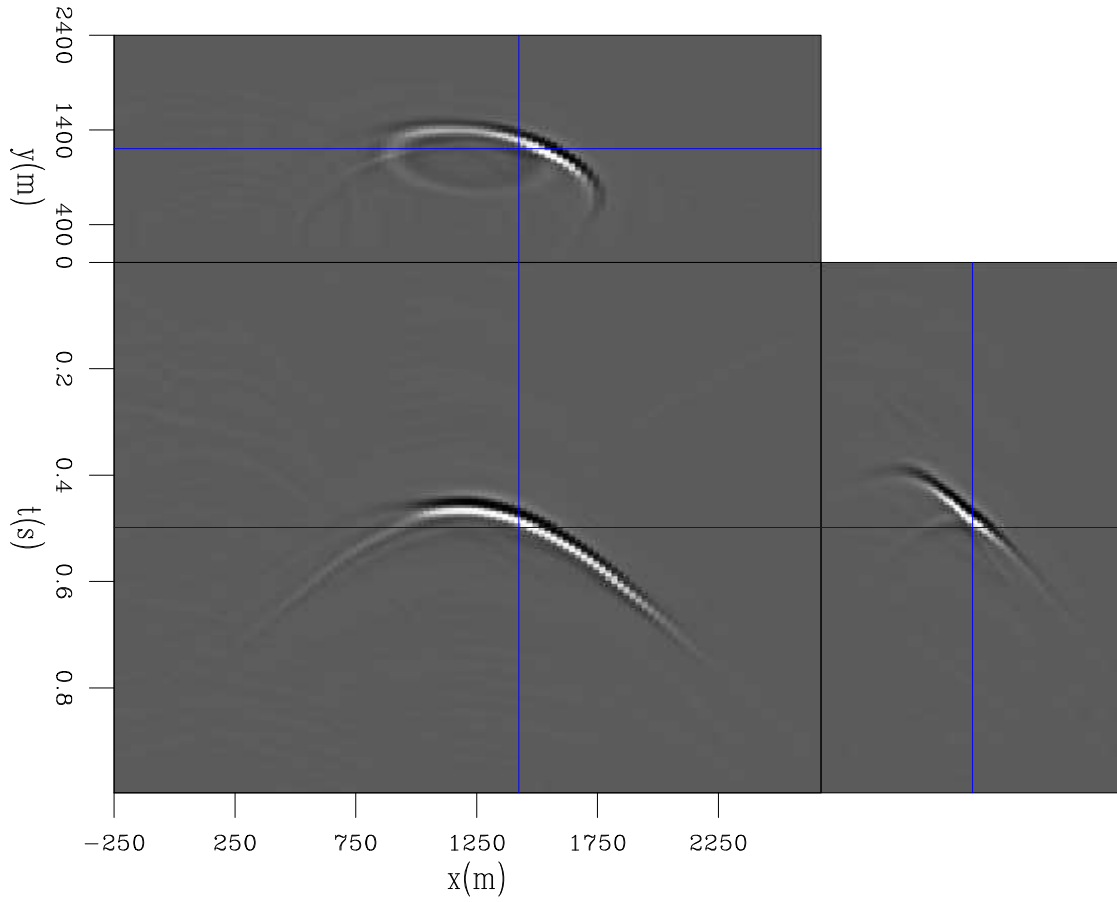


Figure 25: 3D-PERM receiver wavefield. The left panel is the in-line at $y = 1200$ m, the right panel is the cross-line at $x = 1400$ m, and the top panel is the time-slice at $t = 0.5$ s.

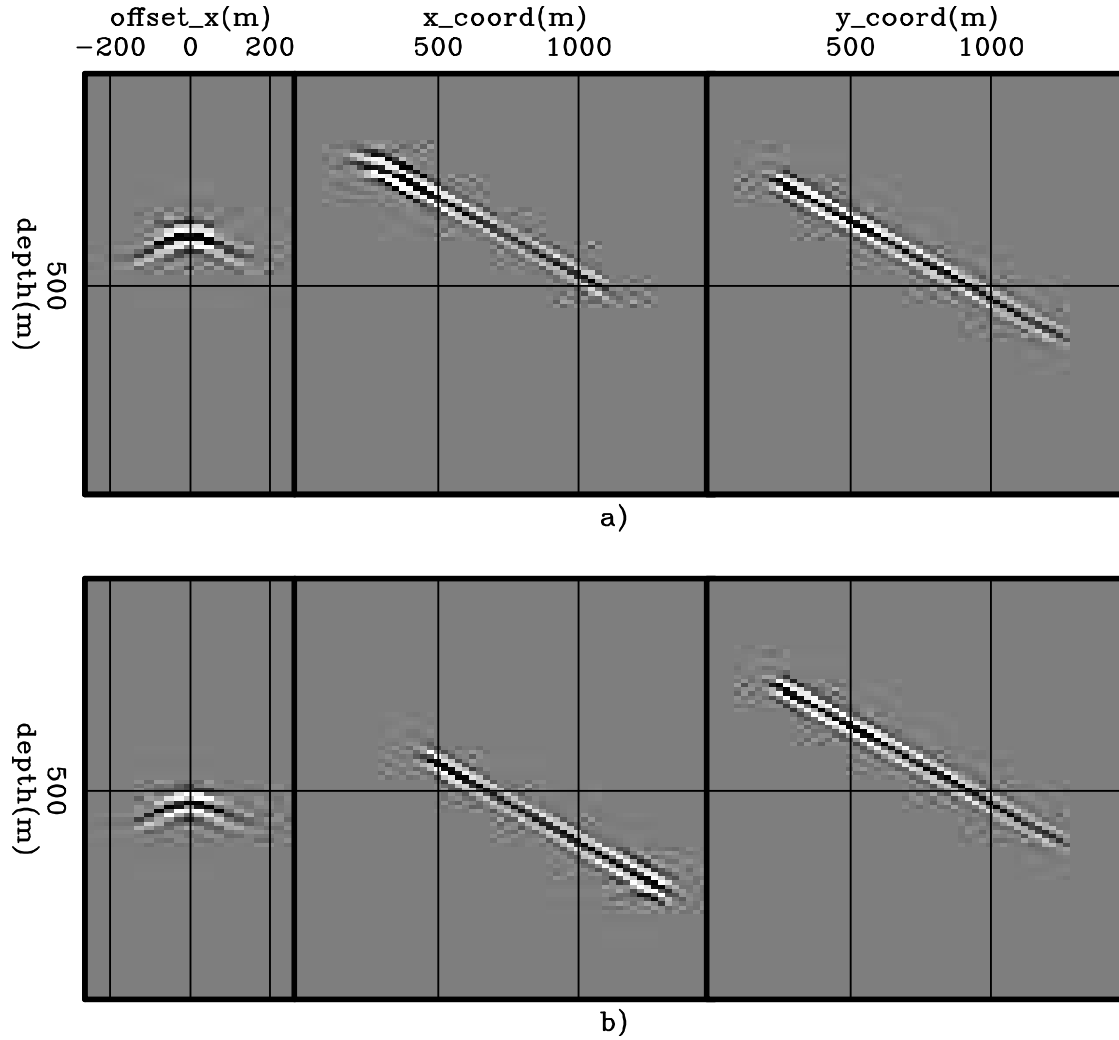


Figure 26: 3D-areal-shot migration of PERM data from non stretched subsurface offset SODCIGs. The panel in the middle is the in-line at the zero-subsurface offset, and $y = 600$ m (Figure 24a) and $y = 1000$ m (Figure 24b). The panel on the right is the cross-line at the zero-subsurface offset, and $x = 750$ m. Compare with Figure 24 and 27.

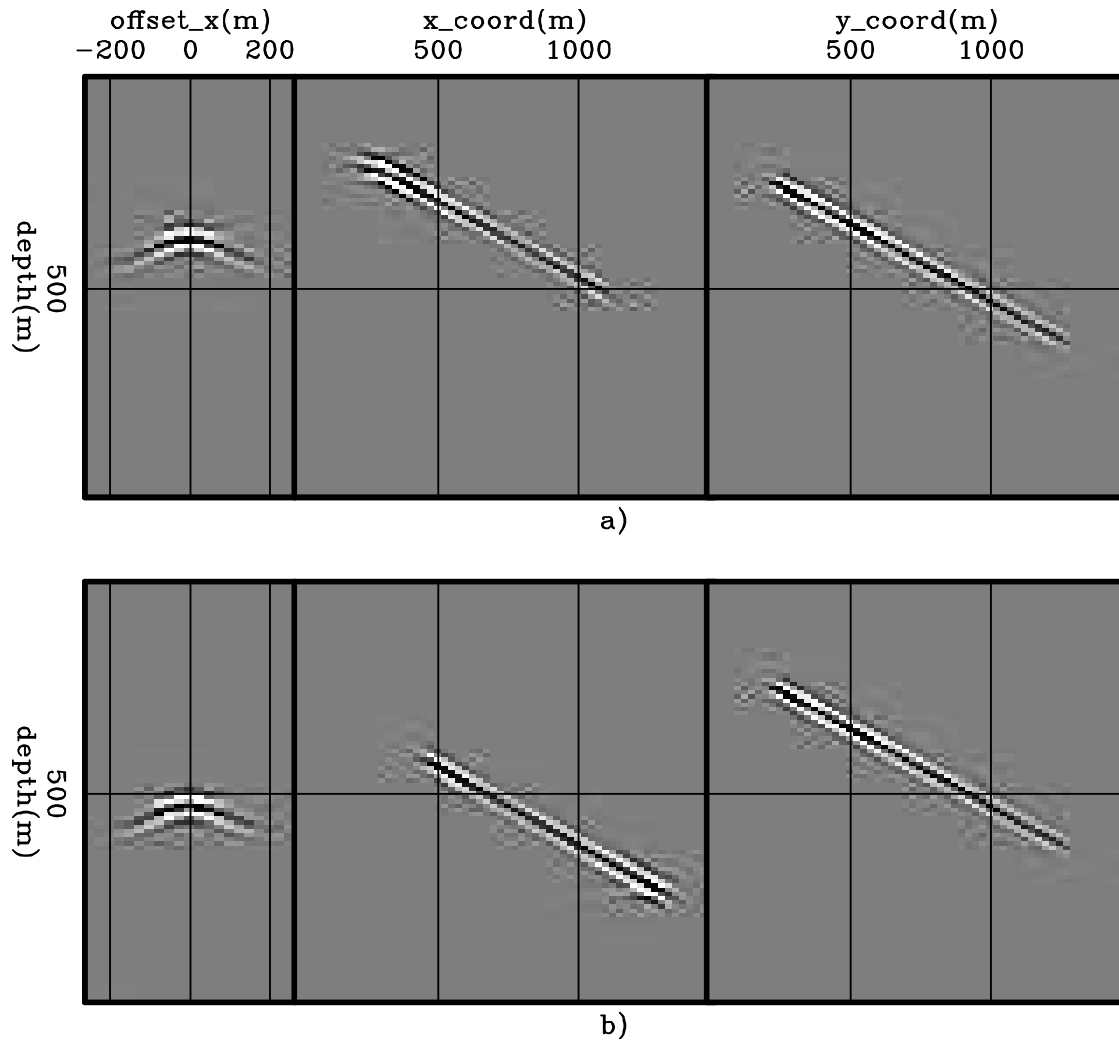


Figure 27: 3D-areal-shot migration of PERM data from stretched subsurface offset SODCIGs. The panel in the middle is the in-line at the zero-subsurface offset, and $y = 600$ m (Figure 24a) and $y = 1000$ m (Figure 24b). The panel on the right is the cross-line at the zero-subsurface offset, and $x = 750$ m. Compare with Figure 24 and 26.

Image-space phase-encoded wavefields

This chapter introduces image-space phase-encoded wavefields (ISPEWs). ISPEWs are computed using PERM along with phase-encoding techniques to further improve data reduction achieved with PERM. In this sense, ISPEWs can also be defined as image-space generalized source wavefields. The phase encoding is performed during the modeling, in which the source function of every event is coded using a particular coding sequence. Phase encoding during the modeling allows injection of more closely spaced SODCIGs than the technique showed in Chapter ?? and multiple reflectors, while diminishing the prejudicial effect of crosstalk during imaging. Modeling of ISPEWs can be confined to a region of the subsurface where the velocity model is inaccurate, allowing migration velocity analysis using wavefield extrapolation to be easily solved in a target-oriented manner. The use of phase encoding combined with the target-oriented modeling dramatically decreases the cost of migration velocity analysis, especially in 3D projects.

INTRODUCTION

Chapter ?? introduced the pre-stack exploding-reflector model (PERM). Using the concept of exploding reflectors, PERM synthesizes new wavefields that enables us to compute pre-stack images by wavefield extrapolation methods at a low cost. In 3D, PERM data size can be up to two orders of magnitude smaller than plane-wave data.

The strategy used in Chapter ?? to ensure that crosstalk of wavefields does not occur during migration is, using of the linearity of wavefield propagation, to simultaneously inject SODCIGs separated by a decorrelation distance equal to twice the subsurface-offset range. This decorrelation distance in PERM modeling plays a role similar to the grating interval in an optical fiber, which influences optical crosstalk in optical transmission systems and networks (Yamada et al., 1998). In this optical fiber communication, crosstalk is further reduced (and bandwidth increased) by phase encoding the optical information (Teh et al., 2001).

Phase encoding is a well-established technique in radar (Levanon and Mozeson, 2004), medical imaging (Bernstein et al., 2005; Weishaupt et al., 2006), cryptography (Wang et al., 1996; Javidi et al., 1996) and wireless communication (Castoldi, 2002; Zigangirov, 2004). Phase encoding enables faster data acquisition, larger bandwidth and more reliable signal recovery. In wireless communication, for instance, systems using Code Division Multiple Access (CDMA), a method for accessing communication channels, allow several users to share the same communication channel without crosstalk. This is achieved by encoding the information during transmission using sequences with unique correlation properties (Gold, 1967; Dinan and Jabbari, 1998). Information is recovered with minimal distortion after decoding with the corresponding sequence.

Phase encoding has been long used in seismic exploration to enable simultaneous shooting for acquisition with seismic vibrators (Ward et al., 1990; Martin, 1993; Bagaini, 2006). To decrease seismic imaging cost, using the concept of generalized sources, wavefields are usually phase-encoded using phase functions like the plane-wave phase function (Schultz and Claerbout, 1978; Whitmore, 1995; Liu et al., 2006; Duquet and Lailly, 2006) and random phase functions (Romero et al., 2000; Sun et al., 2002). Recently, phase-encoded wavefields have also been applied to velocity estimation by waveform inversion (Vigh and Starr, 2008; Ben-Hadj-Ali et al., 2009; Krebs et al., 2009) and migration-velocity analysis using wavefield extrapolation (Shen and Symes, 2008; Guerra et al., 2009). Phase-encoded wavefields can also be used to decrease the cost of computing the Hessian operator in least-squares migration (Tang, 2009).

Usually, phase encoding is applied in the data space. Shot gathers are weighted with, ideally, orthogonal phase functions, and combined into areal shots. The corresponding point sources are also encoded with the same phase functions and combined into areal source functions. During migration, the cross-correlation of related wavefields, encoded with the same phase function, yields strong amplitudes corresponding to the real reflectors. The cross-correlation of unrelated wavefields, encoded with different phase functions, yields attenuated amplitudes corresponding to the attenuated crosstalk.

A similar strategy can be applied in the model space to encode PERM experiments (Guerra and Biondi, 2008b,a). A different pseudo-random sequence is assigned to each SODCIG used in the modeling of a pair of PERM wavefields, so that during migration correlation of unrelated wavefields is attenuated. This characterizes the image-space phase-encoded wavefields (ISPEWs), and it allows decreasing the sampling interval of the combined SODCIGs and using more than one reflector in the initial conditions.

To provide relevant information for velocity updates when using generalized sources, crosstalk must be incoherent. This has been observed by Krebs et al. (2009) in the context of waveform inversion using phase-encoded wavefields, for which using different codes for different iterations yields more accurate models and improves convergence. Similarly, in the context of migration velocity analysis by wavefield extrapolation using ISPEWs, if necessary, several random realizations of ISPEWs can be computed to be used in different velocity iterations.

In migration velocity analysis using ray methods, it is common practice to limit the velocity update to a certain portion of the model space, especially for deeper levels when the velocity model is accurate enough at shallower depths. However, when performing pre-stack depth migration during velocity iterations, the entire model space has to be imaged. To avoid the worthless computation of the migrated image in regions where the velocity is sufficiently accurate, the wavefields can be downward extrapolated up to a datum at the bottom of this region (Berryhill, 1979; Bevc, 1997; Wang et al., 2006). Hence, if the wavefields are datumized, migration can be restricted to the region where the velocity accuracy needs to be improved.

Since PERM wavefields are upward propagated, they can be collected at any depth. Therefore, limiting the velocity update to the inaccurate velocity region is easily achieved using these wavefields. After being upward propagated with the inaccurate velocity of deeper levels, PERM wavefields are collected at the top of the inaccurate velocity region. Thus, PERM naturally datumizes the wavefields. ISPEW takes advantage of this characteristic to decrease the cost of both the modeling and migration velocity analysis iterations.

In this chapter, I describe how crosstalk is generated when migrating PERM data computed from combined SODCIGs separated by an interval that is shorter than the decorrelation distance and with more than one reflector in the initial conditions. I will show that phase-encoding techniques can be applied to the modeling of ISPEWs, yielding further data

size reduction while attenuating the deleterious effects of crosstalk. I will use an example with the Marmousi model to illustrate the usefulness of ISPEWs to migration-velocity analysis.

CROSSTALK GENERATION

In the combination of modeling experiments of Chapter ??, two basic restrictions were applied to the initial conditions. First, the initial conditions contained only one reflector. Second, the sampling period along midpoint was sufficiently large to avoid crosstalk during migration (Figures 22 and 26). Considering that we probably need more than one reflector to define the velocity structure, the first restriction would increase the number of the modeling experiments by a factor equal to the number of selected reflectors. Moreover, because the choice of the sampling period depends on how many subsurface offsets are needed for performing velocity updates, data size reduction is partly conditioned by the velocity inaccuracy, which causes energy to spread to subsurface offsets different from zero. As we will see in this section, if these restrictions are not observed, two different kinds of crosstalk are generated: one related to the correlation of wavefields from different reflectors, and the other related to the correlation of wavefields from unrelated SODCIGs. The first originates during the cross-correlation in time, whereas the second originates during the cross-correlation in space.

Let us first consider the crosstalk from different reflectors. Since reflectors are simultaneously injected in the initial condition, several events are present both in the source wavefield and in the receiver wavefield, as in Figure 12 where we can see two events coming from the dipping and the deeper flat reflector. During migration, in addition to the expected cross-correlations between the source and receiver wavefields synthesized from the same reflector, cross-correlation of wavefields from different reflectors will occur, generating crosstalk between reflectors. Areal-shot migration of a pair of PERM wavefields synthesized from a set of SODCIGs with sampling period of 163 is shown in Figure 28. The intermediate events between the dipping and the deeper reflectors are due to the cross-correlation of wavefields initiated at different reflectors. The panel on the left is the SODCIG taken at $x = 0$ m and the panel on the right is the zero-subsurface offset section.

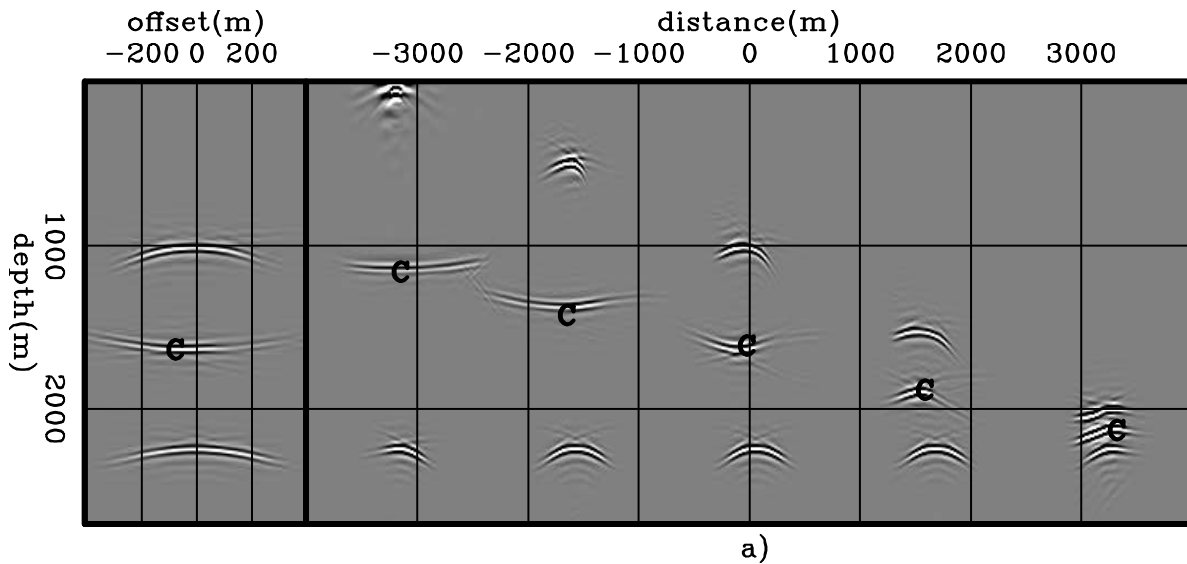


Figure 28: Areal-shot migration of PERM data synthesized from a set of SODCIGs selected with sampling period of 163. The two reflectors are simultaneously injected to the model. Notice the reflector crosstalk, labeled with ‘C’, resulting from the cross-correlation of the wavefields from the horizontal reflector with that from the dipping reflector.

To illustrate the reflector crosstalk generation, snapshots of the wavefield propagation are shown in Figure 29. Both wavefields are represented in the same panel. The panels on the left show the wavefields in the time-depth domain selected at horizontal positions where reflector crosstalk occurs in Figure 28. The panels on the right are taken at the propagation time when the wavefields cross on the left panels. The crossing times vary from 0.14 s to 1.24 s for the SODCIGs from right to left, respectively. The crossing times are a function of local dips, distance and propagation velocity between reflectors \bar{v} . For the simple case of parallel reflectors, the wavefield propagation time at which reflector crosstalk t_{rc} occurs is

$$t_{rc} = \frac{0.5\Delta z_r}{\bar{v}}, \quad (39)$$

where Δz_r is the distance between reflectors.

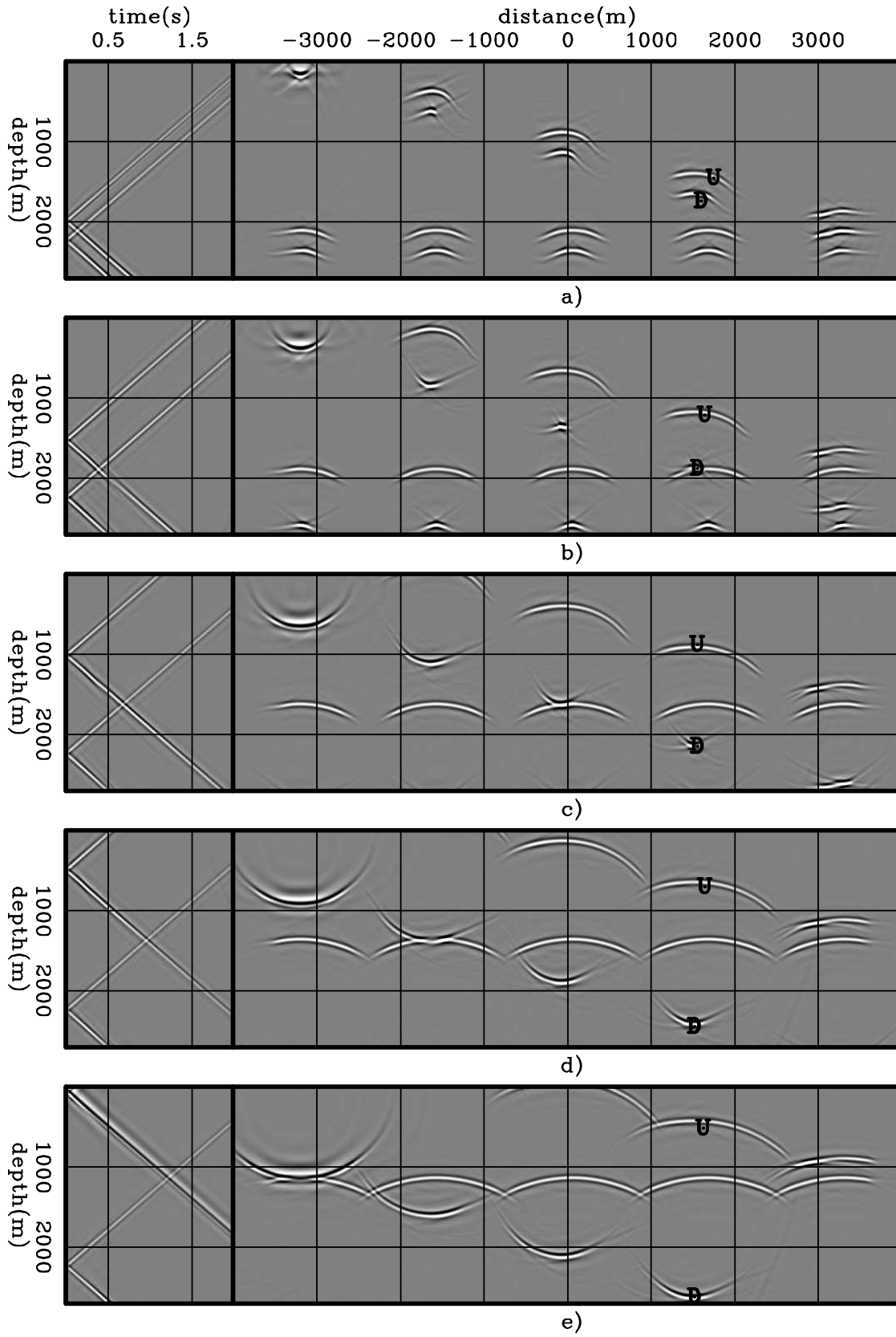


Figure 29: Snapshots of propagation of wavefields used to compute the image of Figure 28. Wavefields are labeled 'D' (Downgoing) for the source wavefield and 'U' (Upgoing) for the receiver wavefield. The panels on the left are selected at horizontal positions where the crosstalk occurs in Figure 28. The panels on the right are taken at the propagation time when the wavefields cross on the left panel.

Now let us consider the crosstalk formed by cross-correlating wavefields from unrelated SODCIGs of the same areal shot. From equation 38, repeated here,

$$\begin{aligned} \widehat{I}_P(\mathbf{x}, \mathbf{h}; \Delta\mathbf{x}) &= I_P(\mathbf{x}, \mathbf{h}; \Delta\mathbf{x}) + \sum_{\xi'} \sum_{\mathbf{x}'} \sum_{\mathbf{h}'} \sum_{\xi''} \sum_{\mathbf{x}''} \sum_{\mathbf{h}''} \sum_{n \neq m} G_0(\xi', \mathbf{x}' - \mathbf{h}') G_1^*(\xi', \mathbf{x} - \mathbf{h}) \\ &\times G_1^*(\xi'', \mathbf{x} + \mathbf{h}) G_0(\xi'', \mathbf{x}'' + \mathbf{h}'') \delta(\widehat{\mathbf{x}}' - m\Delta\mathbf{x}) \delta(\widehat{\mathbf{x}}'' - n\Delta\mathbf{x}) \\ &\times I(\widehat{\mathbf{x}}', \mathbf{h}') I(\widehat{\mathbf{x}}'', \mathbf{h}''). \end{aligned}$$

we see that the crosstalk has structure similar to that of the desired image. In equation 40 G are the Green's functions from a point in the subsurface \mathbf{x} to a point ξ at the datum where the wavefields are collected. The Green's functions can be propagated with different velocities, which is indicated by the subscripts. The sampling functions $\delta(\mathbf{x} - n\Delta\mathbf{x})$ select the image I at periods of $\Delta\mathbf{x}$. Crosstalk is not formed for $\Delta\mathbf{x} > \boldsymbol{\eta}$, where $\boldsymbol{\eta}$ is the decorrelation distance equal to twice the subsurface-offset range. If this criterion is not observed, crosstalk will occur in the SODCIGs according to a period of $\Delta\mathbf{x}$.

To see how crosstalk from unrelated SODCIGs is formed, let us use the same two-reflectors model as in Chapter ???. PERM data were modeled starting from the rotated images of Figure 11 using SODCIGs combined into sets with sampling period of 41 and 81 SODCIGs. Equation 26 shows that no crosstalk is generated if the sampling period is chosen to be the decorrelation distance of twice the subsurface-offset range, which in the present case must be greater than the distance spanned by 162 SODCIGs. Recall that the number of subsurface offsets in the original image is 81. As can be seen in Figures 30a and 30b, crosstalk occurs according periods of one-fourth and one-half of the sampling period, respectively. The corresponding ADCIGs at $x = 0$ m and the ADCIG computed from the image with no crosstalk are shown in the top panels of Figure 31. In the bottom panels we can see the corresponding ρ scans, computed using equation D-7 in Biondi and Symes (2004). Notice that manual picking can identify the correct $\rho = 0.9$ in Figures 31a-b. Therefore, ray-based methods for velocity update can back-project the correct moveout information. However, when wavefield-extrapolation methods are used for velocity update, perturbed images computed from Figures 30a-b or 31a-b will potentially provide incorrect gradients.

CROSSTALK ATTENUATION

Let us now consider two different strategies to attenuate the two different types of crosstalk: the reflector crosstalk and the crosstalk from unrelated SODCIGs. In the first strategy, we will take advantage of the imaging principle to perform time cross-correlations within a window centered at zero time of wavefield propagation to avoid reflector crosstalk. In the second strategy, we will use random-phase encoding to combine the modeling experiments to attenuate both types of crosstalk. These are mutually excluding strategies, because when wavefields are phase encoded, the reference for the zero time of wavefield propagation is lost, since the frequency components of the wavefields are randomly injected in time into the modeling. We illustrate the crosstalk attenuation using a smoothed version of the Marmousi model.

Time-windowed imaging condition

From Figure 29a, notice that for propagation times less than 0.14 s minus the period of the wavelet in time, no crosstalk will occur. This observation can be used to avoid crosstalk by applying a modified imaging condition. As Figure 29 shows, crosstalk is formed at times different from zero. Therefore, if the wavefields are cross-correlated within a time window centered at time zero with a length that excludes the times at which crosstalk is formed, reflector crosstalk can be avoided (Biondi, 2007). The time-windowed imaging condition for a single pair of areal shot reads

$$I_{P_w}(\mathbf{x}, \mathbf{h}) = \sum_{-\frac{t_w}{2} \leq t \leq \frac{t_w}{2}} \mathcal{F}^{-1} [D^*(\mathbf{x} - \mathbf{h})] \mathcal{F}^{-1} [U(\mathbf{x} + \mathbf{h})], \quad (40)$$

where t_w is the length of the time window. When using one-way propagators, the wavefields are inverse Fourier transformed to time by \mathcal{F}^{-1} . Migration using the time-windowed imaging condition of equation 40 is shown in Figure 32. The length of the time window is 0.06 s, which avoids the cross-correlation of events from different reflectors. The image is completely free of reflector crosstalk.

The efficacy of the time-windowed imaging condition for attenuating the reflector crosstalk is independent of the number of modeled events; however, it does depend on the distance between reflectors. This is illustrated using a smoothed Marmousi model example (Figure 33a). This model was input into one-way Born modeling, along with a 2D reflectivity derived from the true Marmousi velocity model, to generate 360 split-spread shot gathers with 6000 m maximum offset.

Shot-profile migration of the Born data was performed with a migration velocity approximately 5% slower than the modeling velocity for depth levels below the horizon shown in Figure 33b. Above this horizon, migration velocity is equal

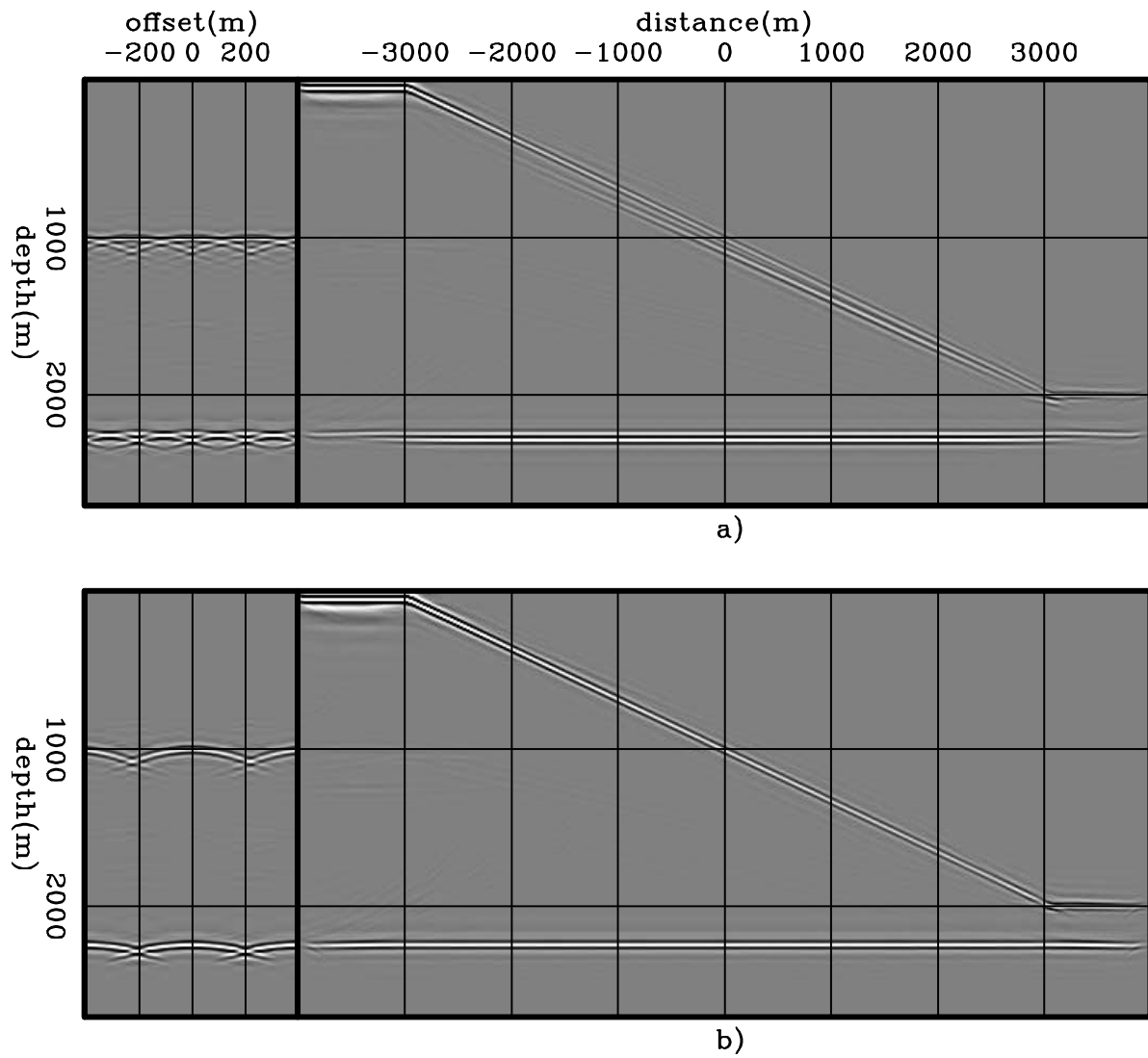


Figure 30: Areal-shot migration of PERM data synthesized from sets of SODCIGs selected with sampling period of: a) 41 and, b) 81.

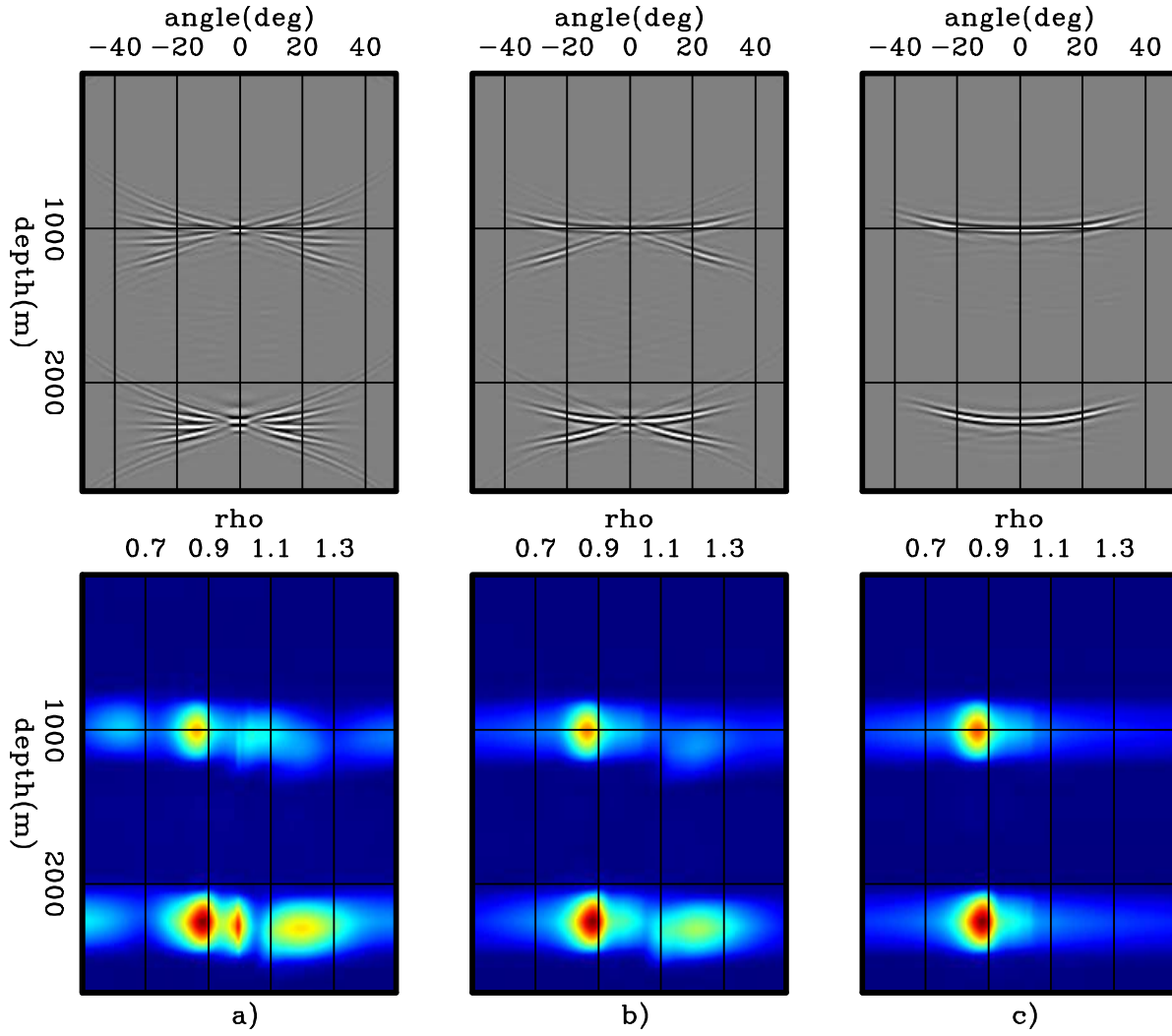


Figure 31: ADCIGs (top) and ρ -panels (bottom) corresponding to images computed by wavefields modeled with sampling period of: a) 41, b) 81, and c) 163. Velocity information has been destroyed by the crosstalk in a) and b).

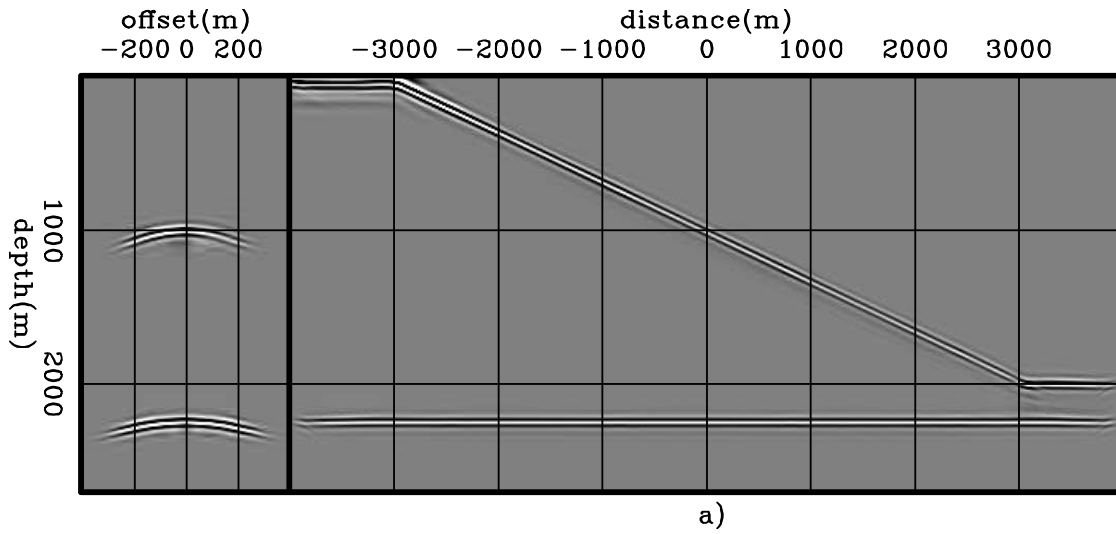


Figure 32: Areal-shot migration using the time-windowed imaging condition (equation 40). The reflector crosstalk is completely eliminated.

to the modeling velocity. All the left panels shown in this example are SODCIGs selected at $x = 5000$ m. The right panel is the zero-subsurface-offset section. The background image contains 17 subsurface offsets 24 m apart, starting at -192 m. Four reflectors were selected to initiate the modeling of PERM wavefields. They were rotated according to the transformation described in Chapter ???. The background image and the selected reflectors are shown in Figures 34a-b, respectively, only for depths between 1500 and 3000 m. The rotated initial conditions for the modeling of source and receiver wavefields are shown in Figures 35a-b, respectively.

The horizontal distance between SODCIGs injected simultaneously into the modeling of one areal shot is 840 m, which means that 35 pairs of PERM wavefields are generated. This number corresponds to 1/10 of the original shot gathers. The spatial sampling interval is greater than the decorrelation distance, which in this case is 792 m. Hence, we do not expect crosstalk from unrelated SODCIGs.

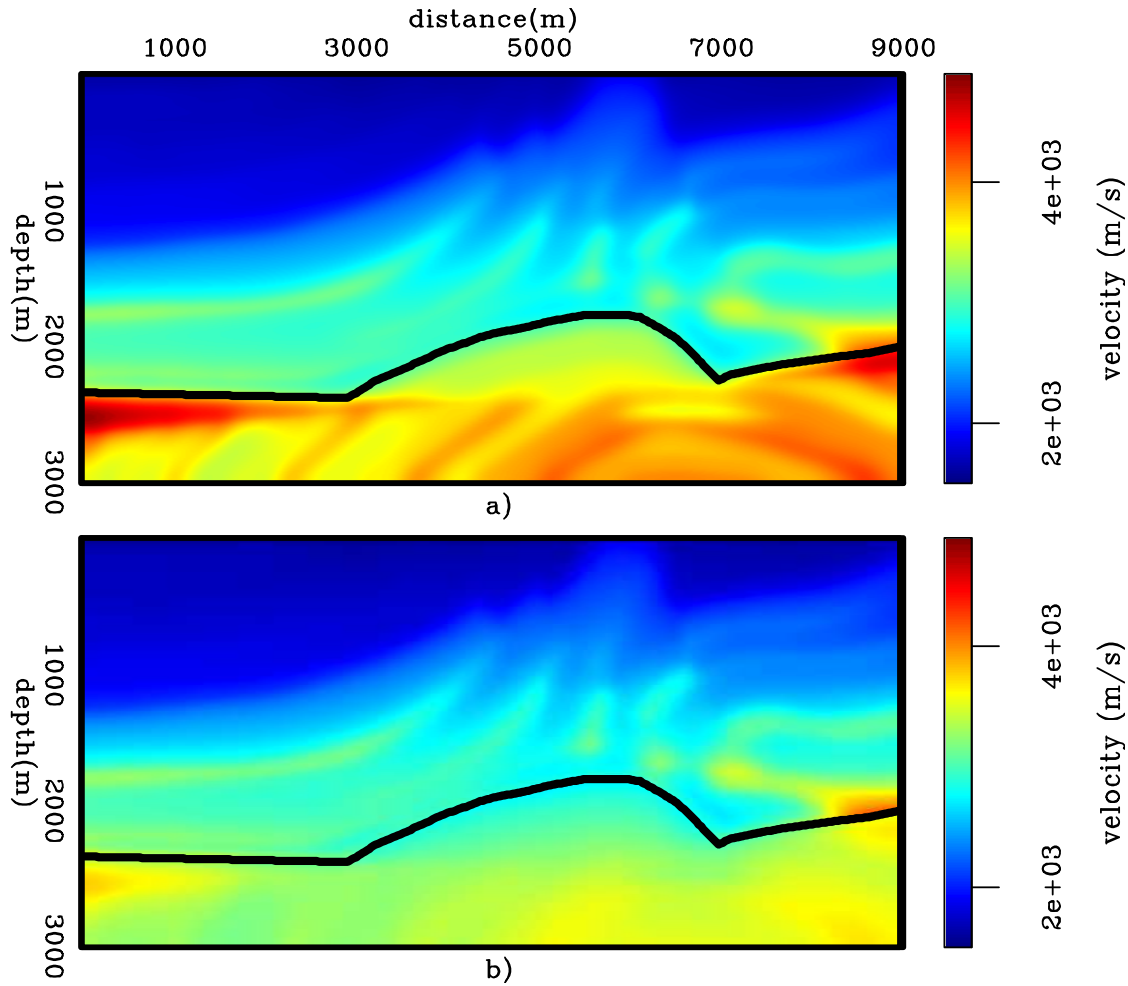


Figure 33: Velocity models for the Marmousi example: a) Smooth velocity model used to model the Born data. b) Background velocity model used to migrate the Born data, and to model and migrate PERM data.

PERM wavefields were modeled and collected at a depth of 1500 m. A pair of PERM wavefields are shown in Figure 36. These wavefields were migrated using the conventional (equation 19) and the time-windowed (equation 40) imaging conditions. The areal-shot migration using the conventional imaging condition is strongly contaminated with reflector crosstalk (Figure 37a). The areal-shot migration of PERM wavefields using the time-windowed imaging condition with a time-window length of 0.016 s successfully attenuated the reflector crosstalk in regions where reflectors are sufficiently separated (Figure 37b). However, as can be seen in the SODCIG in the left panel, some residual crosstalk from closely spaced reflectors still persists. This is because the time of wavefield propagation at which reflector crosstalk occurs is within the time window used for cross-correlation. This is easily seen by inserting the values for the local background velocity of 2540 m/s and the distance of 160 m between the two reflectors responsible for the reflector crosstalk into equation 39. The result, 0.125 s, is slightly smaller than the time-window length. Using a shorter time window could completely avoid crosstalk, but also could cause phase distortion.

The imaging principle states that the reflector image is formed at the zero time of wavefield propagation when the

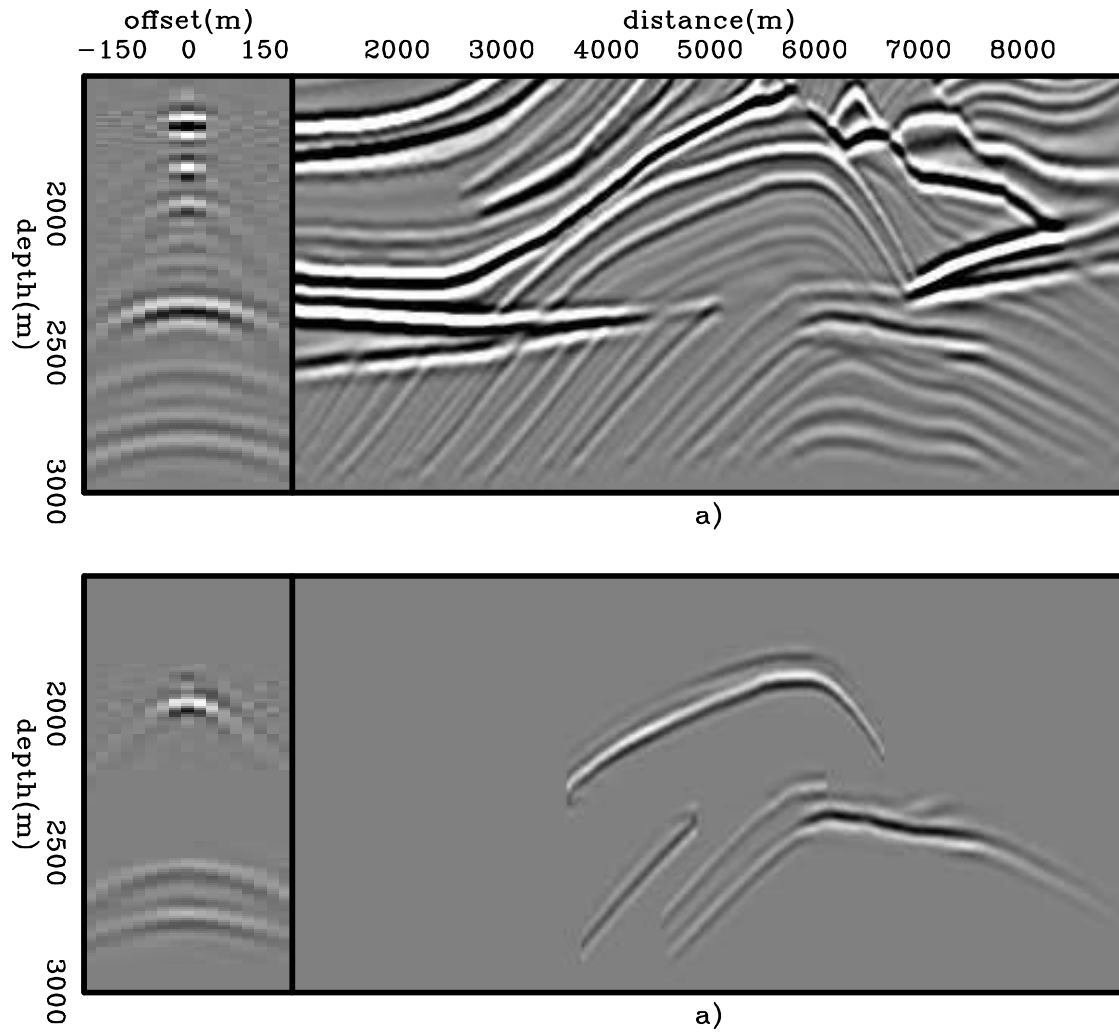


Figure 34: a) Pre-stack image computed with the background velocity model. b) Selected reflectors from the background image to perform modeling of wavefields.

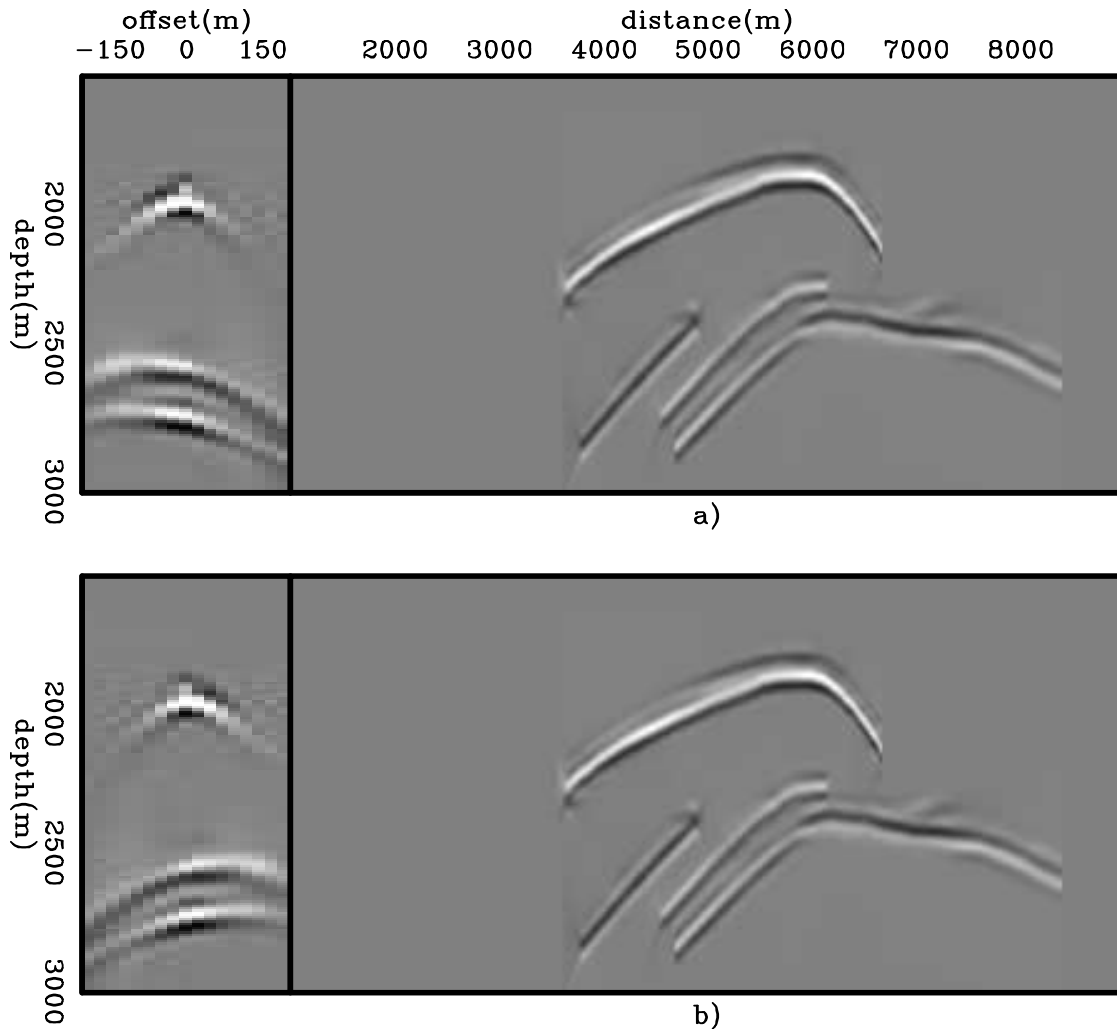


Figure 35: Rotated initial conditions for modeling: a) source wavefields, and b) receiver wavefields.

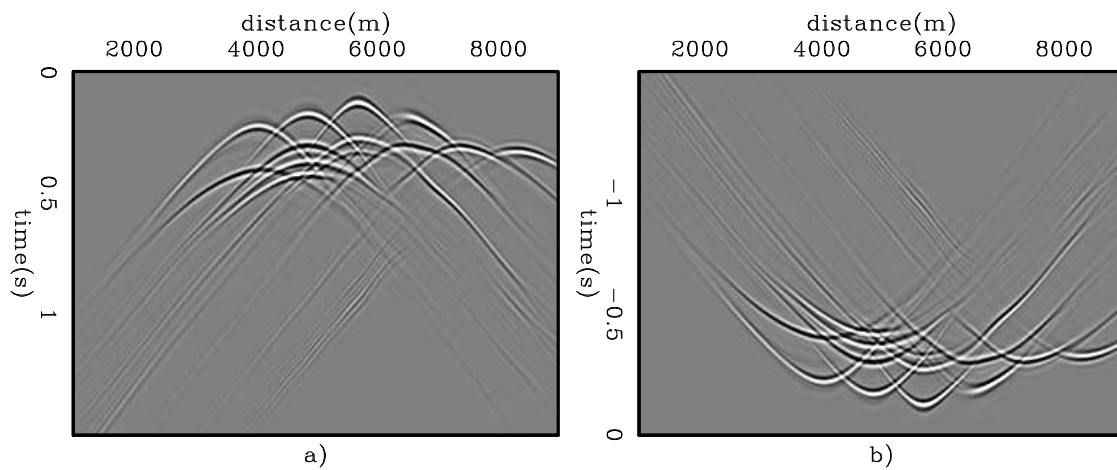


Figure 36: PERM wavefields for the Marmousi example: a) Receiver wavefield. b) Source wavefield.

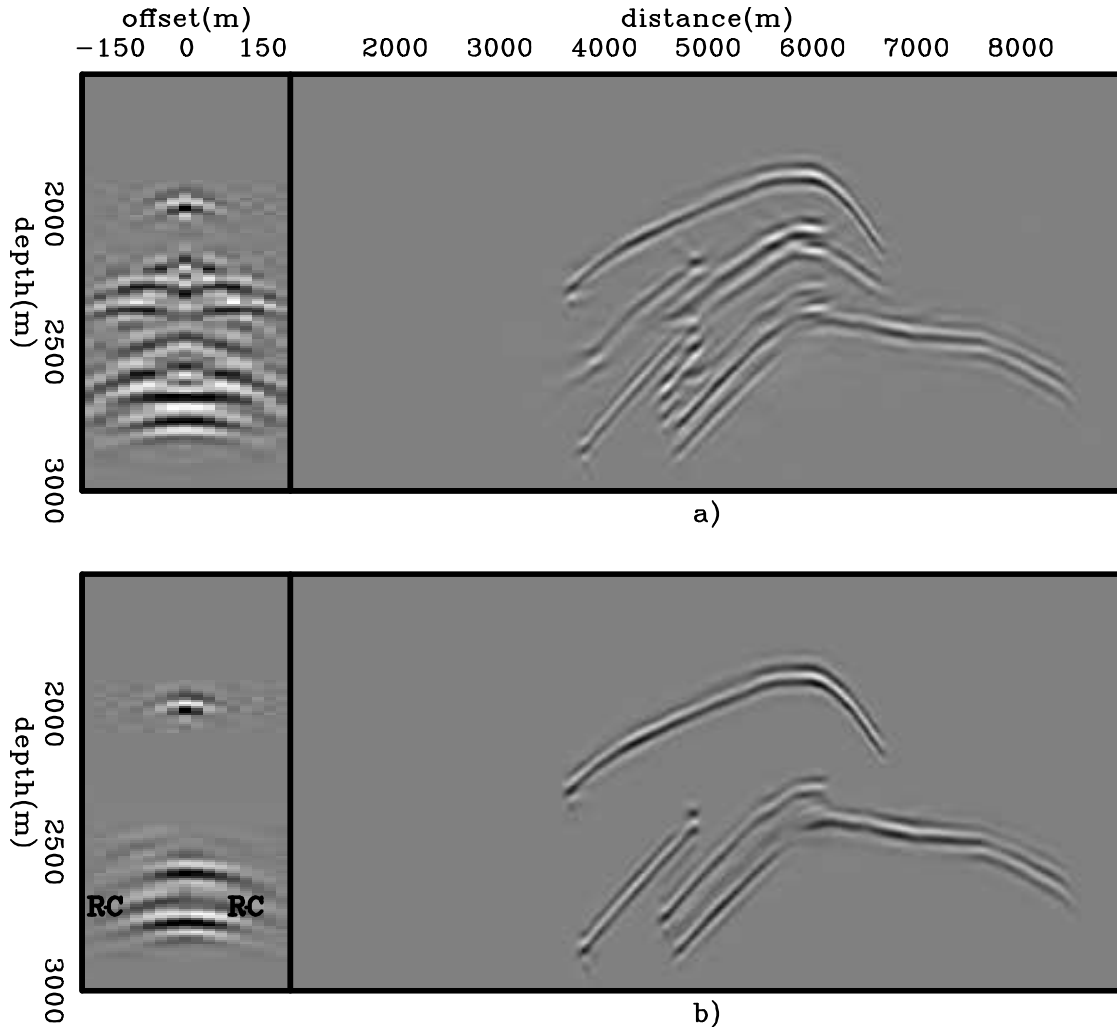


Figure 37: Pre-stack image computed with PERM wavefields and background velocity model using: a) the conventional imaging condition (equation 19), and b) the time-windowed imaging condition (equation 40). Reflector crosstalk is avoided when reflectors are sufficiently separated. However, some residual crosstalk is still present (RC). Notice the phase difference of the PERM image due to the squaring of the wavelet when compared to the windowed reflectors of Figure 34b.

migration velocity is accurate. When the migration velocity is inaccurate, the focusing of the image departs from the zero time, and this can be potentially used to update the velocity model (Sava and Fomel, 2006; Yang and Sava, 2009). Depending on the magnitude of the velocity errors and the distance between reflectors, the use of the time-windowed imaging condition can corrupt the velocity information.

Next, we will see how phase-encoding the modeling experiments can attenuate crosstalk without the risk of affecting the velocity information.

Phase encoding the modeling experiments

Phase encoding is a well-established technique for decreasing the cost of seismic imaging by linearly combining the shot records, while maintaining the image quality (Schultz and Claerbout, 1978; Whitmore, 1995; Romero et al., 2000; Sun et al., 2002; Liu et al., 2006; Duquet and Lailly, 2006). Wavefields are usually phase-encoded in the data space simply because conventional wavefields are initiated and recorded at the boundaries of the reflection seismic problem. Therefore, the phase functions are parametrized according to the source index or source coordinates, which are data space parameters.

In a similar way, PERM wavefields initiated on the reflectors can also be phase-encoded. In this case, the phase functions are parametrized according to the model space coordinates and selected reflector, which are model space parameters. The parametrization of these phase functions characterizes the image-space phase encoding. The resulting wavefields are the image-space phase-encoded wavefields (ISPEWs). We will see that randomly phase-encoding the modeling experiments enables us to have more than one reflector in the initial conditions and to use a spatial sampling period smaller than the decorrelation distance. This is not possible when using the time-windowed imaging condition strategy.

To describe how ISPEWs are generated, let us slightly change the previous formulation of PERM to include the simultaneous modeling of more than one reflector. Horizontal reflectors are used for simplicity. For all the frequencies, using different random realizations \mathbf{q} of the initial conditions \tilde{I} for modeling ISPEWs can be described by

$$\tilde{D}_I(\boldsymbol{\xi}, \mathbf{q}, \omega) = \sum_{\mathbf{x}} \sum_{\mathbf{h}} G_0(\boldsymbol{\xi}, \mathbf{x} - \mathbf{h}, \omega) \tilde{I}(\hat{\mathbf{x}}, \mathbf{h}, \mathbf{q}, \omega), \quad (41)$$

and

$$\tilde{U}_I(\boldsymbol{\xi}, \mathbf{q}, \omega) = \sum_{\mathbf{x}} \sum_{\mathbf{h}} G_0(\boldsymbol{\xi}, \mathbf{x} + \mathbf{h}, \omega) \tilde{I}(\hat{\mathbf{x}}, \mathbf{h}, \mathbf{q}, \omega). \quad (42)$$

The subscript of the Green's function G denotes propagation with a background velocity $s_0(\mathbf{x})$. The initial conditions \tilde{I} are computed as

$$\tilde{I}(\hat{\mathbf{x}}, \mathbf{h}, \mathbf{q}, \omega) = \sum_m \sum_j \delta(\hat{\mathbf{x}} - m\Delta\mathbf{x}) \beta(\hat{\mathbf{x}}, j, \mathbf{q}, \omega) W_j(\hat{\mathbf{x}}, \mathbf{h}) I(\hat{\mathbf{x}}, \mathbf{h}), \quad (43)$$

where W_j selects the reflector j by identifying and windowing it in the pre-stack image I , and $\beta(\hat{\mathbf{x}}, j, \mathbf{q}, \omega)$ is a pseudo-random phase-encoding function defined as

$$\beta(\hat{\mathbf{x}}, j, \mathbf{q}, \omega) = e^{i\epsilon(\hat{\mathbf{x}}, j, \mathbf{q}, \omega)}, \quad (44)$$

with $\epsilon(\hat{\mathbf{x}}, j, \mathbf{q}, \omega)$ usually being a uniformly distributed pseudo-random sequence with zero mean. Guerra and Biondi (2008a) also use Gold codes (Gold, 1967), sequences widely used in third- and fourth-generation cellphones, to phase-encode the modeling. The pseudo-random phase-encoding function causes the frequency components of the initial conditions to be randomly injected into the modeling. Source and receiver wavefields initiated at the same SODCIG and from the same reflector are equally encoded, whereas source and receiver wavefields initiated at different SODCIGs and from the different reflectors have different codes assigned to them.

The recursive downward propagation with a different velocity $s_1(\mathbf{x})$ is performed according to

$$\tilde{D}_I(\mathbf{x}, \omega, \mathbf{q}) = \sum_{\boldsymbol{\xi}} G_1^*(\boldsymbol{\xi}, \mathbf{x}, \omega) \tilde{D}_I(\boldsymbol{\xi}, \omega, \mathbf{q}), \quad (45)$$

and

$$\tilde{U}_I(\mathbf{x}, \omega, \mathbf{q}) = \sum_{\boldsymbol{\xi}} G_1^*(\boldsymbol{\xi}, \mathbf{x}, \omega) \tilde{U}_I(\boldsymbol{\xi}, \omega, \mathbf{q}). \quad (46)$$

The lateral shifts of the wavefields for the multi-offset imaging condition are represented by

$$\begin{aligned} \widetilde{D}_I(\mathbf{x} - \mathbf{h}, \omega, \mathbf{q}) &= \sum_{\xi} \sum_{\mathbf{x}'} \sum_{\mathbf{h}'} \sum_m \sum_j G_1^*(\xi, \mathbf{x} - \mathbf{h}, \omega) G_0(\xi, \mathbf{x}' - \mathbf{h}', \omega) \\ &\times \delta(\widehat{\mathbf{x}} - m\Delta\mathbf{x}) \beta(\widehat{\mathbf{x}}, j, \mathbf{q}, \omega) W_j(\widehat{\mathbf{x}}, \mathbf{h}') I(\widehat{\mathbf{x}}, \mathbf{h}'), \end{aligned} \quad (47)$$

and

$$\begin{aligned} \widetilde{U}_I(\mathbf{x} + \mathbf{h}, \omega, \mathbf{q}) &= \sum_{\xi} \sum_{\mathbf{x}'} \sum_{\mathbf{h}'} \sum_m \sum_j G_1^*(\xi, \mathbf{x} + \mathbf{h}, \omega) G_0(\xi, \mathbf{x}' + \mathbf{h}', \omega) \\ &\times \delta(\widehat{\mathbf{x}} - m\Delta\mathbf{x}) \beta(\widehat{\mathbf{x}}, j, \mathbf{q}, \omega) W_j(\widehat{\mathbf{x}}, \mathbf{h}') I(\widehat{\mathbf{x}}, \mathbf{h}'), \end{aligned} \quad (48)$$

Applying the cross-correlation imaging condition to the wavefields of equations 47 and 48 and summing over frequency and over realizations gives

$$\begin{aligned} \widetilde{I}_I(\mathbf{x}, \mathbf{h}) &= \sum_{\omega} \sum_{\xi'} \sum_{\mathbf{x}'} \sum_{\mathbf{h}'} \sum_{\xi''} \sum_{\mathbf{x}''} \sum_{\mathbf{h}''} \sum_{\mathbf{q}} \sum_m \sum_n \sum_j \sum_l \\ &\times G_0^*(\xi', \mathbf{x}' - \mathbf{h}', \omega) G_1(\xi', \mathbf{x} - \mathbf{h}, \omega) G_1^*(\xi'', \mathbf{x} + \mathbf{h}, \omega) G_0(\xi'', \mathbf{x}'' + \mathbf{h}'', \omega) \\ &\times \delta(\widehat{\mathbf{x}} - m\Delta\mathbf{x}) \delta(\widehat{\mathbf{x}} - n\Delta\mathbf{x}) \beta(\widehat{\mathbf{x}}, j, \mathbf{q}, \omega) \beta(\widehat{\mathbf{x}}, l, \mathbf{q}, \omega) \\ &\times W_j(\widehat{\mathbf{x}}, \mathbf{h}') W_j(\widehat{\mathbf{x}}, \mathbf{h}'') I(\widehat{\mathbf{x}}, \mathbf{h}') I(\widehat{\mathbf{x}}, \mathbf{h}''), \end{aligned} \quad (49)$$

which can be recast as

$$\begin{aligned} \widetilde{I}_I(\mathbf{x}, \mathbf{h}) &= I_{\Delta\mathbf{x}, j}(\mathbf{x}, \mathbf{h}) \\ &+ \sum_{\omega} \sum_{\xi'} \sum_{\mathbf{x}'} \sum_{\mathbf{h}'} \sum_{\xi''} \sum_{\mathbf{x}''} \sum_{\mathbf{h}''} \sum_{\mathbf{q}} \sum_{m \neq n} \sum_{j \neq l} \\ &\times G_0^*(\xi', \mathbf{x}' - \mathbf{h}', \omega) G_1(\xi', \mathbf{x} - \mathbf{h}, \omega) G_1^*(\xi'', \mathbf{x} + \mathbf{h}, \omega) G_0(\xi'', \mathbf{x}'' + \mathbf{h}'', \omega) \\ &\times \delta(\widehat{\mathbf{x}} - m\Delta\mathbf{x}) \delta(\widehat{\mathbf{x}} - n\Delta\mathbf{x}) \beta(\widehat{\mathbf{x}}, j, \mathbf{q}, \omega) \beta(\widehat{\mathbf{x}}, l, \mathbf{q}, \omega) \\ &\times W_j(\widehat{\mathbf{x}}, \mathbf{h}') W_l(\widehat{\mathbf{x}}, \mathbf{h}'') I(\widehat{\mathbf{x}}, \mathbf{h}') I(\widehat{\mathbf{x}}, \mathbf{h}''). \end{aligned} \quad (50)$$

The first term in the right-hand side of equation 50 is the desired image we would obtain by modeling and migrating PERM wavefields initiated at isolated reflectors of isolated SODCIGs and is the result of the cross-correlation of encoded wavefields with $m = n$ and $j = l$. The second term represents the attenuated crosstalk, which includes the attenuated reflector crosstalk and the attenuated crosstalk from unrelated SODCIGs. Crosstalk attenuation is achieved by the cross-correlation of quasi-orthogonal sequences, whose values are small if compared with the zero lag of the auto-correlation. Ideally, the attenuated crosstalk is unstructured and occurs as speckled noise throughout the image.

Theoretically, according to the law of large numbers, if the number of random realizations is sufficiently large, the crosstalk term is negligible. When summing migration results of different random realizations, reflectors constructively interfere, whereas crosstalk destructively interferes. In practice, a satisfactory crosstalk attenuation is achieved using a small number of realizations.

I use the Marmousi data to illustrate the generation and migration of ISPEWs. The rotated SODCIGs of Figure 35 are phase-encoded to generate the initial conditions. We phase-encode the SODCIGs as well as the reflectors. The sampling period is 264 m, which roughly corresponds to 1/3 of the decorrelation distance. We compute four random realizations, corresponding to 44 pairs of ISPEWs. Two pairs of ISPEWs from different random realizations initiated at the same SODCIGs are shown in Figure 38.

The areal-shot migration of ISPEWs is shown in Figure 39. At the top, we see the result of migrating 44 wavefields from the four random realizations. At the bottom, we see the result of migrating 11 wavefields from one single random realization. Although the two images have a comparable quality, more realizations give a cleaner image.

To analyze the quality of the kinematic information, we compute residual-moveout panels from images computed with the original data (Figure 40a), with PERM wavefields and the time-windowed imaging condition (Figure 40b), with all four random realizations (Figure 40c), and with a single realization (Figure 40d). Notice that in the ADCIGs corresponding to images computed with PERM wavefields and ISPEWs, less events are present since we selected some reflectors to model these wavefields. The corresponding reflectors in the original shot-profile image are highlighted by the green boxes in Figure 40a.

The residual moveout information in the four panels is very similar. However, some crosstalk not entirely rejected by the time-windowed imaging condition causes the residual-moveout information lose resolution in Figure 40b when compared to Figures 40c-d.

The cost for obtaining the images in Figure 40 widely varies. For instance, migrating one random realization of ISPEWs is approximately 30 times faster than migrating all the 360 original shots. Using the same wavefields, computing the gradient of the objective function of migration-velocity analysis by wavefield-extrapolation can be 60 times faster. This

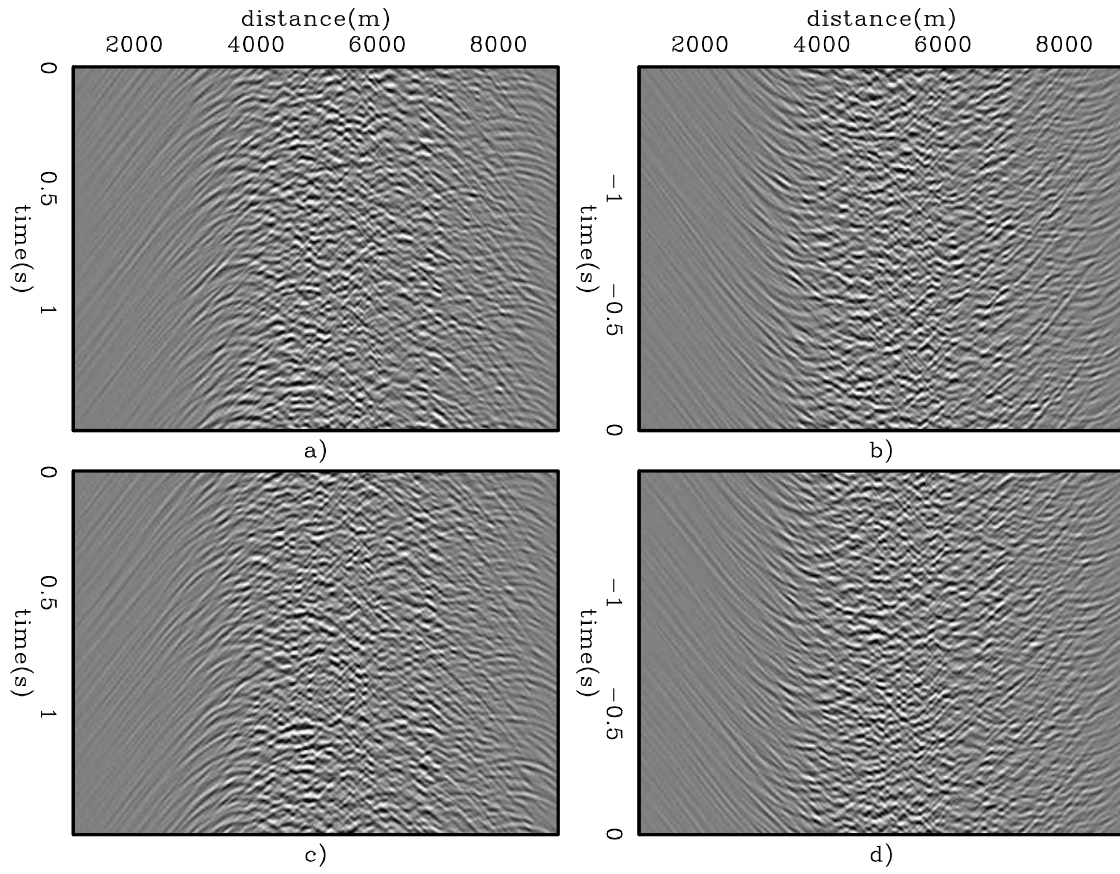


Figure 38: ISPEWs from different random realizations initiated at the same SODCIGs for the Marmousi example: a,c) Receiver wavefields. b,d) Source wavefields.

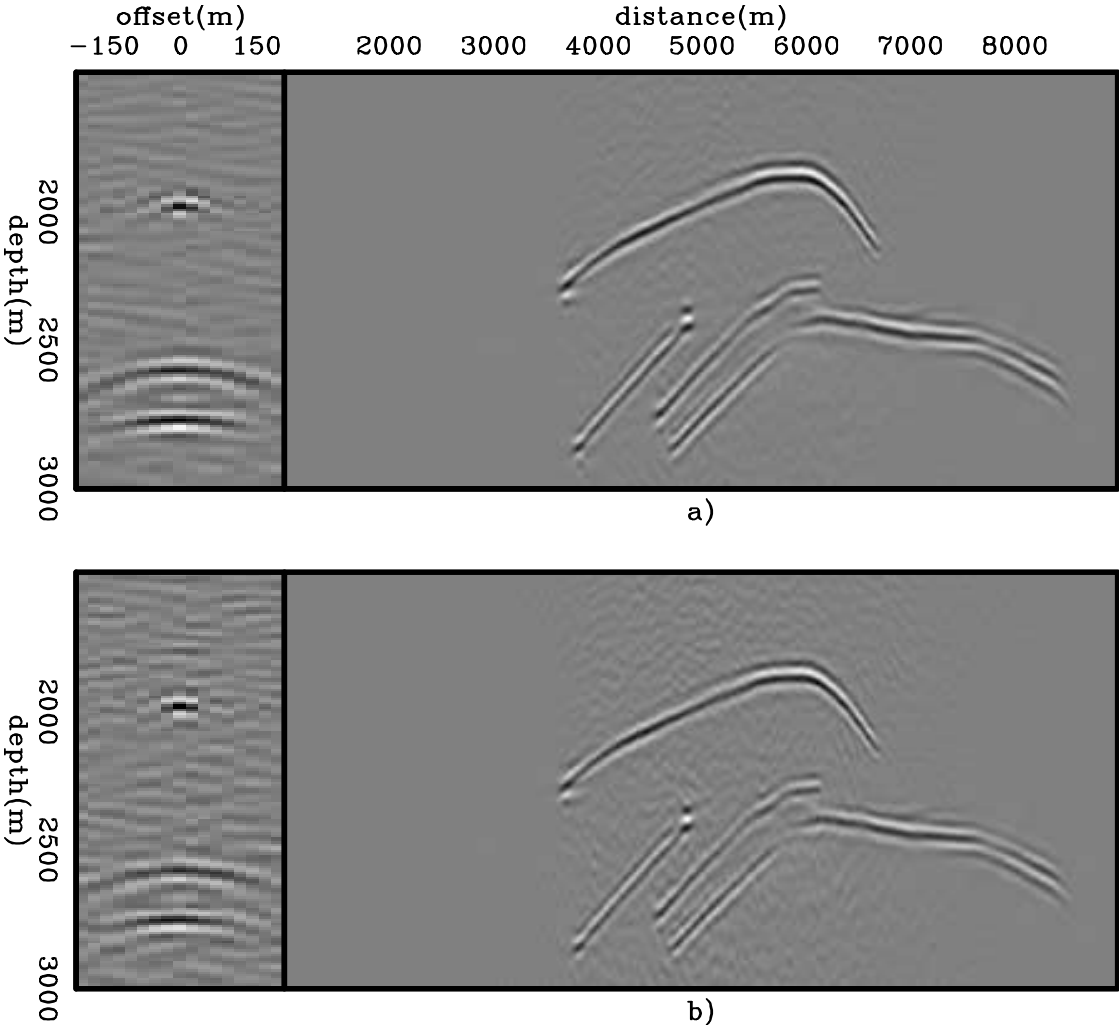


Figure 39: Pre-stack images computed with: a) Four random realizations of ISPEWs, and b) a single random realization.

difference in performance is even more dramatic when we consider that several iterations of migrations and gradient computations are performed during migration velocity optimization by wavefield-extrapolation. In Chapter , we will see the usefulness of ISPEWs in migration velocity optimization by wavefield-extrapolation. Chapter will use these wavefields to optimize the migration velocity for a 3D survey from the North Sea.

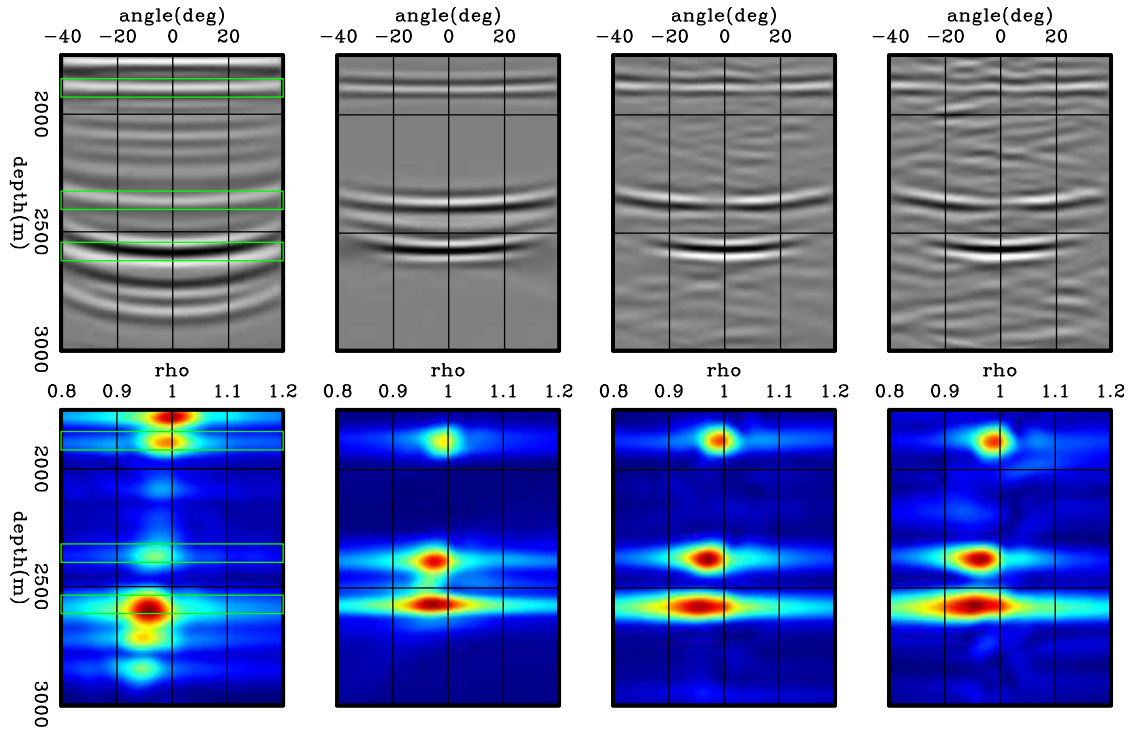


Figure 40: ADCIGs (top) and ρ -panels (bottom) corresponding to images computed by: a) Shot-profile migration of 360 shot gathers, b) areal-shot migration of 35 PERM wavefields using the time-windowed imaging condition, c) areal-shot migration of 44 ISPEWs corresponding to four random realizations, and d) areal-shot migration of 11 ISPEWs corresponding to a single random realization. The moveout information is basically the same.

CONCLUSIONS

In this chapter, PERM was used to model wavefields without observing the decorrelation distance between SODCIGs and using more than one reflector in the initial conditions. Doing this generates two types of crosstalk are generated: the reflector crosstalk and the crosstalk from unrelated SODCIGs. The reflector crosstalk is generated when performing the cross-correlation of the wavefields in time, whereas the crosstalk from unrelated SODCIGs is generated when performing the cross-correlation of the wavefields in space.

Since reflectors are imaged at time zero of wavefield propagation, an effective strategy to almost completely attenuate the reflector crosstalk is to cross-correlate wavefields only within a small time window around the zero time of wavefield propagation. To apply the time-windowed imaging condition, the frequency slices of the wavefields must be stored, which can be impractical for 3D applications. This strategy does not avoid the crosstalk from unrelated SODCIGs and, therefore, the decorrelation distance has to be used. In addition, in the presence of velocity inaccuracy, this strategy can corrupt the velocity information.

A more general method for attenuating crosstalk, independent of its origin, is to phase-encode the modeling experiments. Since the phase-encoding sequences are defined as a function of image parameters, namely spatial coordinates and reflector index, the wavefields are called image-space phase-encoded wavefields – ISPEWs. We exemplified the usefulness of ISPEWs with an example using the Marmousi data. The migrated images using these wavefields have kinematic information similar to that obtained with shot-profile migration for the selected reflectors, as shown in the residual-moveout panels, but at a much lower cost. In the next chapter, we will see that they also provide a similar gradient for the migration-velocity analysis by wavefield-extrapolation objective function.

MVA using image-space generalized sources In this chapter, I extend the theory of migration-velocity analysis (MVA) by wavefield extrapolation to the image-space generalized-sources domain. In this new domain, PERM wavefields and ISPEWs are the carriers of information for defining the migration velocity. These wavefields allow faster velocity updates than when conventional wavefields are used, as in shot-profile migration. The greater computational efficiency is possible due to the small data size of image-space generalized-source wavefields, in addition to their inherent capability for being used in a target-oriented manner. Moreover, with these wavefields, we can incorporate well-established strategies used in ray-based MVA, such as horizon-based tomography and possibly grid-based tomography, into MVA by wavefield extrapolation. This new feature gives more flexibility to MVA by wavefield extrapolation and can improve the convergence to an optimal velocity. I illustrate the use of image-space generalized wavefields in velocity optimization with 2D examples.

INTRODUCTION

Wave-equation tomography solves for earth models that explain observed seismograms under some norm. There are two main categories, depending on the domain in which the objective function is minimized.

In one category, known as waveform inversion, the objective function is minimized in the data space; data is modeled with the current model parameters and compared with the observed data. Extensive research has been being devoted to the application of waveform inversion to seismic exploration (Lailly, 1983; Tarantola, 1984, 1987; Mora, 1987; Woodward, 1992; Pratt et al., 1996). A comprehensive overview of waveform inversion can be found in Virieux and Operto (2009). However, in spite of its maturity as a technology, examples of waveform inversion using 3D-field data are still very limited (Vigh and Starr, 2008; Plessix, 2009). Waveform inversion is a highly nonlinear and ill-posed problem. Nonlinearity arises because the forward-modeling operator is a function of the searched model parameters. The ill-posedness is due to the many local minima of the objective function caused by incomplete acquisition, the band-limited nature of seismic data, the presence of noise, and the incomplete physics of the operators. Because of the non-linearity and ill-posedness, the initial model plays a crucial role in waveform inversion. Ideally, the initial model should adequately describe the lower-frequency components of the velocity model, whose higher-frequency components are to be determined in subsequent iterations.

Under the Born approximation, modeling of seismic data is linearly related to the reflectivity. However, Born modeling nonlinearly depends on the background velocity. These relations allow recasting the imaging of the subsurface into two separate, but related, problems: migration, which reconstructs the reflectivity given a background velocity, and velocity analysis, which determines the background velocity used in migration. These two problems are intimately related, and the degree of accuracy of the background velocity directly influences the quality of the migrated image. This relationship is explored in the second category of wave-equation tomography, here called image-space wave-equation tomography (ISWET). In ISWET, the objective function is minimized in the image space, and the residual is represented by an image perturbation. Similar to waveform inversion, ISWET is also nonlinear and ill-posed. The nonlinearity arises because the migration operator is a function of the background velocity.

Because low-spatial-frequency components (i.e., background velocity) and high-spatial-frequency components (i.e., reflectivity) of the velocity model can be solved separately, the ill-posedness of ISWET is less severe than that of waveform inversion, which inverts for remarkably detailed velocity models. An essential feature of ISWET is that its objective function is intimately related to the final product of seismic processing, which is an image of the subsurface. The optimal velocity is the one which gives the best image. Moreover, less expensive one-way extrapolators can be used, in contrast with the two-way extrapolator used in waveform inversion.

Two major variants of ISWET are wave-equation migration velocity analysis (WEMVA) (Sava and Biondi, 2004a,b) and differential semblance velocity analysis (DSVA) (Shen, 2004; Shen and Symes, 2008). Both variants seek the optimal velocity by driving an image perturbation to a minimum. However, they differ in the way the image perturbation is computed and, consequently, in the numerical optimization scheme. As Biondi (2008) points out, WEMVA is not easily automated. The image perturbation is computed by the linearized-residual prestack-depth migration (Sava, 2003), which uses a manually picked residual-moveout parameter. Since the perturbed image computed with the linearized-residual prestack-depth migration is consistent with the application of the forward wave-equation tomographic operator, WEMVA can be solved using a two-step approach. First, in a nonlinear iteration the background image is computed with the current velocity, a residual-moveout parameter is interpreted using enhanced versions of the background image, and the current perturbed image for the interpreted residual moveout is computed. Then, linear iterations using conjugate-gradients search for a perturbation in velocity that better explains the current perturbed image. The corresponding velocity solution is used to compute a new background image for the next nonlinear iteration.

In DSVA, the perturbed image is computed by applying the fully automated differential-semblance operator (DSO) (Symes and Carazzone, 1991) to SODCIGs or ADCIGs. When applied to SODCIGs, DSO minimizes the energy not focused at zero-offset. When applied to ADCIGs, DSO minimizes energy of the reflectors departing from flatness. Although DSO easily automates ISWET, it produces perturbed images that do not present the depth phase-shift introduced by the forward one-way ISWET operator. Moreover, the amplitude behavior of the perturbed image computed with DSO greatly differs from that of the perturbed image computed with the forward one-way ISWET operator. These differences prevent the use of linear conjugate-gradient methods, and therefore the objective function computed with DSO is typically minimized by nonlinear optimization methods, which require the explicit computation of the gradient of the objective function.

The use of horizons that represent major velocity changes and present good signal-to-noise ratio, a common practice in MVA by ray-based methods (Stork, 1992; Kosloff et al., 1996, 1997; Billette et al., 1997; Clapp, 2003), defines two main strategies for velocity update: grid-based tomography and horizon-based tomography. A residual moveout parameter defined along horizons is back-projected through the entire velocity model for both strategies or, alternatively, can be restricted to certain layers in the horizon-based strategy. Moreover, the horizon-based strategy enables us to apply different regularization parameters for different layers, which can improve convergence.

Like waveform inversion, ISWET is a computationally demanding process. This computational cost is commonly decreased by using generalized sources (Shen and Symes, 2008; Tang et al., 2008). Because of the smaller data size, image-space generalized wavefields can drastically decrease the cost of ISWET. Also, as discussed in the previous chapters, image-space generalized wavefields can be propagated in a limited portion of the model space. Under the framework of migration velocity analysis, this allows their use in a target-oriented manner, since the wavefield propagation can be restricted to a region where the velocity model is inaccurate. Moreover, as these wavefields are initiated at some representative horizons, a horizon-based strategy is naturally incorporated into ISWET. Hence, the velocity model can be easily computed by a layer-stripping scheme using wavefields initiated at an individual reflector or, more appropriately, at group of reflectors. Solving for a group of reflectors instead of using the layer-stripping scheme avoids the propagation to deeper layers of velocity errors from shallower layers.

In this chapter, I describe image-space wave-equation tomography. Then, I discuss the tomographic operator in the shot-profile domain. Next, I extend the tomographic operator to the areal-shot domain using image-space generalized wavefields. Finally, I illustrate the use of image-space phase-encoded wavefields in DVSA for optimizing the velocity of the Marmousi model.

IMAGE-SPACE WAVE-EQUATION TOMOGRAPHY

Image-space wave-equation tomography is a non-linear inverse problem. It searches for an optimal background velocity that minimizes an objective function defined in the image space. The objective function is represented by the residual ΔI , hereafter called perturbed image, which is derived from the background image I computed with the background velocity. The perturbed image represents the residual in the data-parameter space. The minimum of the perturbed image under some norm is unlikely to be global due to the non-linearity and ill-posedness of the problem. Therefore, constraints must be added to the model-parameter space by using a regularization operator.

The perturbed image can be computed by the DSO operator (Symes and Carazzone, 1991), in the DVSA variant of ISWET, and by linearized-residual prestack-depth migration (Sava, 2003), in the WEMVA variant of ISWET. According to Biondi (2008), a general form of the perturbed image can be expressed as

$$\Delta I = I - \mathbf{F}[I], \quad (51)$$

where \mathbf{F} is a focusing operator. Its application highlights the lack of focusing of the migrated image. Here and hereafter, we use bold capital letters for operators. Square brackets indicate the application of the operator to the argument.

In DVSA (Shen, 2004; Shen and Symes, 2008) the focusing operator assumes form

$$\mathbf{F} = \mathbf{1} - \mathbf{H}, \quad (52)$$

where $\mathbf{1}$ is the identity operator, and \mathbf{H} is the DSO operator either in the subsurface offset domain or in the angle domain. The subsurface-offset-domain DSO focuses the energy at zero offset, whereas the angle-domain DSO flattens the ADCIGs. Hereafter, for the sake of simplicity, instead of velocity and velocity perturbation, we use slowness and slowness perturbation in the formulation of ISWET, because of the direct relation between the slowness perturbation and the perturbed image.

In WEMVA (Sava and Biondi, 2004a,b), the focusing operator is the linearized-residual prestack-depth migration (Sava, 2003) defined as

$$\mathbf{F} = \mathbf{1} + \mathbf{K}(\Delta\rho), \quad (53)$$

where $\Delta\rho = 1 - \rho$, and ρ is the ratio between the background slowness s_0 and the true slowness s . The differential-residual-migration operator $\mathbf{K}(\Delta\rho)$, which phase-shifts the image for different reflection angles and geological dips, is defined as

$$\mathbf{K}(\Delta\rho) = \Delta\rho \left. \frac{\partial \mathbf{R}(\rho)}{\partial \rho} \right|_{\rho=1}, \quad (54)$$

where $\mathbf{R}(\rho)$ is the residual-prestack-depth migration. Application of the chain rule to equation 54 gives

$$\mathbf{K}(\Delta\rho) = \Delta\rho \left. \frac{d\mathbf{R}(\rho)}{dk_z} \frac{dk_z}{d\rho} \right|_{\rho=1}, \quad (55)$$

where k_z is the vertical wavenumber. As Sava (2004) shows, all the elements in the right-hand side of equation 55 can be easily computed. Notice that \mathbf{K} implicitly depends on Δs through $\Delta\rho$.

Under the ℓ_2 norm, the ISWET objective function is

$$J = \frac{1}{2} \|\Delta I\|_2 = \frac{1}{2} \|I - \mathbf{F}[I]\|_2. \quad (56)$$

Gradient-based optimization techniques, such as the quasi-Newton method and the conjugate-gradient method, can be used to minimize the objective function J . The gradient of J with respect to the slowness \mathbf{s} is

$$\nabla J = \left(\frac{\partial I}{\partial \mathbf{s}} - \frac{\partial \mathbf{F}[I]}{\partial \mathbf{s}} \right)' (I - \mathbf{F}[I]), \quad (57)$$

where $'$ denotes the adjoint.

In DVSA, the DSO operator \mathbf{H} is independent of the slowness, so we have

$$\frac{\partial \mathbf{F}(\mathbf{I})}{\partial \mathbf{s}} = (\mathbf{1} - \mathbf{H}) \frac{\partial \mathbf{I}}{\partial \mathbf{s}}. \quad (58)$$

Substituting equations 52 and 58 into equation 57 and evaluating the gradient at a background slowness yields

$$\nabla J_{\text{DSO}} = \left(\frac{\partial I}{\partial \mathbf{s}} \Big|_{s=s_0} \right)' \mathbf{H}' \mathbf{H} I_0, \quad (59)$$

where I_0 is the background image computed using the background slowness s_0 .

In WEMVA, the focusing operator depends on the slowness s . To simplify the gradient computation, we apply the focusing operator to the background image I_0 instead of I , and $\Delta\rho$ is interpreted on the background image, that is

$$\mathbf{F}[I_0] = I_0 + \mathbf{K}(\Delta\rho)I_0. \quad (60)$$

With these assumptions, the WEMVA gradient is

$$\nabla J_{\text{WEMVA}} = - \left(\frac{\partial I}{\partial \mathbf{s}} \Big|_{s=s_0} \right)' \mathbf{K}(\Delta\rho)[I_0]. \quad (61)$$

The linear mapping from the slowness perturbation Δs to the perturbed image ΔI is performed by the operator $\frac{\partial I}{\partial \mathbf{s}} \Big|_{s=s_0}$. It is derived by keeping the zero- and first-order terms of the Taylor series expansion of the image around the background slowness

$$\Delta I = \mathbf{T} \Delta s, \quad (62)$$

where $\Delta I = I - I_0$ and $\Delta s = s - s_0$ and, $\mathbf{T} = \frac{\partial I}{\partial \mathbf{s}} \Big|_{s=s_0}$ is the wave-equation tomographic operator. The tomographic operator has been evaluated either in the source and receiver domain (Sava, 2004) or in the shot-profile domain (Shen, 2004). Because it is natural to extend \mathbf{T} from the shot-profile domain to the generalized-sources domain, we review next the forward and adjoint tomographic operator in the shot-profile domain.

Shot-profile domain wave-equation tomographic operator

Our derivation of the wave-equation tomographic operator \mathbf{T} in the shot-profile domain follows Tang et al. (2008). We use the Marmousi model to illustrate the components of the shot-profile domain wave-equation tomographic operator. In the present case, the velocity perturbation occurs below the horizon in Figure 41, where the true and the background velocity models are shown. Data comprise 375 shots computed with the two-way wave equation.

In shot-profile migration, both source and receiver wavefields are downward continued with the following one-way wave equations (Claerbout, 1971):

$$\begin{cases} \left(\frac{\partial}{\partial z} + i\sqrt{\omega^2 s^2(\mathbf{x}) - |\mathbf{k}|^2} \right) D(\mathbf{x}, \mathbf{x}_s, \omega) = 0 \\ D(x, y, z = 0, \mathbf{x}_s, \omega) = f_s(\omega) \delta(\mathbf{x} - \mathbf{x}_s) \end{cases}, \quad (63)$$

and

$$\begin{cases} \left(\frac{\partial}{\partial z} - i\sqrt{\omega^2 s^2(\mathbf{x}) - |\mathbf{k}|^2} \right) U(\mathbf{x}, \mathbf{x}_s, \omega) = 0 \\ U(x, y, z = 0, \mathbf{x}_s, \omega) = Q(x, y, z = 0, \mathbf{x}_s, \omega) \end{cases}, \quad (64)$$

where $D(\mathbf{x}, \mathbf{x}_s, \omega)$ is the source wavefield for a single frequency ω at image point $\mathbf{x} = (x, y, z)$, with the source located at $\mathbf{x}_s = (x_s, y_s, 0)$; $U(\mathbf{x}, \mathbf{x}_s, \omega)$ is the receiver wavefield for a single frequency ω at image point \mathbf{x} for the source located at \mathbf{x}_s ; $\mathbf{k} = (k_x, k_y)$ is the spatial wavenumber vector; $f_s(\omega)$ is the frequency-dependent source signature; $\delta(\mathbf{x} - \mathbf{x}_s)$ defines the point-source function at \mathbf{x}_s , which serves as the boundary condition of equation 63; and $Q(x, y, z = 0, \mathbf{x}_s, \omega)$ is the

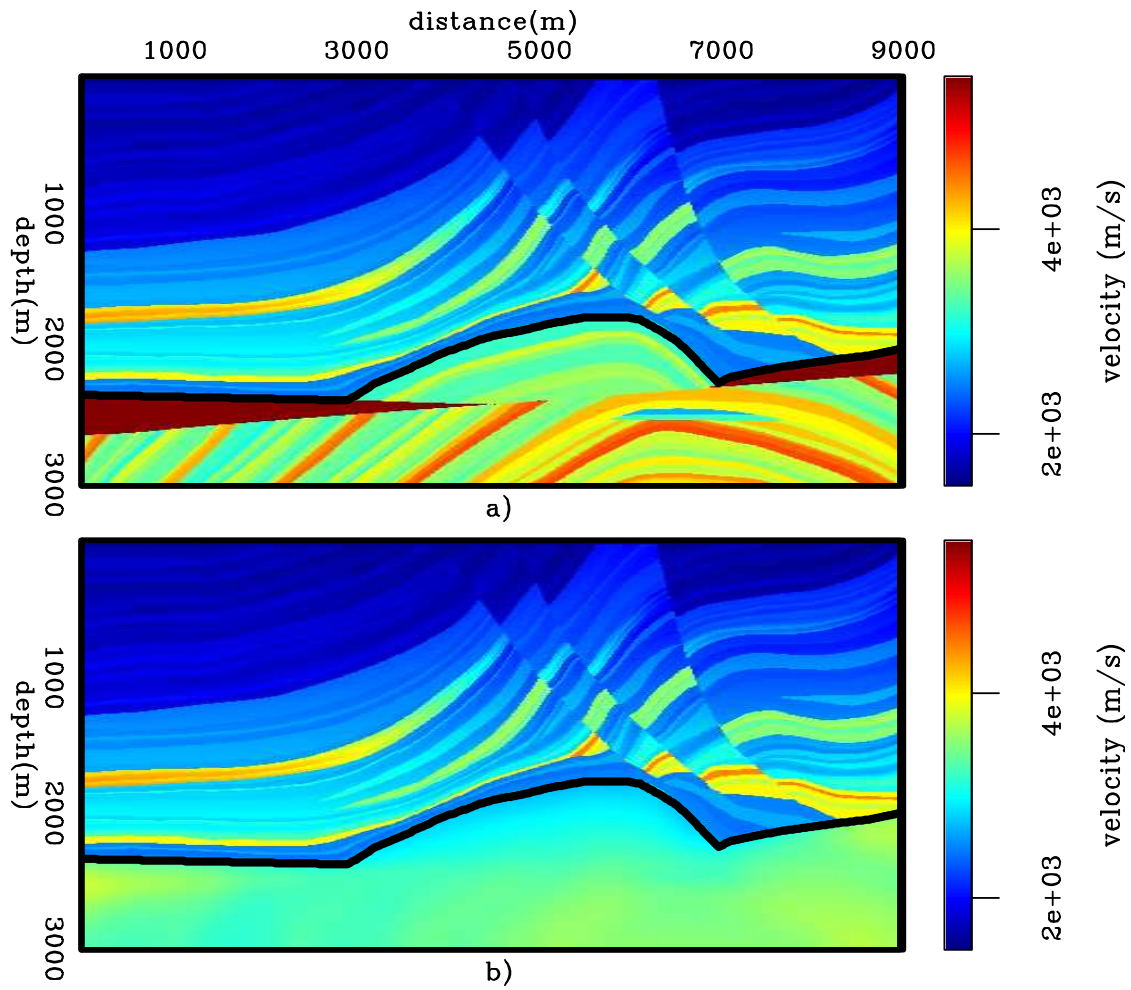


Figure 41: Marmousi velocity models: a) True velocity model. b) Background-velocity model computed by smoothing and scaling down the true model below the horizon indicated by the black line.

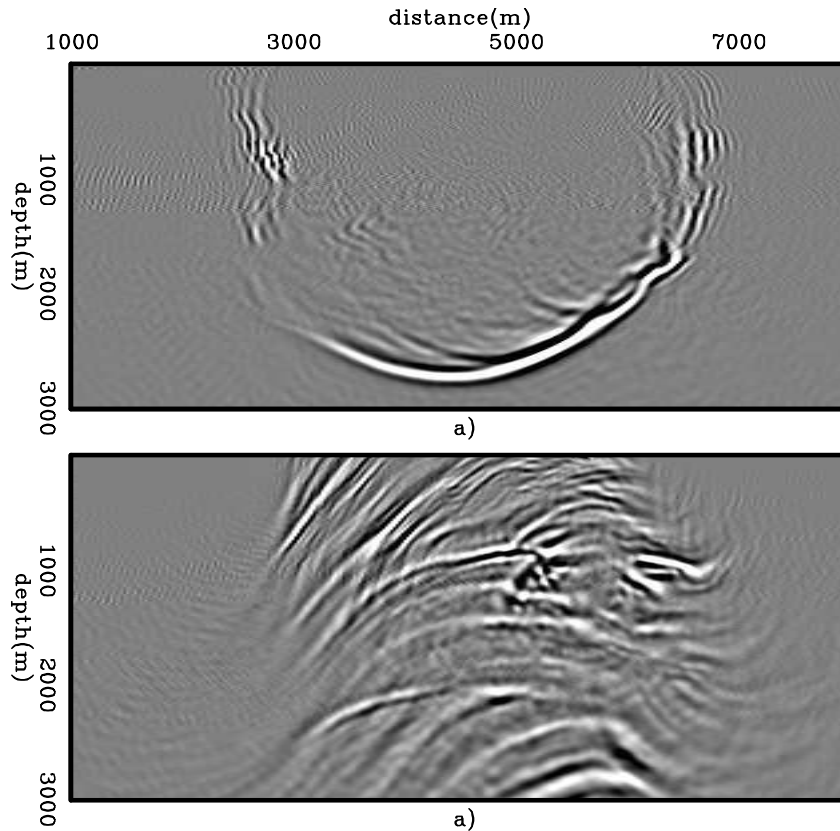


Figure 42: Snapshots of background: a) source, and b) receiver wavefields.

recorded shot gather for the shot located at \mathbf{x}_s , which serves as the boundary condition of equation 64. Snapshots of both source and receiver background wavefields for a shot position around 5000 m are shown in Figure 42.

The cross-correlation imaging condition produces the image $I(\mathbf{x}, \mathbf{h})$:

$$I(\mathbf{x}, \mathbf{h}) = \sum_{\mathbf{x}_s} \sum_{\omega} D^*(\mathbf{x} - \mathbf{h}, \mathbf{x}_s, \omega) U(\mathbf{x} + \mathbf{h}, \mathbf{x}_s, \omega). \quad (65)$$

The background image at zero-subsurface offset and some SODCIGs positioned at their approximate location are shown in Figure 43. Notice the curvature of the reflectors at the region of inaccurate velocity.

The perturbed image shown in Figure 44 is derived by a simple application of the product rule to equation 65, which gives

$$\begin{aligned} \Delta I(\mathbf{x}, \mathbf{h}) = & \sum_{\mathbf{x}_s} \sum_{\omega} \Delta D^*(\mathbf{x} - \mathbf{h}, \mathbf{x}_s, \omega) U_0(\mathbf{x} + \mathbf{h}, \mathbf{x}_s, \omega) + \\ & D_0^*(\mathbf{x} - \mathbf{h}, \mathbf{x}_s, \omega) \Delta U(\mathbf{x} + \mathbf{h}, \mathbf{x}_s, \omega), \end{aligned} \quad (66)$$

where $D_0(\mathbf{x} - \mathbf{h}, \mathbf{x}_s, \omega)$ and $U_0(\mathbf{x} + \mathbf{h}, \mathbf{x}_s, \omega)$ are the background source and receiver wavefields computed with the background slowness, and $\Delta D(\mathbf{x} - \mathbf{h}, \mathbf{x}_s, \omega)$ and $\Delta U(\mathbf{x} + \mathbf{h}, \mathbf{x}_s, \omega)$ are the perturbed source wavefield and perturbed receiver wavefield, respectively. The perturbed source and receiver wavefields are the response to a slowness perturbation. These wavefields satisfy the following one-way wave equations, linearized with respect to the slowness:

$$\begin{cases} \left(\frac{\partial}{\partial z} + i\sqrt{\omega^2 s_0^2(\mathbf{x}) - |\mathbf{k}|^2} \right) \Delta D(\mathbf{x}, \mathbf{x}_s, \omega) = D_{SC}(\mathbf{x}, \mathbf{x}_s, \omega) \\ \Delta D(x, y, z = 0, \mathbf{x}_s, \omega) = 0 \end{cases}, \quad (67)$$

and

$$\begin{cases} \left(\frac{\partial}{\partial z} - i\sqrt{\omega^2 s_0^2(\mathbf{x}) - |\mathbf{k}|^2} \right) \Delta U(\mathbf{x}, \mathbf{x}_s, \omega) = U_{SC}(\mathbf{x}, \mathbf{x}_s, \omega) \\ \Delta U(x, y, z = 0, \mathbf{x}_s, \omega) = 0 \end{cases}. \quad (68)$$

Snapshots of the perturbed source and receiver wavefields are shown in Figure 45. Notice that the perturbed wavefields occur only in the region where velocity perturbation is different from zero.

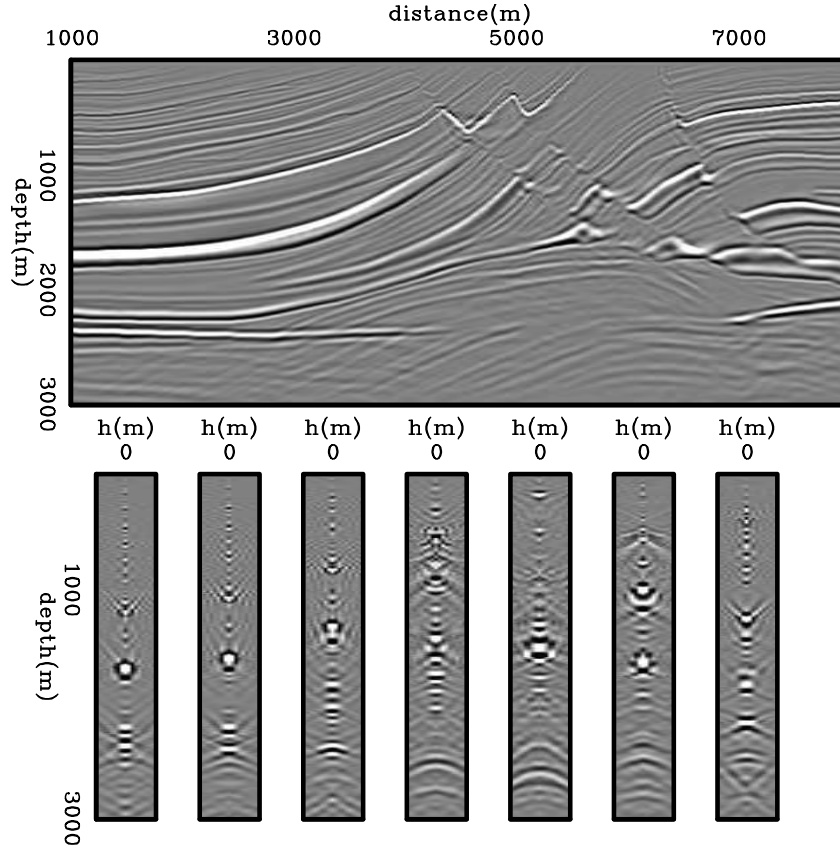


Figure 43: Background image and SODCIGs computed with the background wavefields of Figure 42.

The wavefields in the right-hand side of equations 67 and 68 are the scattered source and receiver wavefields, respectively, which result from the interaction of the background wavefields with a slowness perturbation according to

$$D_{SC}(\mathbf{x}, \mathbf{x}_s, \omega) = \frac{i\omega\Delta s(\mathbf{x})}{\sqrt{1 - \frac{|\mathbf{k}|^2}{\omega^2 s_0^2(\mathbf{x})}}} D_0(\mathbf{x}, \mathbf{x}_s, \omega) \quad (69)$$

and

$$U_{SC}(\mathbf{x}, \mathbf{x}_s, \omega) = \frac{-i\omega\Delta s(\mathbf{x})}{\sqrt{1 - \frac{|\mathbf{k}|^2}{\omega^2 s_0^2(\mathbf{x})}}} U_0(\mathbf{x}, \mathbf{x}_s, \omega). \quad (70)$$

These wavefields are injected at every depth level during the recursive propagation of the perturbed wavefields. The perturbed source and receiver wavefields are used along with the precomputed background source and receiver wavefields in equation 66 to generate the perturbed image. The background source and receiver wavefields are obtained by recursively solving equations 63 and 64 using the background slowness.

To evaluate the adjoint tomographic operator \mathbf{T}' , we first apply the adjoint imaging condition to compute the perturbed source and receiver wavefields, which are represented by the convolutions

$$\begin{aligned} \Delta D(\mathbf{x}, \mathbf{x}_s, \omega) &= \sum_{\mathbf{h}} \Delta I(\mathbf{x}, \mathbf{h}) U_0(\mathbf{x} + \mathbf{h}, \mathbf{x}_s, \omega) \\ \Delta U(\mathbf{x}, \mathbf{x}_s, \omega) &= \sum_{\mathbf{h}} \Delta I(\mathbf{x}, \mathbf{h}) D_0(\mathbf{x} - \mathbf{h}, \mathbf{x}_s, \omega). \end{aligned} \quad (71)$$

These perturbed wavefields are upward propagated using the adjoint counterparts of equations 67 and 68. At every depth level of the upward propagation, the perturbed source wavefield is cross-correlated with the scattered source wavefield, and the perturbed receiver wavefield is cross-correlated with the scattered receiver wavefield to generate the slowness perturbation according to

$$\Delta s(\mathbf{x}) = \sum_{\mathbf{x}_s} \sum_{\omega} D_{SC}^*(\mathbf{x}, \mathbf{x}_s, \omega) \Delta D(\mathbf{x}, \mathbf{x}_s, \omega) + U_{SC}^*(\mathbf{x}, \mathbf{x}_s, \omega) \Delta U(\mathbf{x}, \mathbf{x}_s, \omega). \quad (72)$$

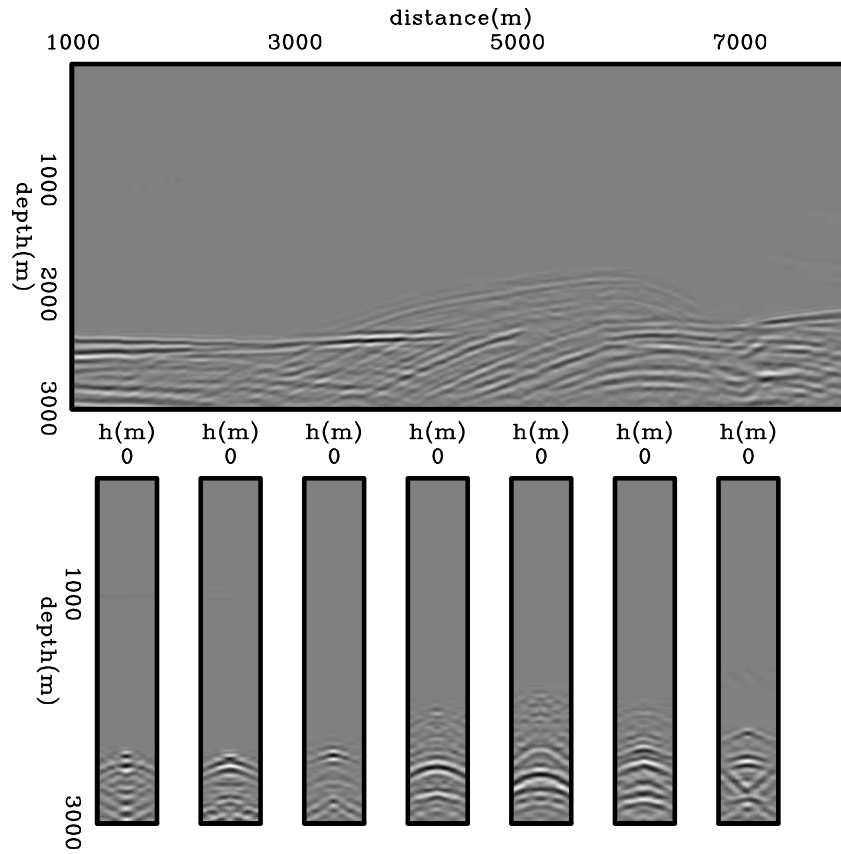


Figure 44: Perturbed image computed with equation 66.

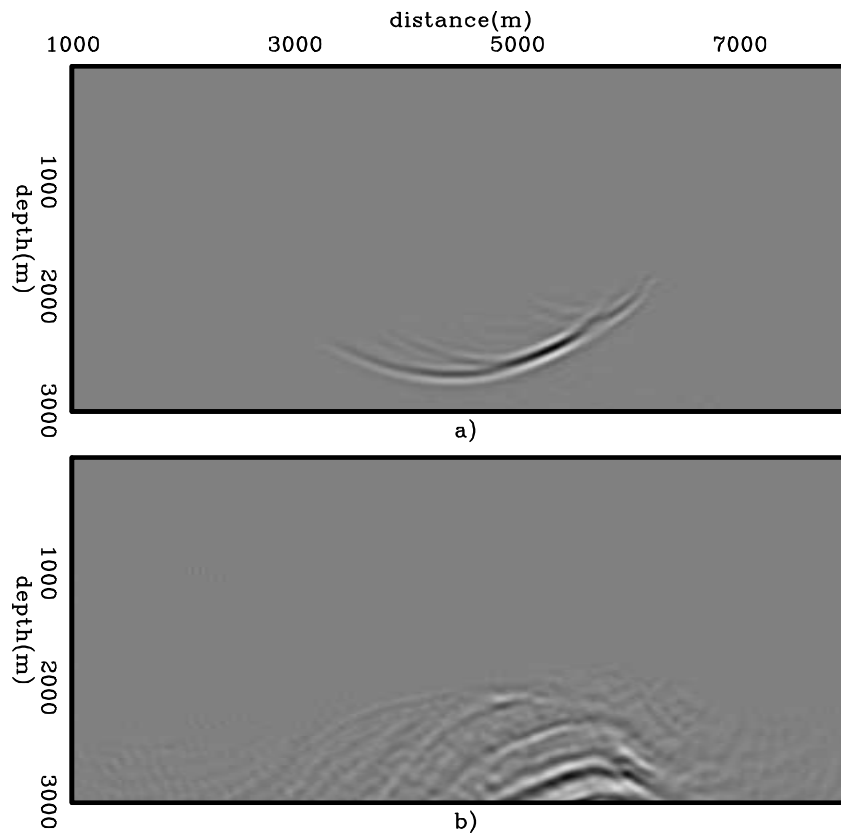


Figure 45: Snapshots of perturbed: a) source, and b) receiver wavefields.

The slowness perturbation for the Marmousi example is shown in Figure 46. Notice that even though the slowness perturbation is restricted to the region below the black horizon, the image perturbation is also back-projected to the region of correct velocity in the model space. These back-projected residuals are gradually decreased during an iterative procedure to optimize the migration-velocity model.

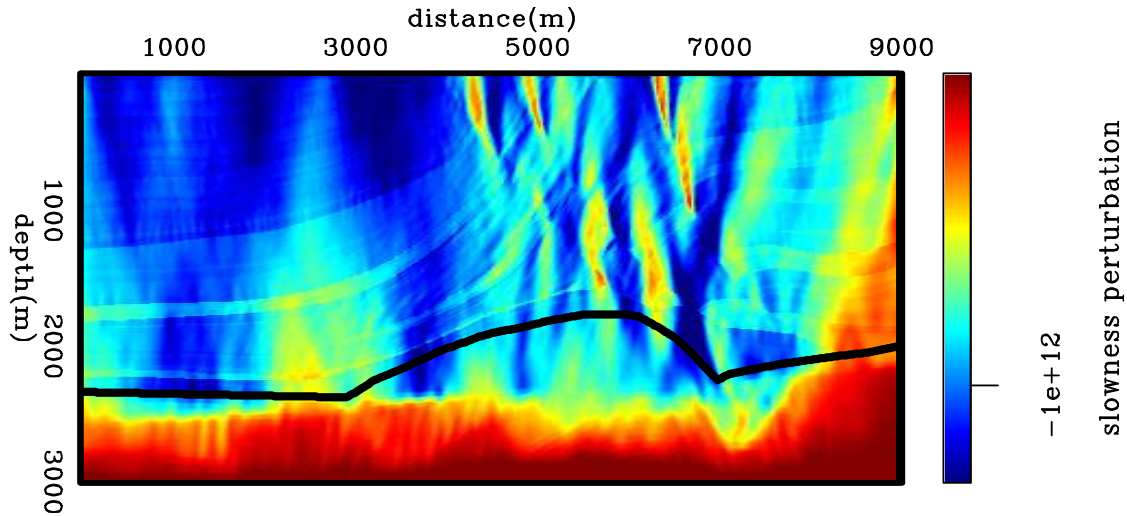


Figure 46: Slowness perturbation from back-projected image perturbations.

Image-space generalized-sources domain wave-equation tomographic operator

We will extend the wave-equation tomographic operator from the shot-profile domain to the image-space generalized-sources domain. Although we will focus on the use of image-space generalized wavefields described in Chapters ?? and , with some minor modifications the derivation presented here is also valid when using data-space generalized wavefields. We use \tilde{D} for the image-space generalized source wavefield and \tilde{U} for the image-space generalized receiver wavefield, irrespective of whether they are PERM wavefields or ISPEWs. For the image computed with these wavefields, we use \tilde{I} .

We also use the Marmousi model to illustrate the components of the image-space generalized-sources domain wave-equation tomographic operator. The image-space generalized source and receiver gathers were computed using 12 selected reflectors from the background image of Figure 42. These selected reflectors are submitted to the rotation of the subsurface offsets according to the apparent geological dip, as discussed in Chapter ?? (Figure 47). Here, we use ISPEWs initiated at a spatial-sampling period of 35 SODCIGs.

In the areal-shot migration of image-space generalized wavefields, both source and receiver wavefields are downward continued with the following one-way wave equations:

$$\begin{cases} \left(\frac{\partial}{\partial z} + i\sqrt{\omega^2 s^2(\mathbf{x}) - |\mathbf{k}|^2} \right) \tilde{D}(\mathbf{x}, \mathbf{p}, \omega) = 0 \\ \tilde{D}(x, y, z = z_{min}, \mathbf{p}, \omega) = \tilde{\tilde{D}}(x, y, z = z_{min}, \mathbf{p}, \omega) \end{cases}, \quad (73)$$

and

$$\begin{cases} \left(\frac{\partial}{\partial z} - i\sqrt{\omega^2 s^2(\mathbf{x}) - |\mathbf{k}|^2} \right) \tilde{U}(\mathbf{x}, \mathbf{p}, \omega) = 0 \\ \tilde{U}(x, y, z = z_{min}, \mathbf{p}, \omega) = \tilde{\tilde{U}}(x, y, z = z_{min}, \mathbf{p}, \omega) \end{cases}, \quad (74)$$

where $\tilde{D}(\mathbf{x}, \mathbf{p}, \omega)$ is the image-space generalized source wavefield for a single frequency ω at image point $\mathbf{x} = (x, y, z)$; \mathbf{p} is the index of the areal shot; $\tilde{U}(\mathbf{x}, \mathbf{p}, \omega)$ is the image-space generalized receiver wavefield for a single frequency ω at image point \mathbf{x} ; and $\tilde{\tilde{D}}(x, y, z = z_{min}, \mathbf{p}, \omega)$ and $\tilde{\tilde{U}}(x, y, z = z_{min}, \mathbf{p}, \omega)$ are the image-space generalized source and receiver gathers synthesized with the pre-stack exploding-reflector model, with or without phase encoding, and collected at $z = z_{min}$, which denotes the top of a target zone. These image-space generalized gathers serve as the boundary conditions of equations 73 and 74, respectively. Snapshots of image-space generalized background wavefields are shown in Figure 48.

The cross-correlation imaging condition produces the image $\tilde{I}(\mathbf{x}, \mathbf{h})$ (Figure 49):

$$\tilde{I}(\mathbf{x}, \mathbf{h}) = \sum_{\mathbf{p}} \sum_{\omega} \tilde{D}^*(\mathbf{x} - \mathbf{h}, \mathbf{p}, \omega) \tilde{U}(\mathbf{x} + \mathbf{h}, \mathbf{p}, \omega). \quad (75)$$

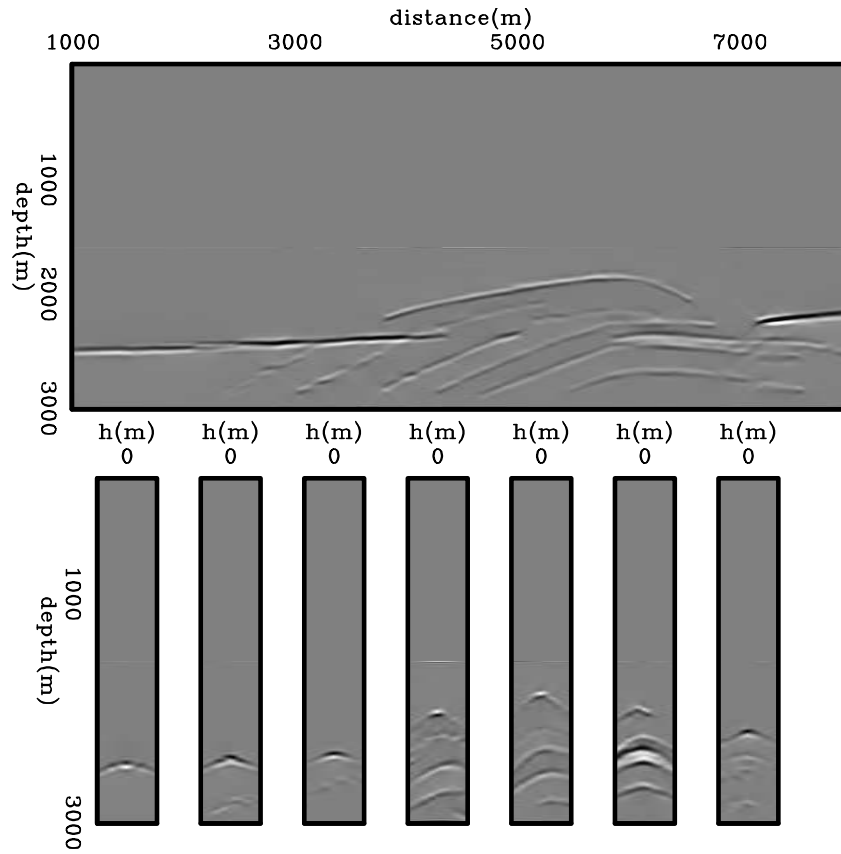


Figure 47: Selected reflectors used to model the image-space generalized source and receiver gathers.

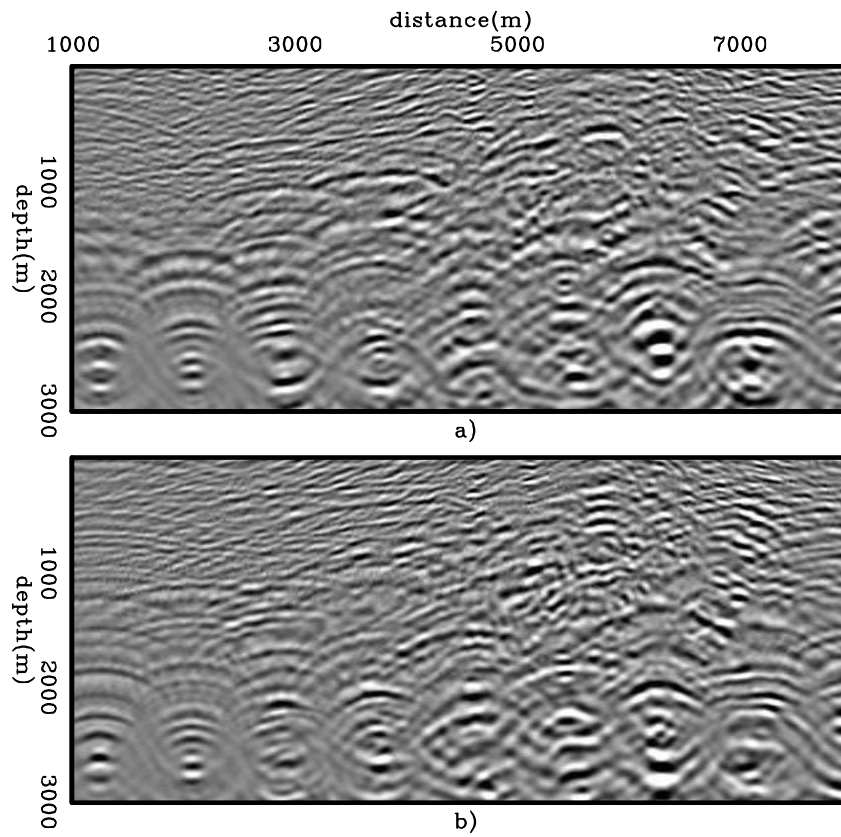


Figure 48: Snapshots of image-space generalized background wavefields: a) source, and b) receiver wavefields.

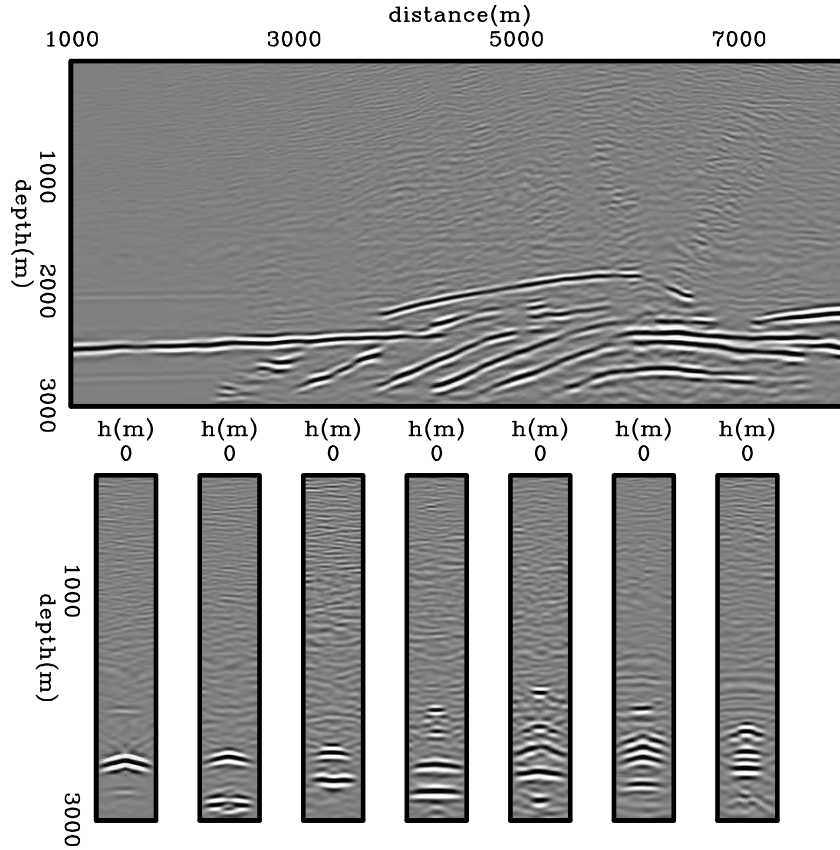


Figure 49: Background image computed with the image-space generalized background wavefields of Figure 48.

The perturbed image is derived by applying the product rule to equation 75, which gives

$$\begin{aligned} \Delta \tilde{I}(\mathbf{x}, \mathbf{h}) &= \sum_{\mathbf{p}} \sum_{\omega} \Delta \tilde{D}^*(\mathbf{x} - \mathbf{h}, \mathbf{p}, \omega) \tilde{U}_0(\mathbf{x} + \mathbf{h}, \mathbf{p}, \omega) + \\ &\quad \tilde{D}_0^*(\mathbf{x} - \mathbf{h}, \mathbf{p}, \omega) \Delta \tilde{U}(\mathbf{x} + \mathbf{h}, \mathbf{p}, \omega), \end{aligned} \quad (76)$$

where $\tilde{D}_0(\mathbf{x} - \mathbf{h}, \mathbf{p}, \omega)$ and $\tilde{U}_0(\mathbf{x} + \mathbf{h}, \mathbf{p}, \omega)$ are the image-space generalized background source and receiver wavefields computed with the background slowness; and $\Delta \tilde{D}(\mathbf{x} - \mathbf{h}, \mathbf{p}, \omega)$ and $\Delta \tilde{U}(\mathbf{x} + \mathbf{h}, \mathbf{p}, \omega)$ are the image-space generalized perturbed source wavefield and the image-space generalized perturbed receiver wavefield, respectively. These image-space generalized perturbed wavefields are the response to a slowness perturbation. The image-space generalized perturbed source and receiver wavefields satisfy the following one-way wave equations linearized with respect to the slowness:

$$\begin{cases} \left(\frac{\partial}{\partial z} + i\sqrt{\omega^2 s_0^2(\mathbf{x}) - |\mathbf{k}|^2} \right) \Delta \tilde{D}(\mathbf{x}, \mathbf{p}, \omega) = \tilde{D}_{SC}(\mathbf{x}, \mathbf{p}, \omega) \\ \Delta \tilde{D}(x, y, z = z_{min}, \mathbf{p}, \omega) = 0 \end{cases}, \quad (77)$$

and

$$\begin{cases} \left(\frac{\partial}{\partial z} + i\sqrt{\omega^2 s_0^2(\mathbf{x}) - |\mathbf{k}|^2} \right) \Delta \tilde{U}(\mathbf{x}, \mathbf{p}, \omega) = \tilde{U}_{SC}(\mathbf{x}, \mathbf{p}, \omega) \\ \Delta \tilde{U}(x, y, z = z_{min}, \mathbf{p}, \omega) = 0 \end{cases}. \quad (78)$$

Snapshots of the image-space generalized perturbed wavefields are shown in Figure 51. Since the boundary conditions at z_{min} are null, no scattering occurs at depth levels shallower than z_{min} . The wavefields in the right-hand side of equations 77 and 78 are the image-space generalized scattered source and receiver wavefields, respectively, which result from the interaction of the image-space generalized background wavefields with a slowness perturbation according to

$$\tilde{D}_{SC}(\mathbf{x}, \mathbf{p}, \omega) = \frac{i\omega \Delta s(\mathbf{x})}{\sqrt{1 - \frac{|\mathbf{k}|^2}{\omega^2 s_0^2(\mathbf{x})}}} \tilde{D}_0(\mathbf{x}, \mathbf{p}, \omega) \quad (79)$$

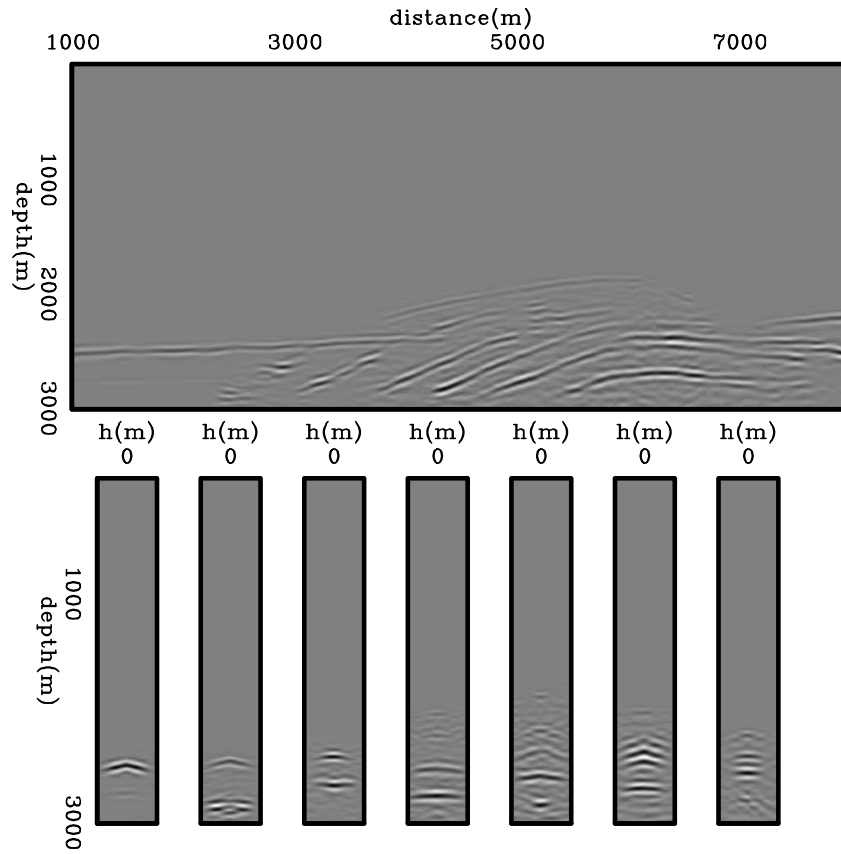


Figure 50: Perturbed image computed with equation 76.

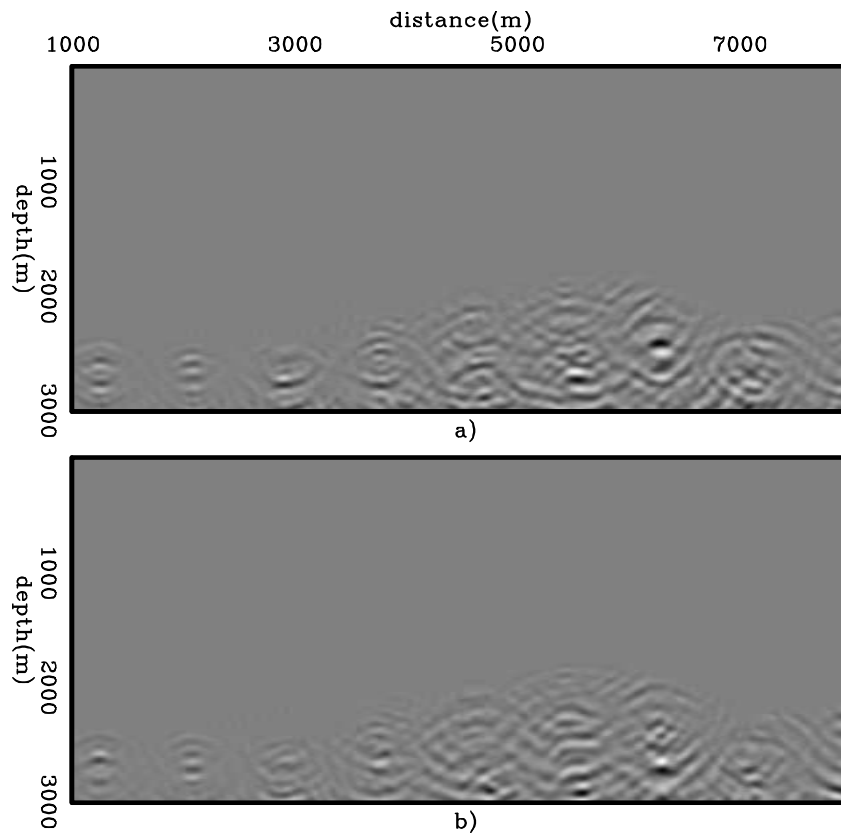


Figure 51: Snapshots of image-space generalized perturbed wavefields: a) source, and b) receiver.

and

$$\tilde{U}_{sc}(\mathbf{x}, \mathbf{p}, \omega) = \frac{-i\omega\Delta s(\mathbf{x})}{\sqrt{1 - \frac{|\mathbf{k}|^2}{\omega^2 s_0^2(\mathbf{x})}}} \tilde{U}_0(\mathbf{x}, \mathbf{p}, \omega). \quad (80)$$

These wavefields are injected at every depth level during the recursive propagation of the perturbed wavefields. The image-space generalized perturbed source and receiver wavefields are used along with the precomputed image-space generalized background source and receiver wavefields in equation 76 to generate the perturbed image. The image-space generalized background source and receiver wavefields are obtained by recursively solving equations 73 and 74 using the background slowness.

The adjoint-tomographic operator \mathbf{T}_{is}' is obtained by applying the adjoint-imaging condition to compute the image-space generalized perturbed source and receiver wavefields given by the following convolutions:

$$\begin{aligned} \Delta\tilde{D}(\mathbf{x}, \mathbf{p}, \omega) &= \sum_{\mathbf{h}} \Delta\tilde{I}(\mathbf{x}, \mathbf{h}) \tilde{U}_0(\mathbf{x} + \mathbf{h}, \mathbf{p}, \omega) \\ \Delta\tilde{U}(\mathbf{x}, \mathbf{p}, \omega) &= \sum_{\mathbf{h}} \Delta\tilde{I}(\mathbf{x}, \mathbf{h}) \tilde{D}_0(\mathbf{x} - \mathbf{h}, \mathbf{p}, \omega). \end{aligned} \quad (81)$$

The image-space generalized perturbed wavefields are upward propagated using the adjoint counterparts of equations 77 and 78. At every depth of their upward propagation, the image-space generalized perturbed source wavefield is cross-correlated with the image-space generalized scattered source wavefield, and the image-space generalized perturbed receiver wavefield is cross-correlated with the image-space generalized scattered receiver wavefield to generate the slowness perturbation according to

$$\begin{aligned} \Delta\tilde{s}(\mathbf{x}) &= \sum_{\mathbf{p}} \sum_{\omega} \tilde{D}_{sc}^*(\mathbf{x}, \mathbf{p}, \omega) \Delta\tilde{D}(\mathbf{x}, \mathbf{p}, \omega) + \\ &\quad \tilde{U}_{sc}^*(\mathbf{x}, \mathbf{p}, \omega) \Delta\tilde{U}(\mathbf{x}, \mathbf{p}, \omega). \end{aligned} \quad (82)$$

The slowness perturbation for the Marmousi example computed in the image-space generalized sources domain using ISPEWs is shown in Figure 52. Compare it with the slowness perturbation computed with in the shot-profile domain (Figure 46). The slowness perturbation computed with ISPEWs shows the correct polarity and a general structure similar to that of the slowness perturbation computed in the shot-profile domain. The main amplitude differences are in the left part of Figure 52, where only one reflector was selected to synthesize ISPEWs.

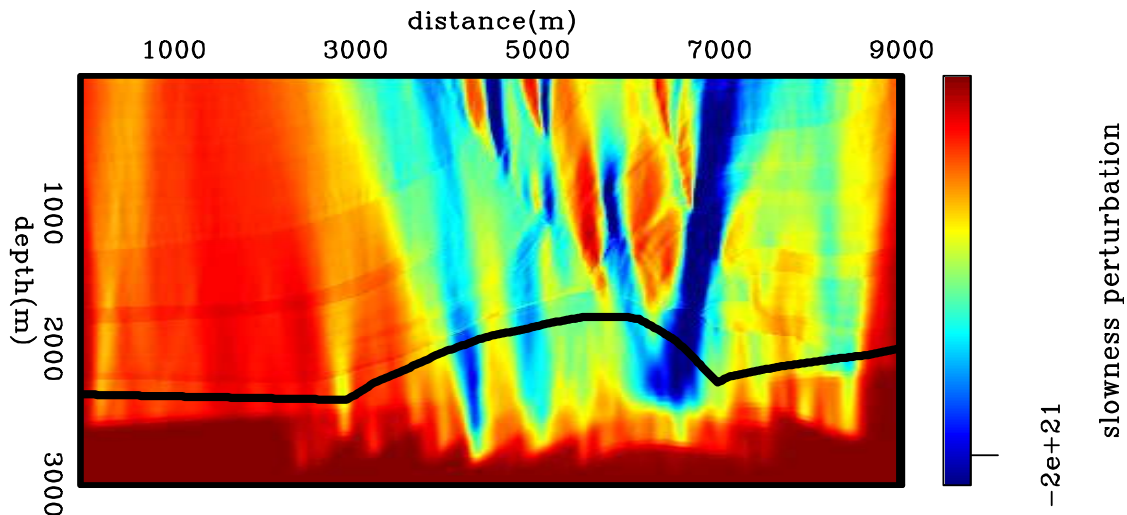


Figure 52: Slowness perturbation from back-projected image perturbations computed with 35 ISPEWs.

VELOCITY OPTIMIZATION USING IMAGE-SPACE GENERALIZED WAVEFIELDS

ISWET is a nonlinear optimization problem in which the optimal migration velocity is determined by driving the objective function (i.e, the perturbed image) to a minimum. The negative of the gradient of the objective function provides search

directions for iterative velocity updating. In DSVA, the DSO operator applied to the current background image computed with the image-space generalized wavefields yields the perturbed image, according to

$$\Delta\tilde{I}(\mathbf{x}, \mathbf{h}) = |\mathbf{h}| \tilde{I}(\mathbf{x}, \mathbf{h}), \quad (83)$$

where \mathbf{h} is the vector of subsurface offsets. The DSO operator penalizes the focusing of reflectors at zero-subsurface offset. Considering complete illumination and infinite frequency bandwidth, energy not focused at zero-subsurface offset indicates velocity errors. DSO easily automates ISWET. However, neither the phase nor the amplitudes of the DSO perturbed image are consistent with those of the perturbed image computed by the forward one-way ISWET operator. These differences prevent the use of linear conjugate-gradient methods, and therefore the objective function computed with DSO is typically minimized by nonlinear optimization methods, such as nonlinear-conjugate gradients, L-BFGS (Nocedal and Wright, 2000). We use a nonlinear-conjugate gradient solver, for which we need to provide the value of the objective function and its gradient for the current velocity model.

As discussed in Chapter ??, image-space generalized wavefields produce migrated images with the wavelet squared. Because of the squaring of the wavelet, images computed with these wavefields present amplitude variations stronger than those in the image computed with the original data. This effect is also present in the DSO perturbed image. When applying \mathbf{T}'_{IS} , the DSO perturbed image is convolved with the image-space generalized background wavefields to generate the image-space generalized perturbed wavefields. Subsequently, the gradient is obtained by cross-correlating the image-space generalized perturbed wavefields with the image-space generalized scattered wavefields. These two operations introduce another squaring of the wavelet. Therefore, the gradient of the objective function computed with the image-space generalized wavefields is a fourth-power version of that computed with the original wavefields. To minimize the effects of squaring the wavelet on the gradient of the objective function, we use a signaled-square-root version of the initial image as the initial conditions for synthesizing image-space generalized gathers.

In addition to the amplitude variations described above, there are also amplitude variations in the migrated image caused by uneven illumination. Considering that the gradient of the objective function is computed along the wave paths, the uneven illumination will be imprinted on the gradient. An eventual velocity update using this unbalanced amplitude gradient can originate a velocity model that violates the smoothness assumption implied by the Born approximation. Since these amplitude variations are not related to velocity inaccuracy, we should ideally attenuate them using some sort of illumination compensation scheme (Valenciano et al., 2009; Tang, 2009). Instead, to prevent these amplitude variations we apply a B-spline smoothing to the gradient, which consists of representing the gradient as B-spline basis functions, using the adjoint operator \mathbf{B}' , and transforming it back to the Cartesian space, using the forward operator \mathbf{B} . Other smoothing schemes could also be applied, such as smoothing along geological dips (Clapp, 2003) computed on the migrated image using the original shot-profiles.

As already described in Chapter , when using image-space generalized wavefields, a target-oriented strategy can be adopted if the velocity model is sufficiently accurate for shallower layers. In this case, the target region, where the image-space generalized wavefields are propagated, lies below the bottom of the accurate velocity region. A mask operator \mathbf{M} is applied to the gradient, zeroing out amplitudes in the accurate velocity region, preventing the velocity model from being updated.

Since the gradient is not properly scaled, we normalize it with the diagonal operator \mathbf{F} , which is the smallest value of the initial slowness. To improve and sometimes guarantee convergence, we would like to limit the velocity update from one iteration with respect to its previous values. In other words, we would like the new velocity to vary within a range defined by a percentage of the velocity from the previous iteration. This can be implemented by applying to the gradient either a nonlinear (since it depends on the velocity) diagonal operator, or a diagonal operator \mathbf{W} linearized around the initial velocity. Therefore, the final gradient ∇J_{IS} is

$$\nabla J_{IS} = \mathbf{W}\mathbf{F}\mathbf{M}\mathbf{B}\mathbf{B}' \mathbf{T}'|_{s=s_0} \mathbf{H}'\mathbf{H} \tilde{I}|_{s=s_0}, \quad (84)$$

We illustrate the use of image-space generalized wavefields in ISWET for of the Marmousi velocity model. The initial velocity model (Figure 41b) differs from the true velocity model only below the black horizon. To evaluate the influence of dispersed crosstalk on ISWET results, we use two different ISPEW datasets. One dataset is modeled with a spatial-sampling period of 35 SODCIGs, herein called 35-ISPEWs. For the other, the spatial-sampling is 11 SODCIGs, herein called 11-ISPEWs. This dataset is expected to generate more crosstalk than the 35-ISPEWs dataset. Both ISPEW datasets were collected at a depth of 1500 m. Therefore, the wavefield propagation in ISWET is performed between this depth and the maximum depth of 3000 m, characterizing a target-oriented strategy. We show some of the optimization results having 1500 m as the initial depth.

A nonlinear conjugate-gradient is used in the optimization. The maximum allowed velocity change between iterations is 10 %. The nodes of the B-spline smoothing of the gradient are separated by 480 m and 160 m in x and z, respectively. Two function evaluations are performed in each iteration, and if the objective function does not decrease, a 50%-smaller step length is used.

The initial and final background images for the 11-ISPEWs and 35-ISPEWs examples are shown in Figures 53 and 54, respectively. In both figures, at the top is the initial image, and at the bottom is the final image. Below the zero subsurface-offset section are shown subsurface-offset gathers. In both figures, the final image is more focused, and the pulled-up reflectors at $x = 6000$ m are better positioned.

The cross-plot of Figure 55 presents the evolution of the objective function, normalized by the highest value, for the two cases. Iteration stopped after 13 iterations in the 11-ISPEWs case and 9 iterations for the 35-ISPEWs case, because the variation of the objective function was less than the predefined value of 0.002%. Overall, both cases present similar convergence. However, the final value of the 11-ISPEWs objective function is slightly greater than that of the 35-ISPEWs case. This can be explained by the different amount of dispersed crosstalk in the images of Figures 53 and 54. The 11-ISPEWs case has more dispersed crosstalk than the 35-ISPEWs case, which contributes to the higher value of the objective function.

The final velocity models are shown in Figure 56. In both cases, velocity has increased by nearly a 12 %. Since the bottom of the velocity model is poorly constrained by reflectors, in this part of the model the velocity update is almost zero.

As previously mentioned, ISWET solves for the long-wavelength component of the velocity model, which is consistent with the Born approximation. The long-wavelength component of the velocity model is responsible for the kinematics of the wavefield propagation. To evaluate how accurate the results are, we smooth the slowness derived from the original velocity model of Figure 41a in a way similar to the gradient of the objective function. This smoothed version of the original velocity model is compared to the initial velocity model and the optimized velocity models within the box of Figure 57a. Histograms of the velocity ratio between the smoothed true velocity model and the initial velocity model, the smoothed true and the 11-ISPEWs optimized velocity model, and the smoothed true and the 35-ISPEWs optimized velocity model are shown in Figure 57b-d. The concentration around one in Figures 57c-d indicates that the long-wavelength components of the velocity model were appropriately recovered by ISWET.

The images computed with shot-profile migration using the optimized velocity models (Figure 58) show focused reflectors, and the pull-up has been corrected. Compare with the image computed with the true velocity model in Figure 59.

Although images computed with 11-ISPEWs dataset have more dispersed crosstalk than that computed with 35-ISPEWs dataset, ISWET results are insignificantly affected. ISWET using either the 11-ISPEWs set, or the 35-ISPEWs set is extremely inexpensive when compared to that with the original shot profiles. Considering shot profiles datumized to a depth of 1500 m, we estimate that the 11-ISPEWs case would be nearly 30 times faster than ISWET in the shot-profile domain, and the 35-ISPEWs case would be 15 times faster.

CONCLUSIONS

This chapter presents ISWET in the image-space generalized-sources domain. It is an extension from the shot-profile domain to this new generalized-sources domain in which a dramatic gain in computational efficiency is achieved by decreasing data size and solving ISWET in a target-oriented manner. Also, by selecting key reflectors to initiate the image-space generalized source and receiver gathers, great flexibility is incorporated, since a horizon-based approach is possible, which can improve convergence.

For the Marmousi velocity model, two different ISPEW datasets were used to optimize the migration-velocity model by ISWET. Using either dataset yields an equally accurate velocity model, which indicates robustness of the velocity inversion in the image-space generalized-sources domain.

ACKNOWLEDGMENTS

I would like to acknowledge Yaxun Tang for the fruitful discussions about ISWET and with whom I collaborated on extending ISWET from the shot-profile domain to the generalized-sources domain (Tang et al., 2008). 3D field-data example In this chapter, I apply ISWET using 3D-image-space generalized wavefields to estimate the migration-velocity model for the 3D North Sea dataset. The challenges for defining the velocity model for this dataset are due to a possibly irregular salt body, the intense faulting, the amplitude variations caused by irregular acquisition, the short source-receiver offsets, and the limited source-receiver azimuths. Because of the narrow azimuthal configuration, the 3D dataset was submitted to azimuth-moveout (AMO), and common-azimuth migration images are used as the initial conditions for the modeling of the 3D-image-space generalized datasets. This enables us to use very few image-space generalized wavefields in 3D-ISWET. For the velocity inversion we used a combination of layer-stripping ISWET and horizon-based tomography ISWET along with salt-flooding for defining the salt-body contours, yielding consistent velocity updates, fast convergence, and a geologically plausible velocity model. The excellent quality of the final image exposes the structural complexity by correctly imaging faults, satisfactorily unveiling the base of salt, and revealing sub-salt sediments.

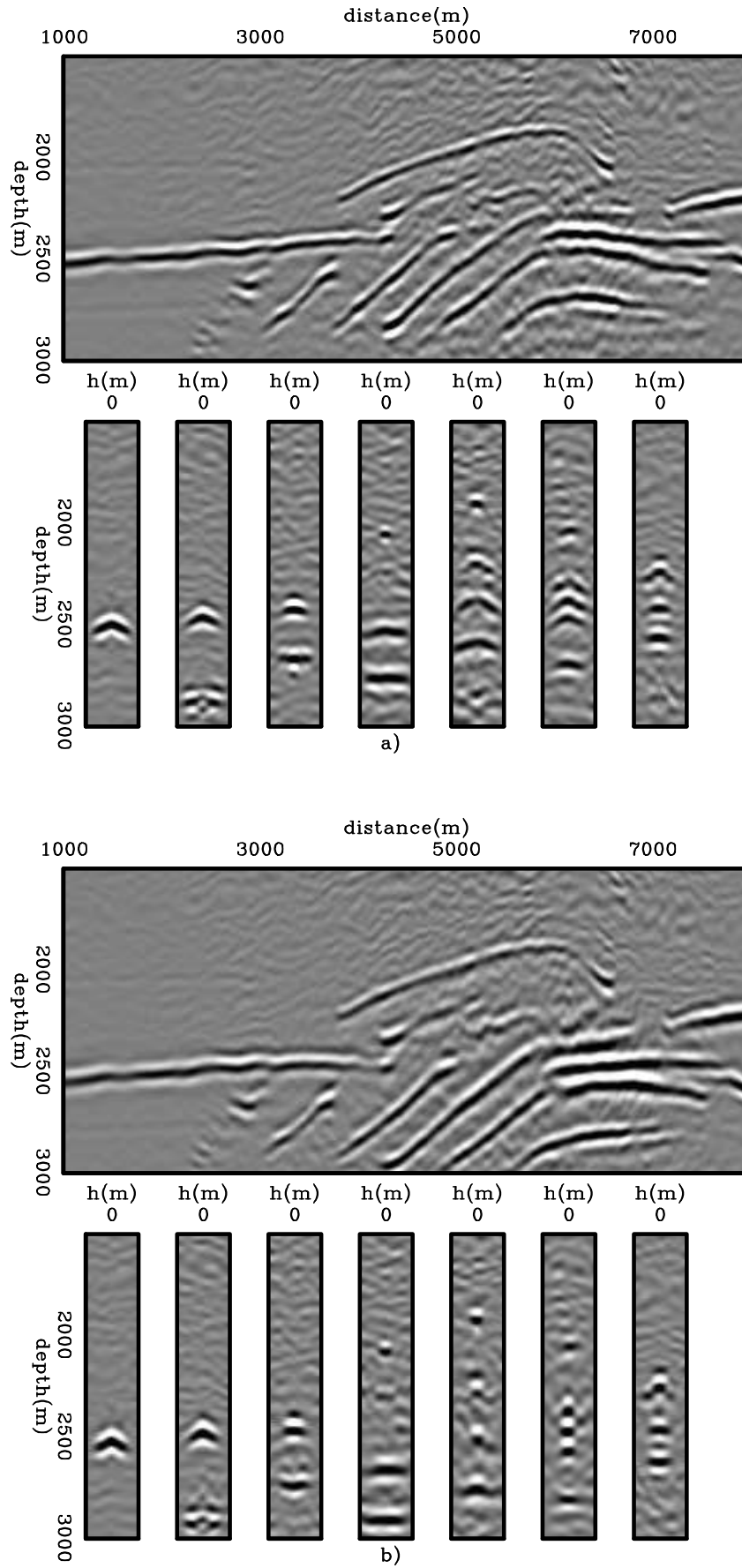


Figure 53: a) Initial and b) final background image for the optimization with 11 ISPEWs.

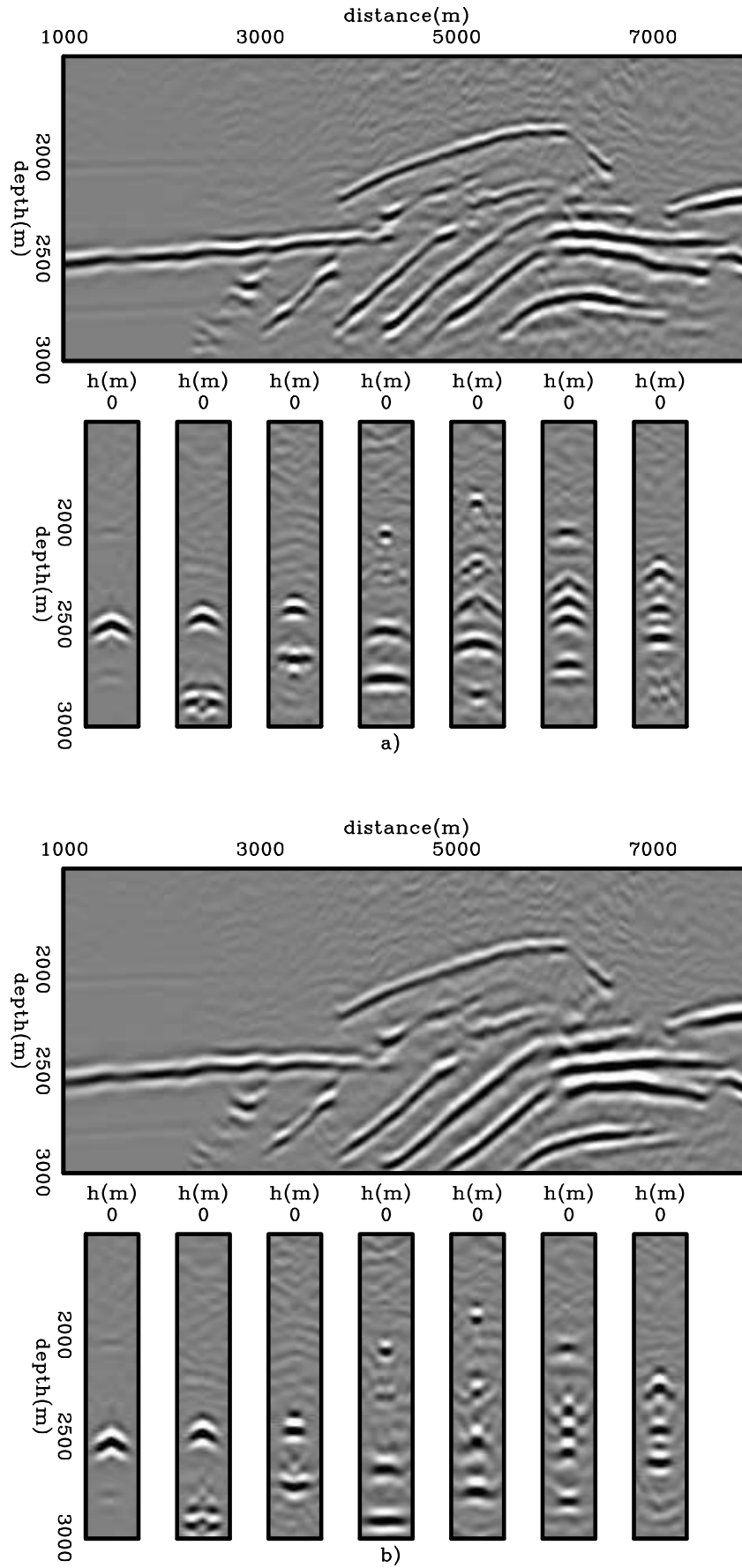


Figure 54: a) Initial and b) final background image for the optimization with 35 ISPEWs.

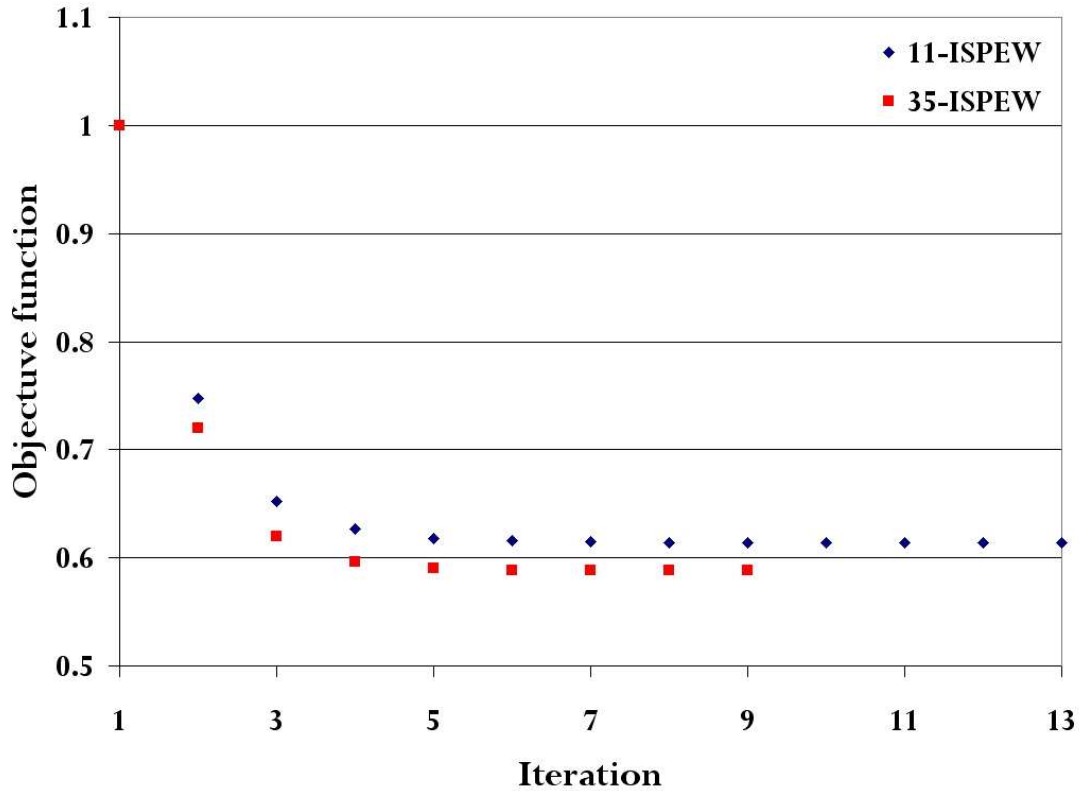


Figure 55: Evolution of the objective function for the 11-ISPEWs case (blue diamonds) and 35-ISPEWs case (red squares).

INTRODUCTION

The 3D North Sea dataset spans over an area of approximately 55 km², with 13.5 km in-lines and 4 km cross-lines. It was acquired using dual sources at intervals of 25 m in the in-line direction and 50 m in the cross-line direction, with three cables with 100 m separation and a maximum offset 3600 m. The limited cross-line offsets (Figure 60d) resulting from this acquisition configuration impose limitations in the azimuthal distribution, as can be seen in Figure 60a and 60b. The overall in-line-offset distribution is quite regular (Figure 60c). However, the offset distribution is spatially quite irregular. The fold of coverage computed for a grid cell of 25 X 25 m for different offset ranges is shown in Figure 61. The acquisition footprint is evident, with a wide low-fold region occurring for in-lines around 4000 m in the y direction.

To mitigate the offset irregularity, considering the limited azimuthal distribution, Clapp (2005, 2006) applies least-squares 3D-data regularization using offset volumes transformed to a common offset via AMO (Biondi et al., 1998). In spite of the good imaging results, the amplitude variation caused by the offset irregularity, although diminished, still persists as can be seen in Figure 62. It shows time slices at 2.8 s through the trace envelope for different offset cubes taken from the regularized data provided by Clapp.

Even though the fold irregularity (Figure 61) and amplitude imbalance (Figure 62) are in the data-space, we will see later that they will be evident in the amplitudes of the gradient of the objective function at approximately the same spatial position.

The velocity model provided along with the data (Figure 63), herein called the original velocity model, presents a general layered structure with an overhanging salt dome connected to a deeper layer with the same velocity as that of the salt dome. In Figure 63, the maximum velocity is 4820 m/s. The final velocity model I derive shows remarkable differences when compared to the original velocity model, especially in the salt body shape.

I start ISWET with an initial velocity model derived from the original velocity model. Initially, the sediment velocity above the chalk layer was refined using residual prestack depth-migration scans. Then, I interpreted the top of chalk on an image migrated with this new velocity. Below the top of chalk, velocity was heavily smoothed using a 5000 m wide 2D median smoother. In addition, to increase the inaccuracy of the initial velocity model, velocity was scaled down by a factor of 0.9 (Figure 64). In Figure 64, the initial velocity model is displayed with the same color scale as that of Figure 63 and the maximum velocity is 4100 m/s. A layer-stripping approach was used to define the velocity for the

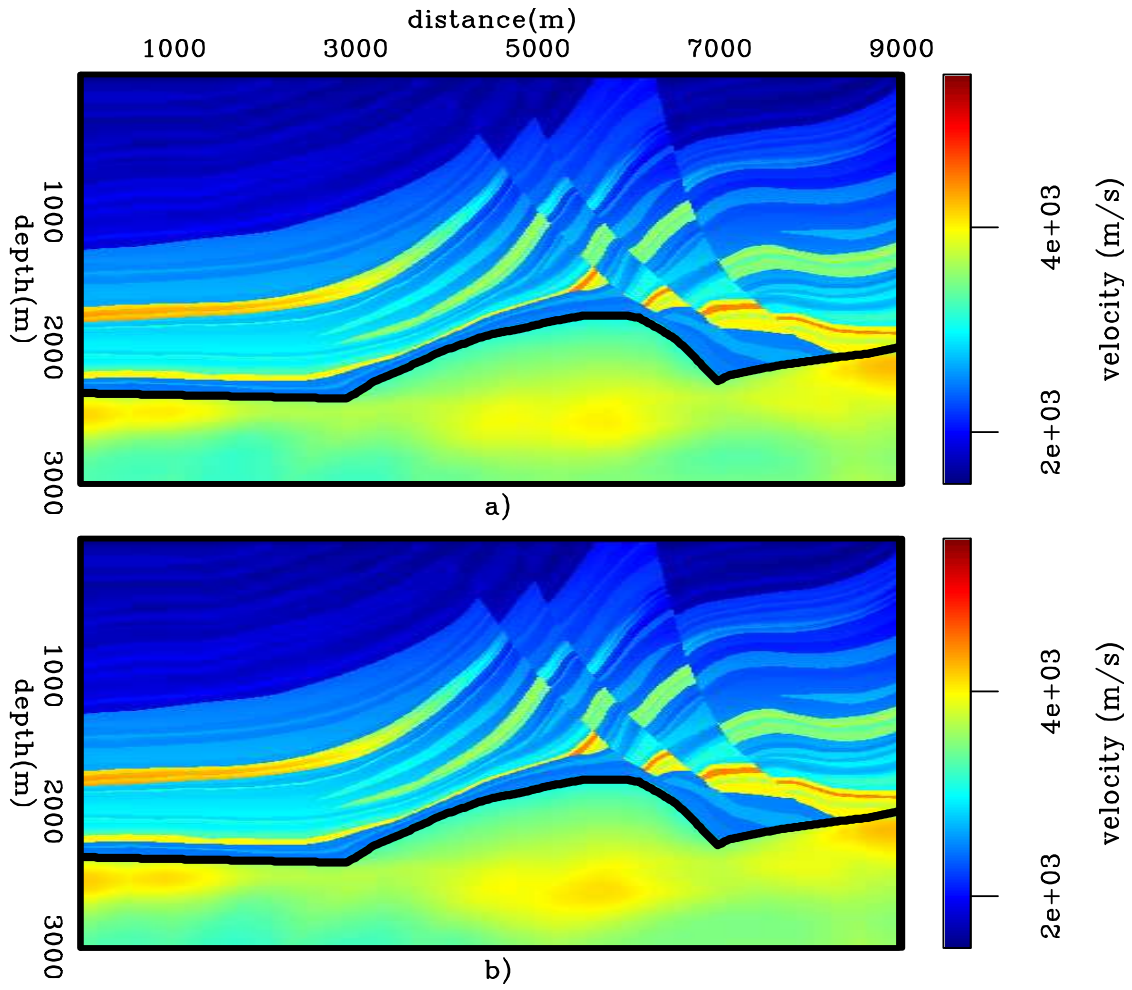


Figure 56: Optimized velocity models for: a) the 11-ISPEWs case, and b) 35-ISPEWs case.

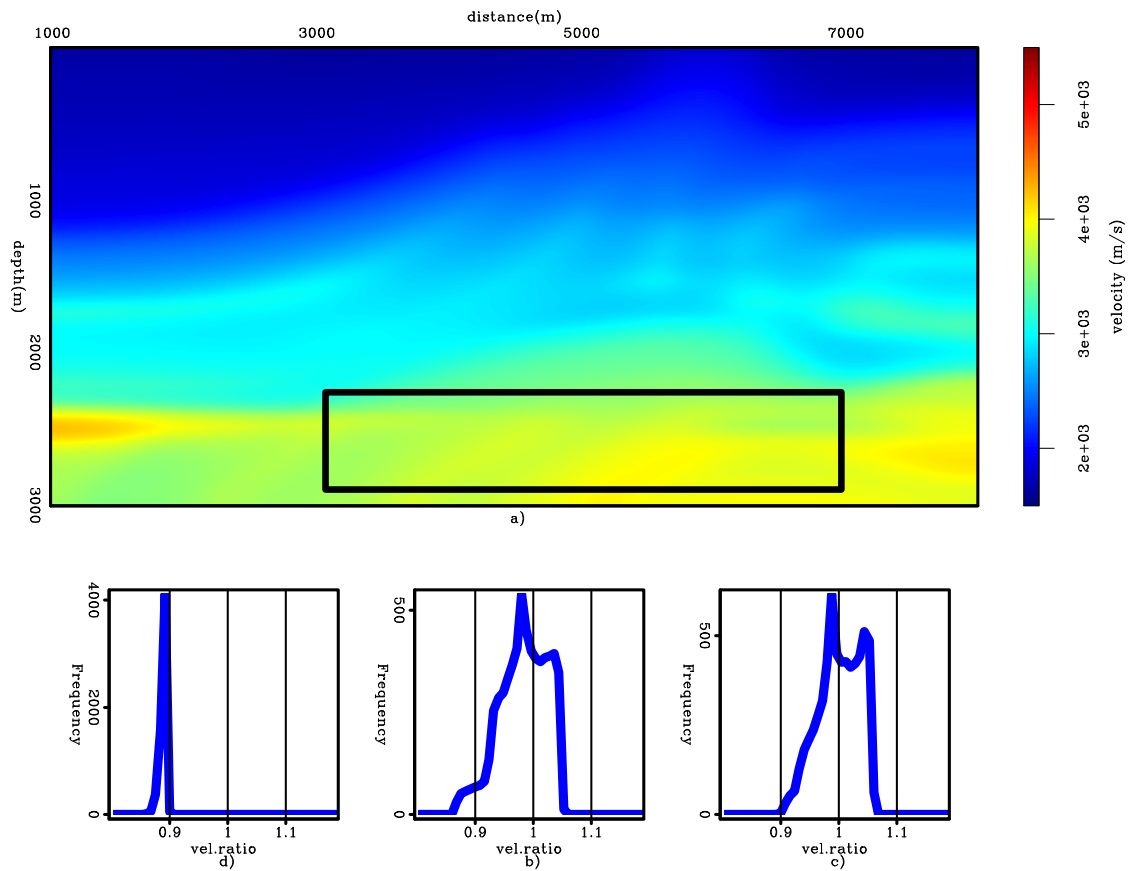


Figure 57: a) Smoothed version of the true velocity model, b) histogram of the velocity ratio between the smoothed true velocity model and the initial velocity model, c) histogram of the velocity ratio between the smoothed true velocity model and the 11-ISPEWs optimized velocity model, and d) histogram of the velocity ratio between the smoothed true velocity model and the 35-ISPEWs optimized velocity model.

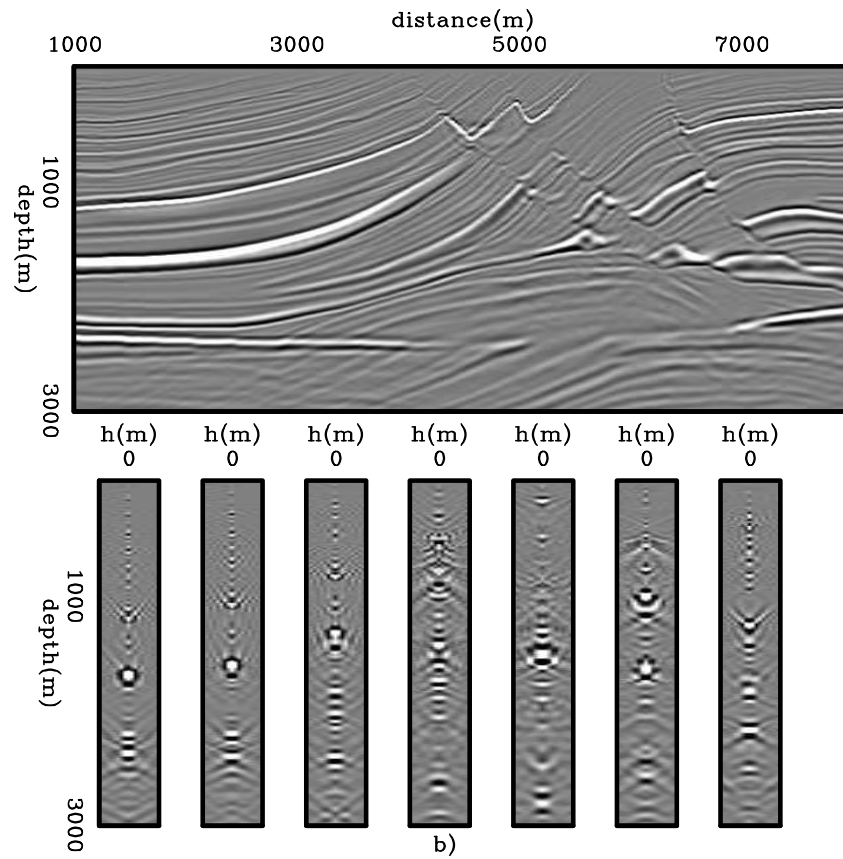
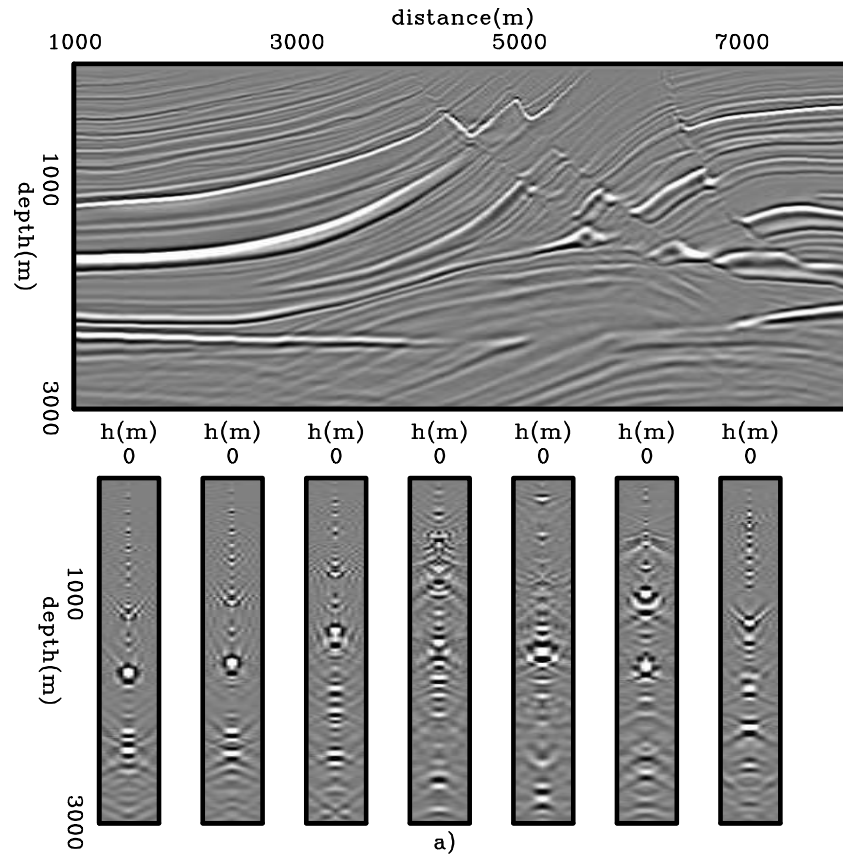


Figure 58: Images computed with shot-profile migration using the optimized velocity models of Figure 56: a) the 11-ISPEWs case, and b) 35-ISPEWs case.

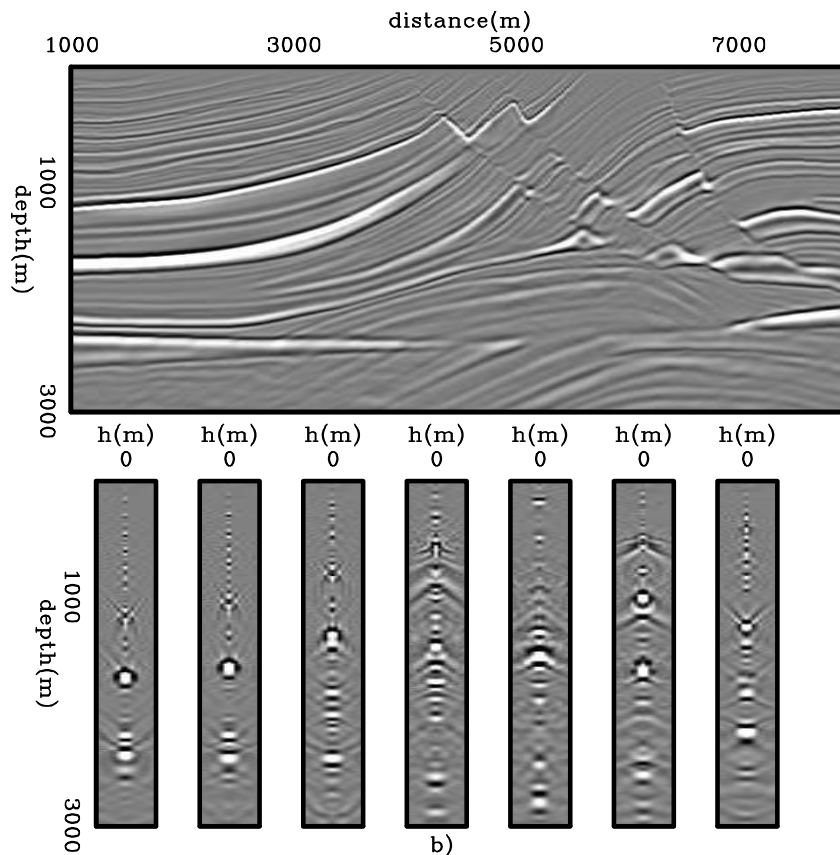


Figure 59: Image computed with shot-profile migration using the true velocity model.

chalk layer, considering a sufficiently accurate velocity for the sediments above. Then, the top salt was interpreted, and a salt flooding procedure enabled the interpretation of the base of salt. The interpretation of the base of salt can be considered the main source of uncertainty of the 3D-field data example, since no previous geological information was available. Finally, a group of reflectors below the salt is used to define the velocity structure for the deeper part.

All the computations were carried out on computer nodes of the Stanford Center for Computational Earth & Environmental Science (CEES). Thirty nodes of Dual Nehalem 5520 with 24Gb RAM were used, accounting to 240 CPUs. To generate 30 pairs of 3D ISPEWs, using 196 frequencies, it took 10 minutes. On average, each iteration of the velocity optimization, consisting of one function evaluation, the gradient computation, and two additional function evaluations for the line search, took approximately two hours.

In this chapter, I give details of the procedures above, which led to a final image with quality superior to that of the image computed with the initial velocity model, as well as to that obtained with the original velocity model. I show that using image-space generalized wavefields lends flexibility and computational efficiency to 3D-ISWET, while maintaining the necessary robustness.

IMPROVING VELOCITY ABOVE THE CHALK

When defining the depth-migration velocity model, it is very important that velocity in the shallow layers is sufficiently accurate, so that velocity errors are not propagated to deeper layers. A first version of the initial velocity Figure 65 was generated in a similar way as that for Figure 64, except that the velocity above the top of the chalk is the same as the original velocity. Migration with this version of the initial velocity revealed slight velocity inaccuracies for the sediment layer above the chalk, evidenced by residual moveout in the SODCIGs (Figure 66). The section on the top is the zero-subsurface-offset section, and the panels at the bottom are SODCIGs at the position corresponding to their x coordinates. Notice the shallow events curving down in the SODCIGs, especially for x coordinates below 6000 m. The strong reflector, which is flat at depths of 1500 m on the left and 1300 m on the right, and curved in the middle of the figure, is the top of chalk. It also presents strong curvature. The residual moveout of these gathers was evaluated with residual-prestack-depth migration velocity analysis (Sava, 2003), in which a residual moveout parameter was interpreted. Since the velocity structure is approximately one-dimensional and the residual-moveout parameter is local, I performed one run of a simple vertical velocity update similar to Deregowski's velocity update (Deregowski, 1990).

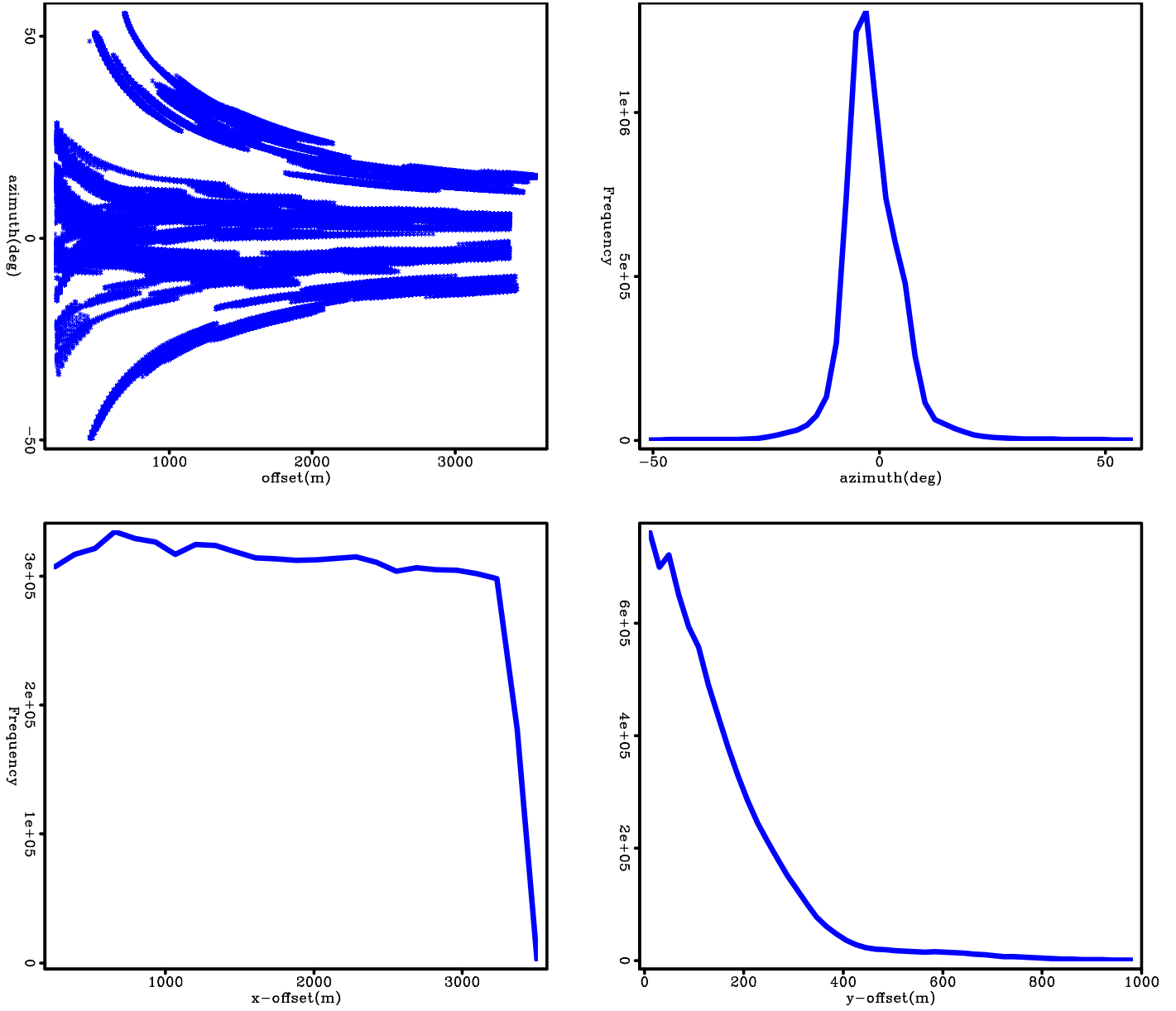


Figure 60: a) Offset – azimuth cross-plot, b) azimuth histogram, c) in-line offset histogram, and d) cross-line offset histogram.

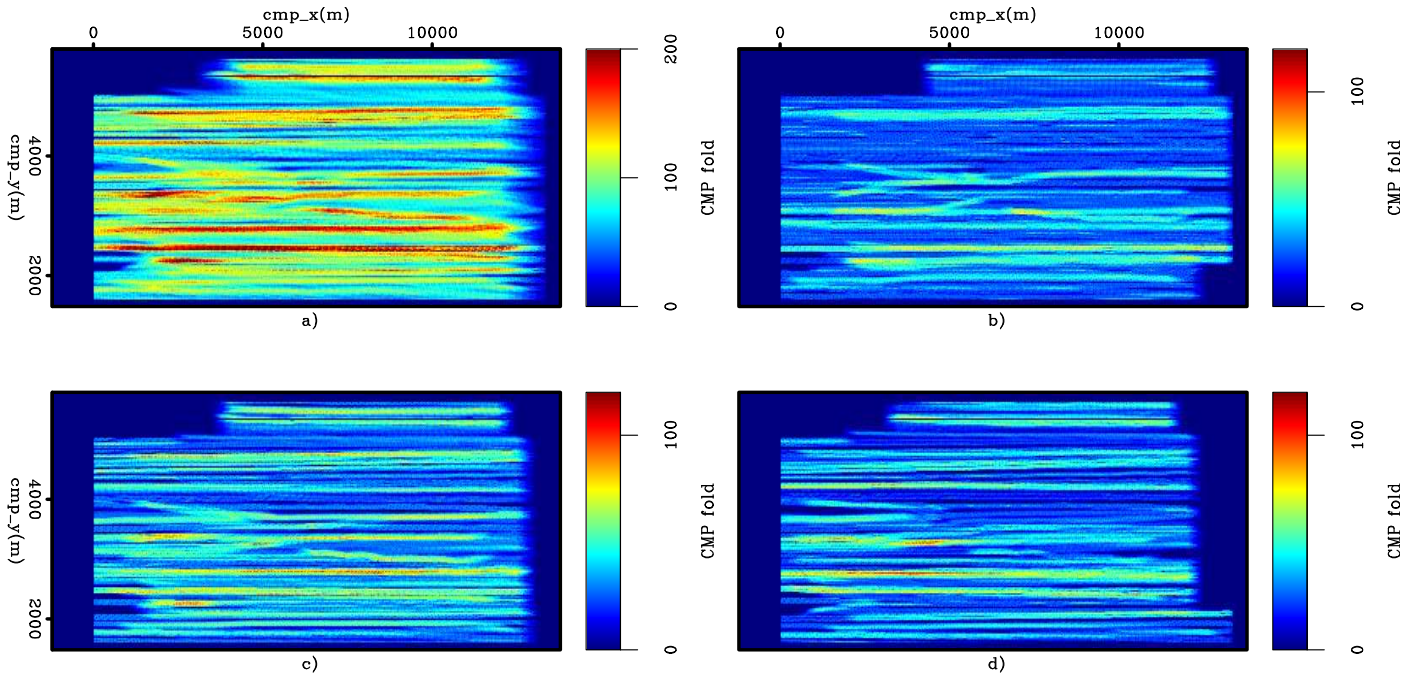


Figure 61: Fold of coverage plots: a) full offset, b) 0 – 1200 m offset, c) 1200 – 2400 m offset, and d) 2400 – 3600 m offset.

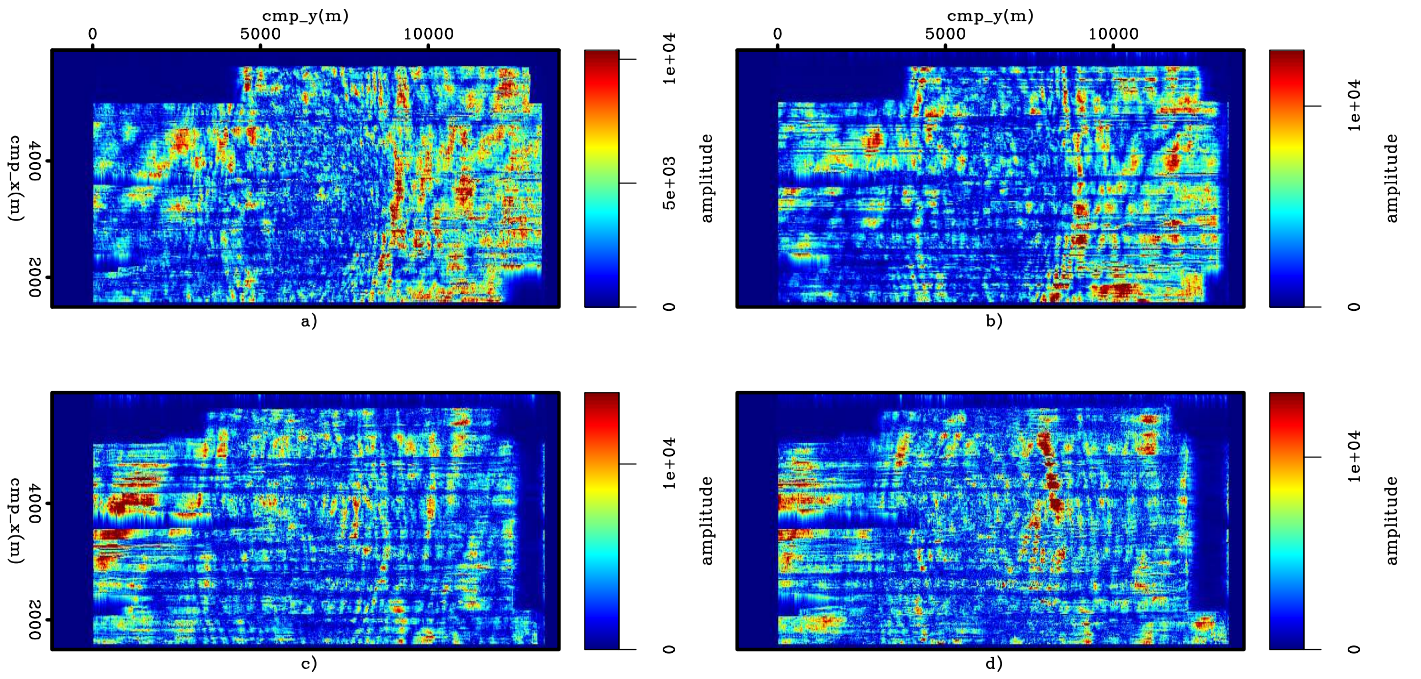


Figure 62: Time slices through the trace envelope for different offset cubes from the regularized data: a) offset 200m, b) offset 1200 m, c) offset 2400 m, and d) offset 3000 m.

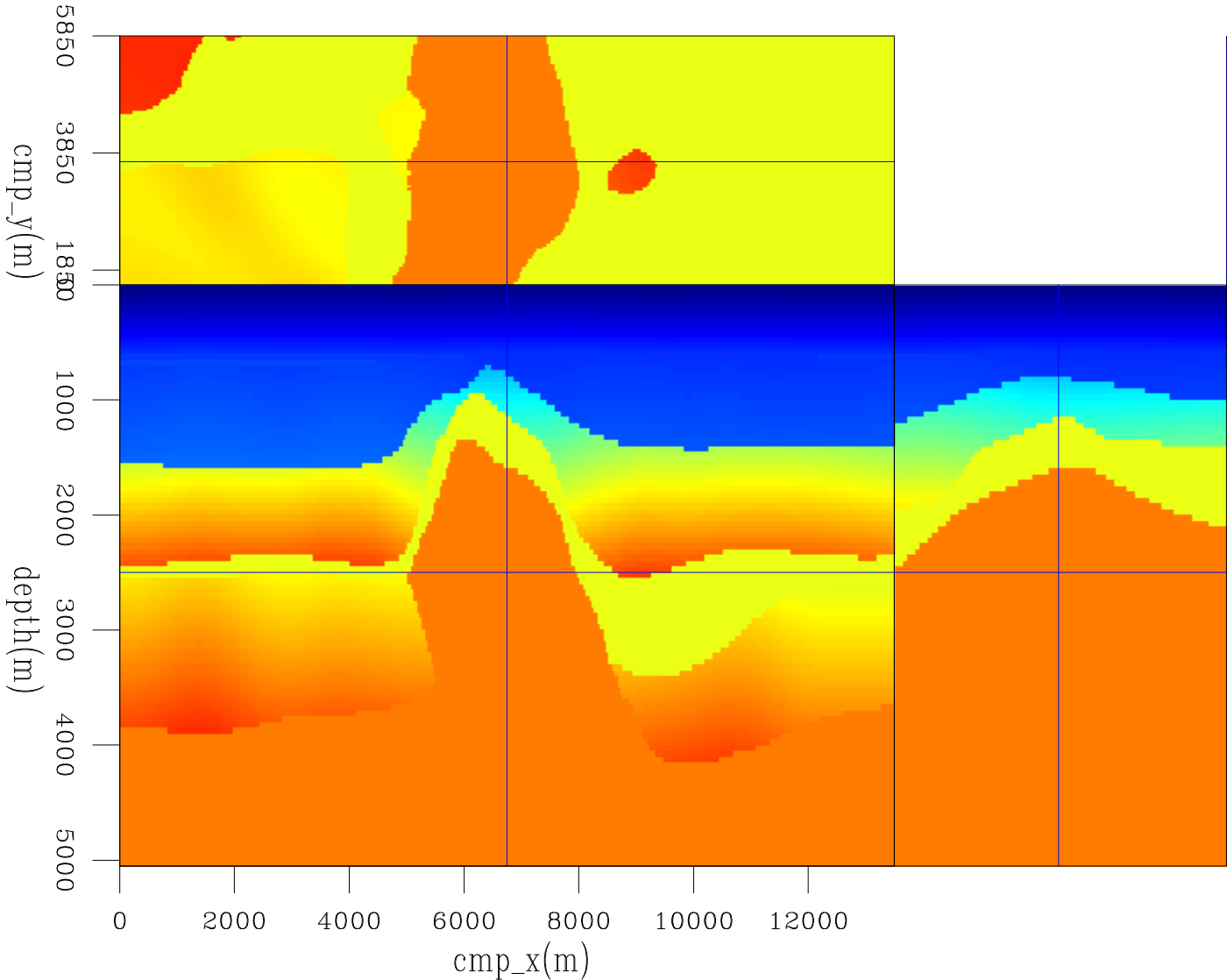


Figure 63: Slices through the IFP velocity model.

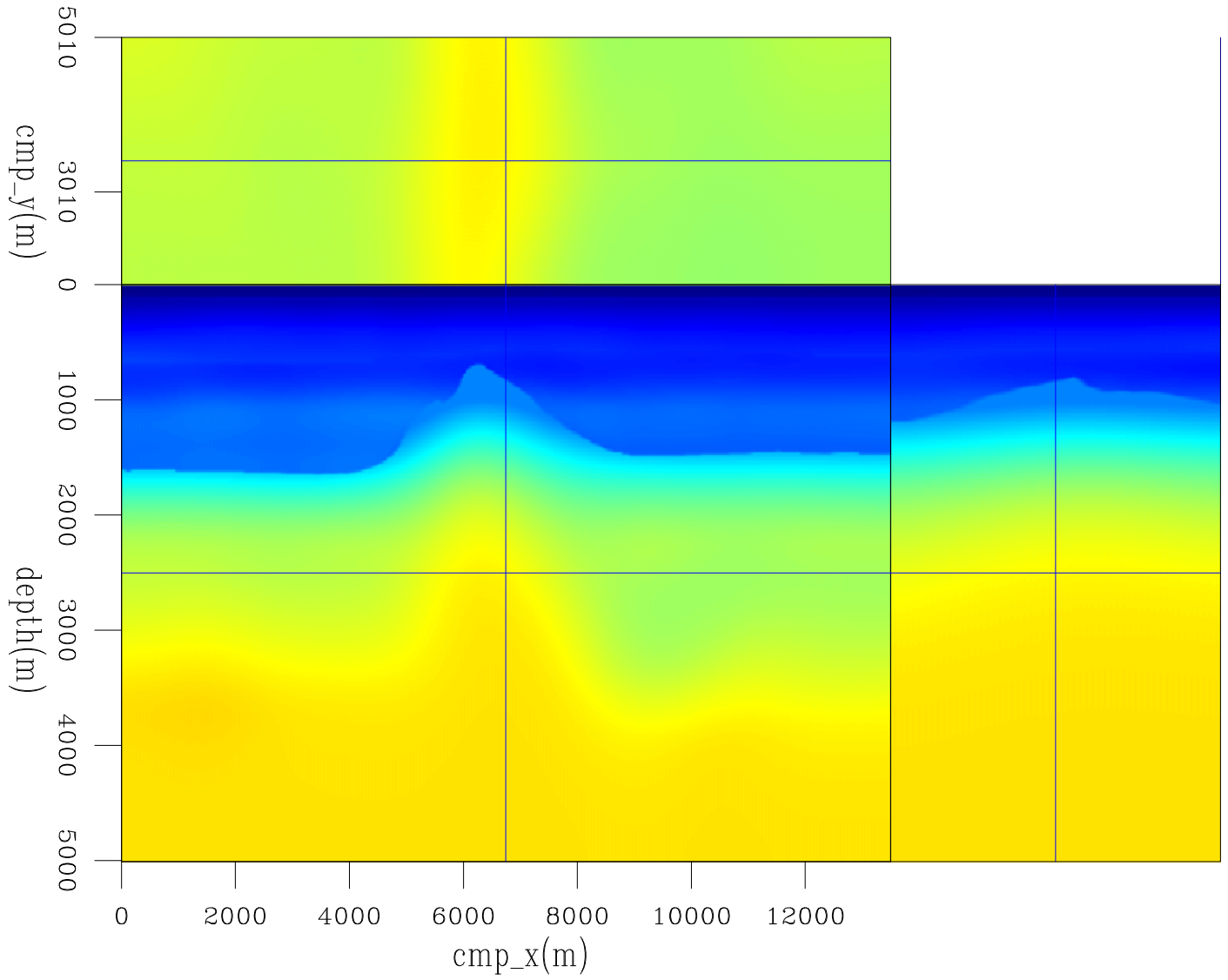


Figure 64: Slices through the initial velocity model used in 3D-ISWET.

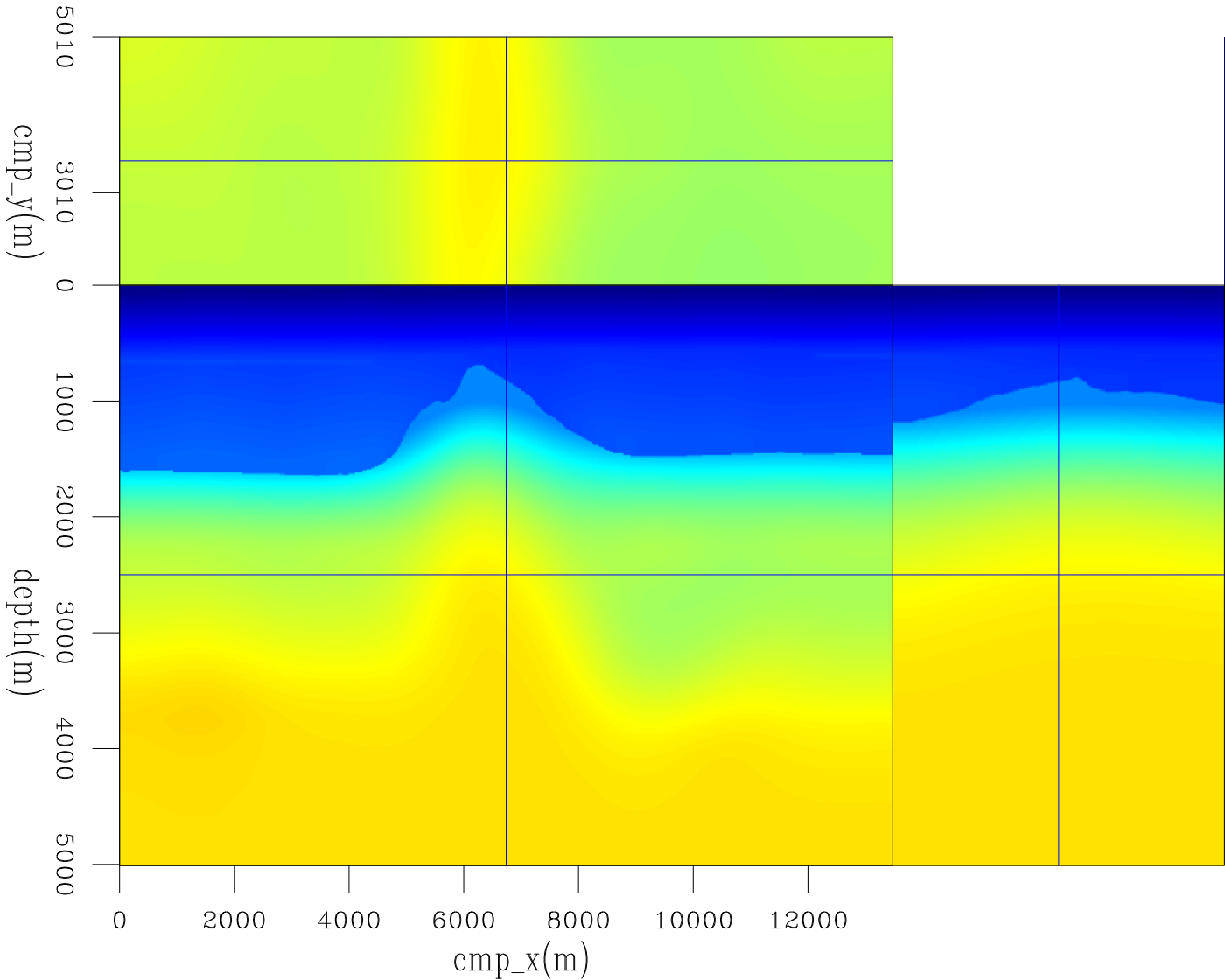


Figure 65: Slices through an initial velocity model generated with the same procedures as that for Figure 64, except for the velocity above the chalk, which is the original velocity.

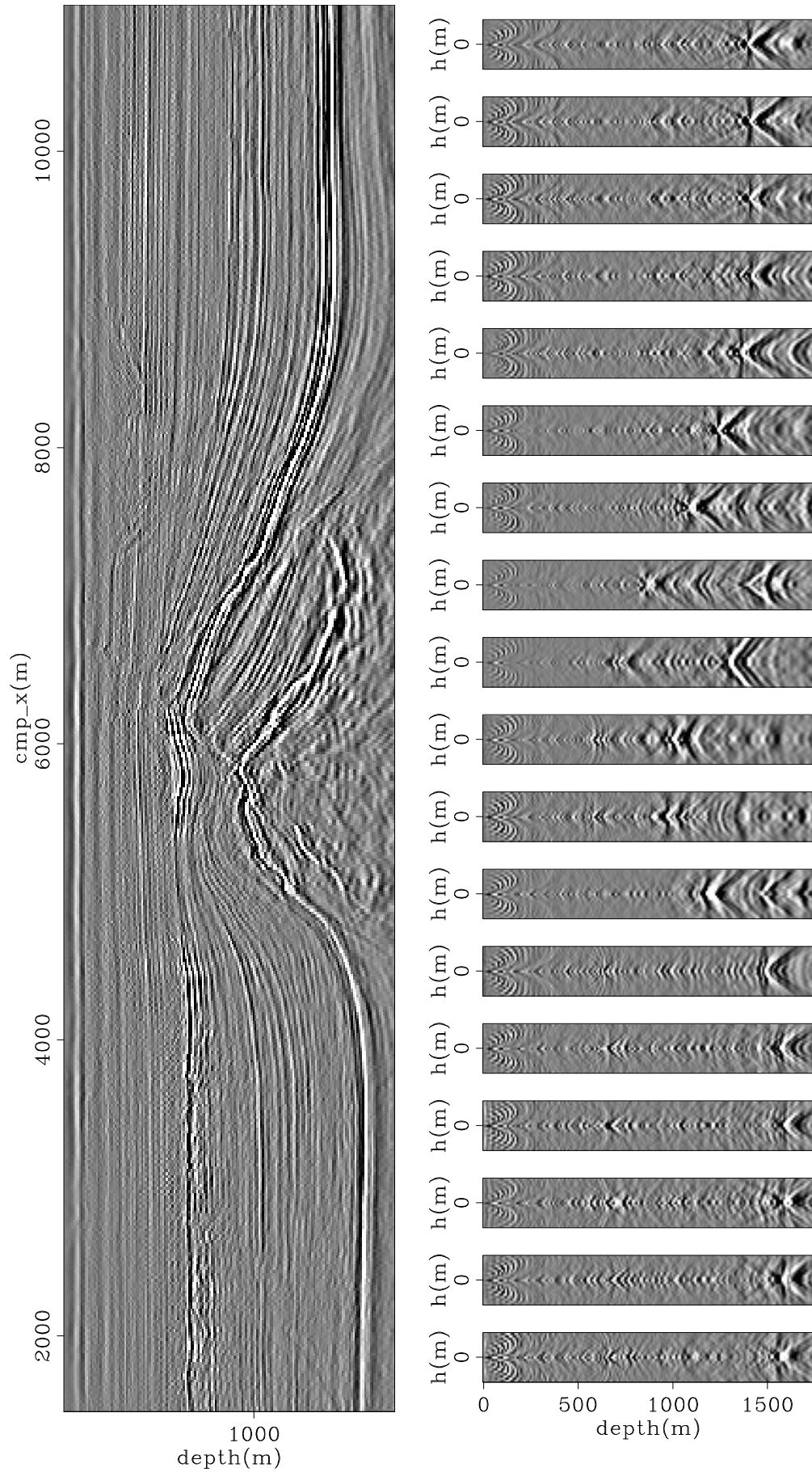


Figure 66: Image computed with the velocity model of Figure 65. The top panel is the zero-subsurface offset section and the panel at the bottom are the SODCIGs.

The new velocity model satisfactorily improved the focusing of the image, as can be seen in Figure 67. Notice how both the shallow reflectors and the top of chalk are much better focused around zero-subsurface offset. Also, since the interval velocities increased, the top of chalk is shifted down. The maximum frequency used to compute images of Figures 66 and 67 is 60 Hz. For velocity optimization and the following common-azimuth migration images, the maximum frequency is 42 Hz.

SOLVING FOR THE CHALK LAYER VELOCITY

Generating 3D ISPEWs for the base of chalk

After improving the accuracy of the initial velocity model for the shallower sediment layers, as previously discussed, common-azimuth migration (CAM) with this initial velocity (Figure 64) produced the images in Figure 68, which shows the volume for the zero subsurface offset, and Figure 69, which shows the zero subsurface offset on the left, and ADCIGs on the right for in-line 3180. The effects of migrating with a too low velocity are evidenced by poorly collapsed diffractions close to the salt flank, poorly imaged faults, and reflectors curving up in the ADCIGs.

For the modeling of ISPEWs, in-line and cross-line intervals of the CAM image were interpolated from 20 m to 30 m, which are the in-line and cross-line intervals used for optimizing the migration velocity. The base of chalk was interpreted in the 3D pre-stack volume, using the latest version of the hypercube viewer (Clapp et al., 2008).

After migration, the wavelet is velocity- and dip-dependent (Tygel et al., 1994). Although simple in 2D, implementing 3D windowing based on the dip- and velocity-dependent wavelet stretching can be cumbersome. Instead, I use a simpler procedure that yields a mask operator to window the reflector. First, I use the pre-stack interpretation to vertically window the target reflectors. Then, for each windowed subsurface-offset cube, I compute the tridimensional envelope with the same smoothing parameter in all directions, which simulates the dip dependency. The amplitudes are clipped to one, based on a threshold value. Amplitude variations are compensated for by applying an RMS gain prior to the computation of the envelope. The mask operator is shown in Figure 70 for the zero subsurface offset (Figure 70a) and for the in-line 3520 (Figure 70b), in which a subsurface-offset gather is shown on the right.

We extract the signed square root of the windowed pre-stack image to minimize the influence of the squaring of the wavelet on the gradient computation, as discussed in Chapter .

As shown in Chapter ??, the CAM initial conditions can be continuously sampled in the cross-line direction, because no cross-line offset is computed; this reduces by at least one order of magnitude the number of image-space generalized wavefields to be synthesized. For the base of chalk, we modeled only 30 3D ISPEWs, which are collected at 600 m depth. Using 30 CEES nodes with 8 CPUs each, the modeling takes approximately 10 minutes. A pair of 3D-ISPEW gathers is shown in Figure 71. Since the number of subsurface offsets that will be used during ISWET is 25 and the spatial sampling in the x direction of 30 SODCIGs is used to model the 3D ISPEWs, crosstalk is expected to be strongly attenuated during imaging in ISWET.

Velocity optimization

A nonlinear conjugate-gradient solver is used for the velocity optimization. Velocity update is constrained to a maximum of 10% variation between iterations. All the wavefield propagation is performed between the depth at which the 30 3D ISPEWs were collected (600 m) and the maximum depth (3300 m). Velocity is updated up to the top of the chalk layer.

The amplitude variations are more pronounced in 3D than in 2D because of the acquisition footprint. To illustrate the amplitude variation problem, we compute the slowness perturbation without applying smoothing, and without extracting the signed square root from the initial conditions, to model 30 pairs of ISPEWs (Figure 72). In this case, the amplitude variation due to acquisition is even more pronounced. The acquisition footprint is clear, specially around the y coordinate 4000 m, which is a region with low-fold of coverage (Figure 61). If we extract the signed square root of the initial conditions for the modeling, or equivalently the signed fourth root of the gradient, the DSO slowness perturbation presents smaller amplitude variations (Figure 73).

The gradient of the objective function must be smooth to yield velocity updates consistent with the Born approximation, as discussed in Chapter . We apply a B-spline smoothing with node intervals of 420 X 420 X 160 m in the in-line, cross-line and depth directions, respectively. Applying B-spline smoothing on the DSO slowness perturbation of Figure 73 mitigates the amplitude-variation problems and yields consistent slowness perturbations (Figure 74).

Two runs of ISWET were necessary to define the velocity model for the chalk layer. In the first, we used the 30 pairs of ISPEWs whose modeling was described in the previous subsection. We used two function evaluations in the line search. After seven iterations, optimization stopped because the variation of the objective function was smaller than 0.1%. Figure 75 shows the evolution of the objective function.

The optimized velocity for the first run of ISWET is shown in Figure 78. As expected, the migration velocity increased compared to the initial velocity of Figure 64. The initial background image and the background image of the seventh

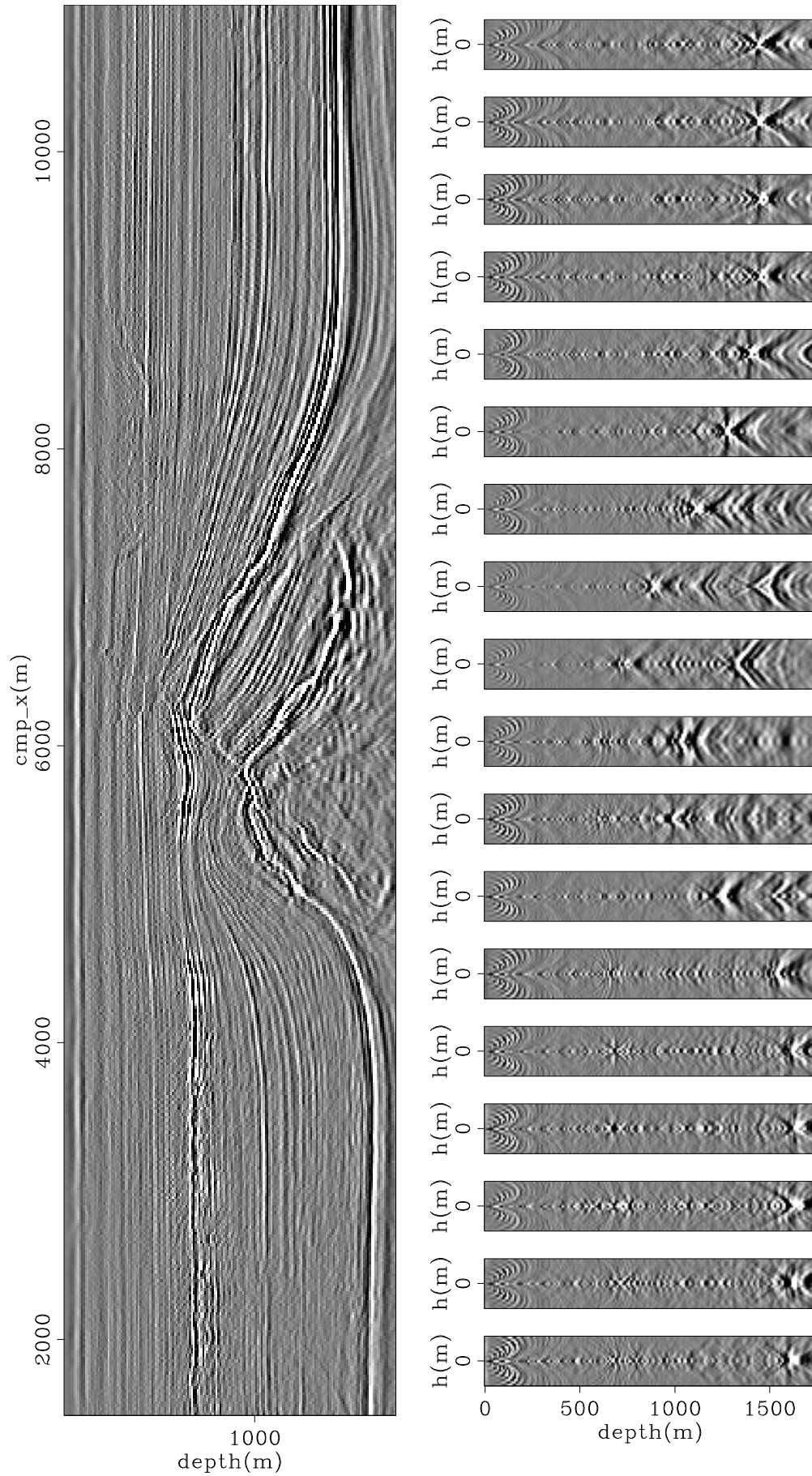


Figure 67: Image computed with the velocity model of Figure 64. The left panel is the zero-subsurface offset section and the panels on the right are the SODCIGs. Compare with Figure 66.

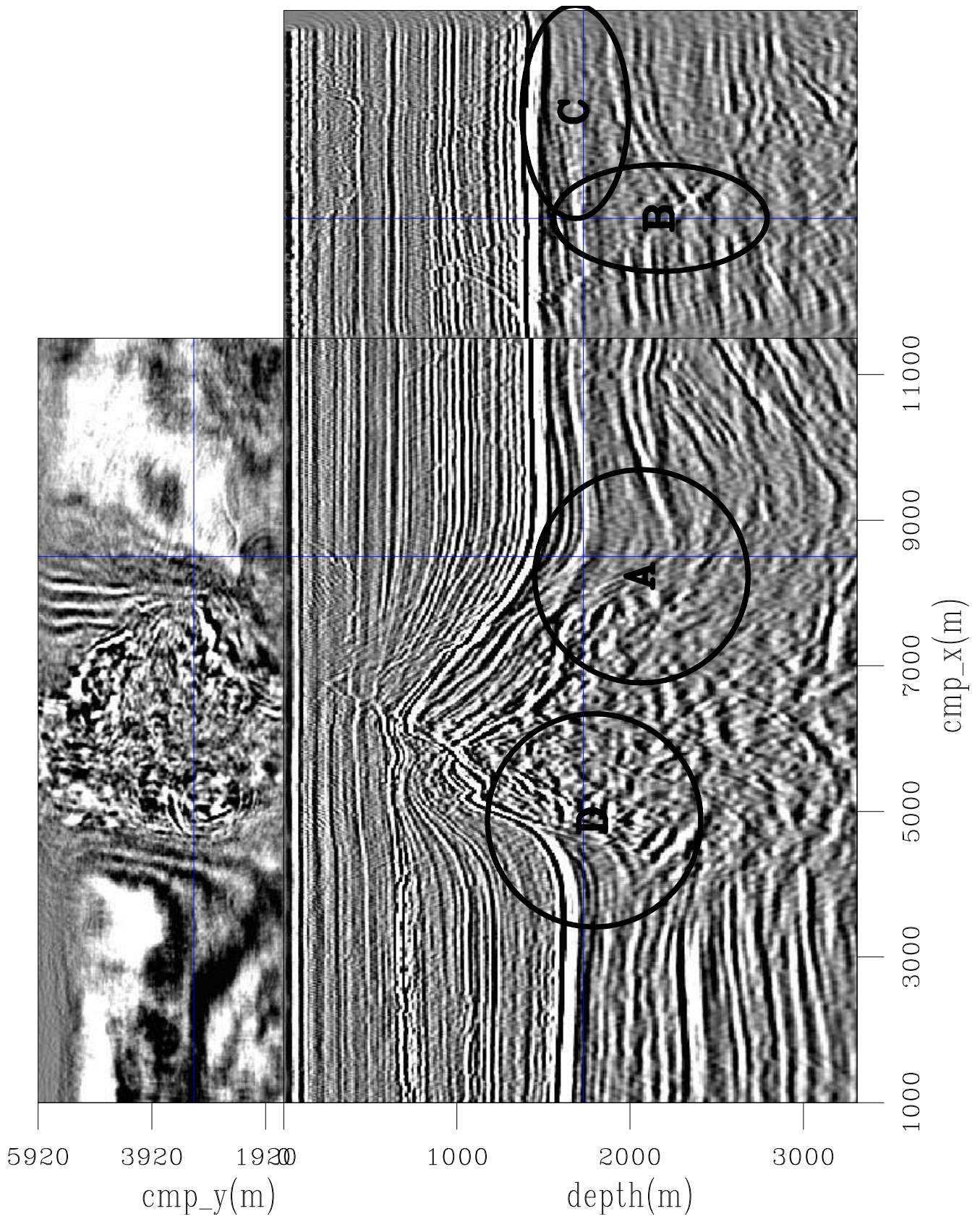


Figure 68: Slices through the CAM image with the initial velocity model of Figure 64. Notice poorly collapsed diffractions close to the salt flank (A and D), and poorly imaged faults (B and C) caused by migrating with an inaccurate velocity.

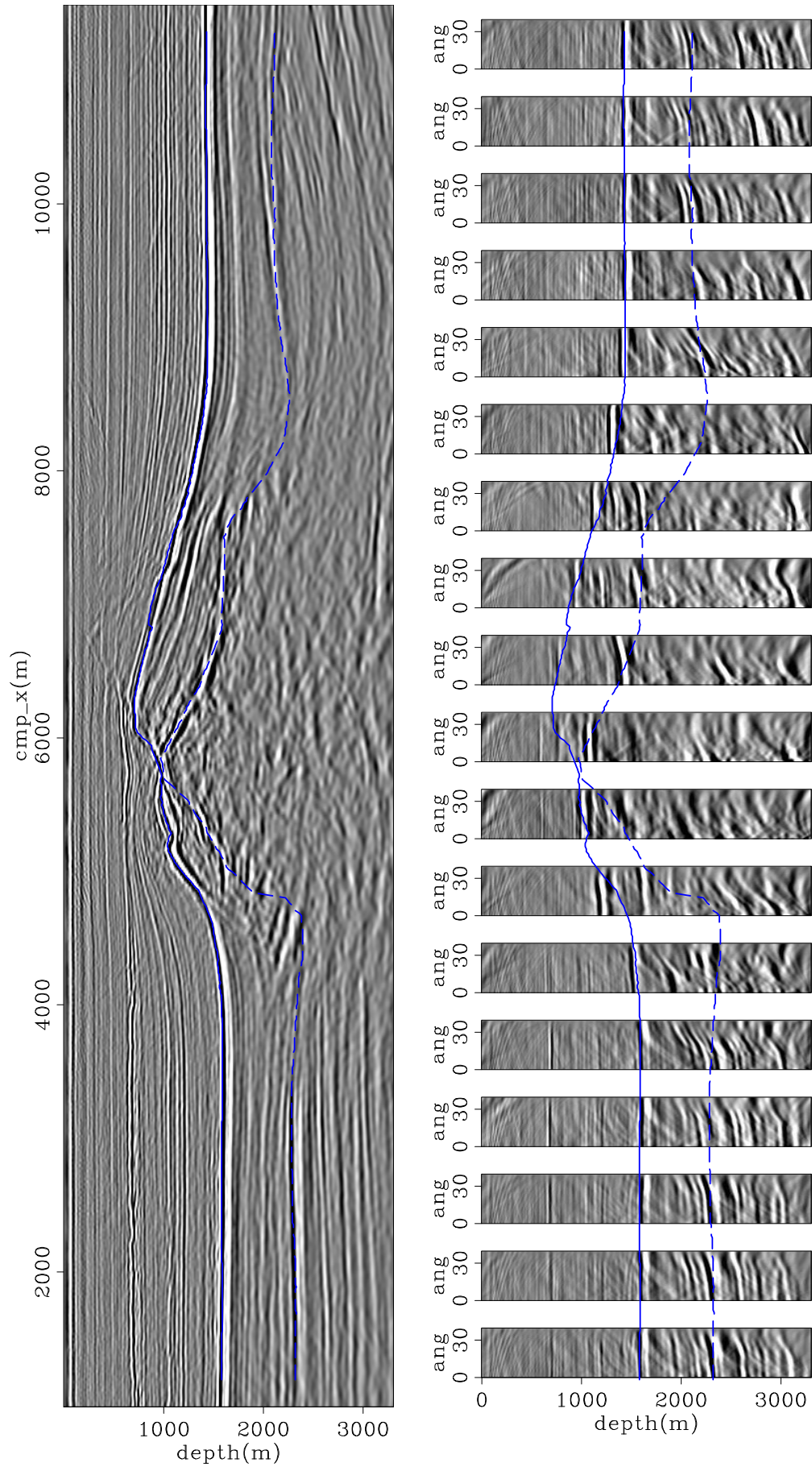


Figure 69: In-line 3180 of the CAM image with the initial velocity model of Figure 64. On the left is the zero-subsurface offset section, and on the right ADCIGs. Notice the strong residual moveout on the ADCIGs. The continuous blue line is the top of chalk, and the dashed blue line it the base of chalk.

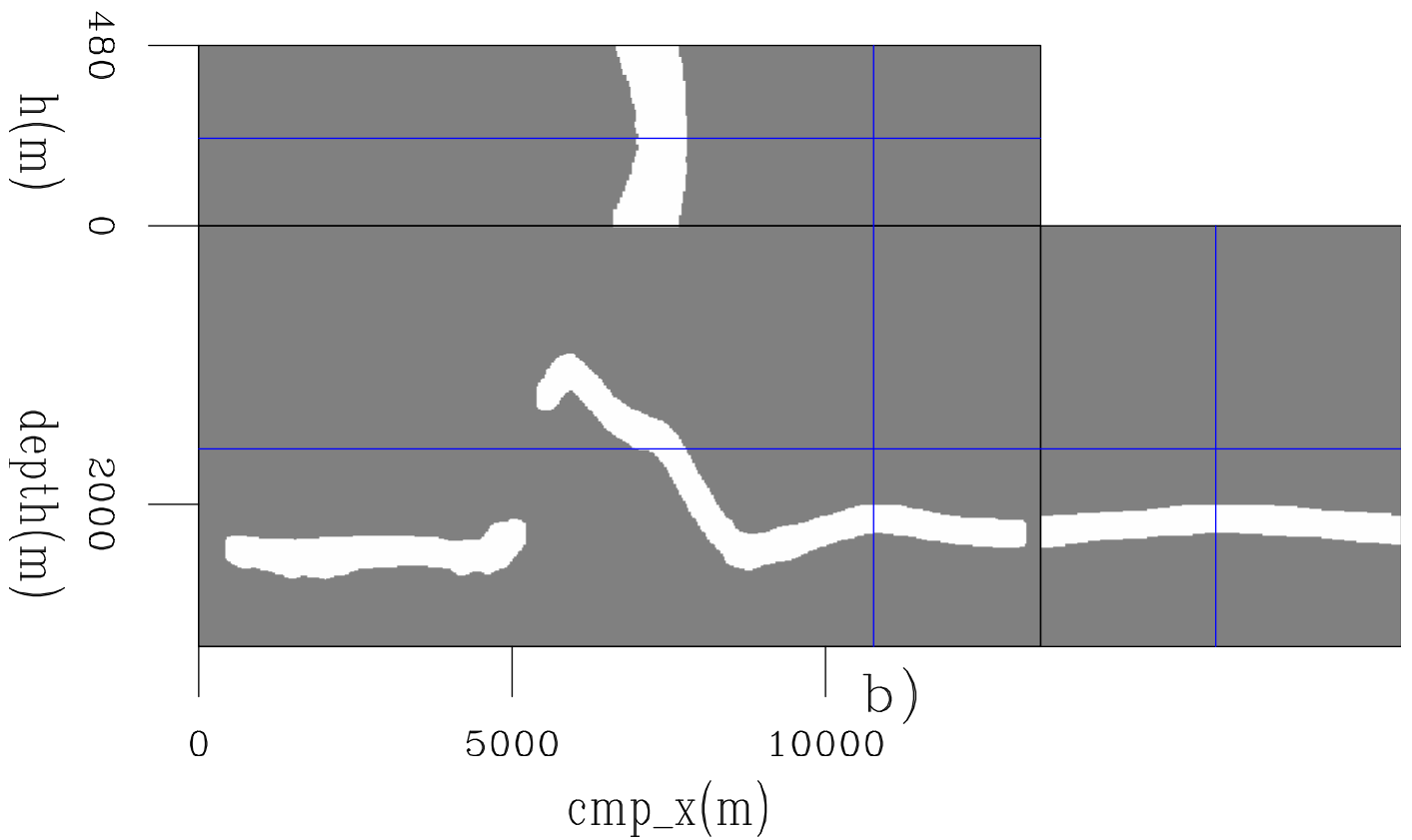
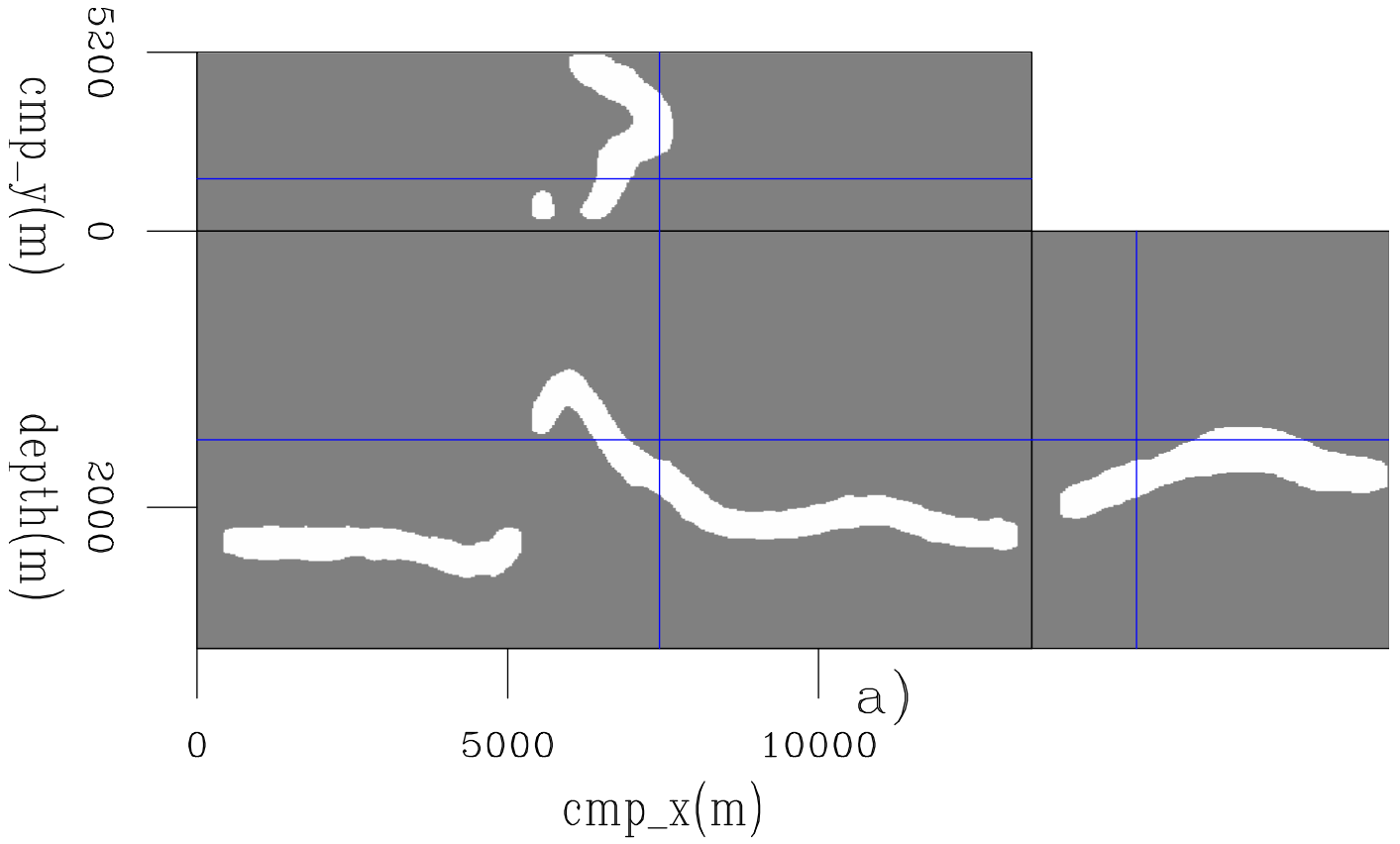


Figure 70: Slices through the prestack-mask operator to select the base of chalk, showing: a) the zero subsurface offset, and b) the in-line 3520.

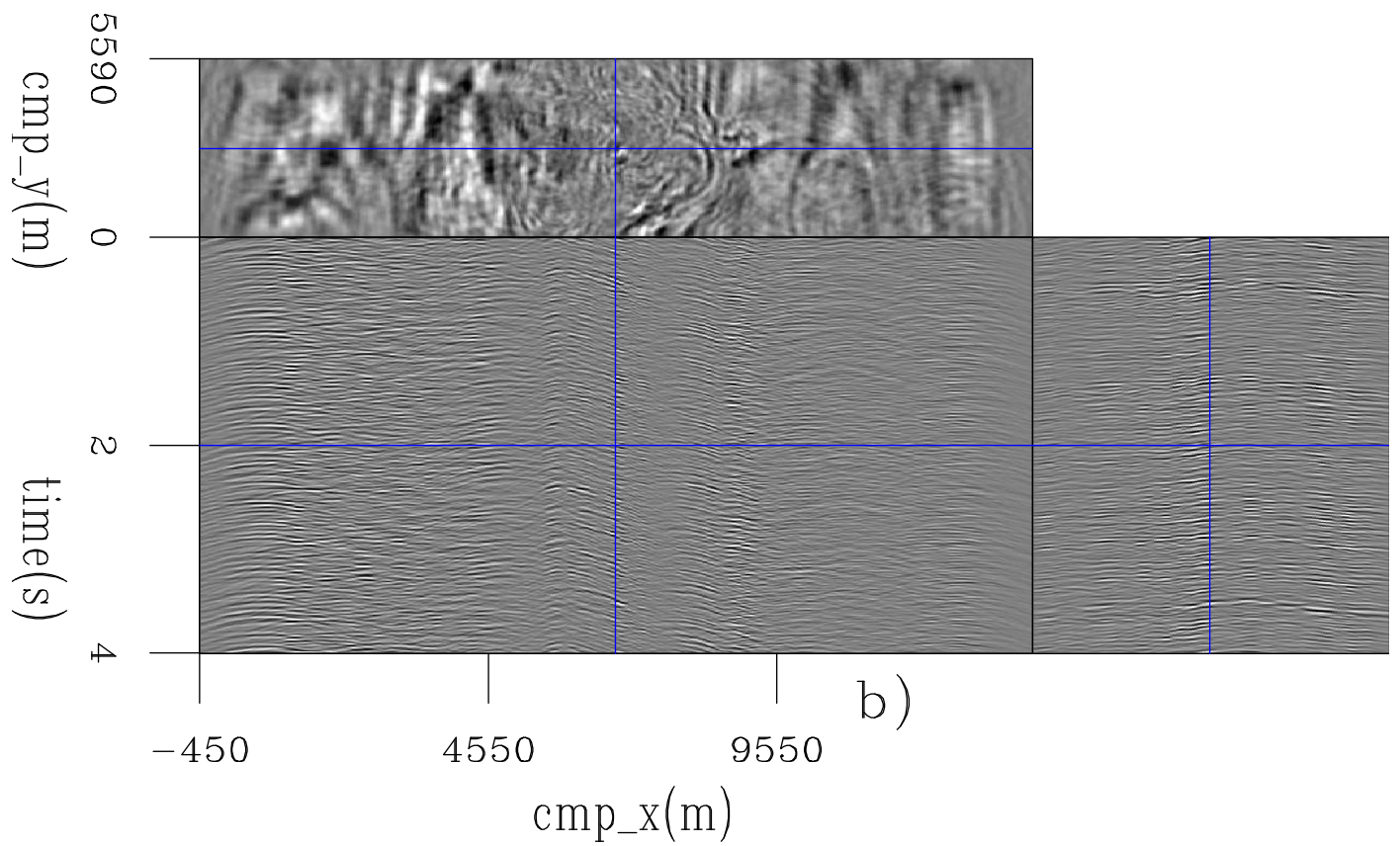
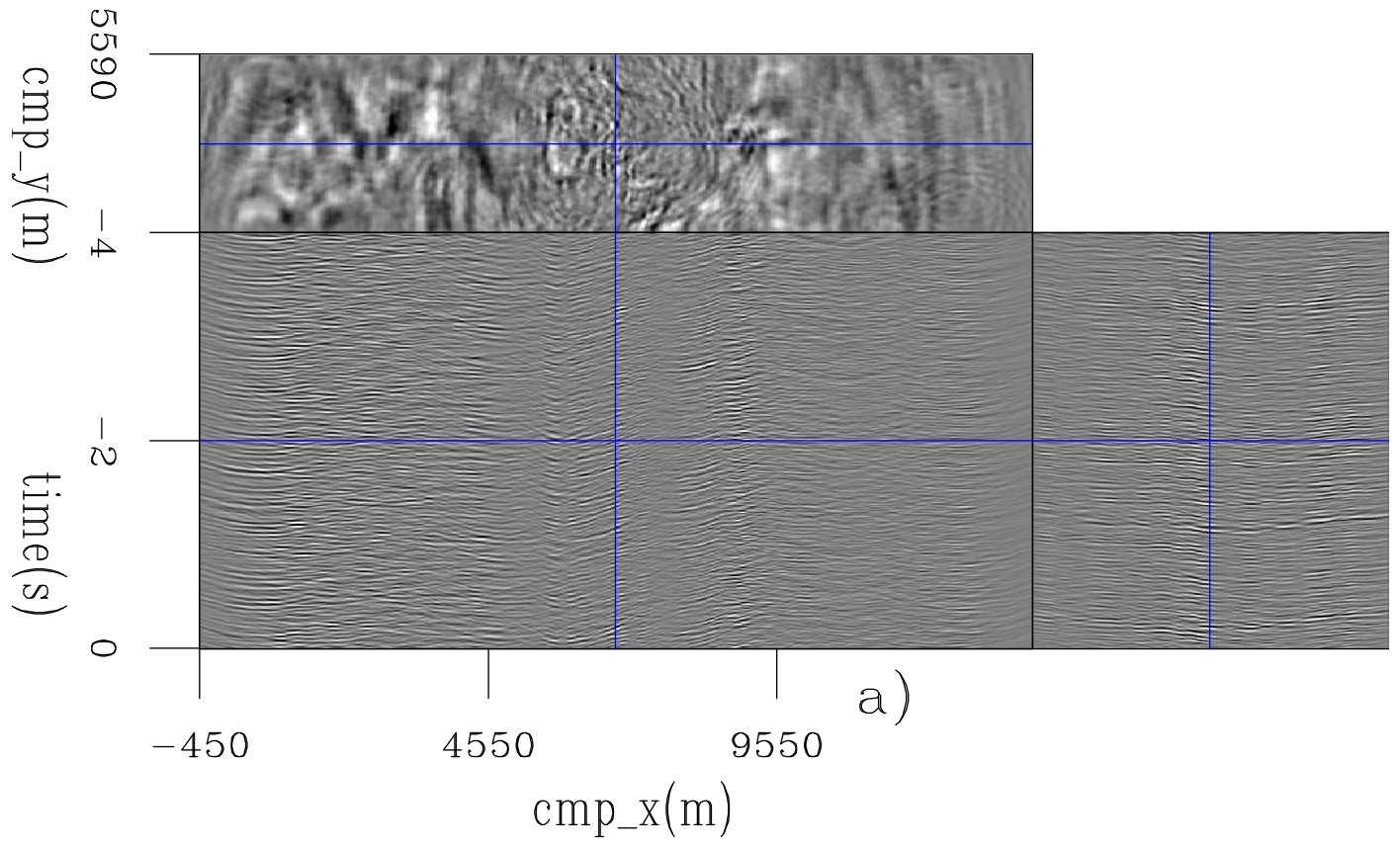


Figure 71: A pair of 3D source (a) and receiver (b) ISPEWs computed for the base of chalk.

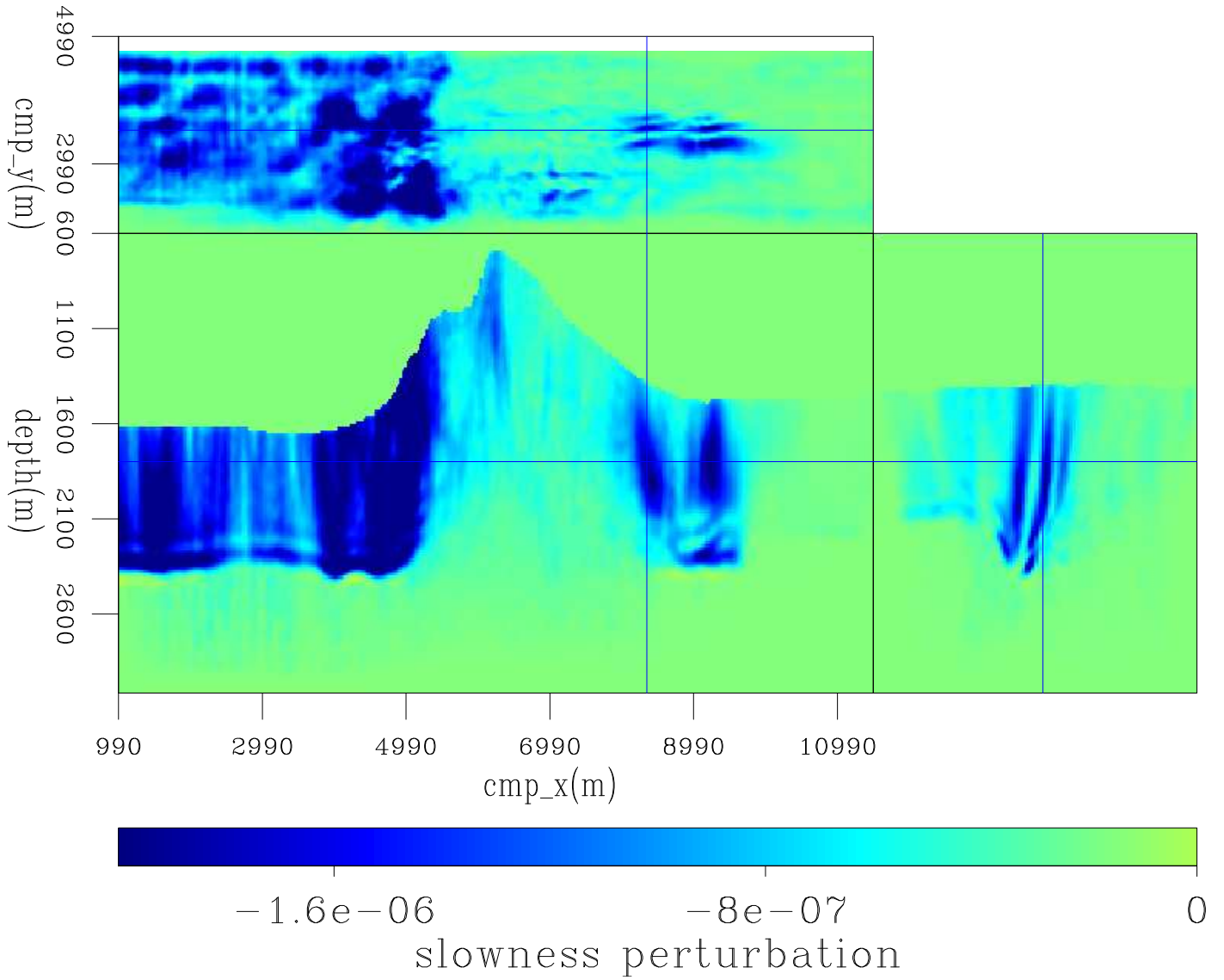


Figure 72: Slowness perturbation without smoothing and without extracting the signed square root from the initial conditions for the modeling of 30 pairs of ISPEWs.

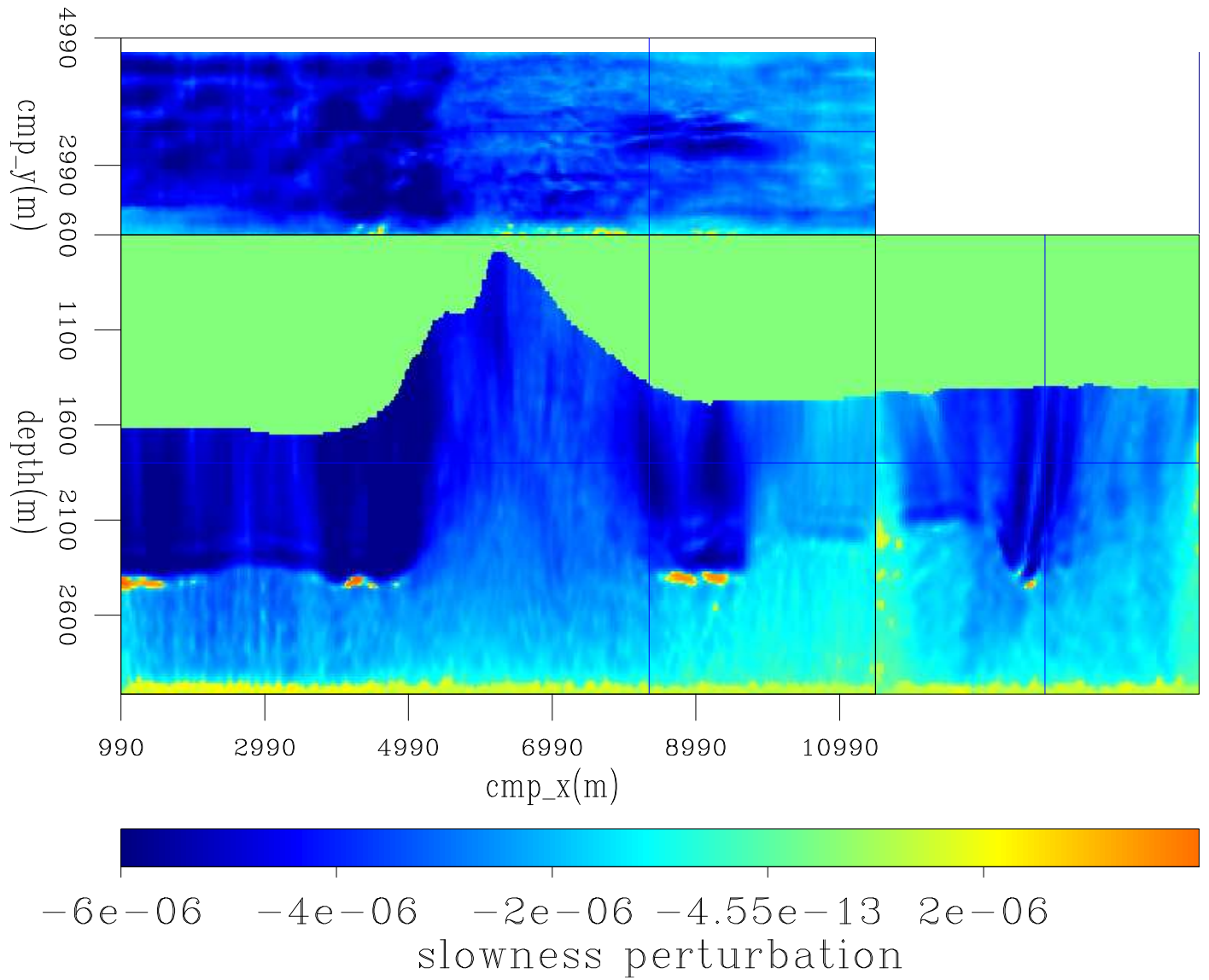


Figure 73: Slowness perturbation without smoothing and extracting the signed fourth root of the gradient.

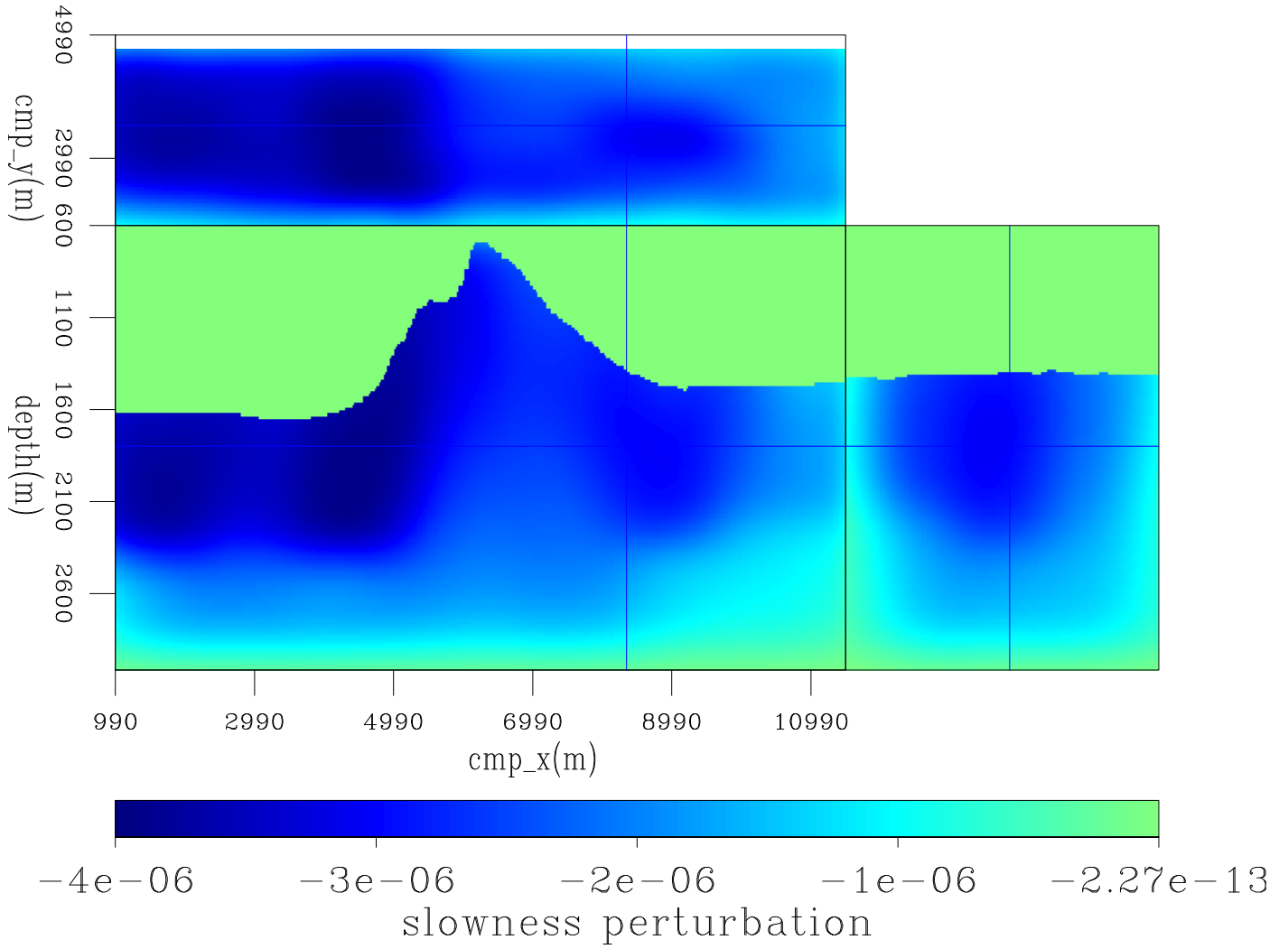


Figure 74: Slowness perturbation after B-spline smoothing the slowness perturbation of Figure 73.

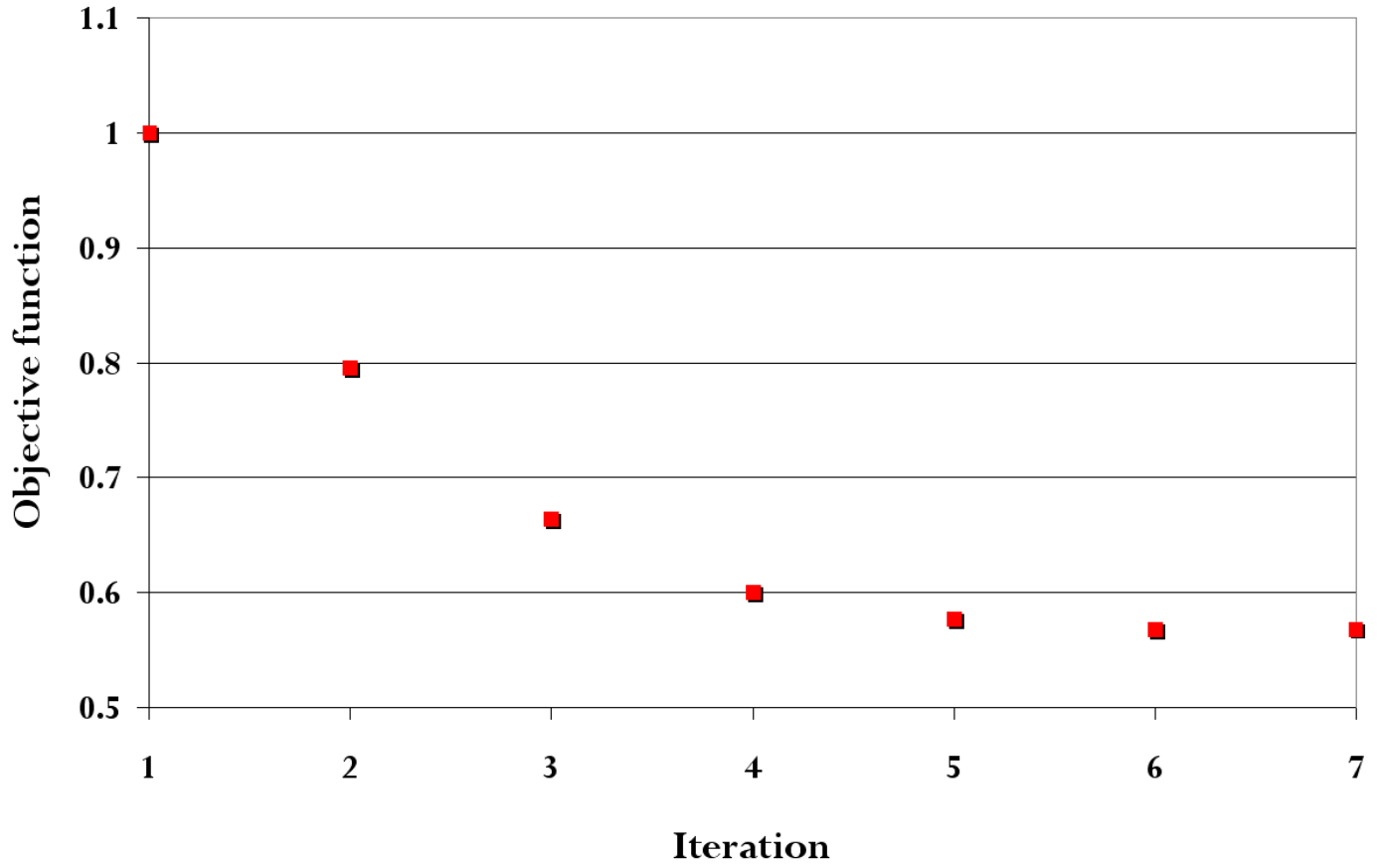


Figure 75: Evolution of the DVSA objective function for the first run of ISWET for the base of chalk.

iteration can be seen in Figures 76 and 77, respectively. On the left is the zero-subsurface-offset section, and on the right are the SODCIGs. Overall, the focusing around the zero subsurface offset improved. However, close to the salt flanks, SODCIGs still show events curving down, indicating velocity inaccuracy.

The velocity inaccuracy close to the salt flanks motivated a second run of ISWET for the base of chalk. Again, 30 pairs of ISPEWs were modeled, but from initial images limited to approximately 2 km around the salt body. By doing this, we explore the localized nature of these wavefields, as discussed in Chapter ??, so that this second run is targeted for updating the velocity close to the salt flanks. The optimized velocity for the second run of ISWET is shown in Figure 79. Migration velocity further increased compared to the optimized velocity of the first run (Figure 78). CAM using this optimized velocity is shown in Figure 80, which shows the volume for the zero subsurface offset, and Figure 81, which shows the zero subsurface offset on the top, and ADCIGs at the bottom for in-line 3180. Compare these figures with Figures 68 and 69, respectively. The optimized velocity model allowed imaging of a complex fault system on the right of the salt body, collapsing diffractions from the salt flank, and flattening reflectors in the ADCIGs.

SALT FLOODING

Once a sufficiently accurate velocity for the chalk layer had been defined, salt flooding was used to delineate the salt body. The top salt was interpreted, and below the velocity was replaced by a constant value of 4500 m/s (Figure 82). The picking of the top of salt is a source of uncertainty for defining the velocity model below, since it is difficult to manually interpret all the high-wavenumber components of the irregular top of salt. A solution to this problem should use automatic procedures to identify the top of salt (Lomask, 2006; Halpert, 2010).

The CAM migrated image (Figure 83) computed with the velocity of Figure 82 was sufficiently focused to support the interpretation of the base of the salt. As can be seen in Figure 83, the lack of a continuous reflector makes the interpretation of the base of salt challenging. Insufficient illumination due to the limited azimuthal coverage and irregular shape of the salt body caused the base of salt to be discontinuous. In this situation, prior geological information would be extremely helpful to constrain the interpretation. The lack thereof is another source of uncertainty for defining the velocity model below the salt.

After the base of salt was interpreted, the velocity was edited again (Figure 84), so that the salt velocity was confined within the salt body and the initial velocity was inserted below the salt and the chalk layer. With this new velocity model, another run of CAM generated the image in Figure 85 from which deeper reflectors are used to model new ISPEWs to be used in ISWET for deeper layers.

SOLVING FOR SUB-SALT VELOCITIES

On the prestack image of Figure 86, resulting from CAM with the sufficiently accurate velocity model for the chalk layer and the salt body, seven reflectors were interpreted (Figure 87) to be used as the initial conditions for the modeling of 3D ISPEWs for defining sub-salt velocities. Again, 30 pairs of 3D-source and -receiver ISPEWs were generated. These wavefields were collected at a depth of 1650 m, which is the minimum depth used in the velocity optimization. The prestack image used as the initial conditions for the modeling has 33 in-line subsurface offsets with 30 m intervals and a maximum offset 480 m. The CMP interval in the x and y directions is 30 m.

The initial velocity used in the sub-salt velocity optimization is shown in Figure 84. The shallower limit for velocity updating is represented by the base of chalk and base of salt, and the deeper limit is 4800 m. The interval between B-spline nodes is 1050 m in the x and y directions and 150 m in the z direction. A maximum of 5% local velocity variation is allowed between iterations, and two function evaluations are performed in the line search.

The evolution of the objective function normalized by its initial value is shown in Figure 88. Velocity optimization stopped after 7 iterations because the update of the objective function was smaller than 0.1%. The final objective function dropped 10%. This decrease is small compared to the 40% decrease of the objective function for the velocity optimization of the base of chalk. For the chalk case, only crosstalk from different SODCIGs was generated because only one reflector was used to generate the 3D ISPEWs. For the sub-salt case, in addition to the crosstalk from different SODCIGs, reflector crosstalk was generated since seven reflectors were used as the initial conditions. Hence, the amount of background dispersed crosstalk is greater in the sub-salt case than in the chalk case, explaining the smaller decrease of the objective function in the sub-salt velocity optimization.

The evolution of the velocity model through iterations is shown in Figure 89.

CAM with the optimized velocity model can be seen in Figure 90. For comparison, CAM with the initial velocity model and CAM with the original velocity model are shown in Figures 91 and 92. When compared with the results using the initial velocity model, the improvements obtained with the optimized velocity model are clear: flatter angle gathers, better focusing of the reflectors, and imaging of the faults. The improvements compared to the original (unmodified) velocity model are also clear: better focusing of reflectors and slightly flatter angle gathers below the salt as well as close to its flanks.

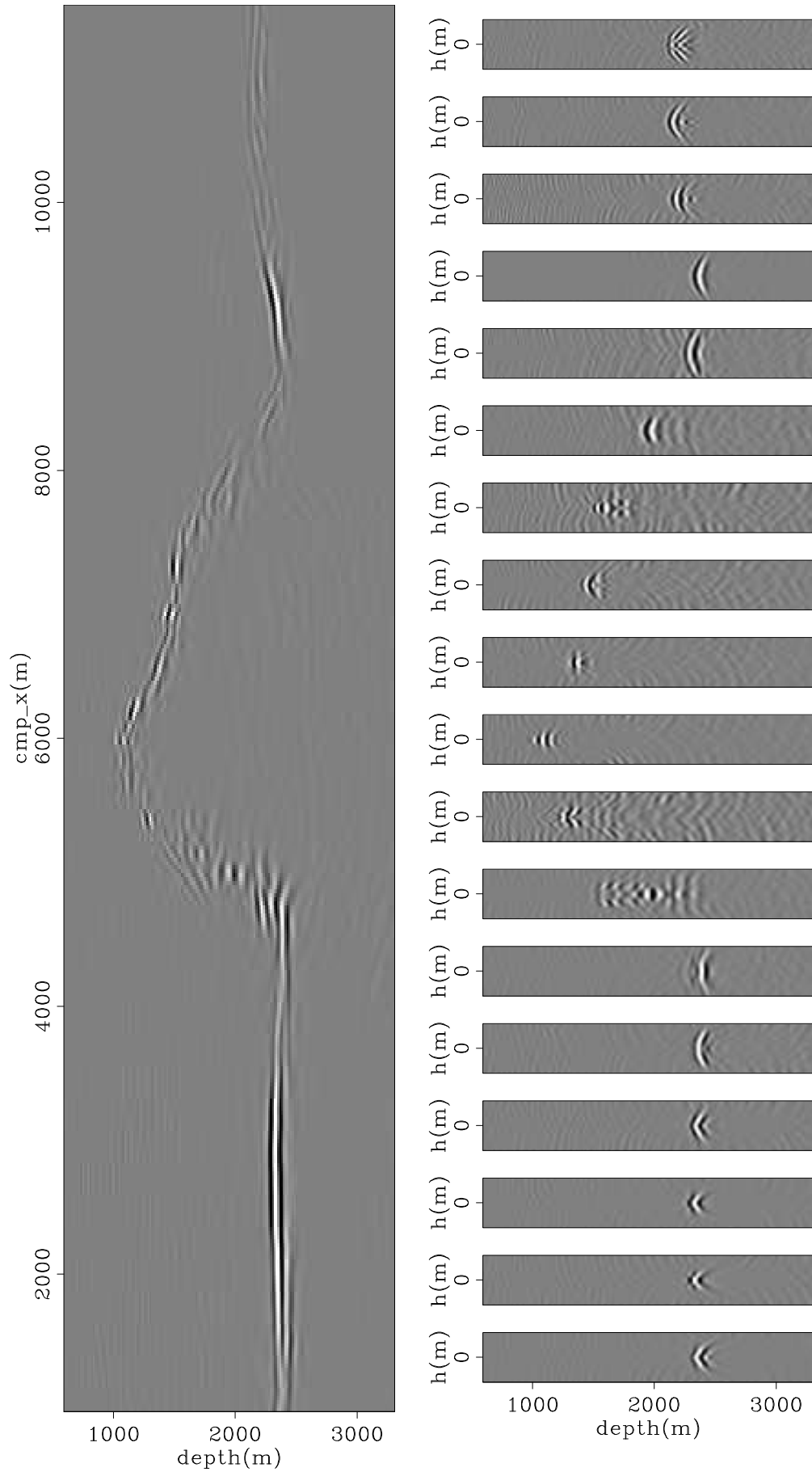


Figure 76: In-line 3520 of the initial background image of the first run of ISWET for the base of chalk.

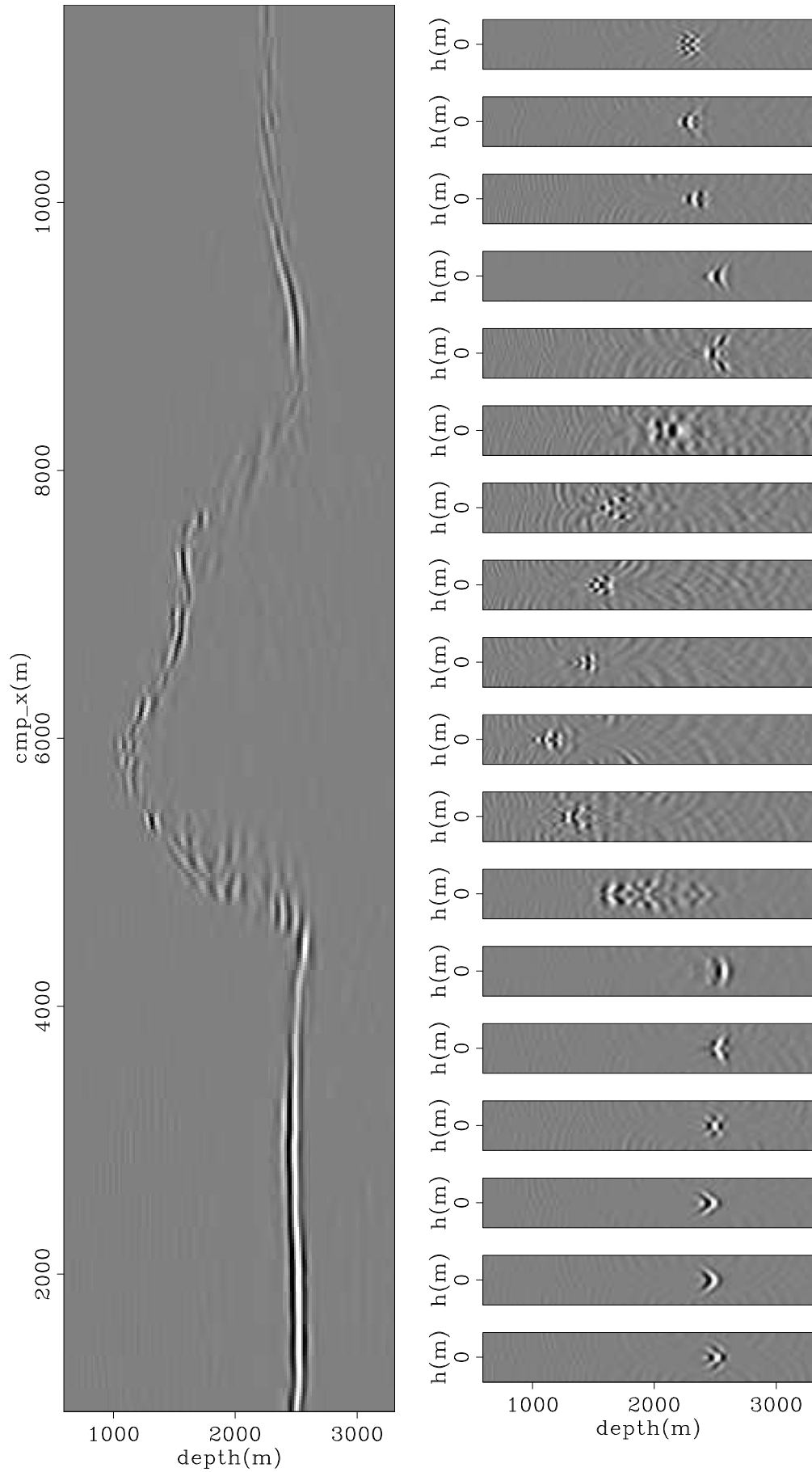


Figure 77: In-line 3520 of the background image computed with the optimized velocity model of the first run of ISWET for the base of chalk.

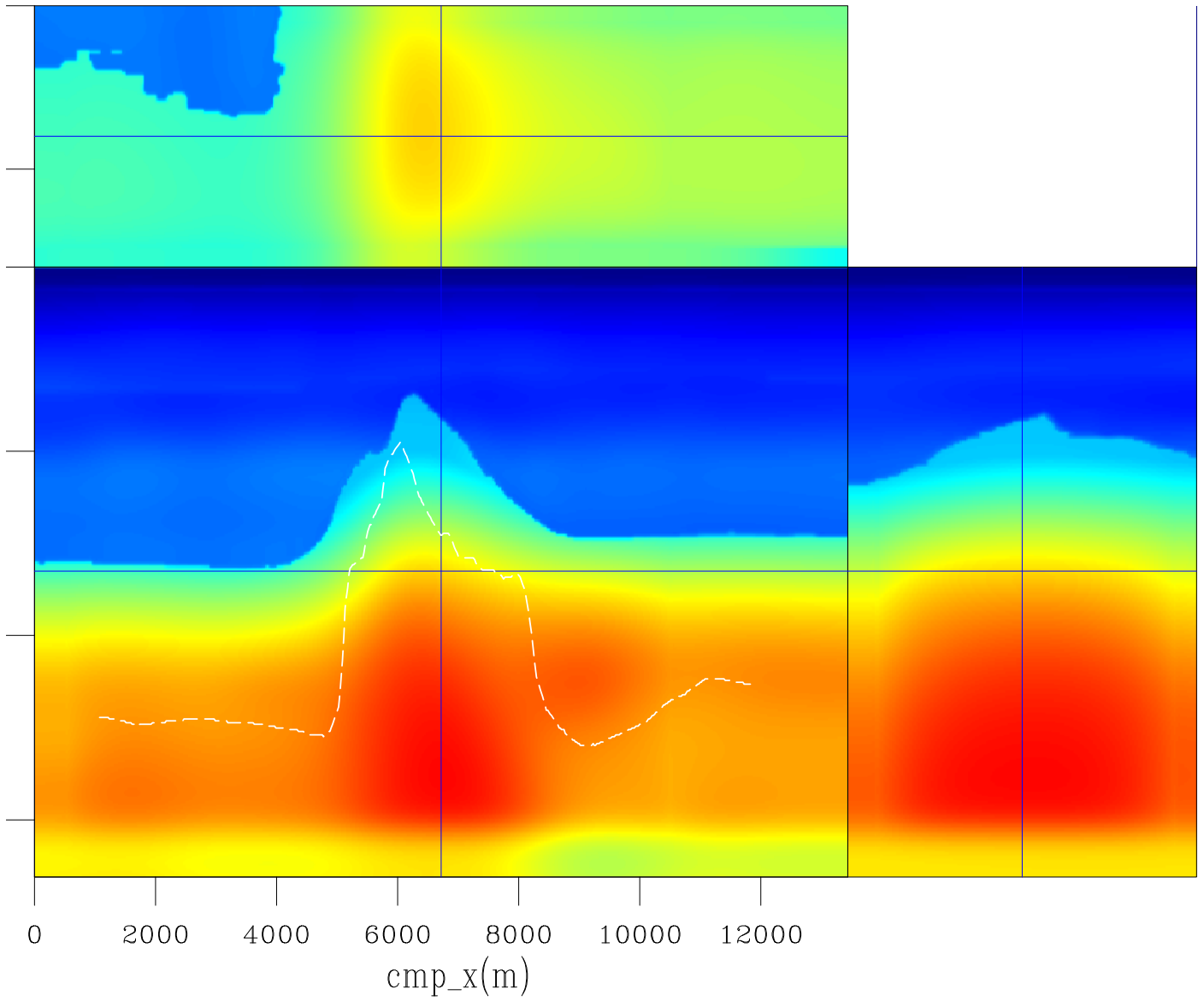


Figure 78: Slices through the optimized velocity from the first run of ISWET for the base of chalk. The dashed white line approximately represents the base of chalk.

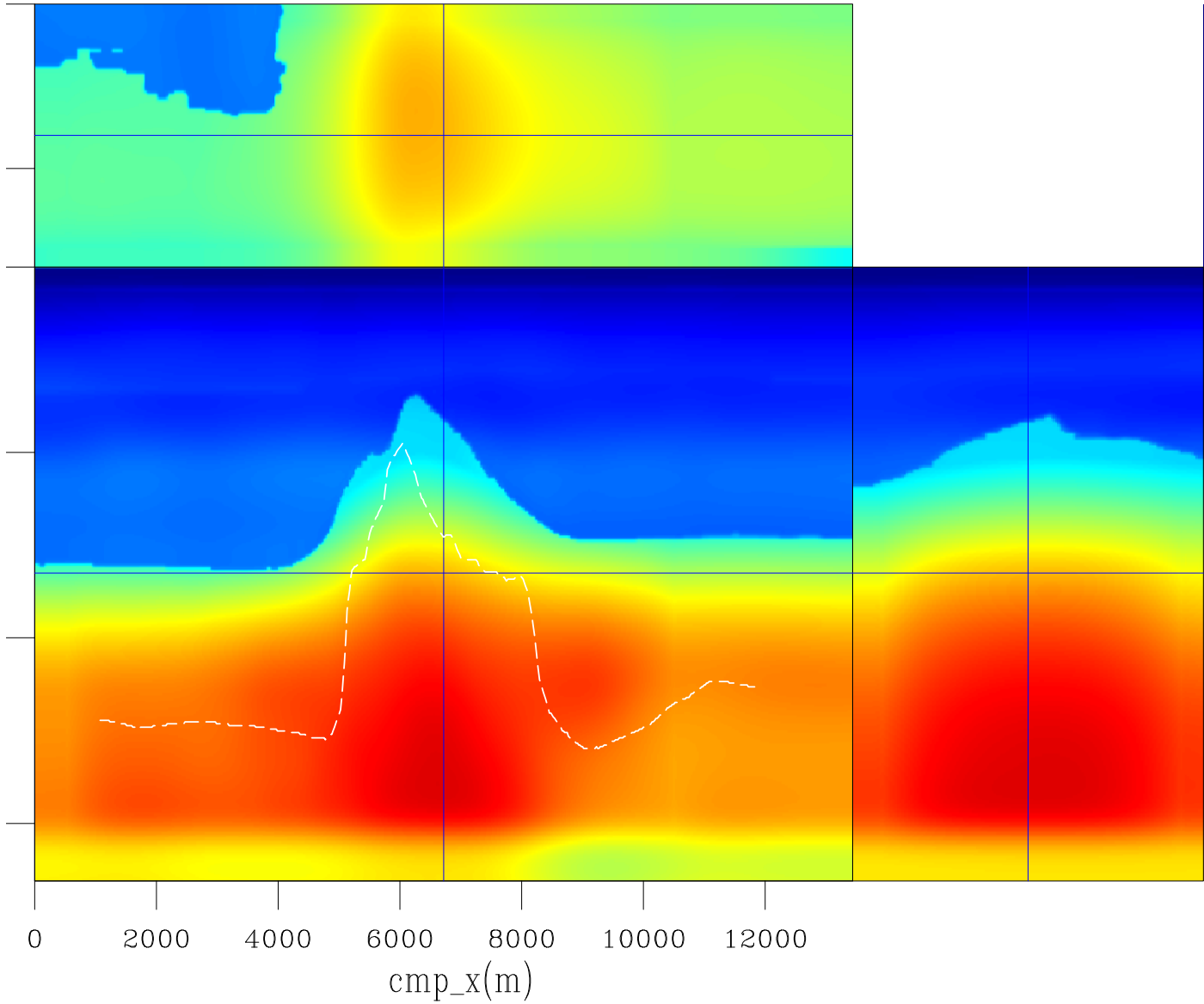


Figure 79: Slices through the optimized velocity from the second run of ISWET for the base of chalk. The dashed white line approximately represents the base of chalk.

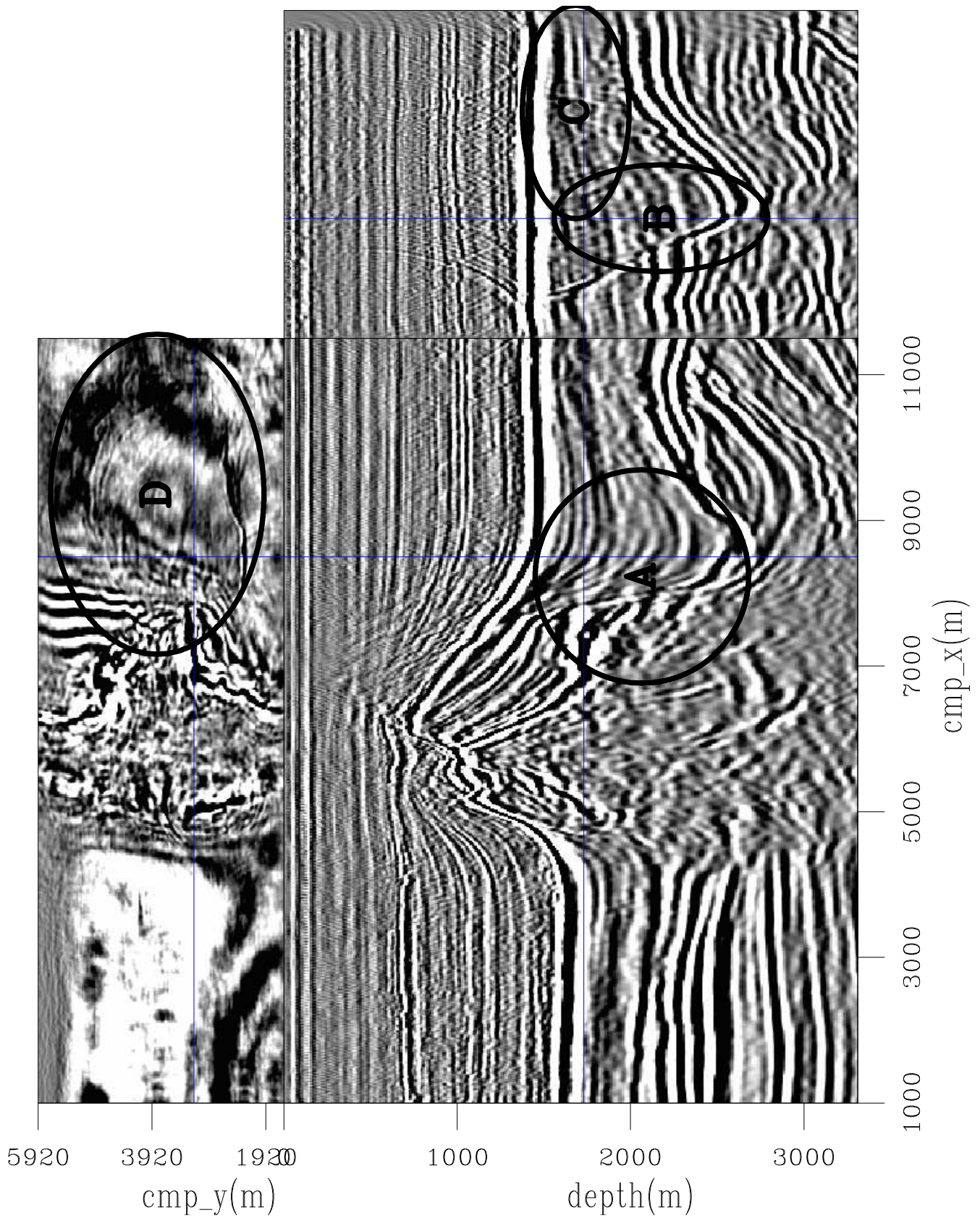


Figure 80: Slices through the CAM image with the optimized velocity model of Figure 79. Notice the imaging of a big fault close to the salt flank (A), and the focusing of a complex fault system (B, C, and D).

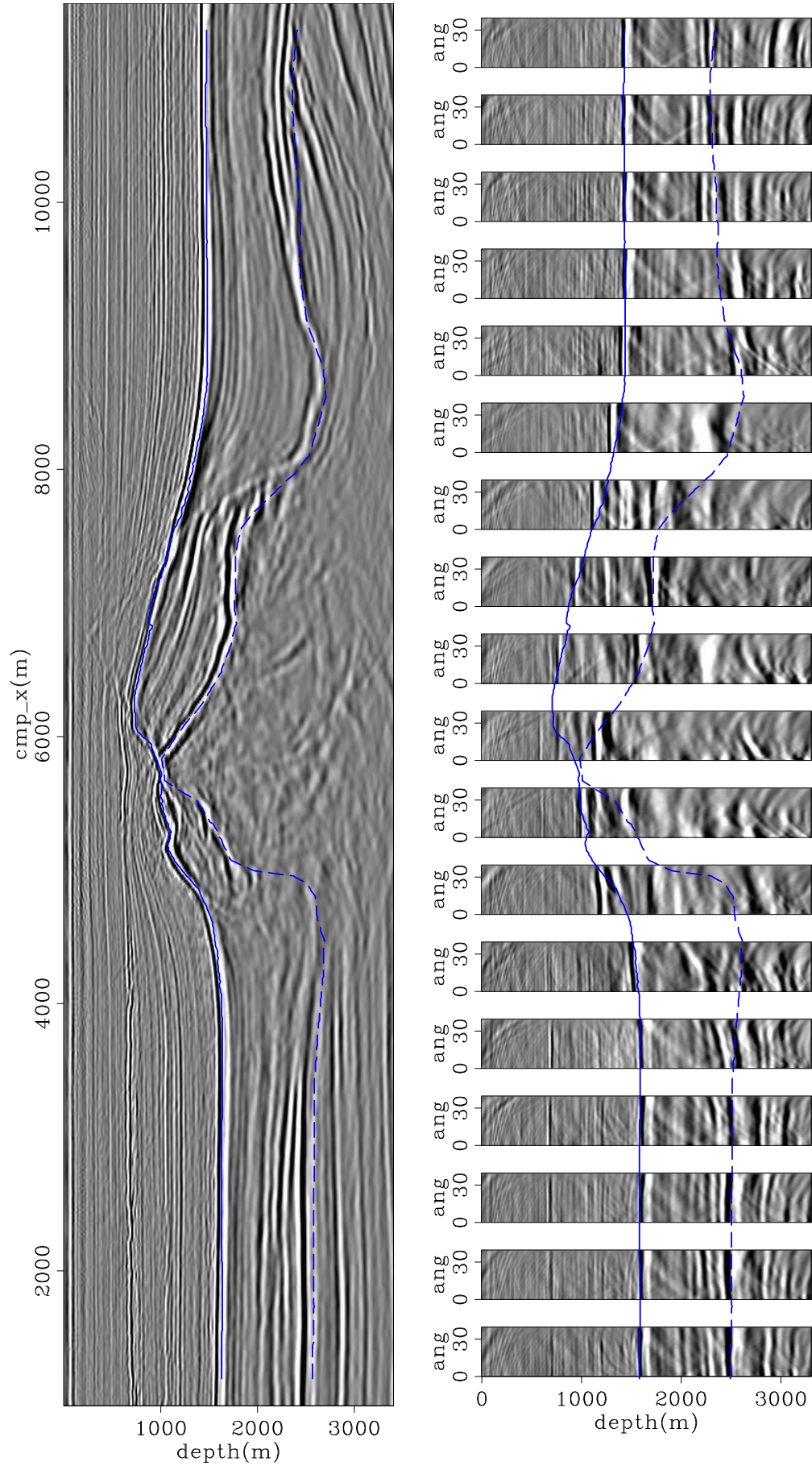


Figure 81: In-line 3180 of the CAM image with the optimized velocity model of Figure 79. On the left is the zero-subsurface offset section, and on the right ADCIGs. Notice flatter reflectors in the ADCIGs compared to those in Figure 69. The continuous blue line is the top of chalk, and the dashed blue line it the base of chalk.

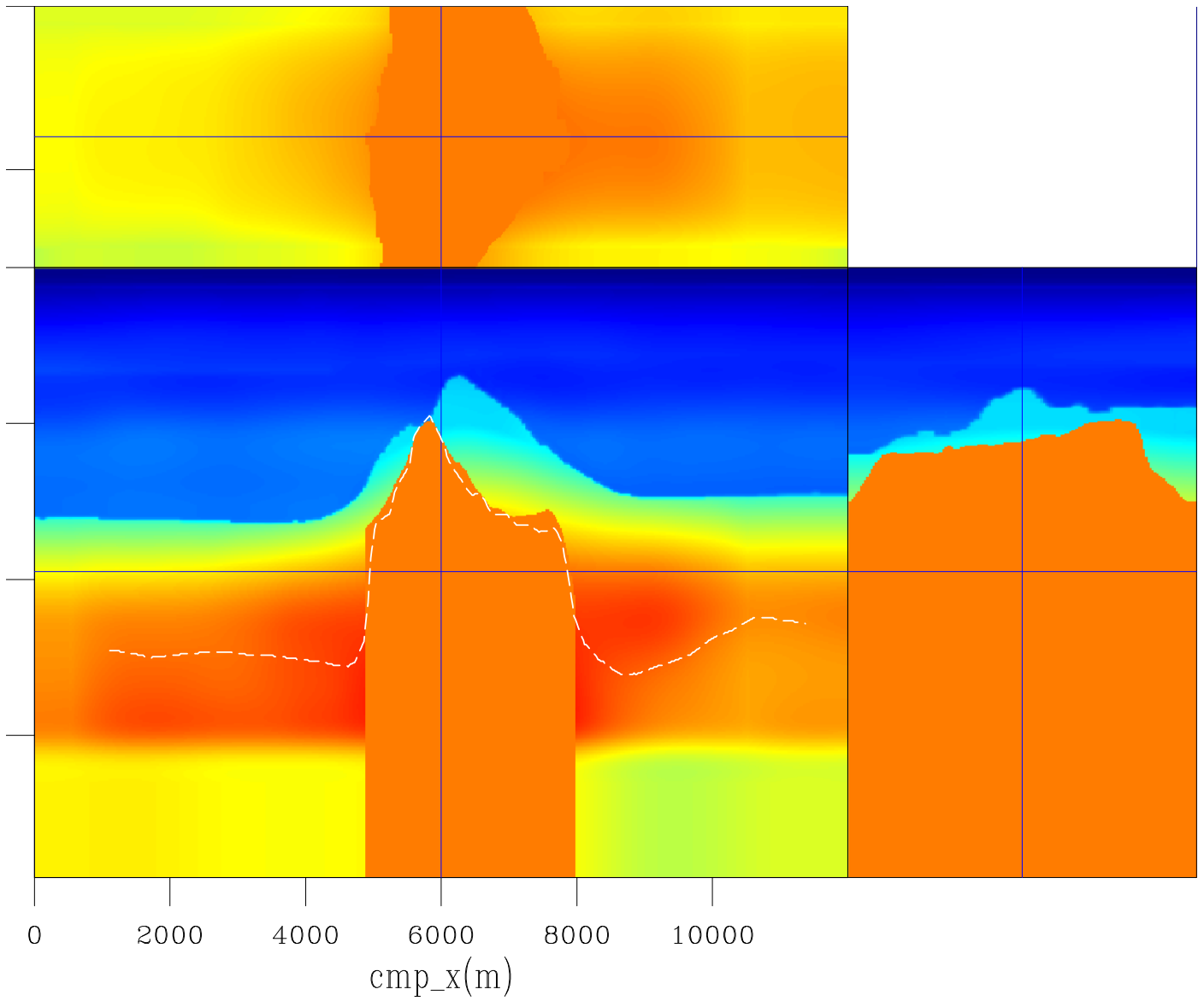


Figure 82: Slices through the velocity volume after salt flooding. The dashed white line approximately represents the base of chalk.

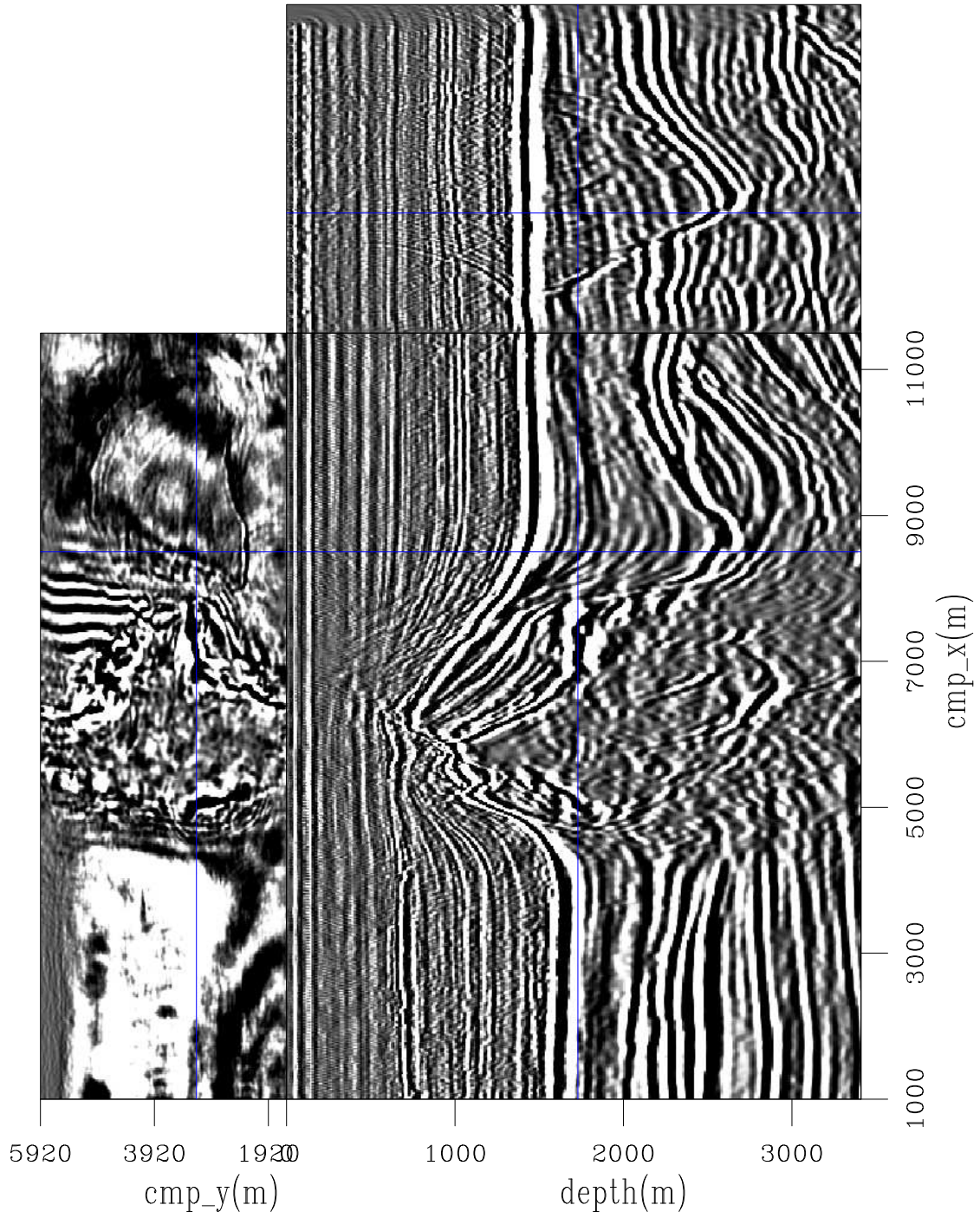


Figure 83: Slices through the CAM migrated image computed with the salt flooding velocity model of Figure 82.

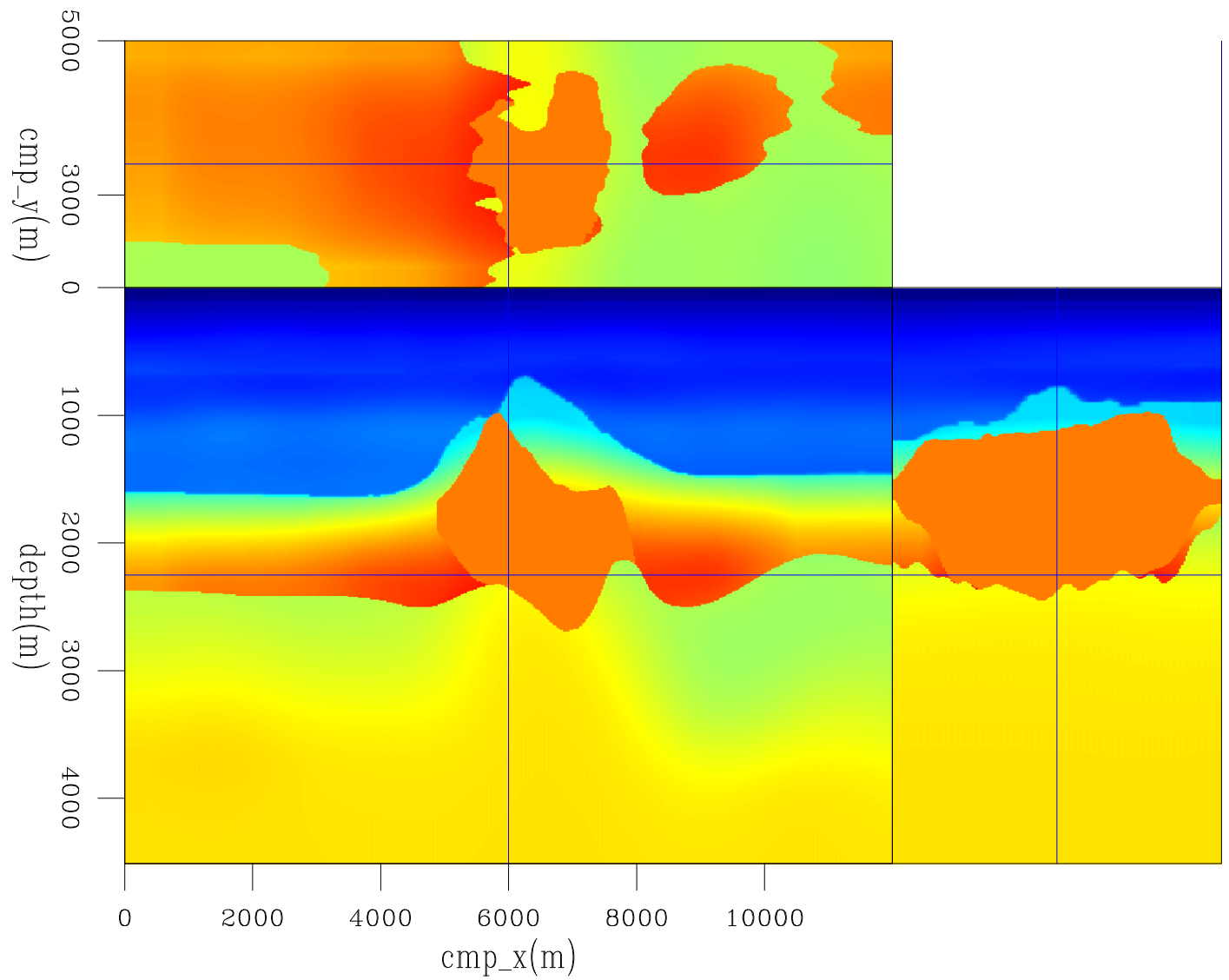


Figure 84: Slices through the velocity volume after interpretation of the base of salt.

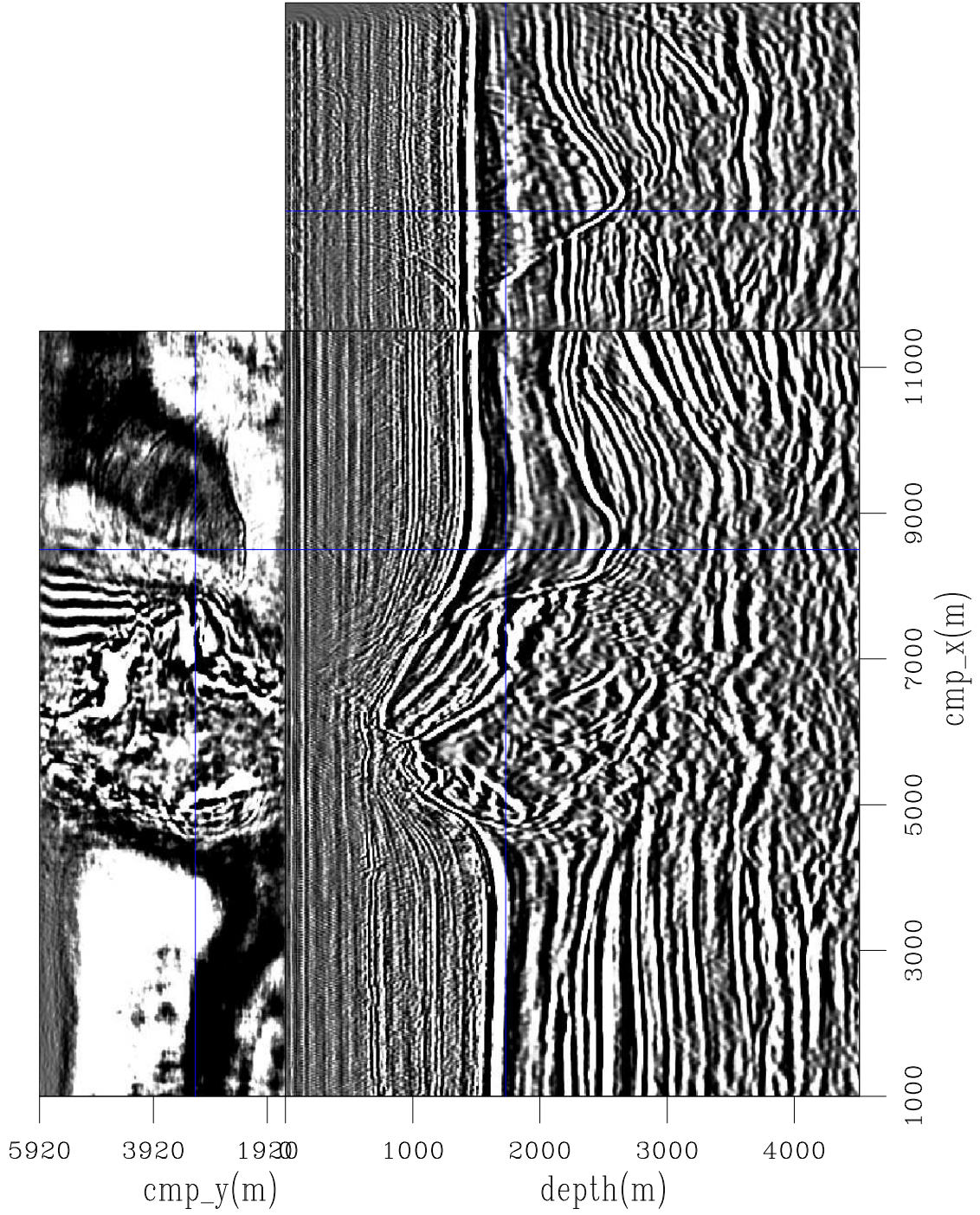


Figure 85: Slices through the CAM migrated image computed with the velocity model of Figure 84.

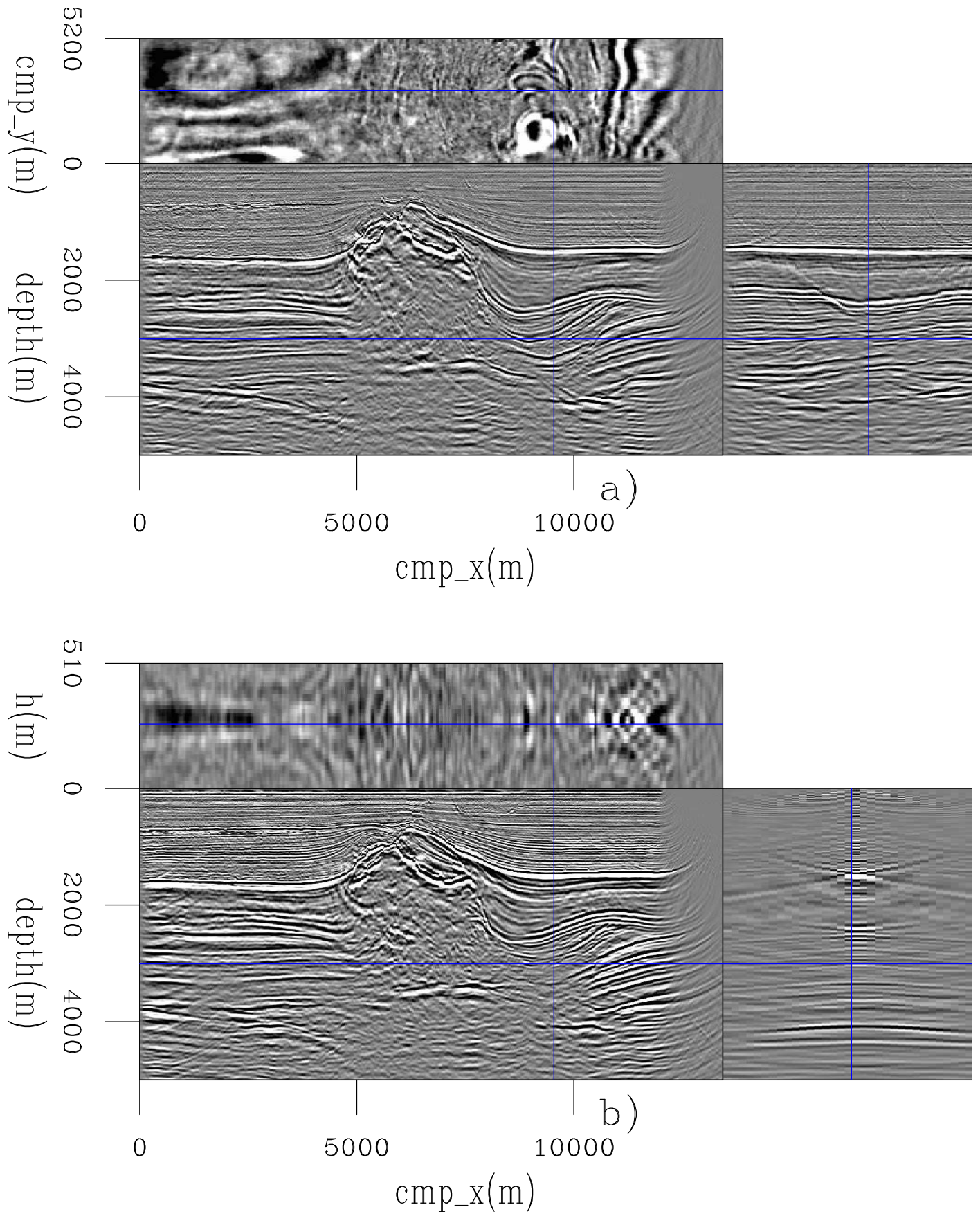


Figure 86: Slices through the prestack image computed with the migration velocity of Figure 84: a) the zero subsurface offset, and b) the in-line 3520.

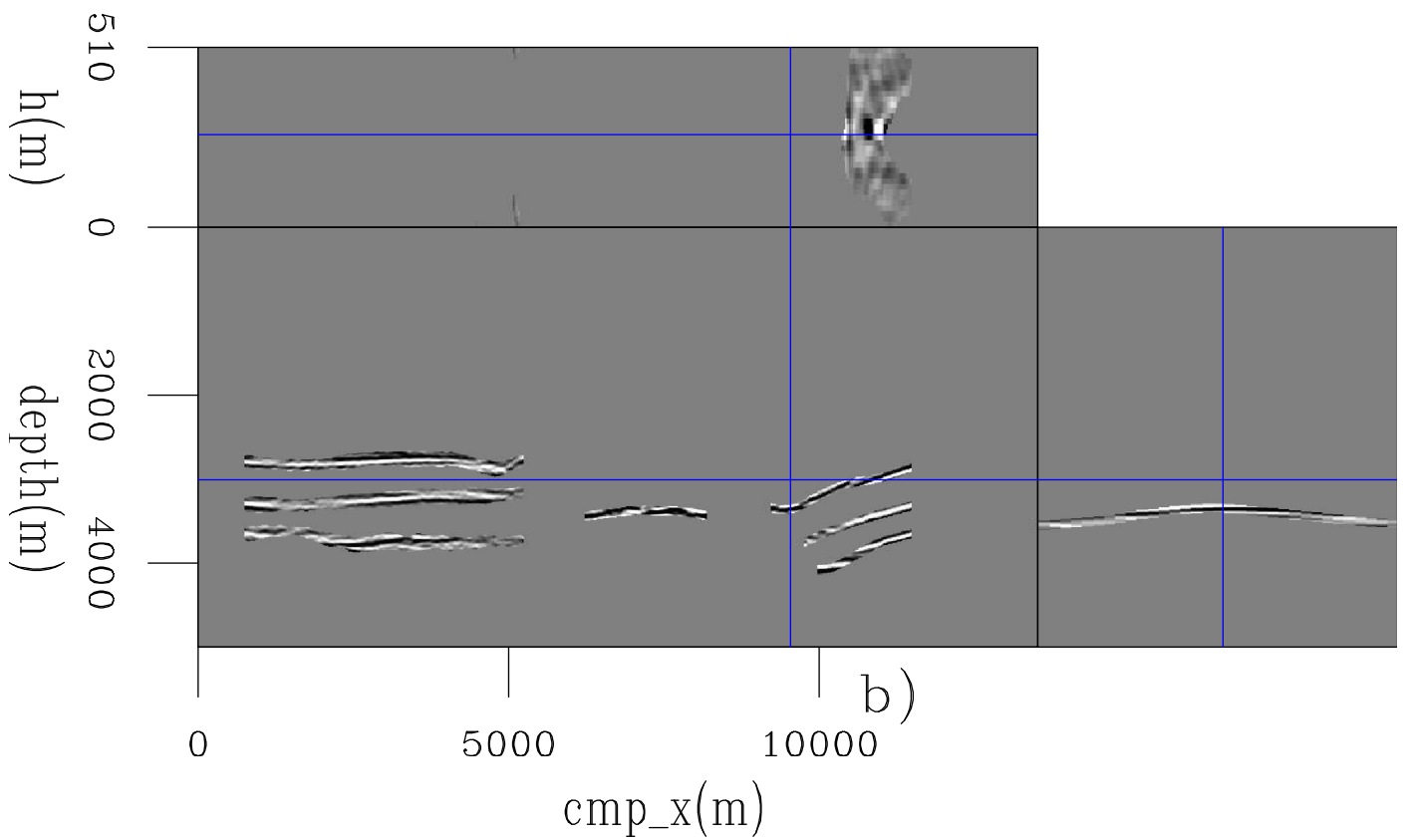
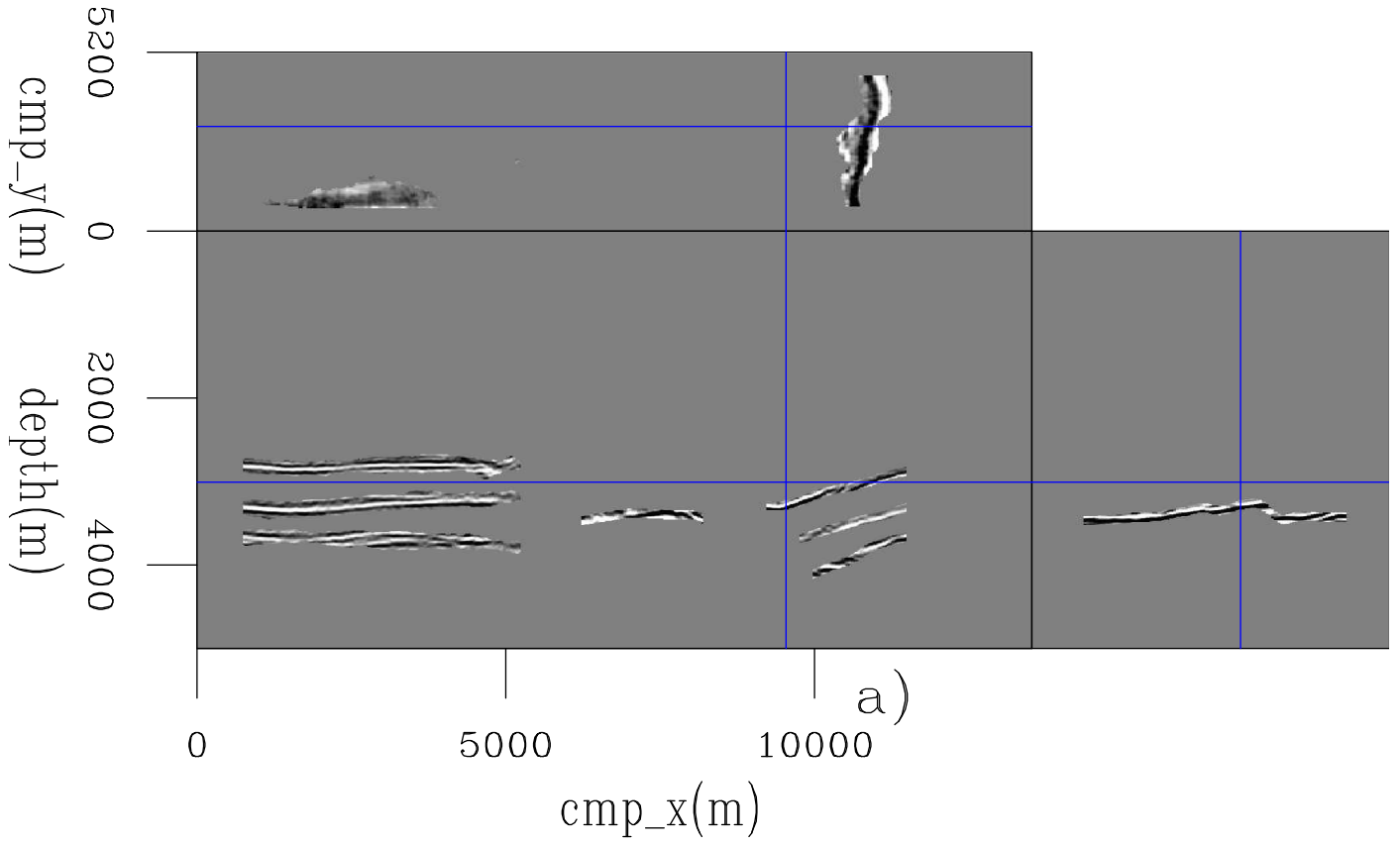


Figure 87: Slices through the windowed prestack image, showing the selected reflectors for the modeling of 30 3D ISPEWs to be used in the sub-salt velocity optimization: a) the zero subsurface offset, and b) the in-line 3520.

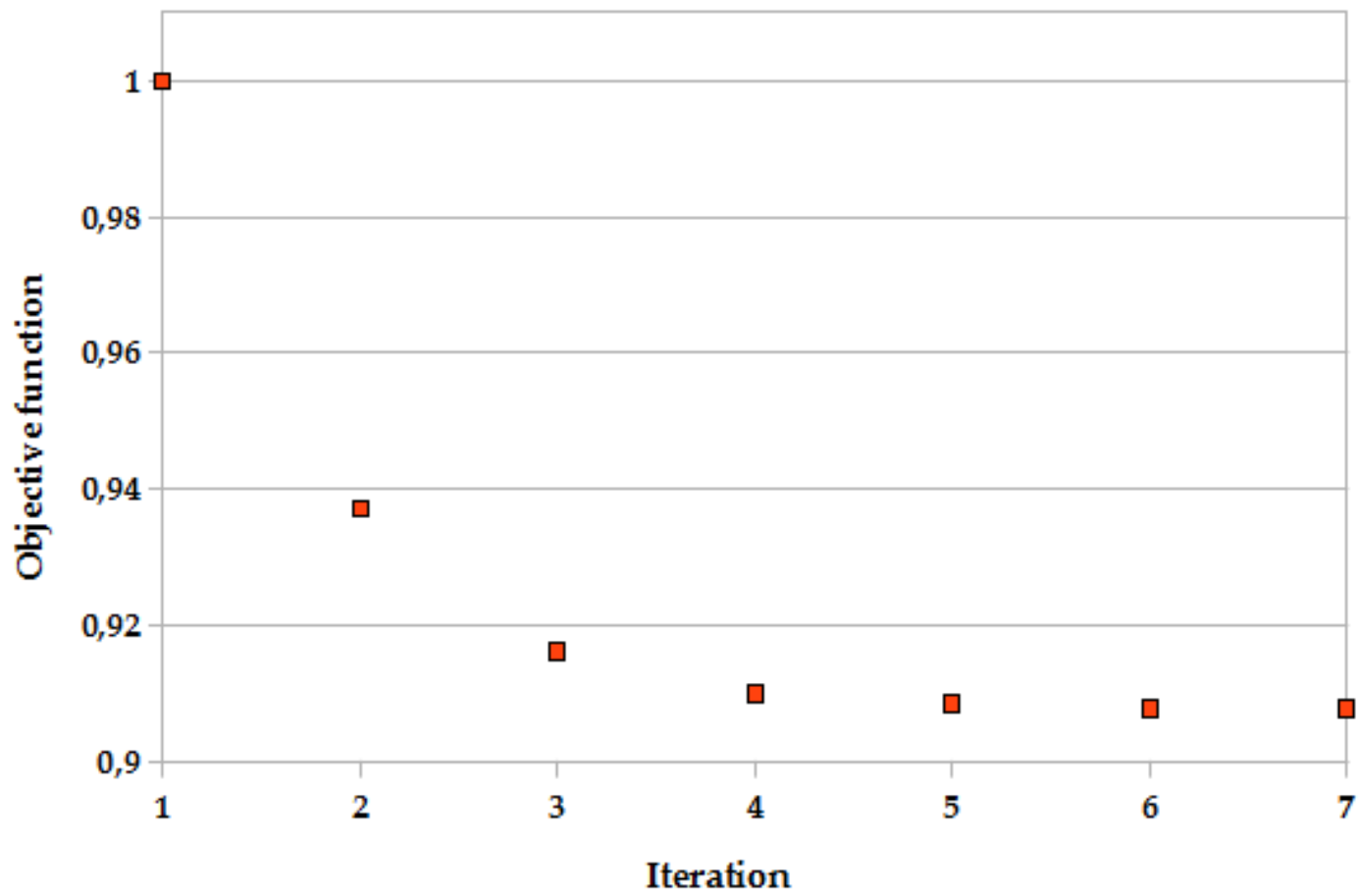


Figure 88: Evolution of the DVSA objective function of the sub-salt velocity optimization.

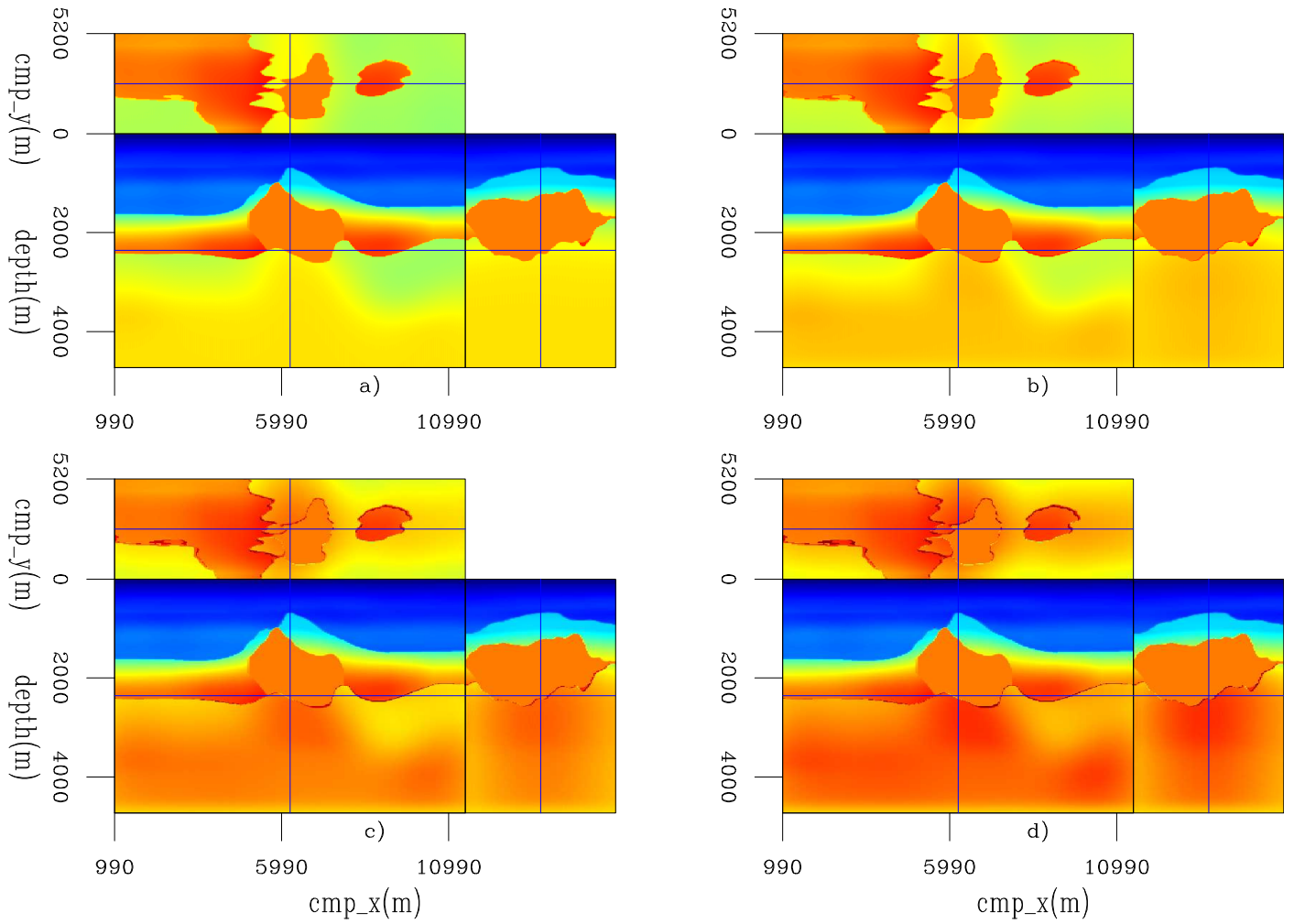


Figure 89: Slices through velocity models for: a) first iteration, b) third iteration, c) fifth iteration, and d) seventh iteration.

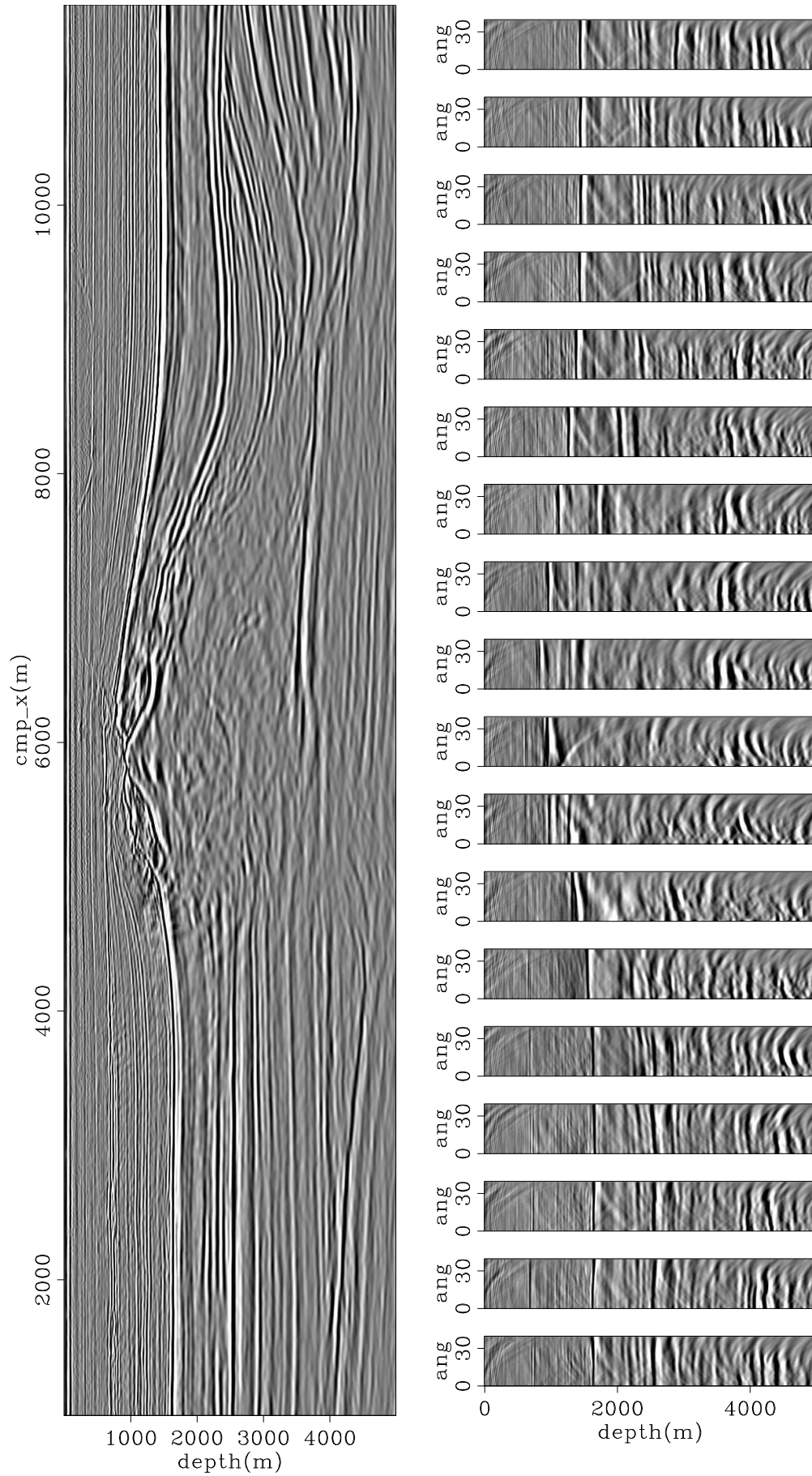


Figure 90: In-line 4060 of the CAM image with the final velocity model after optimization for the chalk layer, salt flooding, and sub-salt velocity optimization. On the top is the zero-subsurface offset section, and at the bottom ADCIGs.

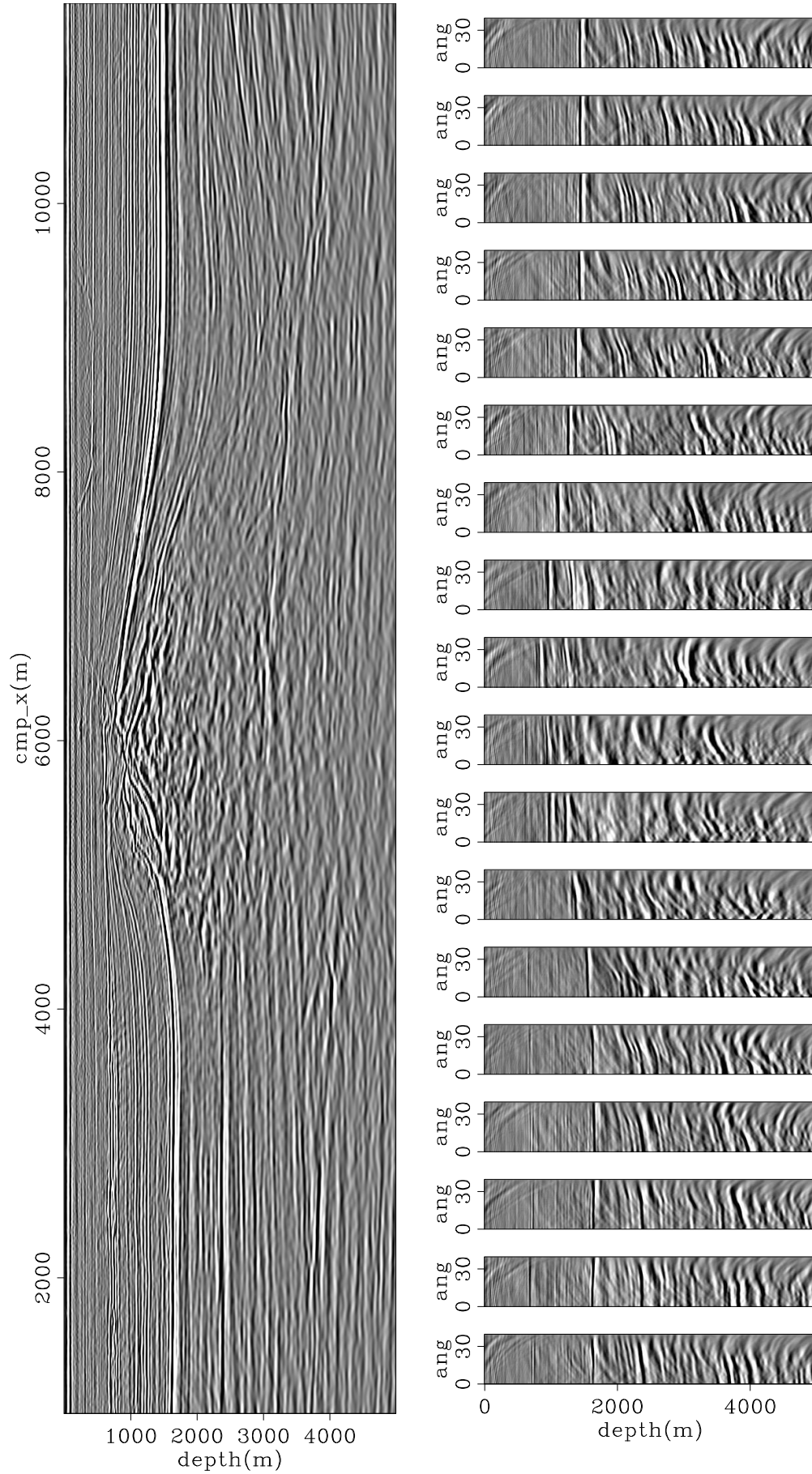


Figure 91: In-line 4060 of the CAM image with the initial velocity model. On the top is the zero-subsurface offset section, and at the bottom ADCIGs.

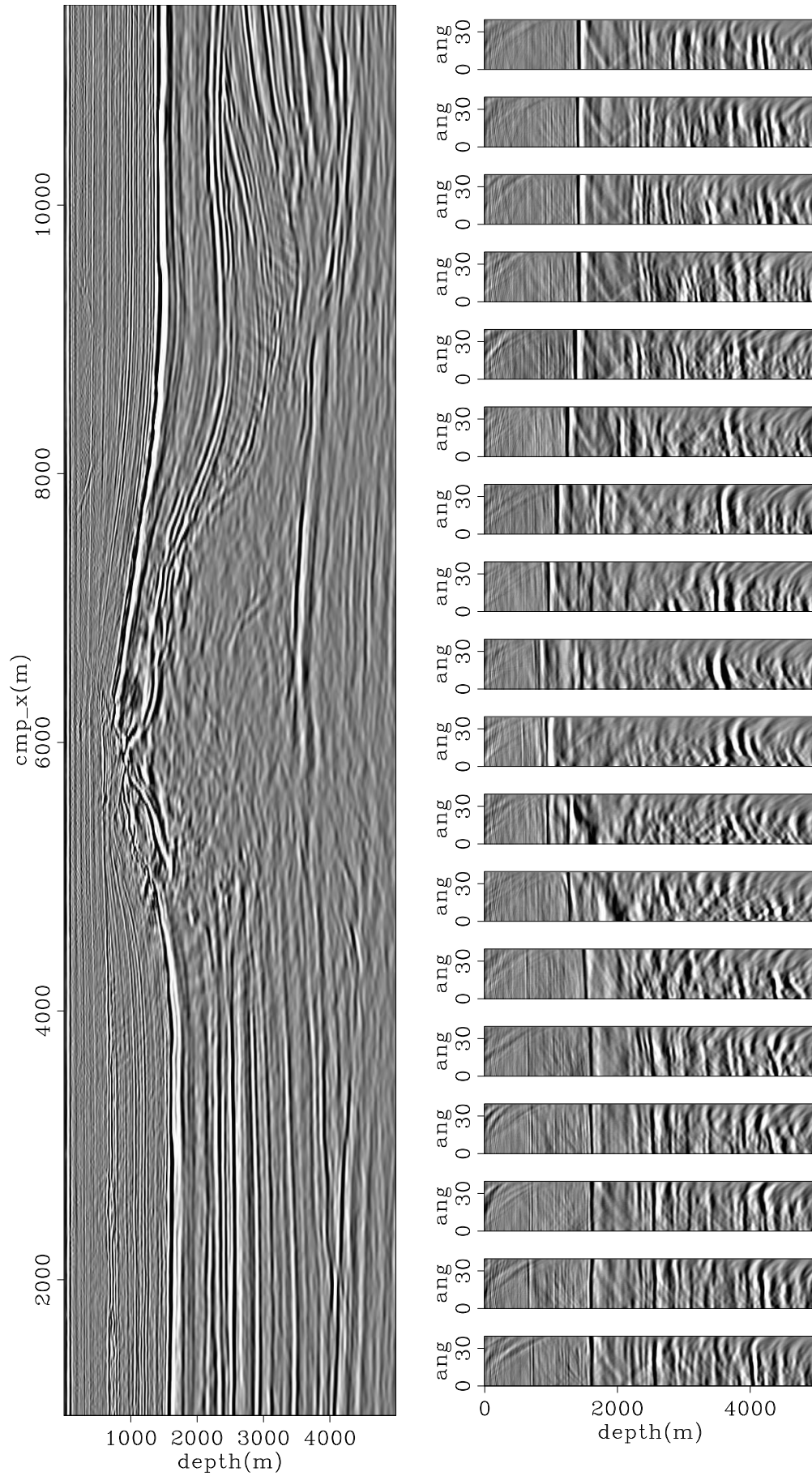


Figure 92: In-line 4060 of the CAM image with the original velocity model. On the top is the zero-subsurface offset section, and at the bottom ADCIGs.

Next, I show more systematic comparisons of the results computed with the initial, original and the final velocity models.

COMPARISONS

Here, I show three comparisons between the CAM images obtained with the initial, with the original, and with the final velocity models, for different in-lines and cross-lines. The images are displayed as vertical slices through the migrated cube and show the zero subsurface offset. The left panel of each figure shows the in-line, and the right panel shows the cross-line.

Figure captions explain the differences highlighted by ovals. Overall, the final images present better quality than do the initial and original images, expressed by better focusing and continuity of reflectors in the chalk layer as well as in the sub-salt region. Certainly, the final image would ease interpretation and understanding of geological and structural history, adding more value to seismic information in an exploratory study.

CONCLUSIONS

The 3D-field data North Sea turned out to be a very challenging dataset. The challenges were represented by the narrow azimuth configuration and irregular fold of coverage, causing incomplete and irregular illumination of the reflectors. Also, the irregular salt body and intense faulting were difficult targets to delineate and image. The problems with the illumination, evidenced by amplitude irregularity of the gradient of the objective function, were mitigated by properly scaling the prestack image used to model the 3D ISPEWs and the gradient of the objective function, and by smoothing the gradient of the objective function.

Using 3D ISPEWs has proved to greatly accelerate 3D ISWET, due to the small number of wavefields needed to satisfactorily describe the kinematics of the prestack image and the fact that they are computed in a target-oriented manner. These synthesized wavefields made it possible to solve 3D ISWET in an academic environment with limited computational resources. Considering the computational resources available in the industry, using 3D ISPEWs can turn 3D ISWET an interactive process, which can yield more reliable solutions.

Solving for migration velocity in a target-oriented manner with wave-equation methods allows updating the velocity model not only within a limited depth range, but also within a limited lateral extent. This is achieved by selecting a specific portion of a reflector or group of reflectors that still present residual moveout. This feature was demonstrated when updating the velocity model in the vicinity of the salt body, using only a small portion of the reflector corresponding to the base of chalk close to the salt.

Besides the computational gain, 3D ISPEWs were able to provide reliable velocity updates. Using the final velocity model produces a CAM image with quality superior to that obtained with the initial velocity model, as expected. Moreover, the image computed with the final velocity model is more accurate than that computed with the original velocity model, with better focusing and continuity of the sub-salt reflectors and better fault imaging.

ACKNOWLEDGMENTS

I would like to thank Bob Clapp for making available the common-azimuth migration code and for continuously improving SEP's 3D-interpretation and visualization capability. I am indebted to Dennis Michael, manager of the High Productivity Technical Computing (HTPC) initiative hosted by CEES, for his continuous support.

Conclusions This thesis focuses on using novel generalized wavefields, the image-space generalized wavefields, to increase the computational efficiency and improve flexibility of ISWET specially in 3D. The computational efficiency is achieved by the data reduction and the use of a target-oriented strategy enabled by image-space generalized wavefields. The flexibility comes from the fact that key horizons are selected to initiate the wavefields, which naturally incorporates a horizon based strategy into ISWET and enables to laterally limit the velocity updates. Although the thesis concentrates on migration-velocity analysis by wavefield methods, the images obtained with image-space generalized wavefields can also be used in migration-velocity analysis by ray-based methods.

Chapter ?? addresses the modeling of image-space generalized wavefields using the pre-stack exploding-reflector model. Pre-stack migrated images computed by wave-extrapolation methods are used as the initial conditions for the modeling. I describe all the necessary steps to generate kinematically correct wavefields, so that the moveout information for migration-velocity analysis is maintained. I show that in 3D data size reduction is significant, specially when using common-azimuth migrated images as the initial conditions. In this case, the number of wavefields is decreased by an order of magnitude when compared to that modeled with multi-azimuth migrated images.

Chapter takes further data reduction obtained in Chapter ?? by increasing the number of wavefields simultaneously modeled combined with phase-encoding techniques to mitigate crosstalk. I describe how crosstalk is created and propose different strategies for attenuating it.

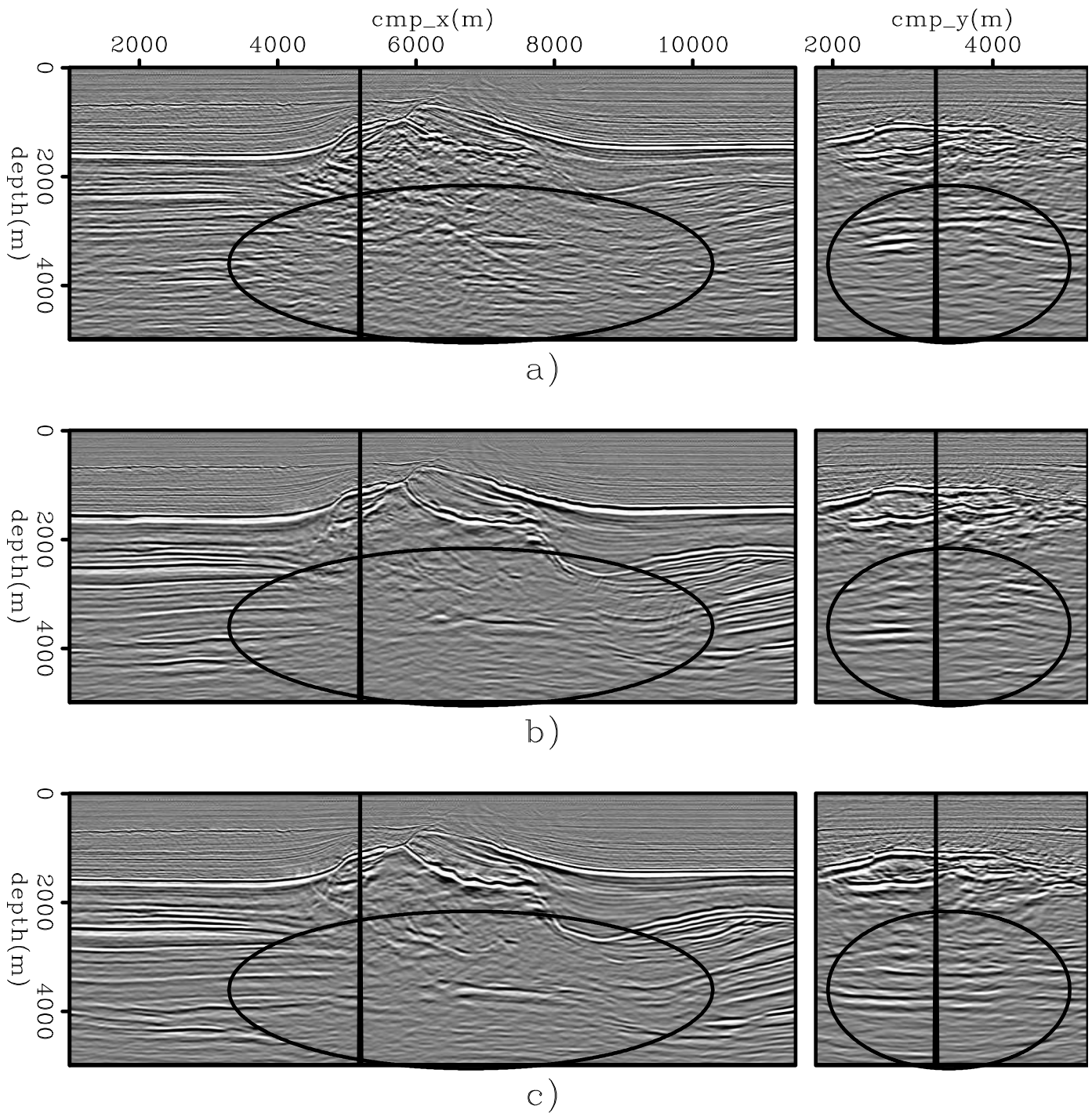


Figure 93: On the left panel is the in-line 3320 and on the right panel is the cross-line 5220 of the CAM images obtained with: a) the initial velocity model, b) the original velocity model, and c) the final velocity model after optimization for the chalk layer, salt flooding, and sub-salt velocity optimization. The oval in the in-line of the final image shows better focusing and continuity for the sub-salt reflectors as well as for the salt flank. Besides focusing and continuity, the oval in the cross-line of the final image shows unstructured sub-salt reflectors not pulled up by velocity errors.

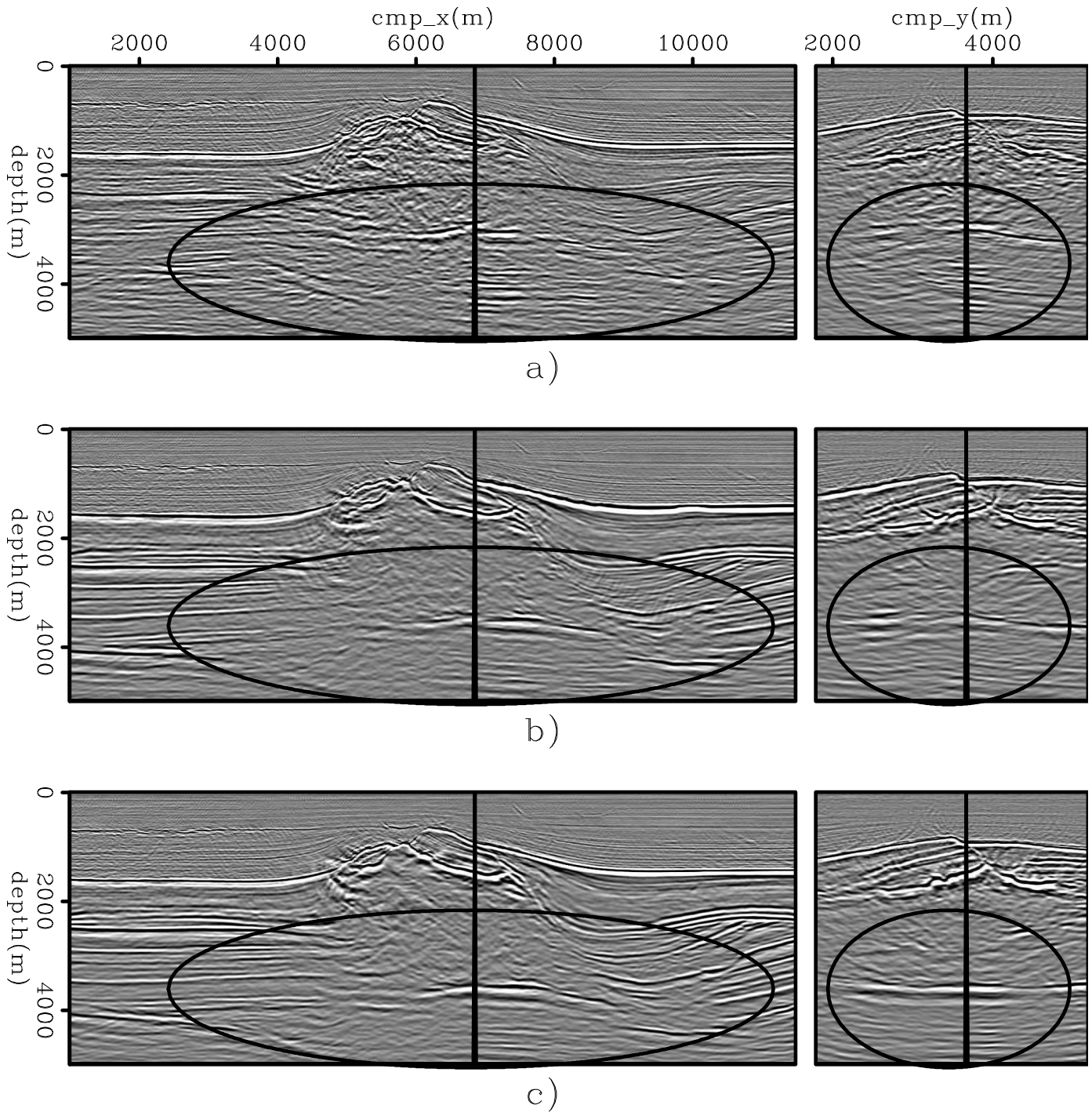


Figure 94: On the left panel is the in-line 3680 and on the right panel is the cross-line 6880 of the CAM images obtained with: a) the initial velocity model, b) the original velocity model, and c) the final velocity model after optimization for the chalk layer, salt flooding, and sub-salt velocity optimization. The oval in the in-line of the final image shows better focusing and continuity for the sub-salt reflectors. Besides focusing and continuity, the oval in the cross-line of the final image shows unstructured sub-salt reflectors not pulled up by velocity errors.

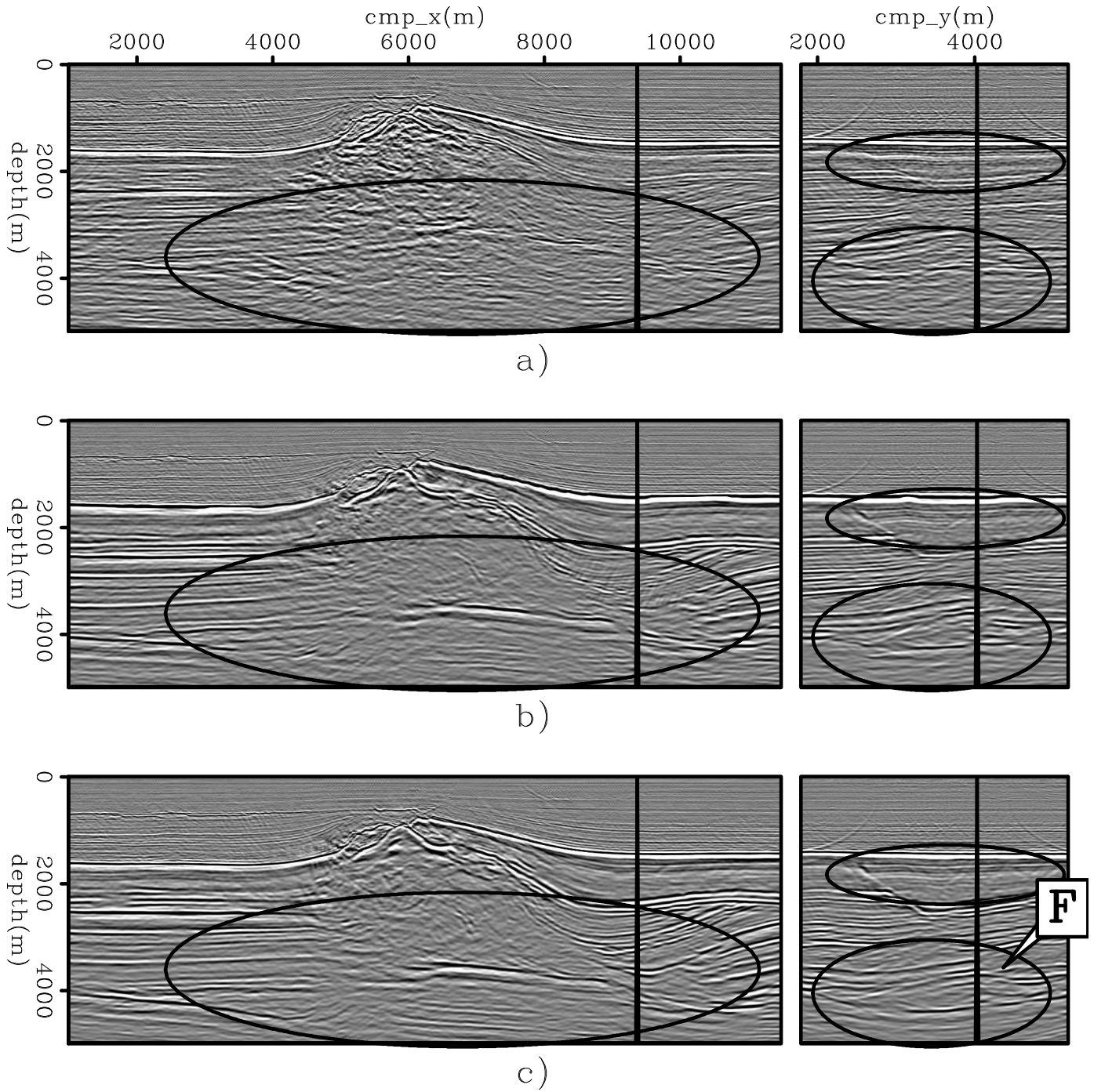


Figure 95: On the left panel is the in-line 4060 and on the right panel is the cross-line 9400 of the CAM images obtained with: a) the initial velocity model, b) the original velocity model, and c) the final velocity model after optimization for the chalk layer, salt flooding, and sub-salt velocity optimization. The oval in the in-line of the final image shows better focusing and continuity for the sub-salt reflectors. In the cross-line, the upper oval of the final image shows better definition of subtle faults in the chalk layer, the lower oval highlights better continuity of the reflectors, and the arrow labeled "F" indicates better fault imaging not clear in the initial and original images.

Chapter extends ISWET from the shot-profile domain to the image-space generalized-sources domain. I describe how the gradient of the DVSA objective function is obtained with wavefields defined in this new domain and give examples on the velocity optimization using the Marmousi model. ISWET was solved in a target-oriented way and the optimized migration-velocity models adequately describe the long-wavelength components of the true velocity models. The migrated images using these optimized models show remarkably good quality.

Chapter applies the theory developed in the previous chapters to a 3D-field data from the North Sea. The challenges this dataset introduces are the amplitude variation due to acquisition footprints, the insufficient illumination due to the narrow azimuth distribution in the presence of an irregular salt body, and the short offsets. Moreover, the lack of geological information to define the salt body shape represents the main uncertainty for the velocity model definition; nevertheless, the final optimized velocity model yields a migrated image of superior quality compared to that obtained with the initial model. The final image also presents superior quality when compared to the image computed with the velocity model available in SEP's database, showing better-focused and continuous sub-salt reflectors and better fault imaging.

The computational efficiency and flexibility achieved with image-space generalized wavefields enables the use of ISWET as a routine procedure to define the 3D-migration-velocity model in areas of complex geology.

REFERENCES

- Bagaini, C., 2006, Overview of simultaneous vibroseis acquisition methods: SEG Technical Program Expanded Abstracts, **25**, 70–74.
- Ben-Hadj-Ali, H., S. Operto, and J. Vineux, 2009, Three-dimensional frequency-domain full waveform inversion with phase encoding: SEG Technical Program Expanded Abstracts, **28**, 2288–2292.
- Bernstein, M. A., K. E. King, X. J. Zhou, and W. Fong, 2005, Handbook of mri pulse sequences: Medical Physics, **32**, 1452–1452.
- Berryhill, J. R., 1979, Wave-equation datuming: Geophysics, **44**, 1329–1344.
- Bevc, D., 1997, Imaging complex structures with semirecursive kirchhoff migration: Geophysics, **62**, 577–588.
- Billette, F., G. Lambare, and P. Podvin, 1997, Velocity macromodel estimation by stereotomography: SEG Technical Program Expanded Abstracts, **16**, 1889–1892.
- Biondi, B., 2006, Prestack exploding-reflectors modeling for migration velocity analysis: 76th Ann. Internat. Mtg., Expanded Abstracts, 3056–3060, Soc. of Expl. Geophys.
- , 2007, Prestack modeling of image events for migration velocity analysis: **SEP-131**, 71–89.
- , 2008, Automatic wave-equation migration velocity analysis: **SEP-134**, 65–78.
- Biondi, B., S. Fomel, and N. Chemingui, 1998, Azimuth moveout for 3-D prestack imaging: Geophysics, **63**, 574–588.
- Biondi, B. and G. Palacharla, 1996, 3-D prestack migration of common-azimuth data: Geophysics, **61**, 1822–1832.
- Biondi, B. and P. Sava, 1999, Wave-equation migration velocity analysis: SEG Technical Program Expanded Abstracts, **18**, 1723–1726.
- Biondi, B. and G. Shan, 2002, Prestack imaging of overturned reflections by reverse time migration: SEG Technical Program Expanded Abstracts, **21**, 1284–1287.
- Biondi, B. and W. W. Symes, 2004, Angle-domain common-image gathers for migration velocity analysis by wavefield-continuation imaging: Geophysics, **69**, 1283–1298.
- Biondi, B. and T. Tisserant, 2004, 3D angle-domain common-image gathers for migration velocity analysis: Geophysical Prospecting, **52**, 575–591.
- Castoldi, P., 2002, Multiuser detection in CDMA mobile terminals: Artech House Publishers.
- Claerbout, J. F., 1971, Toward a unified theory of reflector mapping: Geophysics, **36**, 467–481.
- Clapp, R., 2003, Geologically constrained migration velocity analysis, *in* Ph.D. thesis, Stanford University.
- , 2005, AMO inversion to a common azimuth dataset: **SEP-123**, 91–101.
- Clapp, R. G., 2006, AMO inversion to a common azimuth dataset: SEG Technical Program Expanded Abstracts, **25**, 2097–2101.
- Clapp, R. G., D. M. Chen, and S. Luo, 2008, Hypercube viewer: **SEP-134**, 179–192.
- Deregowski, S., 1990, Common offset migrations and velocity analysis: First Break, **8**, 224–234.
- Dinan, E. and B. Jabbari, 1998, Spreading codes for direct sequence CDMA and wideband CDMA cellular networks: IEEE Communications Magazine, **36**, 48–54.
- Duquet, B. and P. Lailly, 2006, Efficient 3D wave-equation migration using virtual planar sources: Geophysics, **71**, S185–S197.
- Gold, R., 1967, Optimal binary sequences for spread spectrum multiplexing: IEEE Transactions on Information Theory, **14**, 619–621.
- Guerra, C. and B. Biondi, 2008a, Phase encoding with gold codes for wave-equation migration: **SEP-136**, 23–42.
- , 2008b, Prestack exploding reflector modeling: The crosstalk problem: **SEP-134**, 79–92.

- Guerra, C., Y. Tang, and B. Biondi, 2009, Wave-equation tomography using image-space phase encoded data: SEG Technical Program Expanded Abstracts, **28**, 3964–3968.
- Halpert, A., 2010, A new method for more efficient seismic image segmentation: **SEP-140**, 213–228.
- Howe, D., M. Foster, T. Allen, I. Jack, D. Buddery, A. Choi, R. Abma, T. Manning, and M. Pfister, 2009, Independent simultaneous sweeping in libya-full scale implementation and new developments: SEG Technical Program Expanded Abstracts, **28**, 109–111.
- Javidi, B., G. Zhang, and J. Li, 1996, Experimental demonstration of the random phase encoding technique for image encryption and security verification: Optical Engineering, **35**, 2506–2512.
- Kapoor, S. J., M. O'Brian, D. Desta, I. Atakishiyev, and M. Tomida, 2007, Subsalt imaging — the raz/waz experience: SEG Technical Program Expanded Abstracts, **26**, 926–930.
- Kosloff, D., J. Sherwood, Z. Koren, E. Machet, and Y. Falkovitz, 1996, Velocity and interface depth determination by tomography of depth migrated gathers: Geophysics, **61**, 1511–1523.
- Kosloff, D., U. I. Zackhem, and Z. Koren, 1997, Subsurface velocity determination by grid tomography of depth migrated gathers: SEG Technical Program Expanded Abstracts, **16**, 1815–1818.
- Krebs, J. R., J. E. Anderson, D. Hinkley, R. Neelamani, S. Lee, A. Baumstein, and M.-D. Lacasse, 2009, Fast full-wavefield seismic inversion using encoded sources: Geophysics, **74**, WCC177–WCC188.
- Lailly, P., 1983, The seismic inverse problem as a sequence of before stack migrations: Conference on Inverse Scattering, Theory and Application, Society for Industrial and Applied Mathematics, Expanded Abstracts, 206–220.
- Levanon, N. and E. Mozeson, 2004, Radar signals: Wiley, John & Sons, Inc.
- Liu, F., D. W. Hanson, N. D. Whitmore, R. S. Day, and R. H. Stolt, 2006, Toward a unified analysis for source plane-wave migration: Geophysics, **71**, 129–139.
- Loewenthal, D., L. Lu, R. Roberson, and J. Sherwood, 1976, The wave equation applied to migration: Geophysical Prospecting, **24**, 380–399.
- Lomask, J., 2006, Seismic volumetric flattening and segmentation, *in* Ph.D. thesis, Stanford University.
- Martin, J. E., 1993, Simultaneous Vibroseis recording: Geophysical Prospecting, **41**, 943–967.
- Moldoveanu, N., J. Kapoor, and M. Egan, 2008, Full-azimuth imaging using circular geometry acquisition: The Leading Edge, **27**, 908–913.
- Mora, P., 1987, Nonlinear two-dimensional elastic inversion of multioffset seismic data: Geophysics, **52**, 1211–1228.
- Nocedal, J. and S. Wright, 2000, Numerical optimization: Springer Verlag, New York.
- Plessix, R.-E., 2009, Three-dimensional frequency-domain full-waveform inversion with an iterative solver: Geophysics, **74**, WCC149–WCC157.
- Pratt, R. G., Z. Song, P.R. Williamson, and M. Warner, 1996, Two-dimensional velocity model from wide-angle seismic data by wavefield inversion: Geophysical Journal International, **124**, 323–340.
- Regone, C. J., 2007, Using 3d finite-difference modeling to design wide-azimuth surveys for improved subsalt imaging: Geophysics, **72**, SM231–SM239.
- Rickett, J., B. Biondi, and D. Lumley, 1996, Modeling heterogeneous reservoirs using the first order Born approximation: **SEP-92**, 75–82.
- Rickett, J. E. and P. C. Sava, 2002, Offset and angle-domain common image-point gathers for shot-profile migration: Geophysics, **67**, 883–889.
- Rietveld, W. E. A., A. J. Berkhout, and C. P. A. Wapenaar, 1992, Optimum seismic illumination of hydrocarbon reservoirs: Geophysics, **57**, 1334–1345.
- Romero, L., D. Ghiglia, C. Ober, and S. Morton, 2000, Phase encoding of shot records in prestack migration: Geophysics, **65**, 426–436.
- Sava, P., 2003, Prestack residual migration in frequency domain: Geophysics, **68**, 634–640.
- , 2004, Migration and velocity analysis by wavefield extrapolation, *in* Ph.D. thesis, Stanford University.
- Sava, P. and B. Biondi, 2004a, Wave-equation migration velocity analysis-I: Theory: Geophysical Prospecting, **52**, 593–606.
- , 2004b, Wave-equation migration velocity analysis-II: Examples: Geophysical Prospecting, **52**, 607–623.
- Sava, P. and S. Fomel, 2006, Time-shift imaging condition in seismic migration: Geophysics, **71**, S209–S217.
- Sava, P. C. and S. Fomel, 2003, Angle-domain common-image gathers by wavefield continuation methods: Geophysics, **68**, 1065–1074.
- Schultz, P. S. and J. Claerbout, 1978, Velocity estimation and downward continuation by wavefront synthesis: Geophysics, **43**, 691–714.
- Shen, P., 2004, Wave-equation Migration Velocity Analysis by Differential Semblance Optimization: PhD thesis, Rice University.
- Shen, P. and W. W. Symes, 2008, Automatic velocity analysis via shot profile migration: Geophysics, **73**, VE49–VE59.
- Shen, P., W. W. Symes, and C. C. Stolk, 2003, Differential semblance velocity analysis by wave-equation migration: SEG

- Technical Program Expanded Abstracts, **22**, 2132–2135.
- Stork, C., 1992, Reflection tomography in the postmigrated domain: *Geophysics*, **57**, 680–692.
- Sun, P., S. Zhang, and F. Liu, 2002, Prestack migration of areal shot records with phase encoding: 72nd Ann. Internat. Mtg. Soc. Expl. Geophys., Expanded Abstracts, 1172–1175.
- Symes, W. W. and J. J. Carazzone, 1991, Velocity inversion by differential semblance optimization: *Geophysics*, **56**, 654–663.
- Tang, Y., 2009, Target-oriented wave-equation least-squares migration/inversion with phase-encoded hessian: *Geophysics*, **74**, WCA95–WCA107.
- Tang, Y., C. Guerra, and B. Biondi, 2008, Image-space wave-equation tomography in the generalized source domain: **SEP-136**, 1–22.
- Tarantola, A., 1984, Inversion of seismic reflection data in the acoustic approximation: *Geophysics*, **49**, 1259–1266.
- , 1987, *Inverse problem theory: Methods for data fitting and model parameter estimation*: Elsevier.
- Teh, P. C., P. Petropoulos, M. Ibsen, and D. J. Richardson, 2001, A comparative study of the performance of seven and 63-chip optical code-division multiple-access encoders and decoders based on superstructured fiber bragg gratings: *Journal of Lightwave Technology*, **19**, 1352–1365.
- Tygel, M., J. Schleicher, and P. Hubral, 1994, Pulse distortion in depth migration: *Geophysics*, **59**, 1561–1569.
- Valenciano, A. A., B. L. Biondi, and R. G. Clapp, 2009, Imaging by target-oriented wave-equation inversion: *Geophysics*, **74**, WCA109–WCA120.
- Vigh, D. and E. W. Starr, 2008, 3d prestack plane-wave, full-waveform inversion: *Geophysics*, **73**, VE135–VE144.
- Virieux, J. and S. Operto, 2009, An overview of full-waveform inversion in exploration geophysics: *Geophysics*, **74**, WCC1–WCC26.
- Wang, B., V. Dirks, P. Guillaume, F. Audebert, and D. Epili, 2006, A 3d subsalt tomography based on wave-equation migration-perturbation scans: *Geophysics*, **71**, E1–E6.
- Wang, R. K., I. A. Watson, and C. Chatwin, 1996, Random phase encoding for optical security: *Optical Engineering*, **35**, 2464–2469.
- Ward, R. M., R. H. Brune, A. Ross, and L. H. Kumamoto, 1990, Phase encoding of Vibroseis signals for simultaneous multisource acquisition: SEG Technical Program Expanded Abstracts, **9**, 938–941.
- Weishaupt, D., V. Koechli, and J. M. Froehlich, 2006, *How Does MRI Work? : An Introduction to the Physics and Function of Magnetic Resonance Imaging*.
- Whitmore, N. D., 1995, An imaging hierarchy for common angle plane wave seismograms, *in* Ph.D. thesis, University of Tulsa.
- Woodward, M. J., 1992, Wave-equation tomography: *Geophysics*, **57**, 15–26.
- Yamada, H., K. Takada, and S. Mitachi, 1998, Crosstalk reduction in a 10-ghz spacing arrayed-waveguide grating by phase-error compensation: *Journal of Lightwave Technology*, **16**, 364–371.
- Yang, T. and P. Sava, 2009, Wave-equation migration velocity analysis using extended images: SEG Technical Program Expanded Abstracts, **28**, 3715–3719.
- Zigangirov, K., 2004, *Theory of code division multiple access communication*: Wiley, John & Sons, Inc.